

First-principles Based Micro-kinetic Modeling for Catalysts Design

by

Mingxia Zhou

B.S., Beijing University of Chemical Technology, 2013

AN ABSTRACT OF A DISSERTATION

submitted in partial fulfillment of the requirements for the degree

DOCTOR OF PHILOSOPHY

Department of Chemical Engineering
College of Engineering

KANSAS STATE UNIVERSITY
Manhattan, Kansas

2018

Abstract

Efficient and selective catalysis lies at the heart of many chemical reactions, enabling the synthesis of chemicals and fuels with enormous societal and technological impact. A fundamental understanding of intrinsic catalyst properties for effective manipulation of the reactivity and selectivity of industrial catalysts is essential to select proper catalysts to catalyze the reactions we want and hinder the reactions we do not want.

The progress in density functional theory (DFT) makes it possible to describe interfacial catalytic reactions and predict catalytic activities from one catalyst to another. In this study, water-gas shift reaction (WGSR) was used as a model reaction. First-principles based micro-kinetic modeling has been performed to deeply understand interactions between competing reaction mechanisms, and the relationship with various factors such as catalyst materials, structures, promoters, and interactions between intermediates (e.g., CO self-interaction) that govern the observed catalytic behaviors.

Overall, in this thesis, all relevant reaction mechanisms in the model reaction on well-defined active sites were developed with first-principles calculations. With the established mechanism, the promotional effect of K adatom on Ni(111) on WGSR compared to the competing methanation was understood. Moreover, the WGSR kinetic trend, with the hydrogen production rate decreasing with increasing Ni particle diameters (due to the decreasing fractions of low-coordinated surface Ni site), was reproduced conveniently from micro-kinetic modeling techniques. Empirical correlations such as Brønsted-Evans-Polanyi (BEP) relationship for O-H, and C-O bond formation or cleavage on Ni(111), Ni(100), and Ni(211) were incorporated to accelerate computational analysis and generate trends on other transition metals (e.g., Cu, Au, Pt). To improve the numerical quality of micro-kinetic modeling, later interactions of main

surface reaction intermediates were proven to be critical and incorporated successfully into the kinetic models. Finally, evidence of support playing a role in the enhancement of catalyst activity and the impact on future modeling will be discussed.

DFT will be a powerful tool for understanding and even predicting catalyst performance and is shaping our approach to catalysis research. Such molecular-level information obtained from computational methods will undoubtedly guide the design of new catalyst materials with high precision.

First-principles Based Micro-kinetic Modeling for Catalysts Design

by

Mingxia Zhou

B.S., Beijing University of Chemical Technology, 2013

A DISSERTATION

submitted in partial fulfillment of the requirements for the degree

DOCTOR OF PHILOSOPHY

Department of Chemical Engineering
College of Engineering

KANSAS STATE UNIVERSITY
Manhattan, Kansas

2018

Approved by:

Major Professor
Professor Bin Liu

Copyright

© Mingxia Zhou 2018.

Abstract

Efficient and selective catalysis lies at the heart of many chemical reactions, enabling the synthesis of chemicals and fuels with enormous societal and technological impact. A fundamental understanding of intrinsic catalyst properties for effective manipulation of the reactivity and selectivity of industrial catalysts is essential to select proper catalysts to catalyze the reactions we want and hinder the reactions we do not want.

The progress in density functional theory (DFT) makes it possible to describe interfacial catalytic reactions and predict catalytic activities from one catalyst to another. In this study, water-gas shift reaction (WGSR) was used as a model reaction. First-principles based micro-kinetic modeling has been performed to deeply understand interactions between competing reaction mechanisms, and the relationship with various factors such as catalyst materials, structures, promoters, and interactions between intermediates (e.g., CO self-interaction) that govern the observed catalytic behaviors.

Overall, in this thesis, all relevant reaction mechanisms in the model reaction on well-defined active sites were developed with first-principles calculations. With the established mechanism, the promotional effect of K adatom on Ni(111) on WGSR compared to the competing methanation was understood. Moreover, the WGSR kinetic trend, with the hydrogen production rate decreasing with increasing Ni particle diameters (due to the decreasing fractions of low-coordinated surface Ni site), was reproduced conveniently from micro-kinetic modeling techniques. Empirical correlations such as Brønsted-Evans-Polanyi (BEP) relationship for O-H, and C-O bond formation or cleavage on Ni(111), Ni(100), and Ni(211) were incorporated to accelerate computational analysis and generate trends on other transition metals (e.g., Cu, Au, Pt). To improve the numerical quality of micro-kinetic modeling, later interactions of main

surface reaction intermediates were proven to be critical and incorporated successfully into the kinetic models. Finally, evidence of support playing a role in the enhancement of catalyst activity and the impact on future modeling will be discussed.

DFT will be a powerful tool for understanding and even predicting catalyst performance and is shaping our approach to catalysis research. Such molecular-level information obtained from computational methods will undoubtedly guide the design of new catalyst materials with high precision.

Table of Contents

List of Figures	xiv
List of Tables	xxii
Acknowledgements	xxiv
Chapter 1 - Introduction.....	1
1.1 Model Reaction of This Thesis	1
1.2 Computational Catalysts Design.....	2
1.3 Factors Determining Catalyst Performance	4
1.3.1 Role of Catalyst Surface Structure.....	4
1.3.2 Role of Catalyst Particle Size	5
1.3.3 Role of Promoter	7
1.3.4 Role of Supports	8
1.4 Organization of This Thesis.....	10
References.....	10
Chapter 2 - Computational Methods and Theory	25
2.1 Density Functional Theory (DFT)	25
2.1.1 DFT based on Kohn-Sham Formulation.....	25
2.1.2 Plane Wave Basis Set and Brillouin Zone	26
2.1.3 Pseudopotential	28
2.1.4 Electron Exchange-correlation Functionals	28
2.1.5 Electron Self-interaction Errors	29
2.2 Modeling Techniques for Surface Chemistry	30
2.2.1 Generate Single Crystal Surfaces.....	30

2.2.2 Bader Charge Analysis	32
2.2.3 Transition State Search	32
2.2.4 Linear Scaling Relationship	35
2.2.5 Brønsted-Evans-Polanyi (BEP) Relationship	36
2.2.6 Thermodynamic Properties Estimation.....	38
2.2.7 Micro-kinetic Modeling	42
2.2.8 Volcano Plots and Trend Analysis and Predictions	44
References.....	46
Chapter 3 - Mechanism and Selectivity of WGSR on Ni(111) Surface	52
3.1 Introduction.....	52
3.2 Computational Methods.....	54
3.3 WGSR and Methanation Mechanisms on Clean Ni(111).....	55
3.3.1 H ₂ O Dissociation	62
3.3.2 WGSR Pathways on Clean Ni(111) Surface.....	62
3.3.3 Methanation Reaction	65
3.3.4. Comparison between WGSR and Methanation Reaction	68
3.4 Conclusions.....	70
3.5 Acknowledgements.....	70
References.....	71
Chapter 4 - Promoter Effects for Catalyst Reactivity	76
4.1 Introduction.....	76
4.2 Case Study 1: Selectivity of WGSR on Potassium Modified Ni (111)	77
4.2.1 Computational Methods.....	78

4.2.2 Adsorption of WGSR and Methanation Reaction Intermediates on K-modified Ni(111) surface	78
4.2.3 Effect of K on WGSR and Methanation Elementary Steps	82
4.2.4 Effect of Promoter on WGSR Selectivity	86
4.3 Case Study 2: Ni-doping Effect on Oxygen Removal from an Orthorhombic Mo ₂ C(001) Surface	88
4.3.1 Theoretical Methods	89
4.3.2 O* Removal over Mo ₂ C(001) Surfaces	92
4.4 Conclusions.....	108
4.5 Acknowledgements.....	109
References.....	111
Chapter 5 - Structure and Size Effects of Ni Nanocatalysts for Hydrogen Production via WGSR	116
5.1 Introduction.....	116
5.2 Computational Methods.....	118
5.2.1 DFT Calculations	118
5.2.2 Micro-kinetic Modeling	118
5.2.3 Generation of Ni Nanoparticles	119
5.3 WGSR and Methanation on Ni(111), Ni(100), and Ni(211)	119
5.3.1 Adsorptions of Reaction Intermediates.....	119
5.3.2 BEP Relationship	124
5.3.3 Free Energy Diagrams of WGSR and Methanation on Ni(111), Ni(100), and Ni(211)	129

5.4 Micro-kinetic Modeling of WGSR and Methanation	132
5.4.1 First-principles Based Mechanism for Micro-kinetic Modeling.....	132
5.4.2 Ni Nanocatalyst Facets and Size Effects on Reactivity and Selectivity Dependence	133
5.4.3 Feed Composition Effect on WGSR and Methanation	139
5.5 Conclusions.....	140
5.6 Acknowledgements.....	141
References	142
Chapter 6 - Adsorbate-adsorbate Interaction Effects for Hydrogen Production via WGSR	146
6.1 Introduction.....	146
6.2 Computational Methods.....	148
6.3 Chemisorptions on Ni(111), Ni(100), and Ni(211) at Higher Coverages	150
6.3.1 CO Adsorption	150
6.3.2 Lateral Interactions between CO and Other Species	158
6.4 Impact on Hydrogen Production on Ni(111), Ni(100), and Ni(211) at 4/9ML CO Coverage	162
6.4.1 Free Energy Diagrams of WGSR	162
6.4.2 Micro-kinetic Modeling	164
6.4.3 Reaction Orders from Micro-kinetic Modeling	168
6.5 Hydrogen Productions on Other Transition Metals.....	170
6.5.1 Adsorption of Reaction Intermediates on Other Transition Metals	170
6.5.2 Micro-kinetic Modeling on Transition Metals.....	172
6.6 Conclusions.....	178
6.7 Acknowledgments	179

References.....	180
Chapter 7 - Insights into Catalysis at Catalyst-Support Interfaces	182
7.1 Introduction.....	182
7.2 Case Study 1: WGS over Cu/CeO ₂ and Ni/CeO ₂ catalysts.....	183
7.2.1 Computational Methods.....	183
7.2.2 The Structure of Cu/CeO ₂ and Ni/CeO ₂ Catalysts.....	186
7.2.3 Adsorption of Reaction Intermediates	187
7.2.4 WGS Pathways on Cu/CeO ₂ and Ni/CeO ₂ Catalysts	191
7.3 Case Study 2: CO Oxidation over Pt/h-BNNS	195
7.3.1 Computational Details	196
7.3.2 Results and Discussion	197
7.4 Conclusions.....	201
7.5 Acknowledgements.....	201
References.....	202
Chapter 8 - Conclusions.....	208
Appendix A - Vibrational Frequencies of Reaction Intermediates on Ni(111), Ni(100), and Ni(211).....	210
Appendix B - Input Files for Micro-kinetic Modeling on Ni Nanoparticles	213
B.1. Input Energy File.....	213
B.2. Set Up Reaction Parameters.....	217
Appendix C - Mechanisms for Micro-kinetic Modeling on Ni(111), Ni(100) and Ni(211) surfaces	224
C.1 Elementary Steps on Ni(111) and Ni(100):	224

C.2 Elementary Steps on Ni(211):	224
C.3 Elementary Steps for Ni Nanoparticles:	225
Appendix D - Differential Binding Energies of CO on Pt(111)	228

List of Figures

Figure 1.1. Schematic loop describing proposed computational catalyst design strategy based on first-principles modeling.....	3
Figure 2.1. Surface models based on a FCC single crystal: (a) (111), (b) (100), (c) (211), and (d) top view of (211) facet. Available adsorption sites on each surface are labeled. Black dashed lines represent the boundaries of the supercell. The (211) facets in (c) and (d) are further expanded to show the 4-fold site. The edge atoms in (211) are highlighted in turquoise.	31
Figure 2.2. Illustrations of finding saddle point on a potential energy surface using dimer method. ³⁷	34
Figure 2.3. Binding energies of CH_x intermediates (crosses: $x = 1$; circles: $x = 2$; triangles: $x = 3$), plotted against adsorption energies of C, adapted from Ref.[39]......	36
Figure 2.4. Calculated activation energies (E_a) for N_2 , CO, NO, and O_2 dissociation on a number of different metals plotted as a function of the calculated dissociative chemisorption potential energy for the dissociation products (ΔE). ⁴⁰	38
Figure 2.5. (a) Calculated rate as a function of a single descriptor of E_N . A data point of an intermetallic compound with active sites consisting of both Co and Mo is indicated. Experiments show such a material with activity close to that of Ru. ⁵⁴ (b) Ammonia synthesis rate as a function of nitrogen adsorption energy (E_N) and N_2 dissociation barrier ($E_{\text{N-N}}$), with energetics and the corresponding scaling relation for stepped sites (dashed black–white) showing a linear relationship between $E_{\text{N-N}}$ and E_N . The alkali-promoted scaling relation is represented by the magenta line. ⁵²	45

Figure 3.1. Reaction schemes of WGSR and methanation reaction. The asterisks (*) represents an open surface site or an adsorbed species. Water dissociation and H ₂ formation are not shown in this scheme.....	52
Figure 3.2. Optimized structures of reaction intermediates (in Table 3.1) on clean Ni(111). C, O, H, and Ni are depicted in grey, red, white, and blue, respectively.	58
Figure 3.3. Transition state (TS) structures of elementary steps (labeled the same way as in Table 3.2) on clean Ni(111). The side view of each TS structure is shown as inset figure. C, O, H, and Ni are depicted in grey, red, white, and blue, respectively.	61
Figure 3.4. Potential energy surfaces (PESs) of the redox (blue), carboxyl (red), and formate (purple) pathways on clean Ni(111). Transition state species are marked as TS and extra OH* are added to balance the whole step. Two black pathways represent water dissociation and gas product formation.....	63
Figure 3.5. Potential energy surfaces of the five methanation pathways: i) CO (blue), ii) COH (red), iii) CHO (purple), iv) CHOH (brown and yellow), and v) CH ₂ OH (green) pathways considered in this work. Transition-state species are marked as TS, and extra H* is added if necessary to balance the whole step. Two black lines represent water dissociation and CH ₄ formation.....	66
Figure 3.6. Potential energy surfaces of WGSR (redox and carboxyl pathways) and methanation (CHO pathway) on clean Ni(111) surface. Transition state species are marked as TS and extra OH* and H* are added if necessary to balance reactive species. Black pathways represent water dissociation and gas products formation.....	69
Figure 4.1. Optimized structures of reaction intermediates (in Table 4.1) on K-modified Ni(111) surface. C, O, H, Ni, and K are depicted in grey, red, white, blue, and purple, respectively.	80

Figure 4.2. Transition state (TS) structures of elementary steps (labeled the same way as in Table 4.2) on K-modified Ni(111) surface. The side view of each TS structure is shown as inset figure. C, O, H, Ni, and K are depicted in grey, red, white, blue, and purple, respectively.	85
Figure 4.3. Potential energy surfaces of WGSR and methanation pathways on clean Ni(111) (solid paths) and K-modified Ni(111) surfaces (dashed paths).	86
Figure 4.4. Top view and side view of optimized structures of Mo ₂ C(001) surfaces. (a) un-doped T _{Mo} Mo ₂ C(001) surface, (b) un-doped T _C Mo ₂ C(001) surface. The top two layers of Mo atoms are depicted in different color to differentiate Mo on different positions. Same color scheme is utilized throughout the paper.	91
Figure 4.5. Top view of optimized structures of Mo ₂ C(001) surfaces. (a) Ni-adsorbed T _{Mo} Mo ₂ C(001), (b) Ni-replaced T _{Mo} Mo ₂ C (001), (c) Ni-adsorbed T _C Mo ₂ C(001), (d) Ni-replaced T _C Mo ₂ C(001). The purple sphere represents the Ni atom. The red arrow shows the Bader charges of selected atoms. The white arrow shows the distance of Ni dopant to nearby Mo atom.	95
Figure 4.6. Optimized structures of 4 intermediates shown in Table 4.3 on the un-doped and Ni-doped Mo ₂ C(001) surfaces. The purple, red, and white spheres represent Ni, O, and H, respectively. The shortest Ni-O and Ni-H distances at the surfaces are also shown.	96
Figure 4.7. Transition state structures of elementary steps of O* removal from (a) T _{Mo} Mo ₂ C(001) surface, (b) T _C Mo ₂ C(001) surface. The bond lengths of transition states are marked here for better understanding of the transition state structures. The Ni-O distances on the surface are also shown. The energetics and energy barriers associated with the reaction steps are presented in Table 4.4 and Table 4.5	102

Figure 4.8. Potential energy surface of O* removal on Mo ₂ C(001) surface. Transition state species are marked as TS to distinguish from the intermediates. Extra OH* is added or removed to OH-assisted O* removal to balance the whole step.	106
Figure 4.9. Water formation profiles obtained during temperature-programmed reduction of undoped and Ni-doped bulk Mo ₂ C catalysts. Prior to the experiments, the synthesized carbides were passivated with 1% O ₂ /N ₂ and stored for different lengths of time in air. Experimental conditions: reduction gas, 70% H ₂ /Ar; temperature program, stabilization at 100 °C and ramp up to 800 °C at 10 °C/min; H ₂ O profiles determined with a quadrupole mass spectrometer.....	108
Figure 5.1. Optimized structures of the clean surface and the 14 intermediates in Table 5.1 on (a) Ni(100), and (b) Ni(211). The grey, red, white, and blue spheres represent C, O, H, and Ni, respectively. The edge Ni atoms in Ni(211) are highlighted in turquoise. The adsorption sites on Ni(100) and Ni(211) are marked on the clean surface (clean_surf).	122
Figure 5.2. (a) BEP relationship for C–O bond forming/scission; (b) BEP relationship for C–H/O–H bond forming/scission. The elementary steps are expressed in the exothermic direction. E _{FS} and E _{TS} are relative energies to gas phase initial state energies.	124
Figure 5.3. Optimized transition state structures on (a) Ni(100); and (b) Ni(211). The grey, red, white, and blue spheres represent C, O, H, and Ni, respectively. The edge Ni atoms in Ni(211) are highlighted with the turquoise color.	126
Figure 5.4. Free energy diagrams representing the redox and carboxyl pathways on Ni(111), Ni(100) , and Ni(211) surface at 600 K and 1 bar. The black path represents CO adsorption, H ₂ O adsorption, dissociation, and H ₂ formation.....	129

Figure 5.5. Free energy diagrams of the formyl (purple) and HCOH (green) pathway on Ni(111), Ni(100), and Ni(211) facets at 600 K and 1 bar. The black path represents CO adsorption, H ₂ O adsorption, dissociation, and CH ₄ formation steps.	131
Figure 5.6. Turnover frequencies (s ⁻¹) of H ₂ and CH ₄ production on Ni(111), Ni(100), and Ni(211) at 1 bar, respectively. The feed composition has a molar ratio of CO : H ₂ O = 1:2. Vertical black dash line marks the reaction conditions of free energy diagram being generated in section 5.3.3.	134
Figure 5.7. Surface coverage of CO* on (a) Ni(111) and Ni(100) and surface coverage of CO* and O* on (b) Ni(211) with feed composition of molar ratio of CO : H ₂ O = 1:2 at 1bar.	135
Figure 5.8. (a) Atomic fractions of surface Ni atoms (black square), and fractions of Ni atoms at close-packed (solid orange circle), open-packed (solid green circle), and step edge sites (solid red circle) for unsupported cuboctahedral Ni nanoparticles with diameter from 1nm ~ 8nm. The schematic representations of cuboctahedra of 1, 4, and 8 nm diameters are also shown; (b) TOF (s ⁻¹) of H ₂ ; and (c) CH ₄ production at 600K and 1bar. The TOF is the sum of TOF on Ni(111), Ni(100) and Ni(211). The feed composition has a molar ratio of CO: H ₂ O = 1:2. The solid and dashed lines are simply to guide the trend of modeling results.	137
Figure 5.9. Turnover frequencies (s ⁻¹) of CH ₄ production on Ni(111), Ni(100), and Ni(211) at 1bar, respectively. The feed gas molar composition is 2.5% CO, 25% H ₂ O, 12.5% CO ₂ , 37.5% H ₂ , and balance N ₂	140
Figure 6.1. Optimized CO chemisorption geometries on (a) Ni(111), (b) Ni(100), and (c) Ni(211) at different coverages. Adsorption sites are labeled on each clean slab. The clean Ni(211) surface in (c) is further expanded to show the 4-fold site. Ni, C, O, and H are depicted in blue, grey, red, and white, respectively. The edge Ni atoms in Ni(211) are highlighted in	

turquoise. The dashed yellow circle indicates the original location of Ni atom and the yellow arrow indicates the direction of Ni dislocation with high CO coverage on Ni(211). The dashed black lines indicate the boundaries of the supercell..... 152

Figure 6.2. (a) Coverage-dependent CO differential binding energies (BE_{diff}) on Ni(111), Ni(100), and Ni(211) surfaces. (b) CO BE_{diff} as a function of surface area per CO molecule on Ni(111), Ni(100), and Ni(211) surfaces. (c) Coverage-dependent differential CO free energy difference ($G_{diff\theta}$) on Ni(111), Ni(100), and Ni(211) surface. The dashed line indicates that the BE_{diff} or G_{diff} is at 0 eV, corresponding to the *saturation* coverage. 155

Figure 6.3. Top views of optimized H₂O, H, OH, O, and COOH on (a) Ni(111), (b) Ni(100), and (c) Ni(211) at 4/9 ML CO coverage. The white dash circles indicate the original CO locations, and the white arrows indicate the moving direction of CO to the new locations once co-adsorbed H₂O, H, OH, O, and COOH are introduced..... 159

Figure 6.4. Free energy diagrams for redox and carboxyl pathways at 4/9 ML CO coverage on (a) Ni(111), (b) Ni(100), and (c) Ni(211). The solid lines are the original free energies with no pre-adsorbed CO, and the dashed lines corresponding to co-adsorbed 4/9 ML CO. The blue path represents the redox pathway; the red path represents the carboxyl pathway, and the black path represents CO, H₂O adsorption and activation steps, and H₂ formation steps. 163

Figure 6.5. The TOF of H₂ production on (a) Ni(111), (c) Ni(100), and (e) Ni(211) at 1 bar. The predicted reaction intermediates coverages on (b) Ni(111), (d) Ni(100), and (f) Ni(211). The feed has a molar ratio of CO:H₂O = 1:2. 166

Figure 6.6. Comparison of H₂ production TOFs on Ni(111), Ni(100), and Ni(211). The feed has a molar ratio of CO: H₂O = 1:2..... 168

Figure 6.7. Optimized structure of the 6 intermediates for WGSR in **Table 6.3** on (a) Pt(111) surface, (b) Cu(111) surface, (c) Cu(211) surface, and (d) Au(111) surface. The dark blue, pink, and gold atoms represent Pt, Cu, and Au atoms respectively. The edge Cu atoms in Cu(211) surface are highlighted in dark red..... 172

Figure 6.8. The TOF of hydrogen at varying binding energies of CO and H₂O with (a) no CO self-interaction, (b) ¼ CO self-interaction, (c) ½ CO self-interaction, (d) ¾ CO self-interaction, and (e) full CO self-interaction included at T = 573 K, P_{CO} = 24.3 kPa and P_{H₂O} = 31.4 kPa. .. 174

Figure 6.9. The predicted CO coverage as a function of CO and H₂O binding energies, with (a) no CO self-interaction, (b) ¼ CO self-interaction, (c) ½ CO self-interaction, (d) ¾ CO self-interaction, and (e) full CO self-interaction included at T = 573 K, P_{CO} = 24.3 kPa and P_{H₂O} = 31.4 kPa..... 175

Figure 7.1. Optimized structures of (a1) Cu/CeO₂ and (b1) Ni/CeO₂, and (a2) reconstructed Cu/CeO₂ and (b2) reconstructed Ni/CeO₂. The * and # indicate the two type of adsorption sites considered in the analysis (see details in text). Dashed black lines indicate the boundaries of the supercell. Areas enclosed by purple dashed lines indicate the metal/oxide interface. The red arrow indicates the width of the super cell. Ce, O, Cu, and Ni atoms are depicted in white, red, pink, and blue, respectively. 185

Figure 7.2. Optimized structures of (a) Cu/CeO₂ with Ov and (b) Ni/CeO₂ with Ov. The Ov is highlighted as black dots. The § indicates one type of adsorption sites considered in the analysis (see details in text). Black dashed lines indicate the boundaries of the supercell. Areas enclosed in purple dashed lines indicate the metal/oxide interface. 187

Figure 7.3. Optimized structures of reaction intermediates (a) CO*, (b) H₂O§, (c) H#, (d) OH*, and (e) COOH* (in **Table 7.1**) on Cu/CeO₂ surface. H and C atoms are depicted in white and

grey, respectively. The black arrow indicates the position of Ov, which cannot recognize as being overlapped by the adsorbate in (b). 189

Figure 7.4. Optimized structures of reaction intermediates (a) CO*, (b) H₂O*, (c) H#, (d) OH*, and (e) COOH* (in **Table 7.1**) on Ni/CeO₂ surface. The black arrow indicates the position of Ov, which cannot recognize as being overlapped by the adsorbate in (b). 190

Figure 7.5. Potential energy surfaces of the WGSR carboxyl pathway on (a) Cu/CeO₂ (black solid line), and unsupported Cu(111) (black dashed line), (b) Ni/CeO₂ (red solid line) and Ni(111) (red dashed line). 194

Figure 7.6. Schematic illustration of h-BNNS with B_v and N_v. (a) h-BNNS with B vacancy and N-terminated edge. (b) h-BNNS with N vacancy and B-terminated edge. 196

Figure 7.7. Optimized structures and Bader charges of pyramidal Pt₄ cluster on h-BNNS. (a) Pt₄ cluster on clean, vacancy-free h-BNNS, (b) Pt₄ cluster h-BNNS with N_v, and (c) Pt₄ cluster on h-BNNS with B_v. 198

Figure 7.8. The most stable configuration of CO (a-c) and O₂ (d-f) adsorption and BEs on Pt₄ cluster. (a) Pt₄ cluster on clean, vacancy-free h-BNNS, (b) Pt₄ cluster h-BNNS with B_v, and (c) Pt₄ cluster on h-BNNS with N_v, (d) Pt₄ cluster on clean, vacancy-free h-BNNS, (e) Pt₄ cluster h-BNNS with B_v, and (f) Pt₄ cluster on h-BNNS with N_v. 200

List of Tables

Table 3.1. Binding energies (BE, in eV), site preferences, and literature values for WGSR and methanation intermediates on Ni(111) surface.	57
Table 3.2. DFT-calculated reaction energies (ΔE [eV]), energy barriers (E_a [eV], and imaginary frequencies (ν_i [cm^{-1}]) of the transition states of the elementary reactions on clean Ni(111) surface.	59
Table 4.1. Binding energies (BE, in eV), site preferences, and differential binding energies ($\Delta\Delta E$, in eV) for WGSR and methanation intermediates on K-modified Ni(111) surface.	79
Table 4.2. DFT-calculated reaction energies (ΔE [eV]), energy barriers (E_a [eV], and imaginary frequencies (ν_i [cm^{-1}]) of the transition states of the elementary reactions on K-modified Ni(111) surface.	83
Table 4.3. BEs (eV) of O^* (Equation 42), OH^* (Equation 43), H^* (Equation 44), and H_2O^* (Equation 45) on un-doped and Ni-doped $\text{Mo}_2\text{C}(001)$ surfaces.	97
Table 4.4. Calculated reaction energies (ΔE [eV]) of O^* removal via OH^* formation and H_2O^* formation on un-doped and Ni doped $\text{Mo}_2\text{C}(001)$ surfaces.	99
Table 4.5. Calculated energy barriers (E_a [eV]) of O^* removal via OH^* formation and H_2O^* formation on un-doped and Ni doped $\text{Mo}_2\text{C}(001)$ surfaces.	100
Table 5.1. Binding energies (BE), site preferences of reaction intermediates on Ni(111), Ni(100), and Ni(211) surfaces.	120
Table 5.2. Energy barriers of the elementary steps for C-O bond formation/scission and C-H/O-H bond formation/scission on Ni(111), Ni(100), and Ni(211) surfaces.	128

Table 6.1. Binding energies (in eV) of CO, H ₂ O, OH, H, O, and COOH on Ni(111), Ni(100) and Ni(211) without pre-adsorbed CO and at 4/9 ML CO coverage. The italicized numbers highlight the <i>BEA – 4CO</i> enhanced by co-adsorbed CO molecules.	161
Table 6.2. Reaction orders of CO, H ₂ O, CO ₂ and H ₂ (a, b, c, d) on Ni(111), Ni(100), and Ni(211) surfaces, respectively.	169
Table 6.3. Binding energies (BEs) and site preference of WGSR reaction intermediates on Pt(111), Cu(111), Cu(211), and Au(111) surfaces.	171
Table 7.1. Binding energies (BEs) of reaction intermediates on Cu/CeO ₂ , Ni/CeO ₂ catalysts and unsupported Cu(111), Ni(111) surfaces.	188
Table 7.2. DFT calculated reaction energies (ΔE [eV]) of the elementary steps on Cu/CeO ₂ and Ni/CeO ₂ catalysts.	193

Acknowledgements

I would like to express my thanks to my excellent advisor, Professor Bin Liu for encouraging, guiding, teaching, and supporting my PhD studies. I appreciate all his dedications and ideas sharing with me to make my PhD experience productive. His advice on both research and career have been priceless and allowed me to grow as a researcher. I would also like to thank my committee members, Professor Christine Aikens, Professor Keith Hohn, and Professor Placidus Amama served as my committee and time, attention, and guidance they provided.

I also want to thank Larry A. Curtiss, Lei Cheng, and Rajeev S. Assary at Argonne National Laboratory for providing opportunity to work with them and helping me with the researches. I am also grateful to the members of the Liu's group: Song Liu, Nannan Shan, Jiayi Xu that I had a great time to work with.

Last, but not least, I am greatly indebted to my family for all of the sacrifices they have made on my behalf. Especially, I would like to express appreciation to my beloved husband Xu Li who was always my support along the way.

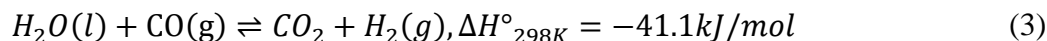
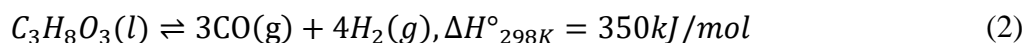
Chapter 1 - Introduction

Fuels and chemicals (e.g., hydrogen, methanol, and alkyl benzenes) that we depend on in every aspect of our lives are often produced through catalytic reactions, such as (de)hydrogenation,^{1,2} hydrogenolysis,³ hydrodeoxygenation (HDO),⁴ and dehydroxylation⁵ involving different feedstocks (e.g., hydrocarbons,⁶ cellulose,⁷ glycerol,⁵ furfural⁸). Efficient and selective catalysts that accelerate and enhance chemical reactions are at the heart of these processes. In order to improve catalyst reactivity and selectivity, the factors that determine catalyst reactivity and selectivity should be developed to favor the reactions we want and hinder the reaction we do not want.

1.1 Model Reaction of This Thesis

Hydrogen is an important clean fuel⁹⁻¹¹ with high energy capacity and the largest amount of energy per mass unit compare to any other known fuels (121 MJ/kg)¹². In addition, hydrogen is also widely used for fuel upgrading¹³, ammonia synthesis¹⁴, and fine chemicals production¹⁵. Steam reforming of hydrocarbons (e.g., CH₄ as shown by Equation (1)) is a major industrial route to obtain hydrogen source in the form of syngas.¹⁶⁻¹⁸ Alternative routes that utilize biomass-derived polyols (e.g., glycerol as shown in Equation (2)) have been successfully employed to demonstrate the feasibility of obtaining biorenewable hydrogen.^{6,19,20} Water-gas shift reaction (WGSR) (Equation (3)) is ubiquitous in reforming reactions, and consumes CO to form CO₂ and boost hydrogen production^{6,21}. To a great extent, WGSR provides the benefits of boosting hydrogen productivity and mitigating catalyst poisoning by removing the strong-binding CO molecules from active sites.^{22,23} WGSR contains different reaction steps such as water activation and CO oxidation, which could also refer to other reactions that contain same

reaction steps (e.g., hydrogen evolution reaction). Therefore, WGSR is a main model reaction in this thesis driven by the need for clean energy to sustain our societal needs.



Detailed insights into how catalyst materials (e.g., pure transition metals, oxide supported transition metals), surface structures (e.g., (111), (100), and (211) surfaces), catalyst particle sizes, promoters (e.g., Ni(111) with K-adatom), process conditions (e.g., temperature, pressure, and feed gas composition), and adsorbate-adsorbate interaction (e.g., CO self-interaction) control WGSR catalyst reactivity and selectivity is studied. In addition, first-principles based micro-kinetic modeling framework is established to analyze, predict, and guide new catalyst materials design.

1.2 Computational Catalysts Design

Extraordinary progress has been made in first-principles based computational methods and presents an unprecedented opportunity for catalyst design.^{24,25} [Figure 1.1](#) shows a closed-loop catalyst design underlined in this thesis. Overall, to describe a catalyst realistically, a hierarchical approach is able to simplify a complex problem so that various key aspects can be understood. The reaction mechanism on this complex catalyst surface should be determined and catalyst reactivity and selectivity are predicted to guide experimental studies.

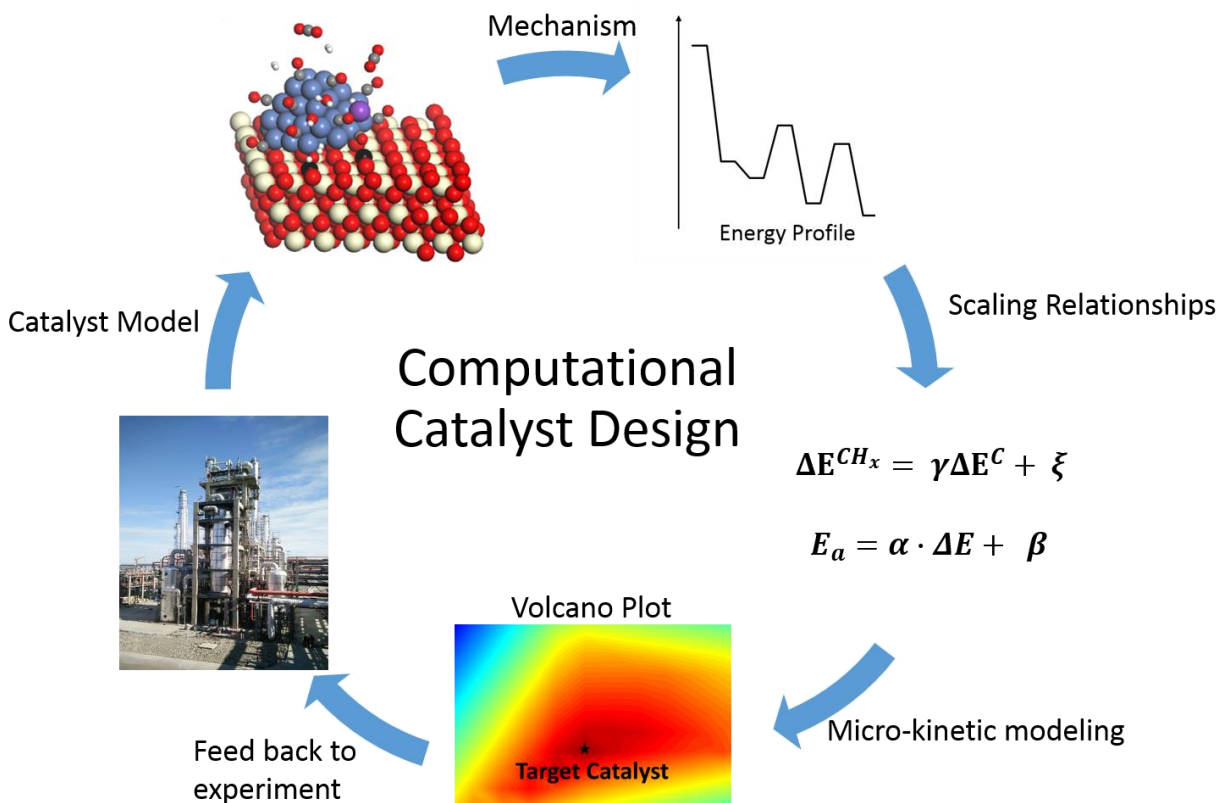


Figure 1.1. Schematic loop describing proposed computational catalyst design strategy based on first-principles modeling.

In particular, the development of scaling relationships accelerates the elucidation of adsorption trends across extensive catalytic surfaces.²⁶ The scaling relationship, coupled with Brønsted-Evans-Polanyi relationships, which predict transition state energies of elementary reactions from the thermodynamics of those reactions,²⁷⁻³¹ can be further applied to describe complex potential and free energy surfaces on catalyst as a function of simple parameters, known as descriptor.³² Then kinetics can be calculated to predict catalytic activity trends, conveniently represented as volcano-type relationships between rate and descriptors.^{24,33} A detailed

description of the modeling techniques for surface chemistry will be presented in Chapter 2 section 2.2.

However, standard (density functional theory) DFT calculations are normally performed at low surface coverage, which is not the case on realistic catalytic surfaces, which are usually crowded with different adsorbates, interacting with each other. Lateral interactions, having significant influence on species adsorption and desorption energies and transition state stabilities,^{34,35} are being recognized to be essential for computational catalytic activity prediction.^{34,36,37} To improve the numerical quality of micro-kinetic modeling, lateral interactions of main surface reaction intermediates need to incorporate into the micro-kinetic models.

1.3 Factors Determining Catalyst Performance

The selection of proper catalyst requires the knowledge of how different catalyst parameters (e.g., materials,³⁸ surface structures,^{39,40} nanoparticle size,⁴¹ promoters⁴², supports^{43,44}) control catalyst ability to catalyze different reactions. Here, the role of different factors determining catalyst performance will be reviewed from both theoretical and experimental studies.

1.3.1 Role of Catalyst Surface Structure

It is well known that there are strong connections between catalyst structure and catalyst reactivity and selectivity. Atoms at different sites (e.g., face, edge, and corner site) have different nearest neighbors, and can have different catalytic properties.^{45,46} Molecular level understanding of surface chemical processes helps the establishment of correlations between surface structure and chemical properties of technological importance.⁴⁷ Catalyst structure–activity correlations

can be determined experimentally through catalytic activity measurements of the isolated crystal surfaces at high pressures.⁴⁷ Early examples are the studies of ammonia synthesis over various Fe crystal facets and showed that certain facets with specific atomic arrangement have significantly higher catalytic activity than other surfaces.³⁹

Developments of theoretical techniques, especially the DFT-based computational methods, are becoming increasingly important to understand the impact of catalyst surface structures on catalyst reactivity.^{34,40,48,49} For instance, Honkala et al.⁴⁰ studied the ammonia synthesis over magnesium aluminum spinel supported ruthenium catalyst and found that stepped Ru surfaces are much more reactive than the close-packed (001) surface for N₂ dissociation step, the rate-limiting step. In addition, the calculated rate of ammonia synthesis from DFT method was within a factor of 3 to 20 of the experimental data, which shows that DFT is sufficiently accurate to predict and design practical catalytic materials.⁴⁰ Yang et al.³⁴ proposed that Ru(211) is ~6 orders of magnitude more active than Rh(111) surface for syn-gas conversion to ethanol and other C₂₊ oxygenates based on DFT calculation, but highly selective toward methane, while the Rh(111) surface is selective toward acetaldehyde. Yang et al.⁵⁰ employed DFT to study the surface structure effect on the activity of Pd based catalysts for acetylene hydrogenation to ethylene. They proposed that the activities of different Pd surface sites for acetylene hydrogenation follows the order of Pd(211) > Pd(111) \approx Pd(211)-defect \gg Pd(100).⁵⁰

1.3.2 Role of Catalyst Particle Size

In close relation to catalyst surface structures, catalyst activity is expected to be sensitive to its sizes,⁵¹⁻⁵⁶ which can be reflected by one of the three factors: (i) variations of adsorption strength of reactants; (ii) change in the structure or surface stoichiometry of the adsorbed

intermediates, and (iii) difference in the active area during steady-state conditions by reason of the variable formation of unreactive residues of the reactant.⁴¹ Factors (i) and (ii) are also related to the surface structure effect on catalyst performance as described in section 1.3.1.

Behaviors of a catalyst can be altered through changing the catalyst particle size.^{41,57-59} For instance, Haruta⁵⁷ observed that gold exhibits surprising high activities and/or selectivities in many important reactions (e.g., the combustion of CO and saturated hydrocarbons, the partial oxidation of hydrocarbon) with diameters smaller than 5 nm on TiO₂. Bond⁴¹ summarized the particle size effect to different reactions and proposed that rates of oxidation reactions of propane, ethylene, and CO generally decrease with decreasing average particle size due to stronger oxygen binding strength on smaller particles; whereas rates of alkane (e.g., ethane, propane, and n-pentane) hydrogenolysis on Ni, Pt, and Pd based catalysts increase with decreasing average particle sizes.

DFT could be a useful method to study particle size effect, which can generate different sizes particles easily, such as through Wulff constructions^{60,61}. For example, Karim et al.⁶² studied ammonia synthesis and decomposition on Ru through DFT and found that the maximum TOF occur at catalyst size at about 7 nm. Nørskov et al.^{63,64} demonstrated that nanoparticle size can affect electrocatalytic activity with the catalytic rate enhanced sharply on Au particles while decreased on Pt particles with increasing particle size based on DFT calculations. Tritsaris et al.⁵⁵ reproduced the experimentally observed trends for the oxygen reduction reaction on Pt in both the specific and mass activities for particle sizes in range of 2 to 30 nm from DFT calculations and observed a maximum mass activity for the oxygen reduction reaction on Pt for particles of a diameter between 2 and 4 nm.

DFT can be employed to probe catalyst reactivities by calculating bonding strengths of key reaction intermediates on particles of various sizes. For instance, Yudanov et al.⁵⁶ found a linear correlation between the average bond length and $n^{-1/3} \sim R_p^{-1}$ where R_p designates the radius of the nanoparticles and n designates the number of atoms for the nanoparticle range from 6 to 260 and established a relationship between the adsorption energy and the size n of the Pd nanoparticle as shown in Equation (4):

$$E_{ads} = E_0 - \varepsilon\tau n^{-1/3} \quad (4)$$

where the slope is $\varepsilon\tau=74.9$ kJ/mol for CO adsorption on Pd nanoparticles.

1.3.3 Role of Promoter

The promoter is an additive that can improve the activity of catalyst by interacting and modulating electronic or crystal structures with the main active components of catalysts.^{65,66} Numerous studies have shown the effect of promoters on catalyst activities and selectivities on various systems.⁶⁷⁻⁷² Typical promoters include metals (or metal ions)⁷³⁻⁷⁷ and metal oxides^{76,78,79}. For example, different kinds of promoters (e.g., noble metals and alkali promoters) have been used in Fischer-Tropsch (FT) synthesis to improve catalytic performance.^{42,67,80-83} Gaube et al.⁴² investigated the effects of alkali promoters (Li, Na, K, Cs) in FT iron and cobalt catalyst, and observed an increased 1-alkene selectivity, a slightly increased reaction rate, an increased growth probability of hydrocarbon chains and also an increased resistance against oxidation of iron by the reaction product water with introducing promoters. Tsubaki et al.⁸² investigated the effects of various noble metal promoters (e.g., Ru, Pt, and Pd) loaded on 10 wt%

Co/SiO₂ catalyst, and proposed that CO hydrogenation rate followed the order of Ru-Co/SiO₂ > Pd-Co/SiO₂ > Pt-Co/SiO₂ > Co/SiO₂. Morales et al.⁸³ studied the effect of manganese oxide (MgO) promoter on Co/TiO₂ FT catalysts and revealed an increase of C₅₊ selectivity and olefinic products with increasing MgO loading on Co/TiO₂ catalysts.

DFT-based computational modeling is again a useful tool to study the promoter effect of catalysts. Through detailed mechanistic analysis, the influence of promoter on the thermodynamics and kinetics of each elementary step can be understood. The modeling provides valuable molecular-level information of promoter effect. For instance, Mortensen et al.⁸⁴ observed the promotional effect of alkali adsorbate on the dissociation of N₂ and thus enhancing the ammonia synthesis on Ru catalyst surface from DFT calculations. In addition, the origin of this promotion effect is predominantly a direct electrostatic attraction between the adsorbed alkali atoms and the N₂ molecule.⁸⁴ Moses et al.⁸⁵ studied the Co promoter effect on MoS₂ for hydrodesulfurization of thiophene and found the Co decreases the barrier of hydrogenation reactions and active site regeneration but increase the barrier of C-S scission reactions based on DFT results.

1.3.4 Role of Supports

Immobilization of noble metal catalysts on a support play a key role in defining catalytic activity and selectivity through either a direct participation of the support^{86,87} or indirect roles via affecting the size and shape of the metal nanoparticles,⁸⁸ charge transfer from or to the metal nanoparticles,^{89,90} metal support interaction,⁹¹ or stabilizing ionic metal species⁹².

Common supports of heterogeneous catalysts can be metal oxides (e.g., TiO₂,^{43,93} CeO₂,^{94,95} Al₂O₃,⁹³ MgO⁹⁶), zeolites,^{97,98} carbon nanofibers,⁹⁹ active carbon,⁹⁶ metal carbide (e.g.,

SiC¹⁰⁰). For metal oxide supports, there exist two different kinds of supports: (1) the non-reducible supports, such as Al₂O₃,^{23,101} MgO,^{102,103} and (2) the reducible supports that can transfer its lattice oxygen with forming oxygen vacancy (Ov), such as CeO₂,¹⁰⁴⁻¹⁰⁷ TiO₂,^{87,108-110} ZrO₂¹⁰³.

The catalyst activities can strongly depend on the type of the support material.^{57,111,112} For example, Bui et al.¹¹¹ compared the zirconia and titania support effect associated with CoMoS catalysts in guaiacol hydrodeoxygenation (HDO) reaction and found that these two different supports give very different selectivity of conversion of guaiacol into deoxygenated hydrocarbons which may come from the different reaction scheme on the catalysts.

In most cases, the role of supports cannot be explained by simply the summation of contribution of metals and supports individually. The formation of new active sites at metal/support interface is one of the reasons believed to be responsible for catalyst reactivity.^{102,113,114} Fu et al.¹¹⁵ studied WGS over Au/CeO₂ and Pt/CeO₂ catalysts, and they proposed that metal nanoparticles do not participate in the WGS over Au/CeO₂ and Pt/CeO₂ catalysts, but the nonmetallic Au and Pt species strongly associated with surface cerium-oxygen groups do. Zhao et al.¹⁰² found that water activation barrier becomes essentially zero on Au/MgO interface compares to ~2 eV on clean Au(111) surface. Zhang et al.¹¹⁴ revealed that the electron transfer at the Ru/TiO₂ interface via the Ru-O bond reduces the activation barrier of CO oxidation over Ru_n/TiO₂ catalyst.

The reducibility^{86,116} and the oxygen storage capacity¹¹⁶ of the support materials can govern their ability to enhance catalytic performance.⁴⁶ For example, the transferability of support lattice oxygen (e.g., TiO₂,¹¹⁷ CeO₂,¹¹⁸ FeO_x¹¹⁹) to the Pt catalysts is a prerequisite for an efficient CO oxidation over supported Pt catalysts.

1.4 Organization of This Thesis

This thesis contains seven chapters. Chapter 1 introduces the background and scope of this thesis. Chapter 2 provides introductions of theory and computational methods used for the study. Chapter 3 describes the reaction mechanism of WGSR on Ni based catalyst. Chapter 4 investigates the promoter effect to WGSR over Ni(111) surface and O* removal reaction over Mo₂C catalyst. Chapter 5 contains catalyst surface structure, nanoparticle size, and process condition effect for hydrogen production via WGSR. Chapter 6 investigates the impact of adsorbate-adsorbate interactions on catalyst performance predictions. Chapter 7 presents the support effect on WGSR and CO oxidation catalytic activities.

Chapters 3, 4, 5, 6, and 7 contain information from published papers with some rearrangements. Each chapter is both self-contained and is a piece of the larger story about catalyst design for fuels and chemicals production.

References

1. Pritchard, J.; Filonenko, G. A.; van Putten, R.; Hensen, E. J. M.; Pidko, E. A. Heterogeneous and homogeneous catalysis for the hydrogenation of carboxylic acid derivatives: history, advances and future directions. *Chem. Soc. Rev.* **2015**, *44*, 3808-3833.
2. Sattler, J. J. H. B.; Ruiz-Martinez, J.; Santillan-Jimenez, E.; Weckhuysen, B. M. Catalytic dehydrogenation of light alkanes on metals and metal oxides. *Chem. Rev.* **2014**, *114*, 10613-10653.

3. Ruppert, A. M.; Weinberg, K.; Palkovits, R. Hydrogenolysis goes bio: from carbohydrates and sugar alcohols to platform chemicals. *Angewandte Chemie-International Edition* **2012**, *51*, 2564-2601.
4. Bu, Q.; Lei, H.; Zacher, A. H.; Wang, L.; Ren, S.; Liang, J.; Wei, Y.; Liu, Y.; Tang, J.; Zhang, Q.; Ruan, R. A review of catalytic hydrodeoxygenation of lignin-derived phenols from biomass pyrolysis. *Bioresour. Technol.* **2012**, *124*, 470-477.
5. ten Dam, J.; Hanefeld, U. Renewable chemicals: dehydroxylation of glycerol and polyols. *Chemsuschem* **2011**, *4*, 1017-1034.
6. Cortright, R. D.; Davda, R. R.; Dumesic, J. A. Hydrogen from catalytic reforming of biomass-derived hydrocarbons in liquid water. *Nature* **2002**, *418*, 964-967.
7. Palkovits, R.; Tajvidi, K.; Procelewska, J.; Rinaldi, R.; Ruppert, A. Hydrogenolysis of cellulose combining mineral acids and hydrogenation catalysts. *Green Chem.* **2010**, *12*, 972-978.
8. Dawes, G. J. S.; Scott, E. L.; Le Notre, J.; Sanders, J. P. M.; Bitter, J. H. Deoxygenation of biobased molecules by decarboxylation and decarbonylation - a review on the role of heterogeneous, homogeneous and bio-catalysis. *Green Chem.* **2015**, *17*, 3231-3250.
9. Breen, J.; Burch, R.; Coleman, H. Metal-catalysed steam reforming of ethanol in the production of hydrogen for fuel cell applications. *Applied Catalysis B-Environmental* **2002**, *39*, 65-74.
10. Crabtree, G. W.; Dresselhaus, M. S.; Buchanan, M. V. The hydrogen economy. *Phys Today* **2004**, *57*, 39-44.
11. Edwards, P. P.; Kuznetsov, V. L.; David, W. I. F.; Brandon, N. P. Hydrogen and fuel cells: towards a sustainable energy future. *Energy Policy* **2008**, *36*, 4356-4362.

12. Alves, H. J.; Bley Junior, C.; Niklevicz, R. R.; Frigo, E. P.; Frigo, M. S.; Coimbra-Araujo, C. H. Overview of hydrogen production technologies from biogas and the applications in fuel cells. *Int J Hydrogen Energy* **2013**, *38*, 5215-5225.
13. Hallale, N.; Liu, F. Refinery hydrogen management for clean fuels production. *Adv. Environ. Res.* **2001**, *6*, 81-98.
14. Rostrup-Nielsen, J. R. Production of synthesis gas. *Catal Today* **1993**, *18*, 305-324.
15. Blaser, H.; Malan, C.; Pugin, B.; Spindler, F.; Steiner, H.; Studer, M. Selective hydrogenation for fine chemicals: recent trends and new developments. *Adv. Synth. Catal.* **2003**, *345*, 103-151.
16. Rostrup-Nielsen, J. R. Catalytic steam reforming. **1984**, 117.
17. Navarro, R. M.; Peña, M. A.; Fierro, J. L. G. Hydrogen production reactions from carbon feedstocks: Fossil fuels and biomass. *Chem. Rev.* **2007**, *107*, 3952-3991.
18. Nieva, M. A.; Villaverde, M. M.; Monzón, A.; Garetto, T. F.; Marchi, A. J. Steam-methane reforming at low temperature on nickel-based catalysts. *Chem. Eng. J.* **2014**, *235*, 158-166.
19. Huber, G. W.; Shabaker, J. W.; Dumesic, J. A. Raney Ni-Sn catalyst for H₂ production from biomass-derived hydrocarbons. *Science* **2003**, *300*, 2075-2077.
20. Chheda, J. N.; Huber, G. W.; Dumesic, J. A. Liquid-phase catalytic processing of biomass-derived oxygenated hydrocarbons to fuels and chemicals. *Angewandte Chemie-International Edition* **2007**, *46*, 7164-7183.
21. Liu, B.; Zhou, M.; Chan, M. K. Y.; Greeley, J. P. Understanding polyol decomposition on bimetallic Pt-Mo catalysts - A DFT Study of Glycerol. *ACS Catal.* **2015**, *5*, 4942-4950.
22. Lemons, R. Fuel-cells for transportation. *J. Power Sources* **1990**, *29*, 251-264.

23. He, R.; Davda, R.; Dumesic, J. In situ ATR-IR spectroscopic and reaction kinetics studies of water-gas shift and methanol reforming on Pt/Al₂O₃ catalysts in vapor and liquid phases. *J Phys Chem B* **2005**, *109*, 2810-2820.
24. Norskov, J. K.; Bligaard, T.; Rossmeisl, J.; Christensen, C. H. Towards the computational design of solid catalysts. *Nature Chemistry* **2009**, *1*, 37-46.
25. Chen, X.; Yang, X. Mechanistic insights and computational design of transition-metal catalysts for hydrogenation and dehydrogenation reactions. *Chemical Record* **2016**, *16*, 2364-2378.
26. Abild-Pedersen, F.; Greeley, J.; Studt, F.; Rossmeisl, J.; Munter, T. R.; Moses, P. G.; Skúlason, E.; Bligaard, T.; Nørskov, J. K. Scaling properties of adsorption energies for hydrogen-containing molecules on transition-metal surfaces. *Phys. Rev. Lett.* **2007**, *99*.
27. Wang, S.; Temel, B.; Shen, J.; Jones, G.; Grabow, L. C.; Studt, F.; Bligaard, T.; Abild-Pedersen, F.; Christensen, C. H.; Nørskov, J. K. Universal Brønsted-Evans-Polanyi relations for C-C, C-O, C-N, N-O, N-N, and O-O dissociation reactions. *Catal Lett* **2011**, *141*, 370-373.
28. Wang, S.; Petzold, V.; Tripkovic, V.; Kleis, J.; Howalt, J. G.; Skúlason, E.; Fernández, E. M.; Hvolbæk, B.; Jones, G.; Toftelund, A.; Falsig, H.; Björketun, M.; Studt, F.; Abild-Pedersen, F.; Rossmeisl, J.; Nørskov, J. K.; Bligaard, T. Universal transition state scaling relations for (de)hydrogenation over transition metals. *Phys. Chem. Chem. Phys.* **2011**, *13*, 20760-20765.
29. Vojvodic, A.; Calle-Vallejo, F.; Guo, W.; Wang, S.; Toftelund, A.; Studt, F.; Martinez, J. I.; Shen, J.; Man, I. C.; Rossmeisl, J.; Bligaard, T.; Norskov, J. K.; Abild-Pedersen, F. On the behavior of Bronsted-Evans-Polanyi relations for transition metal oxides. *J. Chem. Phys.* **2011**, *134*, 244509.

30. Norskov, J.; Bligaard, T.; Logadottir, A.; Bahn, S.; Hansen, L.; Bollinger, M.; Bengaard, H.; Hammer, B.; Sljivancanin, Z.; Mavrikakis, M.; Xu, Y.; Dahl, S.; Jacobsen, C. Universality in heterogeneous catalysis. *Journal of Catalysis* **2002**, *209*, 275-278.
31. van Santen, R. A.; Neurock, M.; Shetty, S. G. Reactivity theory of transition-metal surfaces: A Bronsted-Evans-Polanyi linear activation energy-free-energy Analysis. *Chem. Rev.* **2010**, *110*, 2005-2048.
32. Greeley, J. Theoretical heterogeneous catalysis: scaling relationships and computational catalyst design. *Annual Review of Chemical and Biomolecular Engineering, Vol 7* **2016**, *7*, 605-635.
33. Norskov, J. K.; Abild-Pedersen, F.; Studt, F.; Bligaard, T. Density functional theory in surface chemistry and catalysis. *Proc. Natl. Acad. Sci. U. S. A.* **2011**, *108*, 937-943.
34. Yang, N.; Medford, A. J.; Liu, X.; Studt, F.; Bligaard, T.; Bent, S. F.; Nørskov, J. K. Intrinsic selectivity and structure sensitivity of rhodium catalysts for C₂₊ oxygenate production. *J. Am. Chem. Soc.* **2016**, *138*, 3705-3714.
35. Hammer, B. Coverage dependence of N₂ dissociation at an N, O, or H precovered Ru(0001) surface investigated with density functional theory. *Physical Review B* **2001**, *63*, 205423.
36. Miller, S. D.; Kitchin, J. R. Relating the coverage dependence of oxygen adsorption on Au and Pt fcc(1 1 1) surfaces through adsorbate-induced surface electronic structure effects. *Surf. Sci.* **2009**, *603*, 794-801.
37. Vattuone, L.; Yeo, Y.; King, D. Adatom bond energies and lateral interaction energies from calorimetry: NO, O-2, and N-2 adsorption on Ni{100}. *J. Chem. Phys.* **1996**, *104*, 8096-8102.
38. Grenoble, D. C.; Estadt, M. M.; Ollis, D. F. The chemistry and catalysis of the water gas shift reaction. 1. The kinetics over supported metal catalysts. *J. Catal.* **1981**, *67*, 90-102.

39. Strongin, D.; Carrazza, J.; Bare, S.; Somorjai, G. The importance of C7 sites and surface roughness in the ammonia synthesis reaction over iron. *Journal of Catalysis* **1987**, *103*, 213-215.
40. Honkala, K.; Hellman, A.; Remediakis, I. N.; Logadottir, A.; Carlsson, A.; Dahl, S.; Christensen, C. H.; Norskov, J. K. Ammonia synthesis from first-principles calculations. *Science* **2005**, *307*, 555-558.
41. Bond, G. The origins of particle size effects in heterogeneous catalysis. *Surf. Sci.* **1985**, *156*, 966-981.
42. Gaube, J.; Klein, H. -. The promoter effect of alkali in Fischer-Tropsch iron and cobalt catalysts. *Applied Catalysis A-General* **2008**, *350*, 126-132.
43. Bagheri, S.; Mueh Jalkapli, N.; Bee Abd Hamid, S. Titanium dioxide as a catalyst support in heterogeneous catalysis. *Sci. World J.* **2014**, *2014*.
44. Davis, S. E.; Ide, M. S.; Davis, R. J. Selective oxidation of alcohols and aldehydes over supported metal nanoparticles. *Green Chem.* **2013**, *15*, 17-45.
45. Duan, Z.; Wang, G. Monte Carlo simulation of surface segregation phenomena in extended and nanoparticle surfaces of Pt-Pd alloys. *Journal of Physics-Condensed Matter* **2011**, *23*, 475301.
46. Shekhar, M.; Wang, J.; Lee, W. -.; Williams, W. D.; Kim, S. M.; Stach, E. A.; Miller, J. T.; Delgass, W. N.; Ribeiro, F. H. Size and support effects for the water-gas shift catalysis over gold nanoparticles supported on model Al₂O₃ and TiO₂. *J. Am. Chem. Soc.* **2012**, *134*, 4700-4708.
47. Somorjai, G. A.; Li, Y. Impact of surface chemistry. *Proc. Natl. Acad. Sci. U. S. A.* **2011**, *108*, 917-924.

48. Catapan, R. C.; Oliveira, A. A. M.; Chen, Y.; Vlachos, D. G. DFT study of the water-gas shift reaction and coke formation on Ni(111) and Ni(211) surfaces. *J. Phys. Chem. C* **2012**, *116*, 20281-20291.
49. Mohsenzadeh, A.; Richards, T.; Bolton, K. DFT study of the water gas shift reaction on Ni(111), Ni(100) and Ni(110) surfaces. *Surf. Sci.* **2016**, *644*, 53-63.
50. Yang, B.; Burch, R.; Hardacre, C.; Headdock, G.; Hu, P. Influence of surface structures, subsurface carbon and hydrogen, and surface alloying on the activity and selectivity of acetylene hydrogenation on Pd surfaces: A density functional theory study. *Journal of Catalysis* **2013**, *305*, 264-276.
51. Kuhn, J. N.; Huang, W.; Tsung, C.; Zhang, Y.; Somorjai, G. A. Structure sensitivity of carbon-nitrogen ring opening: impact of platinum particle size from below 1 to 5 nm upon pyrrole hydrogenation product selectivity over monodisperse platinum nanoparticles loaded onto mesoporous silica. *J. Am. Chem. Soc.* **2008**, *130*, 14026.
52. Joo, S. H.; Park, J. Y.; Renzas, J. R.; Butcher, D. R.; Huang, W.; Somorjai, G. A. Size effect of ruthenium nanoparticles in catalytic carbon monoxide oxidation. *Nano Letters* **2010**, *10*, 2709-2713.
53. Bell, A. The impact of nanoscience on heterogeneous catalysis. *Science* **2003**, *299*, 1688-1691.
54. Greeley, J.; Rossmeisl, J.; Hellman, A.; Norskov, J. K. Theoretical trends in particle size effects for the oxygen reduction reaction. *Zeitschrift Fur Physikalische Chemie-International Journal of Research in Physical Chemistry & Chemical Physics* **2007**, *221*, 1209-1220.
55. Tritsarlis, G. A.; Greeley, J.; Rossmeisl, J.; Norskov, J. K. Atomic-scale modeling of particle size effects for the oxygen reduction reaction on Pt. *Catalysis Letters* **2011**, *141*, 909-913.

56. Yudanov, I. V.; Metzner, M.; Genest, A.; Roesch, N. Size-dependence of adsorption properties of metal nanoparticles: A density functional study on palladium nanoclusters. *Journal of Physical Chemistry C* **2008**, *112*, 20269-20275.
57. Haruta, M. Size- and support-dependency in the catalysis of gold. *Catalysis Today* **1997**, *36*, 153-166.
58. den Breejen, J. P.; Radstake, P. B.; Bezemer, G. L.; Bitter, J. H.; Froseth, V.; Holmen, A.; de Jong, K. P. On the origin of the cobalt particle size effects in Fischer-Tropsch catalysis. *J. Am. Chem. Soc.* **2009**, *131*, 7197-7203.
59. Holles, J.; Davis, R.; Murray, T.; Howe, J. Effects of Pd particle size and ceria loading on NO reduction with CO. *Journal of Catalysis* **2000**, *195*, 193-206.
60. Wulff, G. On the question of the rate of growth and dissolution of crystal surfaces. *Krystallogr* **1901**, *34*, 449-530.
61. Barmparis, G. D.; Lodziana, Z.; Lopez, N.; Remediakis, I. N. Nanoparticle shapes by using Wulff constructions and first-principles calculations. *Beilstein J. Nanotechnology* **2015**, *6*, 361-368.
62. Karim, A. M.; Prasad, V.; Mpourmpakis, G.; Lonergan, W. W.; Frenkel, A. I.; Chen, J. G.; Vlachos, D. G. Correlating particle size and shape of supported Ru/gamma-Al₂O₃ catalysts with NH₃ decomposition activity. *J. Am. Chem. Soc.* **2009**, *131*, 12230-12239.
63. Norskov, J. K.; Bligaard, T.; Hvolbaek, B.; Abild-Pedersen, F.; Chorkendorff, I.; Christensen, C. H. The nature of the active site in heterogeneous metal catalysis. *Chem. Soc. Rev.* **2008**, *37*, 2163-2171.
64. Meier, J.; Schiotz, J.; Liu, P.; Norskov, J.; Stimming, U. Nano-scale effects in electrochemistry. *Chemical Physics Letters* **2004**, *390*, 440-444.

65. Andersson, S.; Jostell, U. Electron-structure of Na and K adsorbed on Ni(100). *Surf. Sci.* **1974**, *46*, 625-640.
66. Ribeiro, M. C.; Jacobs, G.; Davis, B. H.; Cronauer, D. C.; Kropf, A. J.; Marshall, C. L. Fischer-tropsch synthesis: An in-situ TPR-EXAFS/XANES investigation of the influence of group i alkali promoters on the local atomic and electronic structure of carburized iron/silica catalysts. *J. Phys. Chem. C* **2010**, *114*, 7895-7903.
67. Jacobs, G.; Das, T.; Zhang, Y.; Li, J.; Racoillet, G.; Davis, B. Fischer-Tropsch synthesis: support, loading, and promoter effects on the reducibility of cobalt catalysts. *Applied Catalysis A-General* **2002**, *233*, 263-281.
68. Hutchings, G. Effect of promoters and reactant concentration on the selective oxidation of N-butane to maleic-anhydride using vanadium phosphorus oxide catalysts. *Applied Catalysis* **1991**, *72*, 1-32.
69. Sarkany, A.; Zsoldos, Z.; Stefler, G.; Hightower, J.; Gucci, L. Promoter effect of Pd in hydrogenation of 1,3-butadiene over Co-Pd catalysts. *Journal of Catalysis* **1995**, *157*, 179-189.
70. Aika, K.; Shimazaki, K.; Hattori, Y.; Ohya, A.; Ohshima, S.; Shirota, K.; Ozaki, A. Support and promoter effect of ruthenium catalyst .1. Characterization of alkali-promoted ruthenium alumina catalysts for ammonia-synthesis. *Journal of Catalysis* **1985**, *92*, 296-304.
71. Wang, S.; Lu, G. Effects of promoters on catalytic activity and carbon deposition of Ni/gamma-Al₂O₃ catalysts in CO₂ reforming of CH₄. *Journal of Chemical Technology and Biotechnology* **2000**, *75*, 589-595.
72. Idem, R.; Bakhshi, N. Production of hydrogen from methanol over promoted coprecipitated Cu-Al catalysts - the effects of various promoters and catalyst activation methods. *Ind Eng Chem Res* **1995**, *34*, 1548-1557.

73. Yang, Y.; Xiang, H.; Xu, Y.; Bai, L.; Li, Y. Effect of potassium promoter on precipitated iron-manganese catalyst for Fischer-Tropsch synthesis. *Applied Catalysis A-General* **2004**, *266*, 181-194.
74. Aika, K.; Takano, T.; Murata, S. Preparation and characterization of chlorine-free ruthenium catalysts and the promoter effect in ammonia-synthesis .3. a magnesia-supported ruthenium catalyst. *Journal of Catalysis* **1992**, *136*, 126-140.
75. Jacobs, G.; Das, T.; Zhang, Y.; Li, J.; Racoillet, G.; Davis, B. Fischer-Tropsch synthesis: support, loading, and promoter effects on the reducibility of cobalt catalysts. *Applied Catalysis A-General* **2002**, *233*, 263-281.
76. Cheng, Z.; Wu, Q.; Li, J.; Zhu, Q. Effects of promoters and preparation procedures on reforming of methane with carbon dioxide over Ni/Al₂O₃ catalyst. *Catalysis Today* **1996**, *30*, 147-155.
77. Alotaibi, R.; Alenazey, F.; Alotaibi, F.; Wei, N.; Al-Fatesh, A.; Fakeeha, A. Ni catalysts with different promoters supported on zeolite for dry reforming of methane. *Applied Petrochemical Research* **2015**, *5*, 329-337.
78. Wang, S.; Lu, G. Effects of oxide promoters on metal dispersion and metal-support interactions in Ni catalysts supported on activated carbon. *Ind Eng Chem Res* **1997**, *36*, 5103-5109.
79. Amiridis, M.; Duevel, R.; Wachs, I. The effect of metal oxide additives on the activity of V₂O₅/TiO₂ catalysts for the selective catalytic reduction of nitric oxide by ammonia. *Applied Catalysis B-Environmental* **1999**, *20*, 111-122.
80. Bukur, D.; Mukesh, D.; Patel, S. Promoter effects on precipitated iron catalysts for Fischer-Tropsch synthesis. *Ind Eng Chem Res* **1990**, *29*, 194-204.

81. Yang, Y.; Xiang, H.; Xu, Y.; Bai, L.; Li, Y. Effect of potassium promoter on precipitated iron-manganese catalyst for Fischer-Tropsch synthesis. *Applied Catalysis A-General* **2004**, *266*, 181-194.
82. Tsubaki, N.; Sun, S.; Fujimoto, K. Different functions of the noble metals added to cobalt catalysts for Fischer-Tropsch synthesis. *Journal of Catalysis* **2001**, *199*, 236-246.
83. Morales, F.; de Smit, E.; de Groot, F. M. F.; Visser, T.; Weckhuysen, B. M. Effects of manganese oxide promoter on the CO and H₂ adsorption properties of titania-supported cobalt Fischer-Tropsch catalysts. *Journal of Catalysis* **2007**, *246*, 91-99.
84. Mortensen, J.; Hammer, B.; Nørskov, J. Alkali promotion of N₂ dissociation over Ru(0001). *Phys. Rev. Lett.* **1998**, *80*, 4333-4336.
85. Moses, P. G.; Hinnemann, B.; Topsoe, H.; Nørskov, J. K. The effect of Co-promotion on MoS₂ catalysts for hydrodesulfurization of thiophene: A density functional study. *Journal of Catalysis* **2009**, *268*, 201-208.
86. Schubert, M. M.; Hackenberg, S.; Van Veen, A. C.; Muhler, M.; Plzak, V.; Behm, R. J. CO oxidation over supported gold catalysts - "Inert" and "active" support materials and their role for the oxygen supply during reaction. *J. Catal.* **2001**, *197*, 113-122.
87. Rodríguez, J. A.; Evans, J.; Graciani, J.; Park, J. -.; Liu, P.; Hrbek, J.; Sanz, J. F. High water-gas shift activity in TiO₂(110) supported Cu and Au nanoparticles: role of the oxide and metal particle size. *J. Phys. Chem. C* **2009**, *113*, 7364-7370.
88. Janssens, T. V. W.; Clausen, B. S.; Hvolbæk, B.; Falsig, H.; Christensen, C. H.; Bligaard, T.; Nørskov, J. K. Insights into the reactivity of supported Au nanoparticles: Combining theory and experiments. *Top. Catal.* **2007**, *44*, 15-26.

89. Sanchez, A.; Abbet, S.; Heiz, U.; Schneider, W. -.; Häkkinen, H.; Barnett, R. N.; Landman, U. When gold is not noble: nanoscale gold catalysts. *J Phys Chem A* **1999**, *103*, 9573-9578.
90. Zhu, W.; Wu, Z.; Foo, G. S.; Gao, X.; Zhou, M.; Liu, B.; Veith, G. M.; Wu, P.; Browning, K. L.; Lee, H. N.; Li, H.; Dai, S.; Zhu, H. Taming interfacial electronic properties of platinum nanoparticles on vacancy-abundant boron nitride nanosheets for enhanced catalysis. *Nature Communications* **2017**, *8*, 15291.
91. Janssens, T. V. W.; Carlsson, A.; Puig-Molina, A.; Clausen, B. S. Relation between nanoscale Au particle structure and activity for CO oxidation on supported gold catalysts. *J. Catal.* **2006**, *240*, 108-113.
92. Costello, C. K.; Kung, M. C.; Oh, H. -.; Wang, Y.; Kung, H. H. Nature of the active site for CO oxidation on highly active Au/ γ -Al₂O₃. *Appl Catal A Gen* **2002**, *232*, 159-168.
93. Chusuei, C. C.; Lai, X.; Luo, K.; Goodman, D. W. Modeling heterogeneous catalysts: Metal clusters on planar oxide supports. *Top. Catal.* **2000**, *14*, 71-83.
94. Rodriguez, J. A.; Liu, P.; Hrbek, J.; Evans, J.; Pérez, M. Water gas shift reaction on Cu and Au nanoparticles supported on CeO₂(111) and ZnO(0001): Intrinsic activity and importance of support interactions. *Angew. Chem. Int. Ed.* **2007**, *46*, 1329-1332.
95. Idriss, H.; Diagne, C.; Hindermann, J. P.; Kiennemann, A.; Barteau, M. A. Reactions of acetaldehyde on CeO₂ and CeO₂-supported catalysts. *J. Catal.* **1995**, *155*, 219-237.
96. Kohler, K.; Wagner, M.; Djakovitch, L. Supported palladium as catalyst for carbon-carbon bond construction (Heck reaction) in organic synthesis. *Catalysis Today* **2001**, *66*, 105-114.
97. Dams, M.; Drijkoningen, L.; Pauwels, B.; Van Tendeloo, G.; De Vos, D. E.; Jacobs, P. A. Pd-zeolites as heterogeneous catalysts in Heck chemistry. *Journal of Catalysis* **2002**, *209*, 225-236.

98. Corma, A.; Nemeth, L. T.; Renz, M.; Valencia, S. Sn-zeolite beta as a heterogeneous chemoselective catalyst for Baeyer-Villiger oxidations. *Nature* **2001**, *412*, 423-425.
99. Pham-Huu, C.; Keller, N.; Ehret, G.; Charbonniere, L. J.; Ziessel, R.; Ledoux, M. J. Carbon nanofiber supported palladium catalyst for liquid-phase reactions - An active and selective catalyst for hydrogenation of cinnamaldehyde into hydrocinnamaldehyde. *Journal of Molecular Catalysis A-Chemical* **2001**, *170*, 155-163.
100. Ledoux, M. J.; Pham-Huu, C. Silicon carbide a novel catalyst support for heterogeneous catalysis. *Cattech* **2001**, *5*, 226-246.
101. Nikolova, D.; Edreva-Kardjieva, R.; Grozeva, T. Water-gas shift activity of K-promoted (Ni)Mo/ γ -Al₂O₃ systems in sulfur-containing feed. *Reaction Kinetics, Mechanisms and Catalysis* **2011**, *103*, 71-86.
102. Zhao, Z. -.; Li, Z.; Cui, Y.; Zhu, H.; Schneider, W. F.; Delgass, W. N.; Ribeiro, F.; Greeley, J. Importance of metal-oxide interfaces in heterogeneous catalysis: A combined DFT, microkinetic, and experimental study of water-gas shift on Au/MgO. *J. Catal.* **2017**, *345*, 157-169.
103. Jeong, D.; Jang, W.; Shim, J.; Han, W.; Roh, H.; Jung, U. H.; Yoon, W. L. Low-temperature water-gas shift reaction over supported Cu catalysts. *Renewable Energy* **2014**, *65*, 102-107.
104. Andreeva, D.; Idakiev, V.; Tabakova, T.; Ilieva, L.; Falaras, P.; Bourlinos, A.; Travlos, A. Low-temperature water-gas shift reaction over Au/CeO₂ catalysts. *Catal Today* **2002**, *72*, 51-57.
105. Aranifard, S.; Ammal, S. C.; Heyden, A. On the importance of metal-oxide interface sites for the water-gas shift reaction over Pt/CeO₂ catalysts. *J. Catal.* **2014**, *309*, 314-324.

106. Gorte, R. J. Ceria in catalysis: From automotive applications to the water-gas shift reaction. *AIChE J.* **2010**, *56*, 1126-1135.
107. Luengnaruemitchai, A.; Osuwan, S.; Gulari, E. Comparative studies of low-temperature water–gas shift reaction over Pt/CeO₂, Au/CeO₂, and Au/Fe₂O₃ catalysts. *Catalysis Communications* **2003**, *4*, 215-221.
108. Kalamaras, C. M.; Panagiotopoulou, P.; Kondarides, D. I.; Efstathiou, A. M. Kinetic and mechanistic studies of the water–gas shift reaction on Pt/TiO₂ catalyst. *Journal of Catalysis* **2009**, *264*, 117-129.
109. Peng, S.; Ho, J. The mechanism of the water-gas shift reaction on Cu/TiO₂(110) elucidated from application of density-functional theory. *Phys. Chem. Chem. Phys.* **2011**, *13*, 20393-20400.
110. Sato, Y.; Soma, Y.; Miyao, T.; Naito, S. The water-gas-shift reaction over Ir/TiO₂ and Ir-Re/TiO₂ catalysts. *Appl. Catal. A Gen.* **2006**, *304*, 78-85.
111. Van Ngoc Bui; Laurenti, D.; Delichere, P.; Geantet, C. Hydrodeoxygenation of guaiacol Part II: Support effect for CoMoS catalysts on HDO activity and selectivity. *Applied Catalysis B-Environmental* **2011**, *101*, 246-255.
112. Okumura, M.; Tsubota, S.; Haruta, M. Preparation of supported gold catalysts by gas-phase grafting of gold acetylacetonate for low-temperature oxidation of CO and of H₂. *J. Mol. Catal. A Chem.* **2003**, *199*, 73-84.
113. Gao, M.; Lyalin, A.; Taketsugu, T. Role of the support effects on the catalytic activity of gold clusters: A Density Functional Theory Study. *Catalysts* **2011**, *1*, 18-39.
114. Zhang, S.; Li, C.; Yan, H.; Wei, M.; Evans, D. G.; Duan, X. Density functional theory study on the metal-support interaction between Ru cluster and anatase TiO₂(101) surface. *Journal of Physical Chemistry C* **2014**, *118*, 3514-3522.

115. Fu, Q.; Saltsburg, H.; Flytzani-Stephanopoulos, M. Active nonmetallic Au and Pt species on ceria-based water-gas shift catalysts. *Science* **2003**, *301*, 935-938.
116. Widmann, D.; Liu, Y.; Schuth, F.; Behm, R. J. Support effects in the Au-catalyzed CO oxidation - Correlation between activity, oxygen storage capacity, and support reducibility. *Journal of Catalysis* **2010**, *276*, 292-305.
117. Zhu, H.; Wu, Z.; Su, D.; Veith, G. M.; Lu, H.; Zhang, P.; Chai, S.; Dai, S. Constructing hierarchical interfaces: TiO₂-supported PtFe-FeO_x nanowires for room temperature CO oxidation. *J. Am. Chem. Soc.* **2015**, *137*, 10156-10159.
118. Vayssilov, G. N.; Lykhach, Y.; Migani, A.; Staudt, T.; Petrova, G. P.; Tsud, N.; Skala, T.; Bruix, A.; Illas, F.; Prince, K. C.; Matolin, V.; Neyman, K. M.; Libuda, J. Support nanostructure boosts oxygen transfer to catalytically active platinum nanoparticles. *Nature Materials* **2011**, *10*, 310-315.
119. Qiao, B.; Wang, A.; Yang, X.; Allard, L. F.; Jiang, Z.; Cui, Y.; Liu, J.; Li, J.; Zhang, T. Single-atom catalysis of CO oxidation using Pt₁/FeO_x. *Nature Chemistry* **2011**, *3*, 634-641.

Chapter 2 - Computational Methods and Theory

2.1 Density Functional Theory (DFT)

DFT is a variational approach to compute the electronic structure of many-body systems, such as atoms, molecules, and solids. DFT calculations produce accurate ground state molecular structures and total energies at a rather efficient computational speed given modern day parallel computing hardware. Here, the DFT fundamentals within the Kohn-Sham framework, which has been employed for this thesis work, will be summarized.

2.1.1 DFT based on Kohn-Sham Formulation

The fundamental rationale of first-principles (i.e. ab initio) methods is to treat interacting, inhomogeneous, N-body system, as in molecules, solids, and surface, without the inclusion of empirical data or parameters, where the wave function, $\psi(r_1, \dots, r_N)$, can be approximated by the product of N single-particle wave functions, $\Psi_i(r_i)$, as expressed in Equation (5):

$$\psi(r_1, \dots, r_N) = \Psi_1(r_1) \dots \Psi_N(r_N) \quad (5)$$

Here, the focus is DFT method developed within the Kohn and Sham's formulation¹, in which the single particle i Schrödinger equation can be written in Equation (6):

$$\left[-\frac{\hbar^2}{2m} \nabla_i^2 + v_{eff}(r) \right] \Psi_i(r) = \varepsilon_i \Psi_i(r) \quad (6)$$

$$v_{eff}(r) = v_{en}(r) + \int \frac{\rho(r')}{|r - r'|} dr' + V_{xc}[\rho(r)] \quad (7)$$

$$\rho(r) = \sum_i |\varphi_i(r_i)|^2 \quad (8)$$

where $-\frac{\hbar^2}{2m}\nabla^2$ in Equation (6) is the electron kinetic term. The $v_{eff}(r)$ represents the effective potential functional, which is a function of electron density $\rho(r)$.

2.1.2 Plane Wave Basis Set and Brillouin Zone

Bloch theorem² establishes the foundation to solve Schrödinger equation for periodic systems. The plane wave function based on Bloch theorem can be expressed by Equation (9):

$$\Psi_k(r) = e^{ik \cdot r} u_k(r) \quad (9)$$

$$\rho(r) \approx \sum_k |\Psi_k(r)|^2 \quad (10)$$

where $u_k(r)$ is a basis set function with the same periodicity as the supercell and $u_k(r + n_1 a_1 + n_2 a_2 + n_3 a_3) = u_k(r)$ for any integers n_1 , n_2 , and n_3 . Thus, it is possible to solve the Schrödinger equation (Equation (6)) for each k value independently. Computationally, the plane-wave based approach is much more efficient to calculate for periodic systems. The space of vector k is called reciprocal space or simply k space. The length of the reciprocal lattice vectors is inversely related to the length of the real space lattice vectors. If a_1, a_2, a_3 are the axis vectors of the real lattice, then the axis vectors of the reciprocal lattice (b_1, b_2, b_3) can be written as Equations (11-13). The primitive cell in reciprocal space named the Brillouin zone.

$$b_1 = 2\pi \frac{a_2 \times a_3}{a_1 * a_2 \times a_3} \quad (11)$$

$$b_2 = 2\pi \frac{a_3 \times a_1}{a_1 * a_2 \times a_3} \quad (12)$$

$$b_3 = 2\pi \frac{a_1 \times a_2}{a_1 * a_2 \times a_3} \quad (13)$$

It is possible to approximate electron density with Equation (10) using a finite number of k-points. Monkhorst-Pack methods ³ can be used to generate equally spaced k-points in the Brillouin zone in DFT calculations. Then the plane wave basis set in the reciprocal space can be expanded into Equation (14) based on Bloch's theorem,

$$\varphi_{ik}(r) = \sum_G c_{ik}(G) e^{i(k+G) \cdot r} \quad (14)$$

where G is the lattice vector in the reciprocal space with $G = n_1 b_1 + n_2 b_2 + n_3 b_3$. $c_{ik}(G)$ is the expansion coefficient corresponding to vector G , which decreases as $|G|^2$ increase. Therefore, it is sufficient to truncate the infinite series in Equation (14) to include the plane waves up to the cutoff energy (E_{cut}) as in Equations (15) and (16). In practice, the ground state energy and density converge quickly with the number of k-points and cutoff energy used.

$$E_{cut} = \frac{\hbar^2}{2m} G_{cut}^2 \quad (15)$$

$$|k + G| < G_{cut} \quad (16)$$

2.1.3 Pseudopotential

As the potential wave function in the proximity to the nuclei becomes very attractive, wave functions oscillate rapidly, thus, making all-electron calculations (i.e. explicit inclusion of core electrons) with full Coulombic rather expensive.⁴ In addition, core electrons are usually not directly responsible for the chemical bonding and other physical characteristics. For these reasons, pseudopotential methods have been developed and widely adapted through representing the valence electrons with full wave functions, but frozen core electrons (i.e. pre-calculated and fixed) to reduce the computational cost. Pseudopotential generated from the projector augmented wave (PAW) method⁵ is a computationally efficient method that can mitigate the artificial effects effectively.

2.1.4 Electron Exchange-correlation Functionals

When solving Equations (6) and (7), only the exchange-correlation energy, which illustrates the interacting electronic kinetic energy and the corrections of Coulomb interactions of an electron with itself, cannot be defined and has to be approximated instead. The generalized gradient approximations (GGA),⁶⁻⁹ which includes both the local electron density and the local gradient of electron density to approximate $E_{xc}(r)$, are one of the forms to approximate exchange-correlation energy. The gradient of electron density can be treated differently which lead to a number of GGA functionals, such as Perdew–Wang (PW91),^{10,11} the Perdew-Burke-Ernzerhof (PBE),¹⁰ the revised PBE (RPBE),¹² the re-parameterized PBE functional for solids and surfaces (PBEsol)¹³ and the Becke–Lee–Yang–Parr functional (BLYP)^{6,14}.

The GGA functionals are very popular due to high accuracy to cost ratio for many system, such as transition metals, ionic crystals, compound metals, surface, interfaces and some

chemical systems. The GGA functionals are well accepted for predicting reliable binding energies and geometries.^{15,16} For example, Hammer et al.¹⁵ compared the chemisorption of O, CO and NO on Ni(100), Ni(111), Rh(100), Pd(100), and Pd(111) surfaces, and found that the GGA functionals, especially for the RPEB functional, produce moderate chemisorption energies with uncertainties less than about 0.25 eV .

Compared to LDA functionals, GGA functionals reduce the bond dissociation error and improve the transition state energy barrier. For instance, Hammer et al.¹⁷ found that GGA functionals predict reasonable values of H₂ chemisorption energy and dissociation barrier on Cu(111). Pederson et al.¹⁸ proposed that GGA leads to a more reasonable hydrogen exchange reaction barrier of the CH₃-CH₄ compared to local density approximation (8.7 kcal/mol vs 0.7 kcal/mol), with experimental value of 14 kcal/mol.

2.1.5 Electron Self-interaction Errors

The GGA functionals are widely adopted to account for the exchange-correlation term (Equation (7)), and have been implemented in many plane wave-based DFT packages (e.g., VASP,^{19,20} Quantum espresso²¹). However, electron self-interaction error occurs when standard GGA functionals are used to calculate lattice parameters, magnetic moments, band gaps, oxygen vacancy formation energies of systems with localized d- or f- orbitals, notably in the case of transition metal oxides (e.g., TiO₂,^{22,23} CeO₂^{24,25}). In order to address this issue, empirical electron Coulomb (U) and exchange (J) parameters are introduced to GGA functionals named GGA + U method for subjecting to the d-, f-electrons in the system.

One way to determine the Hubbard U parameter used in GGA + U methods can be carried out by screening a range of U values based on the known properties of the material.^{26,27}

Alternative approach can treat U as a non-empirical property to introduce a self-consistent procedure based on a linear-response approach to derive the U and J parameters,²⁸ which has been used for trend analysis of MO_2 ($M = \text{Ti, Cr, Mn, Nb, Mo, Ru, Rh, Re, Ir, and Pt}$) activities in oxygen evolution reaction.²⁹ In this thesis, the U and J values for CeO_2 in Chapter 7 section 7.2 are obtained from literature²⁴, based on the second approach mentioned above.

2.2 Modeling Techniques for Surface Chemistry

2.2.1 Generate Single Crystal Surfaces

Surface with well-defined sites participating catalytic reactions are generated for DFT calculations. Such model surfaces are often cleaved from corresponding single crystals. The low-index surfaces, such as (111) and (100) for face-centered cubic (FCC) crystals, are widely used to represent close-packed and open planar surfaces, and are illustrated in [Figure 2.1\(a-b\)](#). The (111) surface in FCC crystal is the most close-packed surface, and the coordination number (CN) of surface layer atoms is 9. The (100) surface is a more open surface, and the CN of surface layer atoms is 8. The (111) facet may contain fcc, hcp, top, and bridge sites, as indicated in [Figure 2.1\(a\)](#). The (100) facet can contain 4-fold hollow site, bridge site, and top site as shown in [Figure 2.1\(b\)](#). It is a common practice in this study that only the most stable configuration of atomic or molecular adsorption is analyzed.

Beside planar facets, step, corner, and defective facets are common in realistic catalyst structures. For example, [Figure 2.1\(c\)](#) represents the (211) facet of the FCC crystal, and the CN of surface layer atoms is 7, which may have both step (edge) sites and the terrace sites. Near the edge of (211) surface, it includes top, bridge, 4-fold, fcc near edge, and hcp near edge sites as shown in [Figure 2.1\(d\)](#). For computational convenience and efficiency, catalyst surfaces are

modeled with slab models bounded in a supercell with periodic boundaries. The slab top and bottom are separated by a vacuum space perpendicular to the surface as shown in Figure 2.1(c). In the slab models, the bottom layers are fixed to the optimized bulk lattice values, while surface and near surface layers are relaxed along with adsorbates. The vacuum should also be sufficiently large in order to avoid the interference between surface adsorbate and bottom layers.

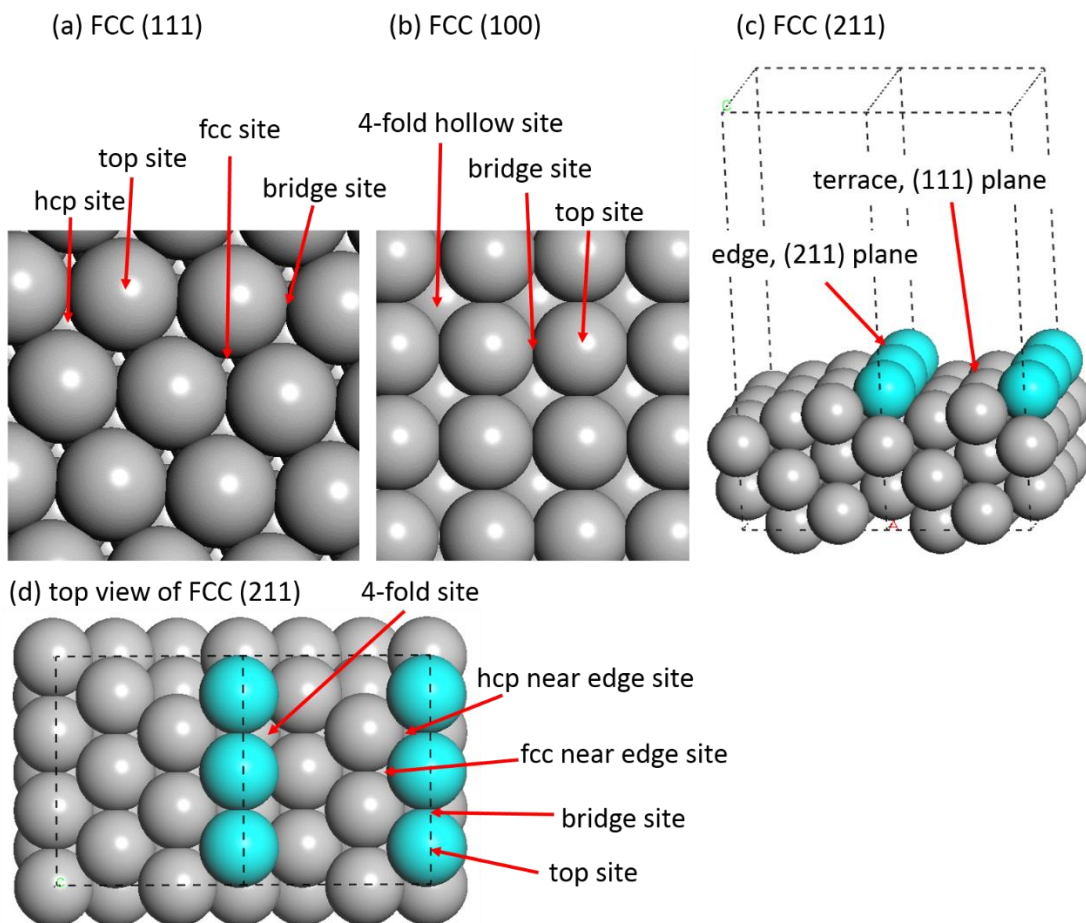


Figure 2.1. Surface models based on a FCC single crystal: (a) (111), (b) (100), (c) (211), and (d) top view of (211) facet. Available adsorption sites on each surface are labeled. Black dashed lines represent the boundaries of the supercell. The (211) facets in (c) and (d) are further expanded to show the 4-fold site. The edge atoms in (211) are highlighted in turquoise.

2.2.2 Bader Charge Analysis

Charge transfers at catalyst active sites can be tied to catalytic activity and selectivity. Theoretical calculations that lead to electronic charge distribution can directly produce information regarding charge transfers. The original concept proposed by Richard Bader³⁰, was developed into the Bader charge analysis³¹⁻³³. In this approach, the electronic charge density is used to partition molecular system into different sections based on zero flux surfaces, which is a 2-D surface with a minimum charge density perpendicular to the surface. The volume of each section can be considered as the occupation volume of each corresponding atomic species.

Bader charge analysis is a simple and useful technique. The calculated charge distribution can be used to determine multiple moments of interacting atoms or molecules, and the cost of removing charge from an atom can be quantified as well. The Bader charge analysis has also been incorporated into many DFT codes, such as VASP.

2.2.3 Transition State Search

Identifying and elucidating the minimum energy paths (MEPs) is important in surface science to describe atomic or molecular diffusion or reaction on given potential energy surface (PES). The transition state (saddle point), which is the highest energy point on the MEP, can be found and used to calculate the reaction energy barriers to determine reaction kinetics. A number of transition state search techniques are available³⁴ and I mainly focus on Nudged Elastic Band

Method (NEB) method and dimer method, which are the main tool for transition state search during my PhD.

2.2.3.1 Nudged Elastic Band method

The NEB method³⁵ is one of the most frequently used methods to find MEP especially when the initial and final states are known. During NEB calculations, the locations of initial intermediate images can be generated from a simple linear interpolation. Then those initial intermediate images along the reaction path are relaxed with finding the lowest energy while maintaining equal spacing to neighboring images to find the real MEP. During relaxation, the true force on each individual image in the elastic band is decomposed into a perpendicular and a parallel component to the MEP. A nudging force, perpendicular to the path, is employed to ensure that there will not be severe corner cutting at the curve of the MEP. Hence, NEB is ideal to map out the MEP; however, multiple saddle points can be identified.

In order to avoid the slip of the image near the saddle point, the modified Climbing Image NEB (CI-NEB) method³⁶ is developed to find saddle points more accurately in which the highest energy image is able to move towards the energy uphill through not feel the nudging force but the inverted force along the tangent. As a result, the image is able to maximize its energy along the band, while minimize in all other directions. When this image converges, the image will fall to the saddle point exactly.

2.2.3.2 Dimer method

When the product state on the MEP is complex and undefined, or only the knowledge of transition state is needed, the dimer method becomes advantageous. Based on the eigenvector-following theory, the first derivatives of the potential energy will be used to search the saddle

point, As shown in Figure 2.2³⁷, the two replicas generated from the initial guess structure (or a ‘dimer’) are rotated, pointing the direction of the lowest frequency normal mode (\hat{N}) during energy minimization.⁴ An effective force (\vec{F}^U), which is calculated using the component of the true force (\vec{F}_R) along the inverted direction of \hat{N} , is added to the dimer image, guiding the movements of the dimer image towards the saddle point.

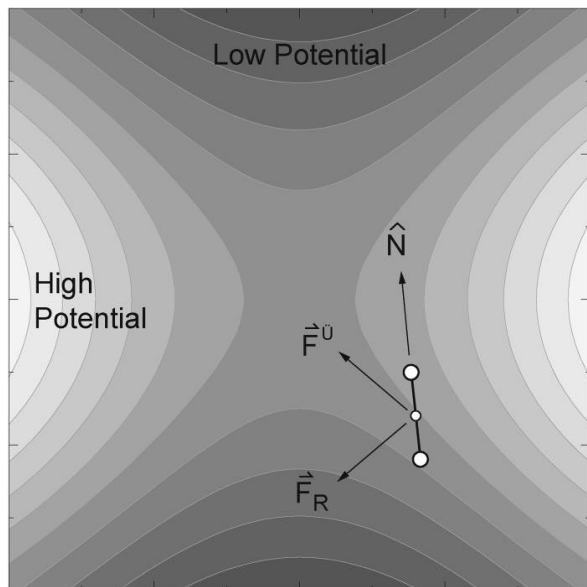


Figure 2.2. Illustrations of finding saddle point on a potential energy surface using dimer method.³⁷

Dimer method can be much more computationally efficient than NEB, as it requires fewer input structures. Recently, the dimer method is performed as a main approach to further refine the initial guess of transition state obtained from NEB calculations to accelerate transition state search.

2.2.4 Linear Scaling Relationship

The cost of DFT calculations can grow exponentially with the size of the model ³⁸, and thus will limit the considerations of surface chemistries involving large molecules and/or large systems. In addition, DFT calculations are only feasible for a limited number of systems, but can hardly do detailed analysis for all interesting systems. In order to overcome these issues, the so-called scaling relationships were established and been adapted and integrated in computational catalysis.

Abild-Pederson et al.³⁹ first formulated linear scaling relationships between the binding energies of several main group elements (i.e. C, O, N, S) and their hydrogenated counterparts (i.e. CH_x, NH_x, OH_x, SH_x) using periodic DFT calculations. [Figure 2.3](#) shows such an example where the elemental carbon (ΔE^c) and CH_x ($x = 1-3$) species (ΔE^{CH_x}) bind in a consistent linear trend described by Equation (17):

$$\Delta E^{CH_x} = \gamma \Delta E^c + \xi \quad (17)$$

where $\gamma = (\chi_{max} - \chi) / \chi_{max}$. χ_{max} represents the maximum number of H atoms that can bind to C, and χ is the total H atoms that actually bind to C. From Equation (17), ξ is independent of the substrate and can be determined from the linear fit. Equation (17) indicates that the binding energies of AH_x (ΔE^{AH_x}) can be estimated directly from ΔE^A , where A represents the main group elements (i.e., C, O, N, S).

These chemical elements (i.e. C, O, N, S) represent a vast number of important catalytic reactions. The physical rationale of these scaling relationships can be explained through orbital

hybridization and charge transfer.³⁹ In addition, the parameters (i.e., slope and intercept) of such scaling theory can be understood with a simple geometric argument, and further facilitate the understanding of molecular behavior on different catalyst surfaces.³⁹ For this reason, the scaling relationship has been quickly adopted and developed into a strategy, coupled with kinetic modeling, for catalyst optimization.

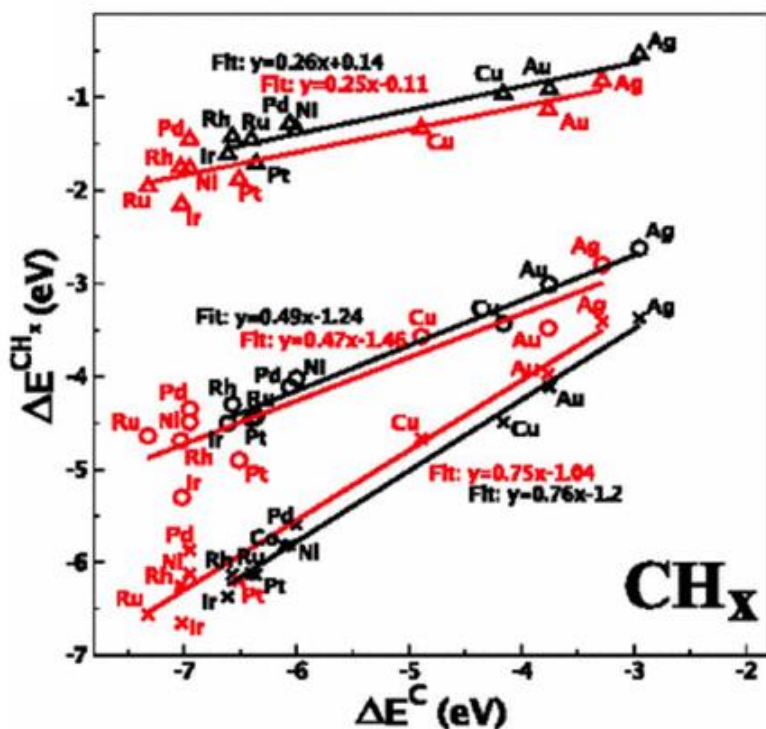


Figure 2.3. Binding energies of CH_x intermediates (crosses: $x = 1$; circles: $x = 2$; triangles: $x = 3$), plotted against adsorption energies of C, adapted from Ref. [39].

2.2.5 Brønsted-Evans-Polanyi (BEP) Relationship

The BEP relationship is another important type of scaling relationship⁴⁰⁻⁴² between reaction energies (ΔE) and energy barriers (E_a), as shown in Equation (18):

$$Ea = \alpha \cdot \Delta E + \beta \quad (18)$$

Energy barriers can be very computationally expensive to calculate using DFT. Therefore, an important use of BEP relationship is to accelerate analysis of reaction kinetics. In this case, elementary reaction kinetics can be characterized using two parameters (α and β , as in Equation (18)), which are functions of reaction types and catalyst. [Figure 2.4](#) presents an example of BEP relationship (the dash black-white line) which shows a good linear relation between the dissociative chemisorption potential energy for the dissociation products and activation energies for N₂, CO, NO, and O₂ dissociation over transition metals (e.g., Cu, Ni, Pt, Ru).⁴⁰

The BEP relationships between activation energy and reaction energy of surface reactions become extremely useful on heterogeneous catalysis to provide data being used in kinetic models. The mean average error is used to quantify the accuracy of the BEP relationships.^{43,44} It is essential to control the mean average error of BEP relationship because an error as small as 0.05 eV on the predicted energy barrier can lead to an error of at least 1 order of magnitude on the corresponding kinetic constant as the exponential nature of the Eyring equation.⁴⁵ Therefore, the reaction models should be refined to have a high quality BEP relationship for high accuracy catalyst screening.

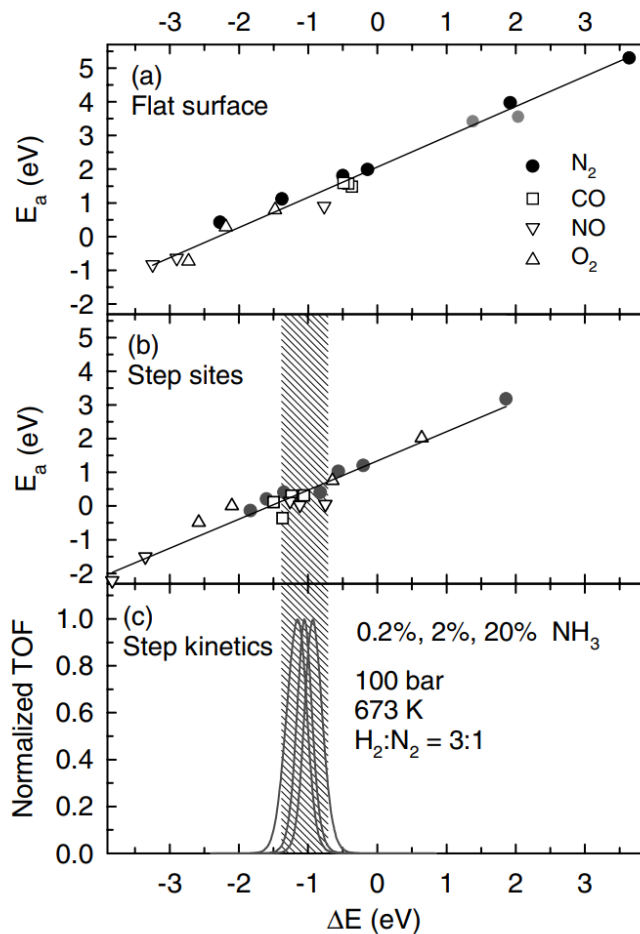


Figure 2.4. Calculated activation energies (E_a) for N_2 , CO, NO, and O_2 dissociation on a number of different metals plotted as a function of the calculated dissociative chemisorption potential energy for the dissociation products (ΔE).⁴⁰

2.2.6 Thermodynamic Properties Estimation

The relationships between macroscopic thermodynamic properties and quantum mechanical calculations can be established through the standard statistical mechanical approach.⁴⁶ The partition functions will be computed in order to derive entropy, enthalpy, and Gibbs free energy. The total partition function, q_{total} , can be expressed by Equation (19):

$$q_{total} = q_{electronic} \times q_{translation} \times q_{rotation} \times q_{vibration}. \quad (19)$$

As shown in Equation (19), the total partition functions can be broken down into the contributions from electronic, translational, rotational, and vibrational modes associated with thermal molecular motions. Detailed derivations and applications of these partition functions can be found in Ref ^{46,47}.

The electronic partition function ($q_{electronic}$) is represented by Equation (20):

$$q_{electronic} = \sum_{j, \text{electronic energies}} g_j e^{-\beta \epsilon_{j,e}} = g_0 + g_1 e^{-\beta \epsilon_{1,e}} + g_2 e^{-\beta \epsilon_{2,e}} + \dots \quad (20)$$

Because the electronic energies are usually quite large and all terms beyond the first term can be neglected. As a result, this approximation restricts the electronic partition function to the ground state only.

For gas phase species (e.g., CO, H₂O, CO₂, H₂, and CH₄), ideal gas law is assumed and the translational partition function ($q_{translation}(V, T)$) can be calculated from Equation (21):

$$q_{translation}(V, T) = \left(\frac{2\pi m k_B T}{h^2} \right)^{3/2} V \quad (21)$$

where m is the mass, k_B and h are Boltzmann and Planck constants, respectively, V is the volume per molecule occupied.

Homonuclear/heteronuclear diatomic gas (e.g., H₂, CO) and the polyatomic gas (e.g., H₂O, CO₂, CH₄) have different forms to calculate rotational partition functions. For homonuclear or heteronuclear diatomic gas, the rotational partition function ($q_{rotation}$) is calculated from Equation (22):

$$q_{rotation} = \frac{8\pi^2 I k T}{\sigma h^2} \quad (22)$$

where $\sigma = 1$ for the heteronuclear diatomic gas, and $\sigma = 2$ for homonuclear diatomic gas. I is the moment of inertia. For polyatomic gas, the rotational partition function is calculated by Equation (23):

$$q_{rotation} = \frac{\pi^{1/2}}{\sigma} \left(\frac{8\pi^2 I_a k_B T}{h^2} \right)^{1/2} \left(\frac{8\pi^2 I_b k_B T}{h^2} \right)^{1/2} \left(\frac{8\pi^2 I_c k_B T}{h^2} \right)^{1/2} \quad (23)$$

where σ is the symmetry factor, and I_a, I_b, I_c are the principles moments of inertia.

The vibrational partition function ($q_{vibration}$) is represented by Equation (24):

$$q_{vibration} = \prod_{i=1}^{3N-6(5)} \left(\frac{1}{1 - e^{-\beta h c v_i}} \right) \quad (24)$$

where $\beta = \frac{1}{k_B T}$, c is a constant representing the speed of light, v_i (cm⁻¹) is the i^{th} vibrational mode, and N is the number of atoms in a molecule.

For adsorbed species, the weakly bounded adsorbates (e.g., H₂O on Ni(111)^{48,49}) can be assumed as two-dimensional gases, which have the translation and rotational modes. Correspondingly, translational, rotational, and vibrational partition functions can be expressed by Equations (25-27):

$$q_{translation(A,T)} = \left(\frac{2\pi m k_B T}{h^2} \right) A \quad (25)$$

$$q_{rotation} = \frac{\pi^{1/2}}{\sigma} \left(\frac{8\pi^2 I_{zz} k_B T}{h^2} \right)^{1/2} \quad (26)$$

$$q_{vibration} = \prod_{i=1}^{3N} \left(\frac{1}{1 - e^{-\beta h c v_i}} \right) \quad (27)$$

where m is the molecular weight, A is the surface area, I_{zz} is the moment of inertia representing the z -axis (the only possible rotational mode on the surface) through the mass center of the adsorbate, c is the speed of light, and v_i is the i^{th} vibrational mode, N is the total number of relaxed atoms, and $\beta = 1/k_B T$.

For strongly bounded adsorbates (e.g., CO adsorption on Ni(111)^{48,49}), the translational and rotational modes are frustrated. In this case, all degrees of freedom are contributed by the vibrational modes, which are assumed to be harmonic and calculated according to Equation (27).

Using the calculated partition functions, the entropy (S°), internal energy (U°), enthalpy (H°), and Gibbs free energy (G°) can be calculated by Equations (28-33) summarized in ref⁴⁷:

$$S_{translation}^{\circ}(T) = R[\ln\left(\frac{2\pi mk_B T}{h^2} A\right) + 1] \quad (28)$$

$$S_{rotation}^{\circ}(T) = R[\ln\left(\frac{\pi^{1/2}}{\sigma} \left(\frac{8\pi^2 I_{zz} k_B T}{h^2}\right)^{1/2}\right) + \frac{1}{2}] \quad (29)$$

$$S_{vibration}^{\circ}(T) = R \sum_i \left[\frac{hcv_i/k_B T}{e^{\beta hcv_i} - 1} - \ln(1 - e^{-\beta hcv_i}) \right] \quad (30)$$

$$U_{corrections}^{\circ}(T) = RT \sum_i \frac{\beta hcv_i}{\exp\left(\frac{hcv_i}{k_B T}\right) - 1} + \frac{3}{2} RT \quad (31)$$

$$H^{\circ} = E_{electronic} + ZPE + U_{corrections}^{\circ} \quad (32)$$

$$G^{\circ} = H^{\circ} - TS^{\circ} \quad (33)$$

where R is the gas constant, $E_{electronic}$ is the total energy from DFT calculation, ZPE is the zero point energy expressed as $ZPE = \frac{1}{2} \sum_i hcv_i$. By following this principle, macroscopic thermodynamic properties can be obtained from theoretical first-principles methods.

2.2.7 Micro-kinetic Modeling

Micro-kinetic modeling is a widely adopted technique linking an atomic level description of a reaction pathway based on DFT calculations to the measurable kinetic behavior (e.g., rate, selectivity) observed in the experiment to analyze the catalyst performance. The ‘Catalysis Micro-kinetic Analysis Package’ (CatMAP)⁵⁰ is the main tool used for micro-kinetic modeling in this thesis. A series of elementary reaction steps are used to represent the overall reaction. The reaction rate of each elementary step is obtained through solving a mean-field micro-kinetic

model at steady state with Equations (34-36).⁵⁰ In this case, surface coverages of reaction intermediates are assumed to be uniformly distributed.

$$r_i = k_i^+ \prod_j \theta_{ij} \prod_j p_{ij} - k_i^- \prod_l \theta_{il} \prod_l p_{il} \quad (34)$$

$$\frac{\delta \theta_i}{\delta t} = \sum_j S_{ij} r_j \quad (35)$$

$$k_i^\pm = \frac{k_B * T}{h} \frac{q_{total,its}}{q_{total,ij}} \exp\left(\frac{-E_{a/b}}{RT}\right) \quad (36)$$

r_i represents the rate of elementary step, i . k_i^\pm is the forward/reverse rate constant. θ_{ij} and θ_{il} represent concentrations (or coverages) of surface reactants and products, while p_{ij} and p_{il} are the unitless pressure of the gas phase reactants and products for elementary step i . S_{ij} are coefficients for the stoichiometry of species i in elementary step j . In addition, $q_{total,its}$ and $q_{total,ij}$ are the total partition function for transition state and reactant in elementary step i calculated in Section 2.2.6. E_a and E_b are the forward and reverse energy barriers of step i , which can be obtained from DFT calculations or estimation based on BEP relationship. At steady state, the solution should satisfy Equation (37):

$$\frac{\delta \theta_i}{\delta t} = 0 \quad (37)$$

which must be solved subject to the site conservation constraint Equation (38):

$$\sum_i \theta_i = \theta^{TOT} \quad (38)$$

where θ^{TOT} is the normalized surface area, which is equal to 1.

2.2.8 Volcano Plots and Trend Analysis and Predictions

With the establishment of linear scaling relationships and BEP relationship, it can be noted that catalytic behavior can be understood in a predictive way. Based on such observation, one step further is to apply first-principles methods toward rational catalyst design. The *Sabatier principle* states that the optimal catalyst should neither bind reactants too weakly nor the products too strongly. This principle essentially dictates that there must be an optimum of the rate of a catalytic reaction as a function of the heat of adsorption, which can be rather conveniently obtained from DFT calculations. Thus, catalytic performance can be qualitatively characterized with so called ‘catalytic descriptors’,⁵¹ which can be further used to quantitatively measure the performance via micro-kinetic modeling. The concept of descriptor can be conveniently adapted as a rational catalyst design parameter. Ammonia synthesis⁵² represents one such prominent example as shown in [Figure 2.5](#). Nitrogen adsorption energy itself ([Figure 2.5\(a\)](#)) or with N₂ dissociation barrier ([Figure 2.5\(b\)](#)) can be the descriptor to identify the activity of those transition metals to ammonia synthesis. Too strong or too weak binding of N₂ are all affecting ammonia synthesis adversely. An optimal strength of interaction is needed according to the Sabatier-type principle.

From [Figure 2.5\(b\)](#), we can know that there are two different ways to increase the activity of catalyst to ammonia synthesis. One way is still obeying the BEP relationship with developing

the catalyst from single metal catalyst to a bimetallic catalyst (e.g., CoMo, red dot in Figure 2.5(a)), the activity of CoMo for ammonia synthesis increase compare to both single metal Co and Mo. Another way is breaking the existing BEP relationship to a different lower lying one with doping alkali promoter on single metal (magenta line in Figure 2.5(b)). In this case, the catalyst activity changes to the direction of favoring the ammonia synthesis. Andersen et al.⁵³ also believed that a combination of different materials such as metals and oxides is another way to circumvent the BEP relationship to increase the catalyst activity for ammonia synthesis.

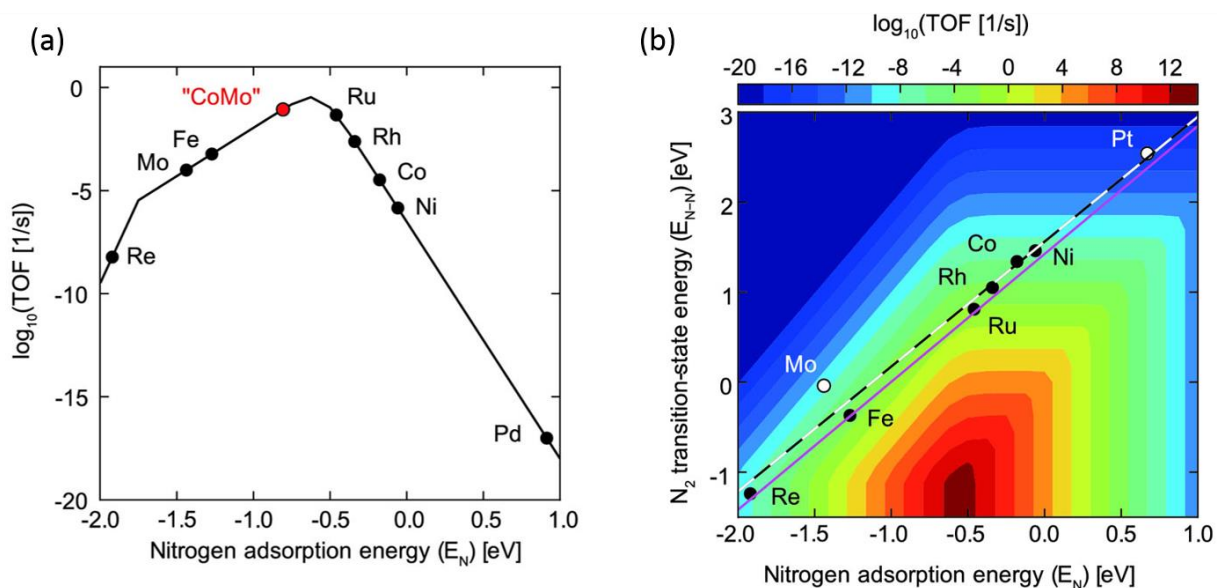


Figure 2.5. (a) Calculated rate as a function of a single descriptor of E_N . A data point of an intermetallic compound with active sites consisting of both Co and Mo is indicated. Experiments show such a material with activity close to that of Ru.⁵⁴ (b) Ammonia synthesis rate as a function of nitrogen adsorption energy (E_N) and N_2 dissociation barrier (E_{N-N}), with energetics and the corresponding scaling relation for stepped sites (dashed black–white) showing a linear relationship between E_{N-N} and E_N . The alkali-promoted scaling relation is represented by the

magenta line.⁵²

References

1. Kohn, W.; Sham, L. J. Self-consistent equations including exchange and correlation effects. *Physical Review* **1965**, *140*.
2. Kittel, C. *Introduction to Solid State Physics*, 7th ed; Wiley: 1996; .
3. Monkhorst, H. J.; Pack, J. D. Special points for Brillouin-zone integrations. *Phys. Rev. B* **1976**, *13*, 5188-5192.
4. Shan, N.; Zhou, M.; Hanchett, M. K.; Chen, J.; Liu, B. Practical principles of density functional theory for catalytic reaction simulations on metal surfaces - from theory to applications. *Molecular Simulation* **2017**, *43*, 861-885.
5. Perdew, J. P.; Ruzsinszky, A.; Tao, J.; Staroverov, V. N.; Scuseria, G. E.; Csonka, G. I. Prescription for the design and selection of density functional approximations: More constraint satisfaction with fewer fits. *J. Chem. Phys.* **2005**, *123*.
6. Becke, A. D. Density-functional exchange-energy approximation with correct asymptotic behavior. *Physical Review A* **1988**, *38*, 3098-3100.
7. Becke, A. D. Density-functional thermochemistry. III. The role of exact exchange. *J. Chem. Phys.* **1993**, *98*, 5648-5652.
8. Becke, A. D. Density-functional thermochemistry. V. Systematic optimization of exchange-correlation functionals. *J. Chem. Phys.* **1997**, *107*, 8554-8560.
9. Becke, A. D. A new inhomogeneity parameter in density-functional theory. *J. Chem. Phys.* **1998**, *109*, 2092-2098.

10. Perdew, J. P.; Burke, K.; Ernzerhof, M. Generalized gradient approximation made simple. *Phys. Rev. Lett.* **1996**, *77*, 3865-3868.
11. Perdew, J. P.; Burke, K.; Ernzerhof, M. Erratum: Generalized gradient approximation made simple (Physical Review Letters (1996) 77 (3865)). *Phys. Rev. Lett.* **1997**, *78*, 1396.
12. Hammer, B.; Hansen, L. B.; Nørskov, J. K. Improved adsorption energetics within density-functional theory using revised Perdew-Burke-Ernzerhof functionals. *Phys. Rev. B Condens. Matter Mater. Phys.* **1999**, *59*, 7413-7421.
13. Perdew, J. P.; Ruzsinszky, A.; Csonka, G. I.; Vydrov, O. A.; Scuseria, G. E.; Constantin, L. A.; Zhou, X.; Burke, K. Restoring the density-gradient expansion for exchange in solids and surfaces. *Phys. Rev. Lett.* **2008**, *100*.
14. Lee, C.; Yang, W.; Parr, R. G. Development of the Colle-Salvetti correlation-energy formula into a functional of the electron density. *Physical Review B* **1988**, *37*, 785-789.
15. Hammer, B.; Nørskov, J. K. Theoretical surface science and catalysis-calculations and concepts. *Adv. Catal.* **2000**, *45*, 71-129.
16. Mavrikakis, M.; Rempel, J.; Greeley, J.; Hansen, L. B.; Nørskov, J. K. Atomic and molecular adsorption on Rh(111). *J. Chem. Phys.* **2002**, *117*, 6737-6744.
17. Hammer, B.; Scheffler, M.; Jacobsen, K. W.; Nørskov, J. K. Multidimensional potential energy surface for H₂ dissociation over Cu(111). *Phys. Rev. Lett.* **1994**, *73*, 1400-1403.
18. Pederson, M. R. Density-functional based determination of the CH₃-CH₄ hydrogen exchange reaction barrier. *Chem. Phys. Lett.* **1994**, *230*, 54-60.
19. Kresse, G.; Furthmüller, J. Efficiency of ab-initio total energy calculations for metals and semiconductors using a plane-wave basis set. *Comput Mater Sci* **1996**, *6*, 15-50.

20. Kresse, G.; Hafner, J. Ab initio molecular-dynamics simulation of the liquid-metalamorphous- semiconductor transition in germanium. *Phys. Rev. B* **1994**, *49*, 14251-14269.
21. Giannozzi, P.; Baroni, S.; Bonini, N.; Calandra, M.; Car, R.; Cavazzoni, C.; Ceresoli, D.; Chiarotti, G. L.; Cococcioni, M.; Dabo, I.; Dal Corso, A.; De Gironcoli, S.; Fabris, S.; Fratesi, G.; Gebauer, R.; Gerstmann, U.; Gougoussis, C.; Kokalj, A.; Lazzeri, M.; Martin-Samos, L.; Marzari, N.; Mauri, F.; Mazzarello, R.; Paolini, S.; Pasquarello, A.; Paulatto, L.; Sbraccia, C.; Scandolo, S.; Sclauzero, G.; Seitsonen, A. P.; Smogunov, A.; Umari, P.; Wentzcovitch, R. M. QUANTUM ESPRESSO: A modular and open-source software project for quantum simulations of materials. *J Phys Condens Matter* **2009**, *21*.
22. Morgan, B. J.; Watson, G. W. A density functional theory plus U study of oxygen vacancy formation at the (110), (100), (101), and (001) surfaces of rutile TiO₂. *Journal of Physical Chemistry C* **2009**, *113*, 7322-7328.
23. Hu, Z.; Metiu, H. Choice of U for DFT plus U calculations for titanium oxides. *Journal of Physical Chemistry C* **2011**, *115*, 5841-5845.
24. Fabris, S.; de Gironcoli, S.; Baroni, S.; Vicario, G.; Balducci, G. Taming multiple valency with density functionals: A case study of defective ceria. *Physical Review B* **2005**, *71*, 041102.
25. Loschen, C.; Carrasco, J.; Neyman, K. M.; Illas, F. First-principles LDA+U and GGA+U study of cerium oxides: Dependence on the effective U parameter (vol 75, 035115, 2007). *Physical Review B* **2011**, *84*, 199906.
26. Cococcioni, M.; de Gironcoli, S. Linear response approach to the calculation of the effective interaction parameters in the LDA+U method. *Physical Review B* **2005**, *71*, 035105.
27. Anisimov, V.; Gunnarsson, O. Density-functional calculation of effective coulomb interactions in metals. *Physical Review B* **1991**, *43*, 7570-7574.

28. Kulik, H. J.; Cococcioni, M.; Scherlis, D. A.; Marzari, N. Density functional theory in transition-metal chemistry: A self-consistent Hubbard U approach. *Phys. Rev. Lett.* **2006**, *97*, 103001.
29. Xu, Z.; Rossmeisl, J.; Kitchin, J. R. A linear response DFT plus U study of trends in the oxygen evolution activity of transition metal rutile dioxides. *Journal of Physical Chemistry C* **2015**, *119*, 4827-4833.
30. Bader, R. F. W. *Atoms in Molecules: A Quantum Theory*; Clarendon Press: 1994; .
31. Henkelman, G.; Arnaldsson, A.; Jónsson, H. A fast and robust algorithm for Bader decomposition of charge density. *Comput Mater Sci* **2006**, *36*, 354-360.
32. Sanville, E.; Kenny, S. D.; Smith, R.; Henkelman, G. Improved grid-based algorithm for Bader charge allocation. *J. Comput. Chem.* **2007**, *28*, 899-908.
33. Tang, W.; Sanville, E.; Henkelman, G. A grid-based Bader analysis algorithm without lattice bias. *J. Phys. Condens. Matter* **2009**, *21*.
34. Henkelman, G.; Jónsson, H.; Arnaldsson, A. Methods for finding saddle points and minimum energy paths. In *Theoretical Methods in Condensed Phase Chemistry*; Schwartz, S. D., Ed.; Springer Netherlands: Dordrecht, 2002; pp 269-302.
35. Henkelman, G.; Jónsson, H. Improved tangent estimate in the nudged elastic band method for finding minimum energy paths and saddle points. *J. Chem. Phys.* **2000**, *113*, 9978-9985.
36. Henkelman, G.; Uberuaga, B. P.; Jónsson, H. Climbing image nudged elastic band method for finding saddle points and minimum energy paths. *J. Chem. Phys.* **2000**, *113*, 9901-9904.
37. Henkelman, G.; Jónsson, H. A dimer method for finding saddle points on high dimensional potential surfaces using only first derivatives. *J. Chem. Phys.* **1999**, *111*, 7010-7022.

38. Liu, B.; Greeley, J. Decomposition pathways of glycerol via C-H, O-H, and C-C bond scission on Pt(111): A density functional theory study. *J. Phys. Chem. C* **2011**, *115*, 19702-19709.
39. Abild-Pedersen, F.; Greeley, J.; Studt, F.; Rossmeisl, J.; Munter, T. R.; Moses, P. G.; Skúlason, E.; Bligaard, T.; Nørskov, J. K. Scaling properties of adsorption energies for hydrogen-containing molecules on transition-metal surfaces. *Phys. Rev. Lett.* **2007**, *99*.
40. Nørskov, J.; Bligaard, T.; Logadottir, A.; Bahn, S.; Hansen, L.; Bollinger, M.; Bengaard, H.; Hammer, B.; Sljivancanin, Z.; Mavrikakis, M.; Xu, Y.; Dahl, S.; Jacobsen, C. Universality in heterogeneous catalysis. *Journal of Catalysis* **2002**, *209*, 275-278.
41. Wang, S.; Temel, B.; Shen, J.; Jones, G.; Grabow, L. C.; Studt, F.; Bligaard, T.; Abild-Pedersen, F.; Christensen, C. H.; Nørskov, J. K. Universal Brønsted-Evans-Polanyi relations for C-C, C-O, C-N, N-O, N-N, and O-O dissociation reactions. *Catal Lett* **2011**, *141*, 370-373.
42. Wang, S.; Petzold, V.; Tripkovic, V.; Kleis, J.; Howalt, J. G.; Skúlason, E.; Fernández, E. M.; Hvolbæk, B.; Jones, G.; Toftelund, A.; Falsig, H.; Björketun, M.; Studt, F.; Abild-Pedersen, F.; Rossmeisl, J.; Nørskov, J. K.; Bligaard, T. Universal transition state scaling relations for (de)hydrogenation over transition metals. *Phys. Chem. Chem. Phys.* **2011**, *13*, 20760-20765.
43. Sutton, J. E.; Vlachos, D. G. A theoretical and computational analysis of linear free energy relations for the estimation of activation energies. *ACS Catalysis* **2012**, *2*, 1624-1634.
44. Sutton, J. E.; Vlachos, D. G. Error estimates in semi-empirical estimation methods of surface reactions. *Journal of Catalysis* **2013**, *297*, 202-216.
45. Zaffran, J.; Michel, C.; Delbecq, F.; Sautet, P. Trade-off between accuracy and universality in linear energy relations for alcohol dehydrogenation on transition metals. *Journal of Physical Chemistry C* **2015**, *119*, 12988-12998.

46. McQuarrie, D. A. *Statistical Mechanics*; University Science Books: Sausalito, 2000; .
47. Le, T. N. -.; Liu, B.; Huynh, L. K. SurfKin: An ab initio kinetic code for modeling surface reactions. *J. Comput. Chem.* **2014**, *35*, 1890-1899.
48. Zhou, M.; Liu, B. DFT Investigation on the competition of the water-gas shift reaction versus methanation on clean and potassium-modified nickel(111) surfaces. *ChemCatChem* **2015**.
49. Zhou, M.; Le, T. N. M.; Huynh, L. K.; Liu, B. Effects of structure and size of Ni nanocatalysts on hydrogen selectivity via water-gas-shift reaction-A first-principles-based kinetic study. *Catal Today* **2016**.
50. Medford, A. J.; Shi, C.; Hoffmann, M. J.; Lausche, A. C.; Fitzgibbon, S. R.; Bligaard, T.; Nørskov, J. K. CatMAP: A software package for descriptor-based micro-kinetic mapping of catalytic trends. *Catal Lett* **2015**, *145*, 794-807.
51. Nørskov, J. K.; Bligaard, T.; Rossmeisl, J.; Christensen, C. H. Towards the computational design of solid catalysts. *Nat. Chem.* **2009**, *1*, 37-46.
52. Vojvodic, A.; Nørskov, J. K. New design paradigm for heterogeneous catalysts. *Natl. Sci. Rev.* **2015**, *2*, 140-143.
53. Andersen, M.; Medford, A. J.; Nørskov, J. K.; Reuter, K. Analyzing the case for bifunctional catalysis. *Angew. Chem. Int. Ed.* **2016**, *55*, 5210-5214.
54. Jacobsen, C. J. H.; Dahl, S.; Clausen, B. G. S.; Bahn, S.; Logadottir, A.; Nørskov, J. K. Catalyst design by interpolation in the periodic table: Bimetallic ammonia synthesis catalysts. *J. Am. Chem. Soc.* **2001**, *123*, 8404-8405.

Chapter 3 - Mechanism and Selectivity of WGSR on Ni(111) Surface

Chapter 3 is reproduced in part with permission from:

Zhou, M.; Liu, B. DFT Investigation on the Competition of the Water-Gas Shift Reaction Versus Methanation on Clean and Potassium-Modified Nickel(111) Surface. *ChemCatChem* **2015**, 7, 3928-3935.

3.1 Introduction

WGSR is commonly catalyzed on transition metals and has been proposed to proceed via the redox, carboxyl, and formate pathways,¹⁻⁵ as shown in Figure 3.1. The redox pathway includes direct CO oxidation. The carboxyl pathway includes the formation and dissociation of COOH^* , while the formate pathway includes the formation and dissociation of HCOO^* .

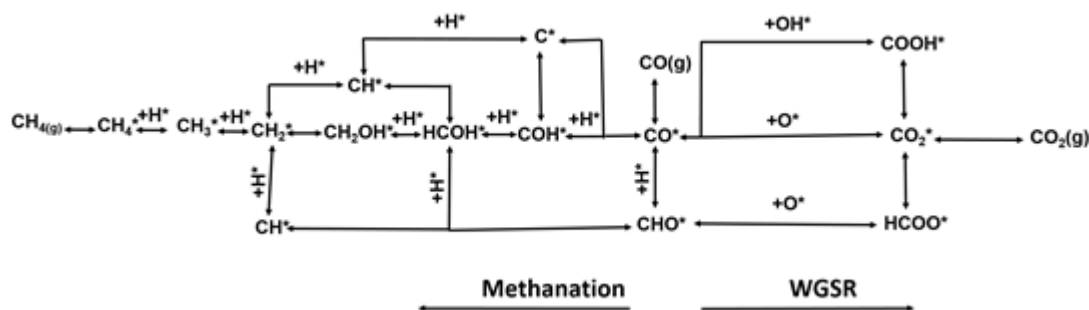


Figure 3.1. Reaction schemes of WGSR and methanation reaction. The asterisks (*) represents an open surface site or an adsorbed species. Water dissociation and H_2 formation are not shown in this scheme.

The preferred pathway for WGSR depends on the catalyst materials. On Pt(111), Cu(111), and Au(111) surfaces, carboxyl pathway is the most significant pathway.^{2,3,6,7} In

comparison, the formate (HCOO) pathway is less competitive than the redox and carboxyl pathways^{1-3,8}, and HCOO has been considered as a spectator species. Water dissociation plays an important role during WGS and has been discussed on transition metals.⁹ For example, water dissociation is the rate-limiting step for WGS catalyzed by Pt, Cu and Au.^{2,3,7} The dissociation products, i.e., O, OH species can actively influence the productions and consumptions of key reaction intermediates.^{2,3}

Studies¹⁰⁻¹³ performed on a number of monometallic catalysts suggest that Ni also exhibits promising reforming and WGS activities when comparing with Co, Cu, Fe, Ir, Rh, Ru, Pt, and Pd. The natural abundance enables Ni-based catalysts to be an appealing material for practical, large-scale hydrogen production¹⁴⁻¹⁶. For Ni, one of the challenges in heterogeneous catalysis is its tendency to cleave the C–O bond via methanation (as in Equation (39))^{17,18} or hydrogenolysis¹³, adversely affecting hydrogen selectivity.



A systematic study on methanation via CO hydrogenation has been conducted by Vannice over group VIII metals,¹¹ where Ni, Co, Ru, and Fe are among the most active methanation catalysts from the generated volcano plot with CO as descriptor. Methanation has also been extensively examined in the context of Fischer-Tropsch synthesis.¹⁹ The detailed Fischer-Tropsch mechanism is still under debate, and various reaction pathways have been investigated using DFT calculations^{20,21} to reveal that the C–O bond scission elementary steps are the rate-determining step. Regarding C–O bond scission, both direct and hydrogen-assisted

methanation mechanisms have been proposed^{20,22}, where the energy barrier can be significantly reduced once CO is partially hydrogenated.

In this chapter, the molecular pathways for WGSR and methanation will be established using density functional theory (DFT) calculations as two main parallel competing mechanisms on Ni catalysts.^{1,5,23} The most likely methanation pathways that compete with WGSR on Ni(111) surfaces are elucidated.

3.2 Computational Methods

Periodic, spin polarized DFT calculations were performed using Vienna *ab initio* simulation package (VASP).²⁴⁻²⁷ The exchange-correlation energy is calculated with the generalized gradient approximation PBE (GGA-PBE) functional.²⁸ A three-layer Ni(111) slab with a $p(3 \times 3)$ surface unit cell was used. The top layer and adsorbate were allowed to relax, whereas the bottom two layers are fixed at the corresponding bulk lattice value. The equilibrium lattice constant of a 4-atom Ni bulk unit cell is 3.52Å, which is in good agreement with the bulk value at 3.52Å.²⁹ The vacuum between any two successive slabs is 20 Å, and the plane wave energy cutoff is 385 eV. The first Brillouin zone of the slab model was sampled by a $4 \times 4 \times 1$ k-point mesh.³⁰ Convergence tests on water adsorption were carried out using higher k -points ($6 \times 6 \times 1$) and larger energy cutoff (400 eV), resulting in binding energy change below 0.01 eV.

In this Chapter, the binding energies (BEs) are defined as Equation (40),

$$BE_{A*} = E_{A*} - E_A - E_* \quad (40)$$

where E_{A*} is the total energy of the adsorbate (A), E_A is the total energy of the adsorbate (A) in gas phase calculated in a large box ($10 \text{ \AA} \times 10 \text{ \AA} \times 10.5 \text{ \AA}$), and E_* is the total energy of the clean surface.

Energy barriers of elementary steps were calculated using CI-NEB³¹ and dimer³² methods introduced in Chapter 2. All calculated transition state structures were also confirmed using vibrational frequency analysis to show that there is only one imaginary frequency associated with each transition state. The energy barrier (E_a) is calculated from Equation (41):

$$E_a = E_{TS} - E_{IS} \quad (41)$$

where E_{TS} is the total energy of the transition state and E_{IS} is the total energy of the initial state, with reactant species treated at infinite separations.

3.3 WGSR and Methanation Mechanisms on Clean Ni(111)

The competing pathways in the reaction networks are represented in terms of elementary steps describing adsorption, desorption, and chemical reactions on pre-defined sites of catalyst surfaces. The reaction network with combined WGSR and methanation consists of 18 reactive intermediates and 32 elementary steps as illustrated in [Figure 3.1](#). Essentially, the competition between WGSR and methanation is distinguished by C-O bond formations versus C-O bond cleavage ([Figure 3.1](#)). As shown in [Figure 3.1](#), the formyl group (CHO) is one of the few major intermediates involved in both reactions.

The binding energies and preferred binding sites of each reaction intermediate on clean Ni(111) surfaces are listed in **Table 3.1**. It can be seen that a good agreement between this work

and literature with same functional (GGA-PBE functional) regarding binding energies and predicted adsorption sites on clean Ni(111) surface has been achieved.

The calculated reaction energies, and the energy barriers of the elementary reaction steps, are given in **Table 3.2**. The optimized structures of reactive intermediates listed in **Table 3.1** and the transition state structures for elementary steps in **Table 3.2** are shown in [Figures 3.2 and 3.3](#), respectively.

Table 3.1. Binding energies (BE, in eV), site preferences, and literature values for WGSR and methanation intermediates on Ni(111) surface.

	BE[eV]	Site	Literature BE [eV]
CH ₄	0.00	physisorption	-0.02 ²³
CO ₂	-0.01	physisorption	-0.02 ²³ , -0.12 ¹
H ₂	-0.25	top	-0.22 ²³
H ₂ O	-0.27	top	-0.29 ²³ , -0.47 ¹
CH ₂ OH	-1.56	fcc	-1.54 ²³
CH ₃	-1.89	fcc	-1.91 ²³
CO	-1.93	hcp	-1.92 ²³ , -2.09 ¹
COOH	-2.25	bridge	-2.26(fcc) ²³ , -2.54(bridge-top) ¹
CHO	-2.27	fcc, hcp	-2.26(fcc) ²³ , -2.49(bridge)
H	-2.80	fcc	-2.81 ²³ , -2.77 ¹
HCOO	-2.88	top-top	-3.02 ¹
OH	-3.27	fcc	-3.42 ²³ , -3.34 ¹
HCOH	-3.88	fcc	-3.88 ²³
CH ₂	-4.03	fcc	-4.01 ²³
COH	-4.39	fcc, hcp	-4.39(hcp) ²³ , -4.42 ¹
O	-5.39	fcc	-5.67 ²³ , -4.81 ¹
CH	-6.41	fcc	-6.43 ²³
C	-6.48	hcp	-6.78 ²³ , -6.61 ¹

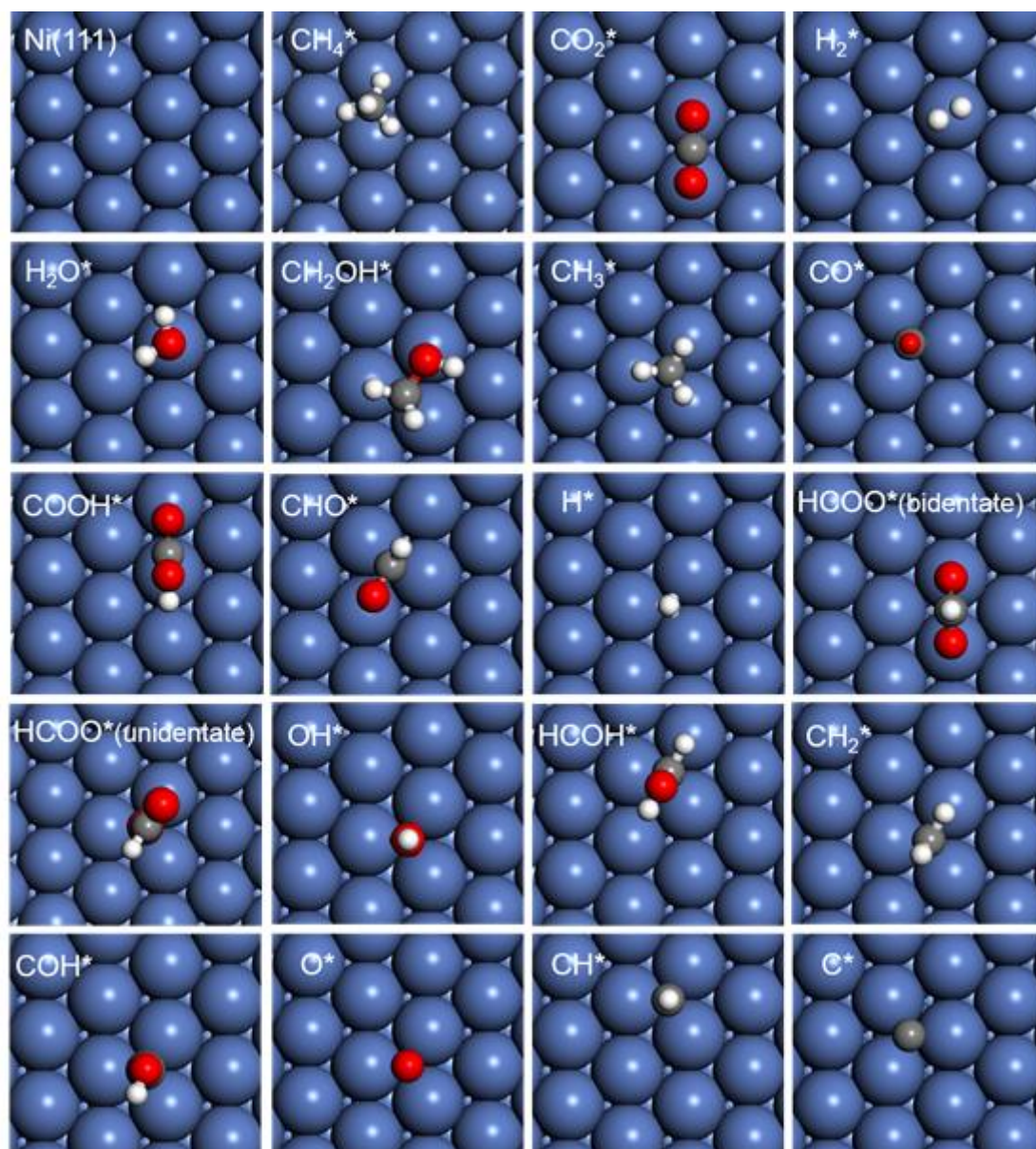


Figure 3.2. Optimized structures of reaction intermediates (in **Table 3.1**) on clean Ni(111). C, O, H, and Ni are depicted in grey, red, white, and blue, respectively.

Table 3.2. DFT-calculated reaction energies (ΔE [eV]), energy barriers (E_a [eV], and imaginary frequencies (ν_i [cm^{-1}]) of the transition states of the elementary reactions on clean Ni(111) surface.

	Elementary step	ΔE [eV]	$E_{a,f}(E_{a,b})^{[a]}$ [eV]	ν_i [cm^{-1}]
R1	$\text{CO (g)} + * \rightleftharpoons \text{CO}^*$	-1.93		
R2	$\text{H}_2\text{O (g)} + * \rightleftharpoons \text{H}_2\text{O}^*$	-0.27		
R3	$\text{CO}_2^* \rightleftharpoons \text{CO}_2 \text{ (g)} + *$	0.01		
R4	$\text{H}^* + \text{H}^* \rightleftharpoons \text{H}_2^* + *$	0.83	0.83(0.01)	-641
R5	$\text{H}_2^* \rightleftharpoons \text{H}_2 \text{ (g)} + *$	0.25		
R6	$\text{CH}_3^* + \text{H}^* \rightleftharpoons \text{CH}_4\text{(g)} + 2^*$	-0.03		
R7	$\text{H}_2\text{O}^* + * \rightleftharpoons \text{OH}^* + \text{H}^*$	-0.41	0.86(1.27)	-878
R8	$\text{OH}^* + * \rightleftharpoons \text{O}^* + \text{H}^*$	-0.20	0.98(1.17)	-1219
R9	$\text{OH}^* + \text{OH}^* \rightleftharpoons \text{H}_2\text{O}^* + \text{O}^*$	0.22	0.48(0.27)	-137
R10	$\text{CO}^* + \text{O}^* \rightleftharpoons \text{CO}_2^* + *$	0.97	1.56(0.60)	-455
R11	$\text{CO}^* + \text{OH}^* \rightleftharpoons \text{COOH}^* + *$	0.96	1.40(0.44)	-289
R12	$\text{COOH}^* + * \rightleftharpoons \text{CO}_2^* + \text{H}^*$	-0.19	0.93(1.11)	-1343
R13	$\text{COOH}^* + \text{O}^* \rightleftharpoons \text{CO}_2^* + \text{OH}^*$	0.01	0.20(0.19)	-929
R14	$\text{COOH}^* + \text{OH}^* \rightleftharpoons \text{CO}_2^* + \text{H}_2\text{O}^*$	0.22	0.00(0.00)	-101
R15	$\text{CO}^* + \text{H}^* \rightleftharpoons \text{CHO}^* + *$	1.25	1.44(0.19)	-245
R16	$\text{CHO}^* + \text{O}^* \rightleftharpoons \text{HCOO}^* + *$	-0.41	0.73(1.14)	-318
R17	$\text{HCOO}^* + * \rightleftharpoons \text{CO}_2^* + \text{H}^*$	0.13	0.99(0.86)	-195
R18	$\text{HCOO}^* + \text{O}^* \rightleftharpoons \text{CO}_2^* + \text{OH}^*$	0.33	1.75(1.42)	-1115

R19	$\text{HCOO}^* + \text{OH}^* \rightleftharpoons \text{CO}_2^* + \text{H}_2\text{O}^*$	0.54	1.88(1.33)	-126
R20	$\text{CO}^* + * \rightleftharpoons \text{C}^* + \text{O}^*$	1.28	2.88(1.60)	-472
R21	$\text{CO}^* + \text{CO}^* \rightleftharpoons \text{CO}_2^* + \text{C}^*$	2.25	3.49(1.24)	-320
R22	$\text{CHO}^* + * \rightleftharpoons \text{CH}^* + \text{O}^*$	-0.50	1.04(1.54)	-344
R23	$\text{CO}^* + \text{H}^* \rightleftharpoons \text{COH}^* + *$	0.96	1.91(0.95)	-1557
R24	$\text{COH}^* \rightleftharpoons \text{C}^* + \text{OH}^*$	0.52	1.86(1.34)	-323
R25	$\text{CHO}^* + \text{H}^* \rightleftharpoons \text{HCOH}^* + *$	0.43	1.14(0.71)	-1267
R26	$\text{COH}^* + \text{H}^* \rightleftharpoons \text{HCOH}^* + *$	0.73	0.83(0.10)	-631
R27	$\text{HCOH}^* + * \rightleftharpoons \text{CH}^* + \text{OH}^*$	-0.74	0.72(1.45)	-425
R28	$\text{HCOH}^* + \text{H}^* \rightleftharpoons \text{CH}_2\text{OH}^* + *$	0.34	0.87(0.53)	-901
R29	$\text{CH}_2\text{OH}^* + * \rightleftharpoons \text{CH}_2^* + \text{OH}^*$	-0.70	0.65(1.35)	-417
R30	$\text{C}^* + \text{H}^* \rightleftharpoons \text{CH}^* + *$	-0.53	0.86(1.39)	-877
R31	$\text{CH}^* + \text{H}^* \rightleftharpoons \text{CH}_2^* + *$	0.38	0.74(0.36)	-758
R32	$\text{CH}_2^* + \text{H}^* \rightleftharpoons \text{CH}_3^* + *$	-0.03	0.63(0.66)	-854

^[a]Energy barriers of reverse reaction are shown in the parentheses.

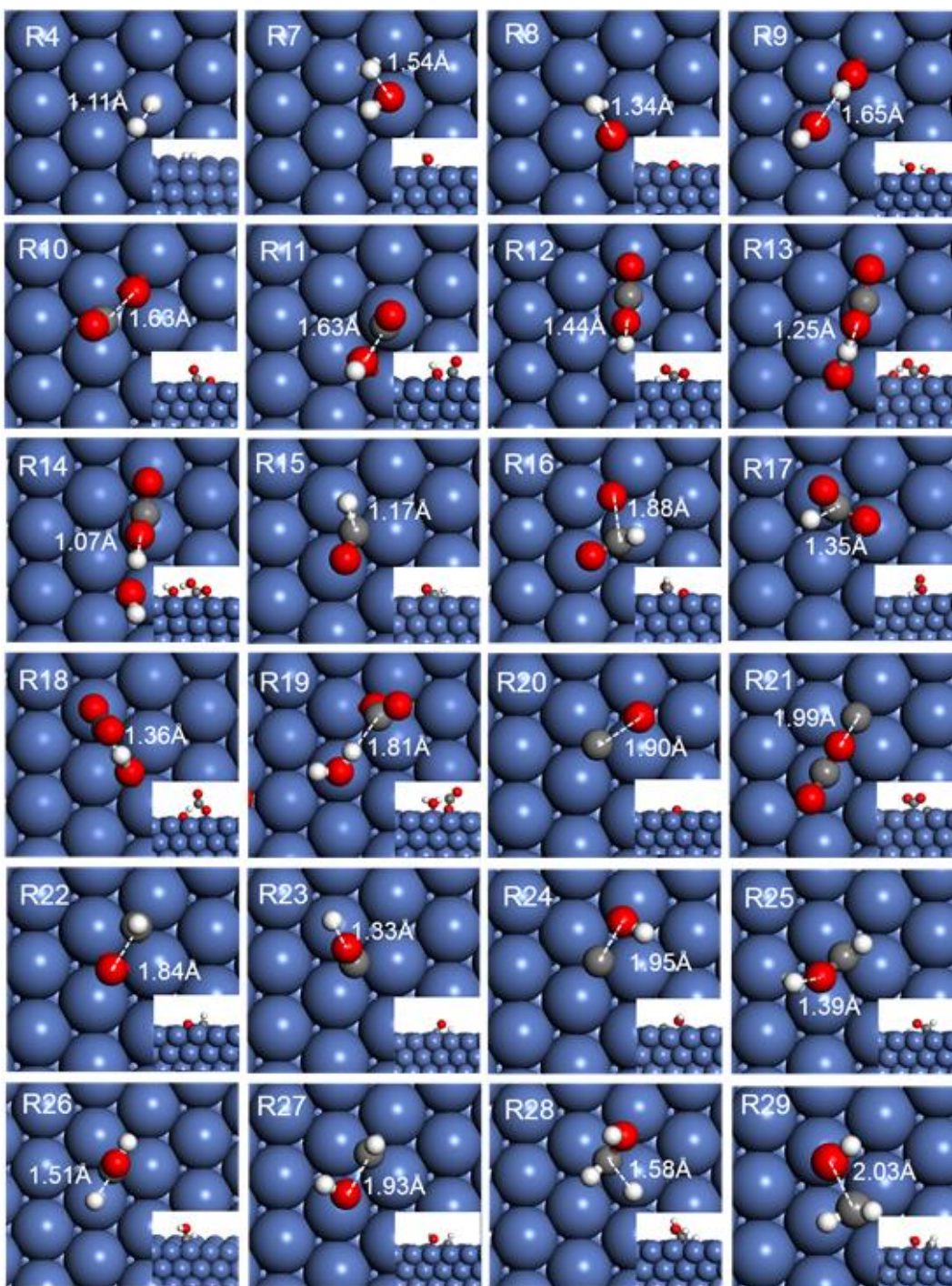


Figure 3.3. Transition state (TS) structures of elementary steps (labeled the same way as in **Table 3.2**) on clean Ni(111). The side view of each TS structure is shown as inset figure. C, O, H, and Ni are depicted in grey, red, white, and blue, respectively.

The above calculated binding energies and reaction barriers produce the most fundamental data to establish molecular-level mechanism. Optimized structures of these reaction intermediates provide the opportunity to rationalize the calculated reaction energetic and kinetic data. The elementary steps on close-packed nickel catalyst surface will be discussed in more detail.

3.3.1 H₂O Dissociation

On clean Ni(111), the adsorption energy of H₂O is -0.27 eV on the top site. R7 is exothermic (-0.41 eV) with an energy barrier of 0.86 eV. OH* dissociation to produce O* and H* (R8) is also exothermic (-0.20 eV) with an energy barrier of 0.98 eV. The energy barriers of these two steps are lower than that on Cu(111)² and Pt(111)³.

The disproportionation of OH* (R9) is an alternative pathway to produce atomic O*. The reaction is endothermic by 0.22 eV with an energy barrier of 0.48 eV, which is approximately half as low as the barrier for OH* dissociation. Unlike WGSR on Cu(111) or Pt(111), in which the disproportionation reaction is favored both energetically and kinetically,^{2,3} the advantage of R9 is not as clear on Ni(111). Even though R9 becomes kinetically favorable (0.48 vs. 0.98 eV), it is thermodynamically more endothermic (0.22 vs. -0.20 eV) compared to R8.

3.3.2 WGSR Pathways on Clean Ni(111) Surface

The calculated reaction energetics and kinetics of redox, carboxyl, and formate pathways on clean Ni(111) surface are all considered here and summarized in [Figure 3.4](#).

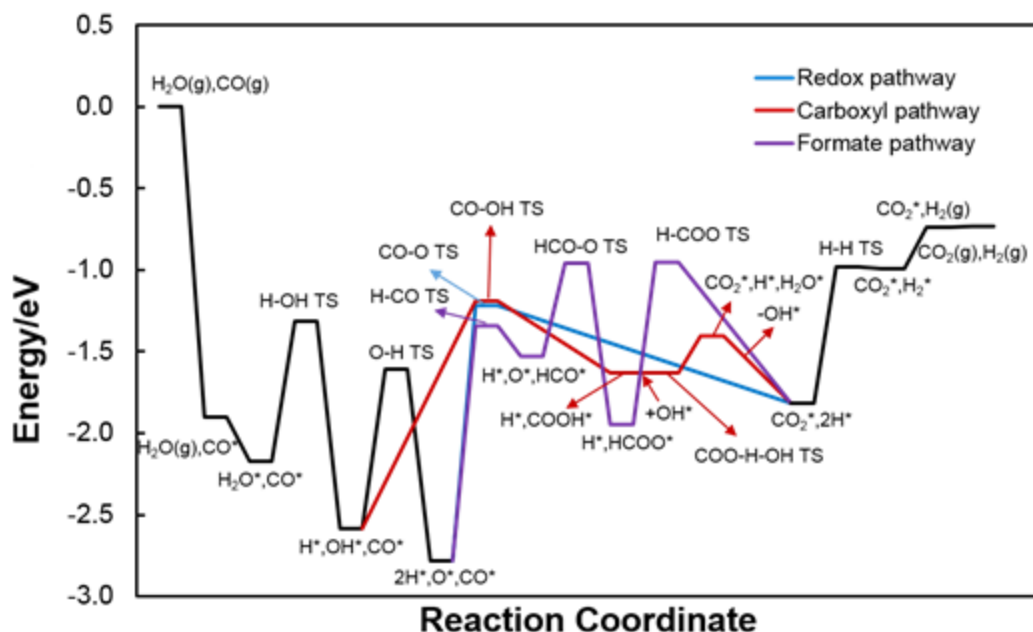


Figure 3.4. Potential energy surfaces (PESs) of the redox (blue), carboxyl (red), and formate (purple) pathways on clean Ni(111). Transition state species are marked as TS and extra OH* are added to balance the whole step. Two black pathways represent water dissociation and gas product formation.

Redox pathway: Direct CO*oxidation by surface O* species (generated from water dissociation) forming CO₂* (R10) is endothermic (0.97 eV). The energy barrier is 1.56 eV, which is consistent with Catapan's work,¹ and higher than that on Cu(111)² and Pt(111)³ (0.82 eV and 0.96 eV, respectively). Step R10 is the rate-limiting step in the redox pathway (Figure 3.4, blue pathway).

Carboxyl pathway: The carboxyl group (COOH*) is formed by R11 and adsorbs at the bridge site in which H points down towards the surface. The formation of COOH* is endothermic (0.96 eV) with an energy barrier of 1.40 eV. The formation of COOH* is rate-limiting (Figure 3.4, red pathway).

CO₂ can be formed by carboxyl dehydrogenation as in R12, which is exothermic (-0.19 eV) with an energy barrier of 0.93 eV. Aside from direct COOH* dehydrogenation, the participation of nearby O* and OH* species in R13 and R14 can reduce the energy barrier, as suggested in previous studies.¹⁻³ In R13, with the assistance of O*, O-H bond cleavage becomes nearly thermally neutral (0.01 eV). The energy barrier for H* transfer from COOH* to O* becomes approximately 0.20 eV, much lower than that of direct COOH* dissociation. With OH* (R14), the reaction energy is 0.22 eV and the reaction barrier is negligible (~ 0 eV), which indicates that the H* in COOH* can be transferred to nearby OH* species almost spontaneously to form water and CO₂.

Formate pathway and formate formation: From CO, the formyl species (CHO*) is the precursor for formate formation (Figure 3.4, purple pathway). CHO is produced by the combination of CO* and H* (R15), which is highly endothermic (1.25 eV) with an energy barrier of 1.44 eV.

The formation of HCOO* by C-O bond formation between CHO* and O* (R16) is exothermic (-0.41 eV) with an energy barrier of 0.73 eV. CO₂* can be formed from HCOO* adsorbed in a unidentate manner, which is 0.58 eV metastable (Figure 3.2), by R17. On clean Ni(111), R17 is endothermic (0.13 eV) with an energy barrier of 0.99 eV. Similar to COOH* dehydrogenation, the O- and OH-assisted mechanisms were investigated as R18 and R19, respectively. R18 is endothermic (0.33 eV) with an energy barrier of 1.75 eV. R19 is also endothermic (0.54 eV) with an energy barrier of 1.88 eV. Unlike O- and OH-assisted carboxyl dehydrogenation, the O*/OH* species cannot increase either energetic or kinetic favorability, and similar conclusions were obtained for other metals.¹⁻³ Instead, the reverse reaction, that is, formate formation from CO₂ hydrogenation, are both energetically and kinetically more

favorable on Ni(111) (**Table 3.2**). Thus, at a higher CO₂ pressure, it can be expected that the WGSR could be adversely affected by formate site blockage.

Comparison of WGSR pathways: R10 and R11 are the rate-limiting steps for the redox (blue) and carboxyl (red) pathways ([Figure 3.4](#)), respectively, and both pathways are energetically and kinetically comparable. The redox pathway is more sensitive to the availability of O* species, in which the OH disproportionation (R9) step can act as an alternative source for O* in addition to R8, but with much lower reaction barriers. In the formate pathway (purple), the formation of formate is limited by the slow kinetics caused by R16 and R17. Hence, the formate pathway will not be as competitive as the redox or carboxyl pathways and will not be included in the discussion in section 3.3.4.

3.3.3 Methanation Reaction

Five C-O bond cleavage pathways were considered, that is, (1) direct C-O bond cleavage of CO*; (2) C-O bond cleavage of CHO*; (3) C-O bond cleavage of COH*; (4) C-O bond cleavage of HCOH*; and (5) C-O bond cleavage of CH₂OH* ([Figure 3.5](#)). Gas-phase CO, H₂O (the H source), and a clean surface were used to produce the potential energy surface.

produces CH^* and O^* (Figure 3.5, purple pathway). This elementary step is exothermic (-0.50 eV) with an energy barrier of 1.04 eV. Compared to R16 for formate formation, the energetics of R22 are slightly more favorable (-0.5 vs. -0.41 eV in R16). However, the C-O bond cleavage energy barrier is higher (1.04 vs. 0.73 eV).

C-O bond cleavage of COH^* : The hydrogenation of the O site of CO produced COH through R23, which is endothermic (0.96 eV), with an energy barrier of 1.91 eV. This barrier of COH* formation is higher than that of the hydrogenation of the C in CO to form CHO. The C-O bond cleavage of COH* (R24; Figure 3.5, red pathway) is endothermic (0.52 eV) with an energy barrier of 1.86 eV.

C-O bond cleavage of HCOH^* : Further hydrogenation of CHO^* or COH^* can produce HCOH* by R25 (Figure 3.5, brown pathway) and R26 (Figure 3.5, yellow pathway). Both reactions are endothermic (0.43 and 0.73 eV, respectively), and the corresponding energy barriers are 1.14 and 0.83 eV, respectively. The C-O bond cleavage of HCOH* through R27 (Figure 3.5, yellow pathway) to form CH^* and OH^* is exothermic (-0.74 eV) with an energy barrier of 0.72 eV, which is much lower than the energy barriers of C-O bond cleavage for CO^* , COH^* , and CHO^* discussed above.

C-O bond cleavage of CH_2OH^* : The formation of CH_2OH^* through R28 from HCOH* is endothermic (0.34 eV) with an energy barrier of 0.87 eV. The dissociation of CH_2OH^* through R29 (Figure 3.5, green pathway) to form CH_2^* and OH^* is exothermic (-0.70 eV) with an energy barrier of 0.65 eV.

Comparison of methanation routes: C-O bond cleavage is usually the rate-limiting step in each methanation route. The C-O bond cleavage energy barrier decreases for partially hydrogenated CO intermediates in the order of: $\text{C-O} > \text{C-OH} > \text{CH-O} > \text{CH-OH} > \text{CH}_2\text{-OH}$ (Table 3.2). This

indicates that on the clean Ni(111) surface, it is likely that C-O bond dissociation occurs at much lower energy barriers upon hydrogenation.^{20,34} The consumption of surface H species causes the decreased H₂ selectivity directly.

Hydrogenation of CO may occur as early as the first step of H₂O dissociation. The first CO hydrogenation produces either CHO* (the more kinetically competitive step) or COH* (the more energetically competitive step). The formyl group can undergo C-O bond cleavage directly (Figure 3.5, purple pathway) to form CH* or continue to be hydrogenated to form HCOH*, which is a metastable intermediate in comparison. For COH*, because of the high barrier of C-O bond cleavage, it is more likely that COH follows the pathway to first form HCOH* through R26 → R27 (Figure 3.5, yellow pathway). Finally, even though the C-O bond cleavage energy barrier is the lowest (0.65 eV) among all the considered pathways, the formation of CH₂OH is overall endothermic according to Figure 3.5. Therefore, the CH₂OH pathway is not as competitive as the CHO, H-COH, or CHO-H pathways.

3.3.4. Comparison between WGSR and Methanation Reaction

If we combine the most competitive pathways for the WGSR and methanation on clean Ni(111), the selectivity between the two reactions is summarized in Figure 3.6. Firstly, the selectivity of WGSR can be affected by the competition between CO oxidation by OH (R11) and CO hydrogenation (R15). Both steps have comparable energy barriers (1.40 eV versus 1.44 eV; Figure 3.6). However, R11 is less endothermic than R15 (0.96 eV versus 1.25 eV). As discussed in section 3.3.2, the carboxyl group can form CO₂ easily (0.00 eV energy barrier for R14), whereas formyl decomposition via R22 requires a very large energy barrier (1.04 eV), even though R22 (to produce CH* and O*) is more exothermic. In addition, the redox pathway of

WGSR can also be competitive as the overall potential energy is comparable to that of carboxyl pathway.

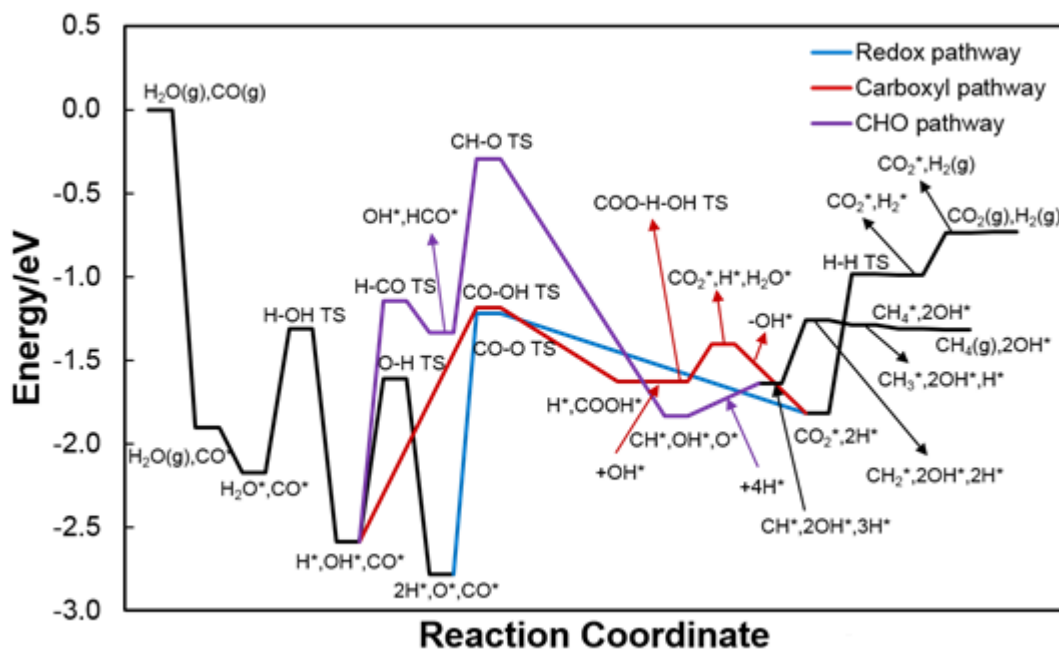


Figure 3.6. Potential energy surfaces of WGSR (redox and carboxyl pathways) and methanation (CHO pathway) on clean Ni(111) surface. Transition state species are marked as TS and extra OH* and H* are added if necessary to balance reactive species. Black pathways represent water dissociation and gas products formation.

Energetically, methanation by the $\text{CO}^* \rightarrow \text{CHO}^* \rightarrow \text{CH}^*$ route can be competitive against WGSR routes: $\text{CO}^* \rightarrow \text{COOH}^* \rightarrow \text{CO}_2^*$ (carboxyl pathway), and $\text{CO}^* \rightarrow \text{CO}_2^*$ (redox pathway) on clean Ni(111). However, on the *flat* Ni(111) surface, the selectivity favors WGSR as methanation through the CHO pathway is hindered by the large energy barrier of R22. Nevertheless, it should be noted that the methanation rate-limiting steps, such as R22 (and R24),

are sensitive to catalyst surface structures.^{20,35,36} It has been shown that the stepped or defect sites can lower the barriers of C-O bond cleavage in R22 and R24 and accelerate methanation in the competition against WGSR.¹

3.4 Conclusions

DFT calculations were performed on the WGSR and methanation elementary steps on Ni(111) surfaces. A comprehensive comparison of different reaction pathways was performed using the DFT-calculated energetics and kinetics to gain the reaction mechanism of WGSR. The redox pathway and carboxyl pathway are both thermodynamically and kinetically competitive.

The selectivity of WGSR can be affected by methanation reaction on Ni(111) surface. The key steps for methanation reaction, that is, formyl (CHO*) formation and dissociation through C-O bond cleavage, were found to be energetically competitive against the WGSR. The large C-O bond cleavage barrier hinders methanation on flat Ni(111).

3.5 Acknowledgements

This work was supported in part by the Start-up fund provided by Kansas State University, the National Science Foundation under Award No. EPS-0903806, and matching support from the State of Kansas through the Kansas Board of Regents. DFT calculations were carried out thanks to the supercomputing resources and services from the Center for Nanoscale Materials (CNM) supported by the Office of Science of the US Department of Energy under the contract No. DE-AC02-06CH11357; the Beocat Research Cluster at Kansas State University, which is funded in

part by NSF grants CNS-1006860; and the National Energy Research Scientific Computing Center (NERSC) under the contract No. DE-AC02-05CH11231.

References

1. Catapan, R. C.; Oliveira, A. A. M.; Chen, Y.; Vlachos, D. G. DFT study of the water-gas shift reaction and coke formation on Ni(111) and Ni(211) surfaces. *J. Phys. Chem. C* **2012**, *116*, 20281-20291.
2. Gokhale, A. A.; Dumesic, J. A.; Mavrikakis, M. On the mechanism of low-temperature water gas shift reaction on copper. *J. Am. Chem. Soc.* **2008**, *130*, 1402-1414.
3. Grabow, L. C.; Gokhale, A. A.; Evans, S. T.; Dumesic, J. A.; Mavrikakis, M. Mechanism of the water gas shift reaction on Pt: First principles, experiments, and micro-kinetic modeling. *J. Phys. Chem. C* **2008**, *112*, 4608-4617.
4. Tao, F.; Ma, Z. Water-gas shift on gold catalysts: Catalyst systems and fundamental studies. *Physical Chemistry Chemical Physics* **2013**, *15*, 15260-15270.
5. Lin, C.; Chen, C.; Wang, J. -. Mechanistic studies of water-gas-shift reaction on transition metals. *J. Phys. Chem. C* **2011**, *115*, 18582-18588.
6. Zhao, Z.; Li, Z.; Cui, Y.; Zhu, H.; Schneider, W. F.; Delgass, W. N.; Ribeiro, F.; Greeley, J. Importance of metal-oxide interfaces in heterogeneous catalysis: A combined DFT, micro-kinetic, and experimental study of water-gas shift on Au/MgO. *J. Catal.* **2017**, *345*, 157-169.
7. Rodriguez, J. A.; Senanayake, S. D.; Stacchiola, D.; Liu, P.; Hrbek, J. The activation of gold and the water-gas shift reaction: Insights from studies with model catalysts. *Acc. Chem. Res.* **2014**, *47*, 773-782.
8. Zhou, M.; Liu, B. DFT investigation on the competition of the water-gas shift reaction versus methanation on clean and potassium-modified nickel(111) surfaces. *ChemCatChem* **2015**.

9. Phatak, A. A.; Delgass, W. N.; Ribeiro, F. H.; Schneider, W. F. Density functional theory comparison of water dissociation steps on Cu, Au, Ni, Pd, and Pt. *J. Phys. Chem. C* **2009**, *113*, 7269-7276.
10. Sinfelt, J. H. Specificity in catalytic hydrogenolysis by metals. *Advances in Catalysis* **1973**, *23*, 91-119.
11. Vannice, M. A. The catalytic synthesis of hydrocarbons from H₂/CO mixtures over the Group VIII metals. V. The catalytic behavior of silica-supported metals. *J. Catal.* **1977**, *50*, 228-236.
12. Grenoble, D. C.; Estadt, M. M.; Ollis, D. F. The chemistry and catalysis of the water gas shift reaction. 1. The kinetics over supported metal catalysts. *J. Catal.* **1981**, *67*, 90-102.
13. Davda, R. R.; Shabaker, J. W.; Huber, G. W.; Cortright, R. D.; Dumesic, J. A. Aqueous-phase reforming of ethylene glycol on silica-supported metal catalysts. *Appl. Catal. B* **2003**, *43*, 13-26.
14. Haryanto, A.; Fernando, S. D.; To, S. D. F.; Steele, P. H.; Pordesimo, L.; Adhikari, S. Hydrogen production through the water - gas shift reaction: Thermodynamic equilibrium versus experimental results over supported Ni catalysts. *Energy Fuels* **2009**, *23*, 3097-3102.
15. Hwang, K.; Lee, C.; Park, J. Advanced nickel metal catalyst for water-gas shift reaction. *J. Power Sources* **2011**, *196*, 1349-1352.
16. Arbeláez, O.; Reina, T. R.; Ivanova, S.; Bustamante, F.; Villa, A. L.; Centeno, M. A.; Odriozola, J. A. Mono and bimetallic Cu-Ni structured catalysts for the water gas shift reaction. *Appl. Catal. A Gen.* **2015**, *497*, 1-9.

17. Kim, S. H.; Nam, S.; Lim, T.; Lee, H. Effect of pretreatment on the activity of Ni catalyst for CO removal reaction by water–gas shift and methanation. *Applied Catalysis B: Environmental* **2008**, *81*, 97-104.
18. Senanayake, S. D.; Evans, J.; Agnoli, S.; Barrio, L.; Chen, T. -.; Hrbek, J.; Rodriguez, J. A. Water-gas shift and CO methanation reactions over Ni-CeO₂(111) catalysts. *Top. Catal.* **2011**, *54*, 34-41.
19. Ojeda, M.; Nabar, R.; Nilekar, A. U.; Ishikawa, A.; Mavrikakis, M.; Iglesia, E. CO activation pathways and the mechanism of Fischer-Tropsch synthesis. *Journal of Catalysis* **2010**, *272*, 287-297.
20. Andersson, M. P.; Abild-Pedersen, F.; Remediakis, I. N.; Bligaard, T.; Jones, G.; Engbæk, J.; Lytken, O.; Horch, S.; Nielsen, J. H.; Sehested, J.; Rostrup-Nielsen, J. R.; Nørskov, J. K.; Chorkendorff, I. Structure sensitivity of the methanation reaction: H₂-induced CO dissociation on nickel surfaces. *J. Catal.* **2008**, *255*, 6-19.
21. Filot, I. A. W.; van Santen, R. A.; Hensen, E. J. M. The optimally performing Fischer-Tropsch catalyst. *Angewandte Chemie-International Edition* **2014**, *53*, 12746-12750.
22. Shetty, S.; Jansen, A. P. J.; van Santen, R. A. Direct versus hydrogen-assisted CO dissociation. *J. Am. Chem. Soc.* **2009**, *131*, 12874.
23. Zhu, Y.; Chen, D.; Zhou, X.; Yuan, W. DFT studies of dry reforming of methane on Ni catalyst. *Catalysis Today* **2009**, *148*, 260-267.
24. Kresse, G.; Furthmüller, J. Efficient iterative schemes for ab initio total-energy calculations using a plane-wave basis set. *Phys. Rev. B Condens. Matter Mater. Phys.* **1996**, *54*, 11169-11186.

25. Kresse, G.; Furthmüller, J. Efficiency of ab-initio total energy calculations for metals and semiconductors using a plane-wave basis set. *Comput Mater Sci* **1996**, *6*, 15-50.
26. Kresse, G.; Hafner, J. Ab initio molecular-dynamics simulation of the liquid-metalamorphous- semiconductor transition in germanium. *Phys. Rev. B* **1994**, *49*, 14251-14269.
27. Kresse, G.; Hafner, J. Ab initio molecular dynamics for liquid metals. *Phys. Rev. B* **1993**, *47*, 558-561.
28. Perdew, J. P.; Burke, K.; Ernzerhof, M. Generalized gradient approximation made simple. *Phys. Rev. Lett.* **1996**, *77*, 3865-3868.
29. Kittel, C. *Introduction to Solid State Physics*, 7th ed; Wiley: 1996; .
30. Monkhorst, H. J.; Pack, J. D. Special points for Brillouin-zone integrations. *Phys. Rev. B* **1976**, *13*, 5188-5192.
31. Henkelman, G.; Uberuaga, B. P.; Jónsson, H. Climbing image nudged elastic band method for finding saddle points and minimum energy paths. *J. Chem. Phys.* **2000**, *113*, 9901-9904.
32. Henkelman, G.; Jónsson, H. A dimer method for finding saddle points on high dimensional potential surfaces using only first derivatives. *J. Chem. Phys.* **1999**, *111*, 7010-7022.
33. Inderwildi, O. R.; Jenkins, S. J.; King, D. A. Fischer-tropsch mechanism revisited: Alternative pathways for the production of higher hydrocarbons from synthesis gas. *Journal of Physical Chemistry C* **2008**, *112*, 1305-1307.
34. Remediakis, I. N.; Abild-Pedersen, F.; Nørskov, J. K. DFT study of formaldehyde and methanol synthesis from CO and H₂ on Ni(111). *J Phys Chem B* **2004**, *108*, 14535-14540.
35. Shabaker, J. W.; Huber, G. W.; Dumesic, J. A. Aqueous-phase reforming of oxygenated hydrocarbons over Sn-modified Ni catalysts. *Journal of Catalysis* **2004**, *222*, 180-191.

36. Mohsenzadeh, A.; Richards, T.; Bolton, K. A density functional theory study of hydrocarbon combustion and synthesis on Ni surfaces. *Journal of Molecular Modeling* **2015**, *21*.

Chapter 4 - Promoter Effects for Catalyst Reactivity

Case study 1 is reproduced in part with permission from:

Zhou, M.; Liu, B. DFT Investigation on the Competition of the Water-Gas Shift Reaction Versus Methanation on Clean and Potassium-Modified Nickel(111) Surface. *ChemCatChem* **2015**, 7, 3928-3935.

Case study 2 is reproduced with permission from:

Zhou, M.; Cheng, L.; Choi, J.; Liu, B.; Curtiss, L.; Assary, R. Ni-Doping Effects on Oxygen Removal from an Orthorhombic Mo₂C(001) surface: A Density Functional Theory Study. *J. Phys. Chem. C*. Accepted.

4.1 Introduction

In the development of catalysis, it was recognized that promoters could help to improve the catalytic properties. In general, the purpose of adding promoter is to facilitate the desired reaction and/or suppress the unwanted reactions. This chapter aims to provide a molecular level description of promoter effect in catalytic activity using WGS over potassium modified Ni(111) surface and O* removal reaction forming H₂O (includes O-H bond formation) over Ni-doped Mo₂C surfaces as two model reactions. The thermochemical energies and energy barriers related to the elementary steps for WGS and O* removal reaction were calculated using DFT method and potential energy surfaces (PESs) were generated to demonstrate the promoter effect to catalyst reactivity.

4.2 Case Study 1: Selectivity of WGSR on Potassium Modified Ni (111)

Alkali metals (e.g., Na, K) can act as catalytic promoters in both natural and synthetic catalyst materials.¹⁻³ Potassium is one common and efficient promoter species as it functions as an electron donor (mainly through its 4s electron) to the surrounding metallic substrate and lowers the surface work function as a result.⁴ Regarding the role of potassium in WGSR and methanation, Ma et al.⁵ found that by increasing K loading on 100 Fe/5.1 Si/2 Cu/x K ($x = 1.25$ or 3), the WGSR rate during Fischer-Tröpsch synthesis (FT) is significantly enhanced, and in turn provides enough H_2 for the FT reaction even at low CO conversion level. In addition, Hwang et al.⁶ found that potassium-modified Ni catalysts exhibit higher activity and selectivity for WGSR than the unmodified Ni catalyst and methanation reaction is suppressed over the potassium-modified Ni catalyst because of the increase of density for active hydroxyl group that takes part in the WGSR.

The effect of alkali promoters are determined by the interaction characteristics between K and reaction intermediates of the pathways. With alkali metals, the adsorptions of more electronegative species (e.g., CO and H_2O) are enhanced.² Bornemann et al.⁷ showed that at low K coverage ($\theta < 0.14$), water molecules bind stronger on K-precovered Ni(111) than on clean Ni(111) surface. Also, it has been found that water shall decompose at even higher K coverage. Using DFT calculations, Liu et al.¹ showed that the effective CO dissociation barrier can be substantially reduced by the pre-adsorbed K adatom on Rh(111). On the other hand, for less electronegative species (e.g., CH_4), Bengaard et al.⁸ showed that the energy barrier for CH_4 dissociation is increased by 0.21 eV and 0.20 eV, when 0.125 ML of K is added on Ni(111) and Ni(100), respectively.

In this section, the most likely molecular pathways for WGS and methanation will be established using DFT calculations on K-modified Ni catalysts. By this way, insights revealing the promoter effects on enhanced hydrogen selectivity will be understood.

4.2.1 Computational Methods

The computational methods are same with computational methods in Chapter 3.

4.2.2 Adsorption of WGS and Methanation Reaction Intermediates on K-modified Ni(111) Surface

Numerous studies have shown that alkali metals can influence catalytic characters by lowering the work function of catalyst surface.^{4,9} The adsorptions of more electronegative species are enhanced by the electropositive alkali metals. The binding energies, preferred binding sites, and the differential binding energies for WGS and methanation intermediates on K-modified Ni(111) surface are listed in **Table 4.1**. The optimized structures of the intermediates (illustrated in [Figure 4.1](#)) in both WGS and methanation reactions were obtained with K as an adatom.

Table 4.1. Binding energies (BE, in eV), site preferences, and differential binding energies ($\Delta\Delta E$, in eV) for WGSR and methanation intermediates on K-modified Ni(111) surface.

	BE [eV]	site	$\Delta\Delta E$ [eV] ^[a]
CH ₄	-0.05	physisorption pointing at K top	-0.05
CO ₂	-0.29	physisorption pointing at K top	-0.28
H ₂	-0.06	top	0.19
H ₂ O	-0.68	K adatom	-0.41
CH ₂ OH	-1.72	top	-0.16
CH ₃	-1.59	fcc	0.30
CO	-2.35	hcp	-0.42
COOH	-2.73	top	-0.48
CHO	-2.49	fcc	-0.22
H	-2.81	fcc	-0.01
HCOO	-2.98	top-top	-0.10
OH	-3.24	bridge	0.03
HCOH	-4.00	fcc	-0.12
CH ₂	-3.90	fcc	0.13
COH	-4.44	fcc	-0.05
O	-5.65	fcc	-0.26
CH	-6.38	fcc	0.03

^[a] $\Delta\Delta E = BE_{K\text{-modified Ni(111)}} - BE_{Ni(111)}$, a negative value means enhanced binding

energy with K promoter. The $BE_{Ni(111)}$ is obtained from **Table 3.1** in Chapter 3.

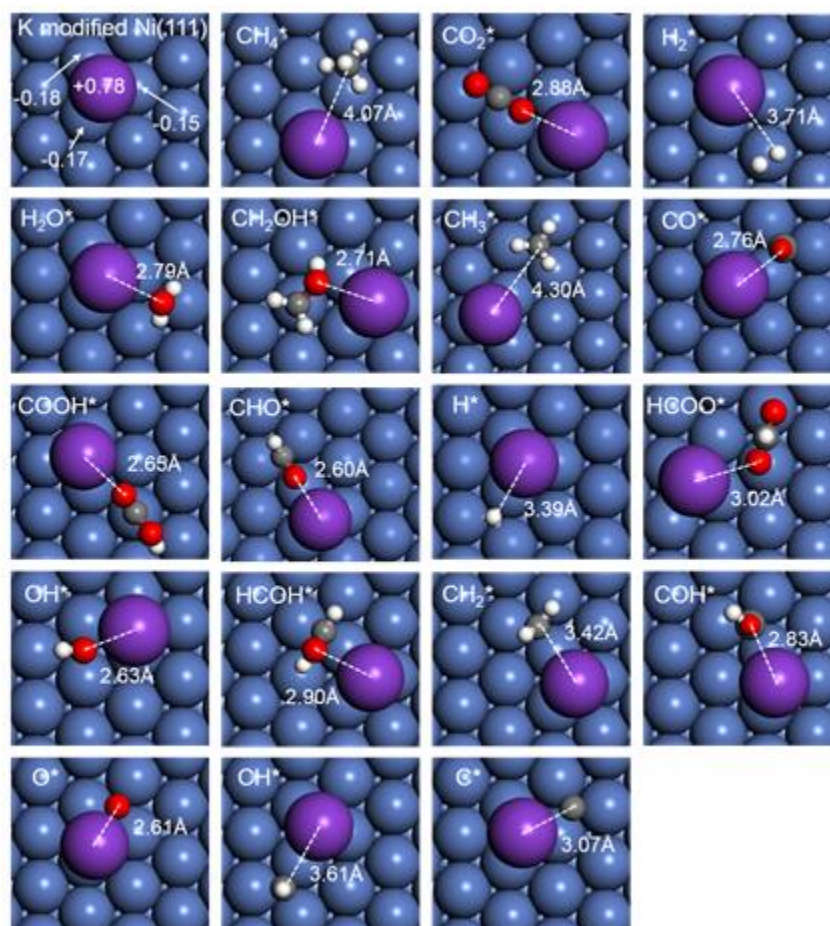


Figure 4.1. Optimized structures of reaction intermediates (in **Table 4.1**) on K-modified Ni(111) surface. C, O, H, Ni, and K are depicted in grey, red, white, blue, and purple, respectively.

The calculated charge, based on Bader charge analysis,^{10,11} on the K adatom is +0.78, which indicates that the K 4s electron has transferred to the nearby Ni substrate. The K adatom prefers to interact with the more electronegative sites (i.e., O) in the adsorbate molecules ([Figure](#)

4.1). In such cases, the binding energies increase. The binding energies of COOH (with carbonyl O), CO, H₂O, CO₂, and atomic O all increase noticeably by more than 0.25 eV (**Table 4.1**).

For CHO*, CH₂OH*, HCOH*, HCOO*, and COH*, the K adatoms also increase their binding energies but less than 0.25 eV. Bindings of CHO*, CH₂OH*, HCOH*, HCOO*, and COH* are 0.22 eV, 0.16 eV, 0.12 eV, 0.10 eV, and 0.05 eV stronger than that on the clean Ni(111) surface, respectively.

The varying degrees of alkali metal promoting effects are reflected by changes in molecular geometries, which include adsorption sites and adsorbate orientations. For instance, the binding energy of COH* is only lowered by 0.05 eV, which is because the perpendicular COH* configuration at the face-centered cubic (fcc) site constrains the O species at a longer distance from the K adatom (**Figure 4.1**). For CH₂OH* and HCOO*, the interactions with K adatoms cause these adsorbates to dislocate from their preferred sites (e.g., CH₂OH* moves from an fcc to a top site) or readjust their adsorption configuration by rotation (e.g., HCOO*).

The exception in the adsorbate promoting effect is OH adsorption, in which the binding energy increases by 0.03 eV. In this case, the hydroxyl group moved from the preferred fcc site to the bridge site. Like HCOH*, the electrostatic interactions with the K adatoms have been used to overcome the energetics required by OH to migrate to the less favorable bridge site. Correspondingly, the K adatom also shows noticeable migration from the hexagonal close packed (hcp) site to the near top site (**Figure 4.1**).

For the less electronegative C and H, the effects of K adatoms on the binding energies are either nearly neutral (e.g., CH₄*, H*, and CH*), or inhibitive in terms of destabilizing the adsorptions (e.g., H₂*, CH₂*, and CH₃*; **Table 4.1**). The exception of this trend is atomic C*, which binds more strongly by 0.15 eV than on the clean Ni(111) surface. The calculated binding

energy of atomic C is consistent with the work on CO dissociation on Rh(111) surfaces, in which the K adatom stabilizes the unpaired electrons in atomic C.¹ The trend in the binding energy variation found in this study is consistent with previous findings.⁹

4.2.3 Effect of K on WGSR and Methanation Elementary Steps

The effects on transition states by the K adatom were also investigated explicitly. The transition state structures of the WGSR and methanation elementary steps on K-modified Ni(111) surfaces are shown in [Figure 4.2](#). Details on the promoting effects (i.e., the lowering of the energy barrier by K) are listed in **Table 4.2** expressed as the actual energy barriers of each elementary step.

The energy barriers for H₂O and CO dissociation do not change noticeably and are only 0.05 and 0.03 eV lower than that of the corresponding clean Ni(111) surface.

For WGSR, in the presence of K adatoms, the energy barrier for R10 in the redox pathway increases by 0.05 eV. The energy barrier of carboxyl formation (R11) is lowered by 0.1 eV. For COOH* dehydrogenation (R12), the energy barrier is significantly lower, by 0.42 eV. However, as the energy barrier for COOH* dissociation is already negligible by R14, such beneficial effect from K is not expected to further enhance the kinetics of this step. The energy barriers for formyl (R15) and formate formation (R16) increase by 0.17 and 0.24 eV, respectively. Hence, the WGSR carboxyl pathway benefits from the presence of adsorbed K kinetically.

Table 4.2. DFT-calculated reaction energies (ΔE [eV]), energy barriers (E_a [eV], and imaginary frequencies (ν_i [cm^{-1}]) of the transition states of the elementary reactions on K-modified Ni(111) surface.

	Elementary step	ΔE [eV]	$E_{a,f}(E_{a,b})^{[a]}$ [eV]	ν_i [cm^{-1}]
R1	$\text{CO (g)} + * \rightleftharpoons \text{CO}^*$	-2.35		
R2	$\text{H}_2\text{O (g)} + * \rightleftharpoons \text{H}_2\text{O}^*$	-0.68		
R3	$\text{CO}_2^* \rightleftharpoons \text{CO}_2 \text{ (g)} + *$	0.29		
R4	$\text{H}^* + \text{H}^* \rightleftharpoons \text{H}_2^* + *$	1.04		
R5	$\text{H}_2^* \rightleftharpoons \text{H}_2 \text{ (g)} + *$	0.06		
R6	$\text{CH}_3^* + \text{H}^* \rightleftharpoons \text{CH}_4\text{(g)} + 2^*$	-0.32		
R7	$\text{H}_2\text{O}^* + * \rightleftharpoons \text{OH}^* + \text{H}^*$	0.01	0.81(0.80)	-1042
R8	$\text{OH}^* + * \rightleftharpoons \text{O}^* + \text{H}^*$	-0.50	0.70(1.21)	-1218
R9	$\text{OH}^* + \text{OH}^* \rightleftharpoons \text{H}_2\text{O}^* + \text{O}^*$	-0.51		
R10	$\text{CO}^* + \text{O}^* \rightleftharpoons \text{CO}_2^* + *$	1.40	1.61(0.21)	-475
R11	$\text{CO}^* + \text{OH}^* \rightleftharpoons \text{COOH}^* + *$	0.89	1.30(0.40)	-239
R12	$\text{COOH}^* + * \rightleftharpoons \text{CO}_2^* + \text{H}^*$	0.00	0.51(0.51)	-1138
R13	$\text{COOH}^* + \text{O}^* \rightleftharpoons \text{CO}_2^* + \text{OH}^*$	0.51		
R14	$\text{COOH}^* + \text{OH}^* \rightleftharpoons \text{CO}_2^* + \text{H}_2\text{O}^*$	-0.01		
R15	$\text{CO}^* + \text{H}^* \rightleftharpoons \text{CHO}^* + *$	1.49	1.61(0.05)	-350
R16	$\text{CHO}^* + \text{O}^* \rightleftharpoons \text{HCOO}^* + *$	-0.03	0.97(1.07)	-303
R17	$\text{HCOO}^* + * \rightleftharpoons \text{CO}_2^* + \text{H}^*$	-0.06	0.33(0.39)	-428
R18	$\text{HCOO}^* + \text{O}^* \rightleftharpoons \text{CO}_2^* + \text{OH}^*$	0.44		

R19	$\text{HCOO}^* + \text{OH}^* \rightleftharpoons \text{CO}_2^* + \text{H}_2\text{O}^*$	-0.07		
R20	$\text{CO}^* + ^* \rightleftharpoons \text{C}^* + \text{O}^*$	1.30	2.85(1.55)	-404
R21	$\text{CO}^* + \text{CO}^* \rightleftharpoons \text{CO}_2^* + \text{C}^*$	2.70	3.22(0.52)	-278
R22	$\text{CHO}^* + ^* \rightleftharpoons \text{CH}^* + \text{O}^*$	-0.51	0.94(1.52)	-483
R23	$\text{CO}^* + \text{H}^* \rightleftharpoons \text{COH}^* + ^*$	1.37	2.09(0.72)	-1563
R24	$\text{COH}^* \rightleftharpoons \text{C}^* + \text{OH}^*$	0.44	1.49(1.06)	-323
R25	$\text{CHO}^* + \text{H}^* \rightleftharpoons \text{HCOH}^* + ^*$	0.55	1.05(0.58)	-1340
R26	$\text{COH}^* + \text{H}^* \rightleftharpoons \text{HCOH}^* + ^*$	0.67	0.89(0.22)	-681
R27	$\text{HCOH}^* + ^* \rightleftharpoons \text{CH}^* + \text{OH}^*$	-0.55	0.61(1.17)	-376
R28	$\text{HCOH}^* + \text{H}^* \rightleftharpoons \text{CH}_2\text{OH}^* + ^*$	0.31	1.12(0.81)	-956
R29	$\text{CH}_2\text{OH}^* + ^* \rightleftharpoons \text{CH}_2^* + \text{OH}^*$	-0.39	0.71(1.10)	-391
R30	$\text{C}^* + \text{H}^* \rightleftharpoons \text{CH}^* + ^*$	-0.32		
R31	$\text{CH}^* + \text{H}^* \rightleftharpoons \text{CH}_2^* + ^*$	0.48		
R32	$\text{CH}_2^* + \text{H}^* \rightleftharpoons \text{CH}_3^* + ^*$	0.16		

^[a]Energy barriers of reverse reaction are shown in the parentheses.

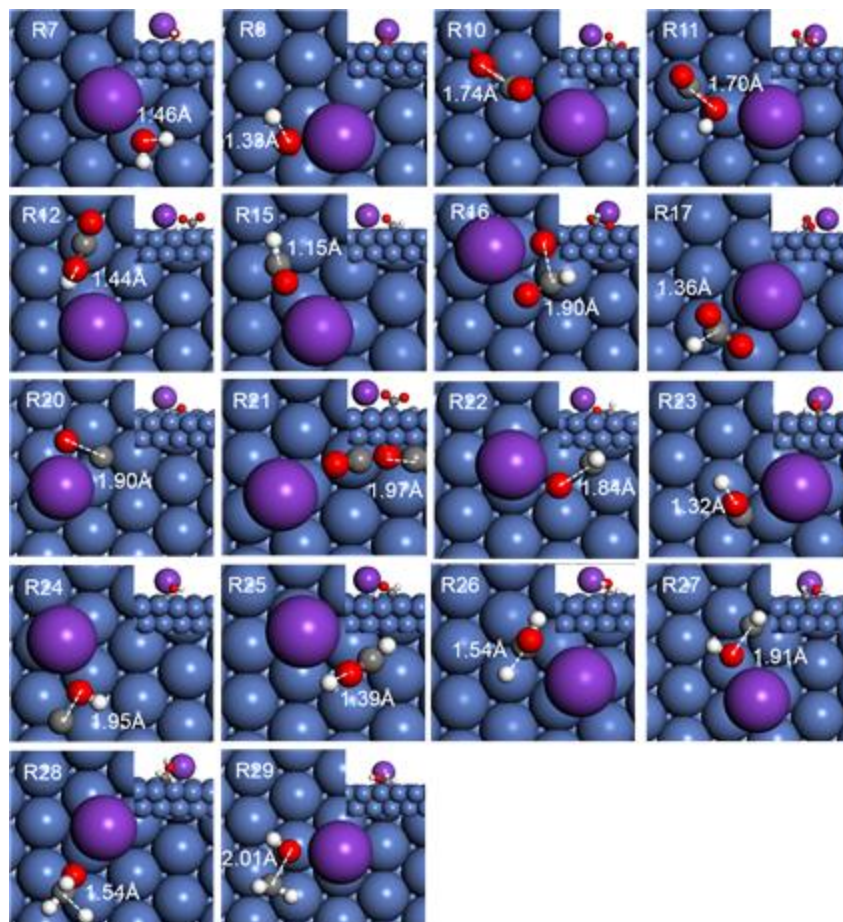


Figure 4.2. Transition state (TS) structures of elementary steps (labeled the same way as in **Table 4.2**) on K-modified Ni(111) surface. The side view of each TS structure is shown as inset figure. C, O, H, Ni, and K are depicted in grey, red, white, blue, and purple, respectively.

For methanation, the energy barriers of direct C-O bond cleavage decrease by 0.03, 0.27, and 0.37 eV for R20, R21, and R24, respectively. Nevertheless, these barriers are still too high to allow these pathways to compete.

The C-O bond cleavage barrier for R22 (CHO pathway) and R27 (HCOH pathway) decreases by 0.10 and 0.11 eV, respectively. The barriers for R23 (COH pathway) and R29 (CH₂OH pathway) increase by 0.18 and 0.06 eV, respectively. Overall, the K adatom can

promote the kinetics of C-O bond cleavage in the CHO and HCOH pathways, which have already been shown to be the main competing routes against the WGSR.

4.2.4 Effect of Promoter on WGSR Selectivity

If we combine the calculated energetics and kinetics by focusing on the competition between the carboxyl and redox pathways of the WGSR against the CHO pathway of methanation, the overall potential energies for WGSR and methanation on the K-modified Ni(111) surfaces are summarized in Figure 4.3 (dashed pathways) along with the original clean Ni(111) surfaces (solid pathways, data from Table 3.2).

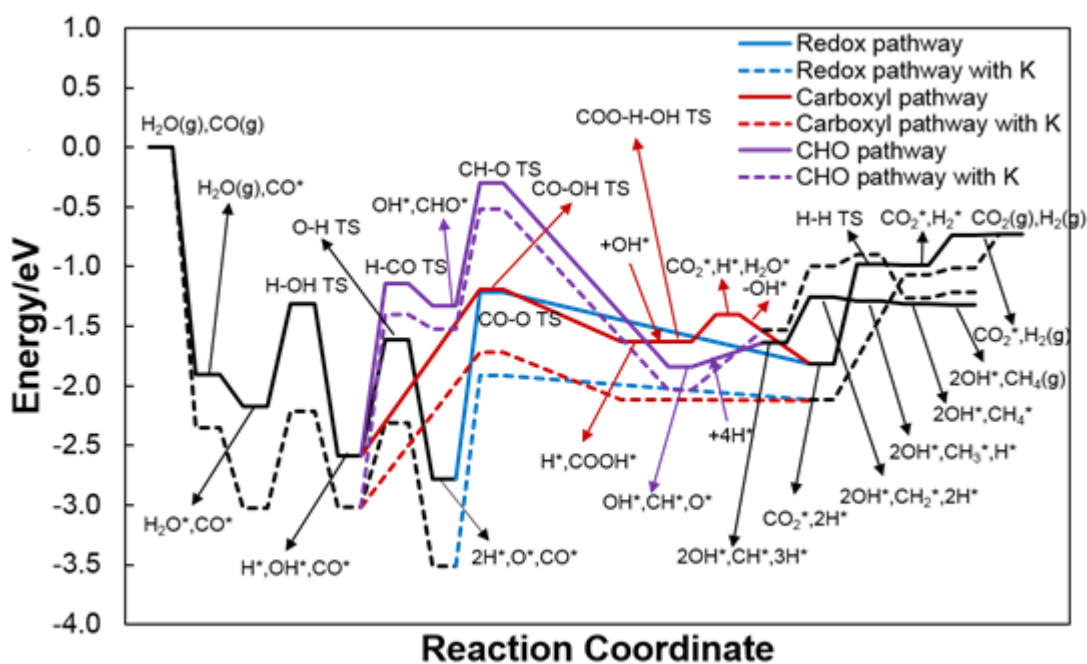


Figure 4.3. Potential energy surfaces of WGSR and methanation pathways on clean Ni(111) (solid paths) and K-modified Ni(111) surfaces (dashed paths).

Because of the stronger binding energies for both CO and H₂O, (a combined 0.83 eV lower) in the presence of K adatoms, the overall potential energies for both the WGSR and methanation pathways shift downward noticeably.

Although the first step of H₂O* dissociation (R7) becomes less exothermic on the K-modified Ni(111), the potential energies still remain much more favorable than that on the clean Ni(111) surface, as shown in the comparison between the dashed and solid pathways for the corresponding steps in [Figure 4.3](#).

Between the WGSR carboxyl pathway and the methanation CHO pathway, the energy barrier of R11 (carboxyl formation) decreases by 0.10 eV and the barrier of R15 (formyl formation) increases by 0.17 eV. So do the reaction energies, in which R11 becomes more exothermic by 0.07 eV and R15 becomes more endothermic by 0.24 eV. As a result, the addition of K adatoms to Ni(111) effectively lowers the transition state energies and the energetics to favor the WGSR.

The redox pathway in the WGSR consumes O* species produced at the second step of water dissociation. On the K-modified Ni(111) surface, R8 becomes more exothermic (by 0.3 eV) with a reduced energy barrier (by 0.28 eV). Therefore, the adatom promotes the energetics and kinetics of the O formation, although the energy barrier of R10 remains almost unchanged (1.61 vs. 1.56 eV on clean Ni(111)). Still, if we combine the promoted OH dissociation and stronger CO binding, the potential energies of the WGSR redox pathway are also lower (even than the carboxyl pathway). Hence, the redox pathway becomes the most competitive pathway ([Figure 4.3](#)).

4.3 Case Study 2: Ni-doping Effect on Oxygen Removal from an Orthorhombic Mo₂C(001) Surface

Introducing a suitable dopant (e.g., Ni, Co, Fe, and Cu) can enhance the Mo₂C catalytic activity, selectivity, and stability in various hydrocarbon conversion reactions including oxygenates by generating new active sites or influencing existing sites.¹²⁻¹⁶ Zhang et al. have found that with Ni promotion, the stability of Mo₂C was improved in the hydrodeoxygenation reaction of model bio-derived compounds such as ethyl benzoate, acetone, and acetaldehyde.¹⁷ Ma et al. have proposed that the highest activity and stability of Mo₂C for steam reforming of methanol occurs at lower Ni doping amount.¹⁸ Choi et al. have observed that the catalytic performance of Mo₂C in hydroprocessing of fast pyrolysis bio-oil was sensitive to the type of metal dopant and Ni-doped Mo₂C outperformed Co-, Cu-, or Ca-doped counterparts.¹⁶ However, the fundamental reason behind the increased catalytic performance of Mo₂C with Ni doping is not well known.

While the fundamental catalytic effect of Mo₂C in C-O/C=O cleavage is via the binding of 'O' to the catalytic surface, the strong binding of 'O' to Mo or C site promotes the scission of C-O/C=O bonds. However, with strong binding, the removal of the adsorbed atomic oxygen (O*: the asterisk (*) representing the adsorption site) is difficult and could hinder the overall catalytic reaction kinetics leading to catalyst poisoning.¹⁹ Additionally, the coverage dependency of oxygen and carbon (from various sources) binding with the dominant catalyst surfaces influence the efficacy of any deoxygenation catalysts.²⁰⁻²² A catalyst with intermediate binding strength towards the 'O' atom (or oxygenated intermediates) is desirable for the favorable C-O/C=O bond cleavage as well as surface 'O' removal. We hypothesize that the promoting effect

of Ni dopant on Mo₂C-based catalysts in hydroprocessing of biomass derivatives as reported in the literature is partly due to the role of Ni in facilitating the O* removal.¹⁶

In this section, we present results of density functional investigation into reaction energetics and reaction barriers of oxygen removal from un-doped and Ni-doped Mo₂C(001) surfaces. The models for the surface calculations and the methods are described in Section 2. The results and a discussion are presented in Section 3.

4.3.1 Theoretical Methods

In this investigation, Mo₂C(001) was chosen as a starting reaction surface model to investigate Ni effect on O* removal. Though the model does not have the lowest surface energy, the Mo₂C(001) surface is stable²³ and expected to exist on nanoparticles based on Wulff constructions.^{24,25} Additionally, the area proportional to the Mo₂C(001) surface on the Wulff shape increases with the increase of H₂ partial pressure,²⁵ which is the main hydrogen source for the catalytic hydrogenation of O* species¹⁹. The binding energies (BEs) of reaction intermediates such as of O*, OH*, H₂O*, H* and the activation energies of OH* and H₂O* formation on un-doped and Ni-doped Mo₂C(001) surfaces were calculated using the density functional theory (DFT) method.

The spin-polarized DFT calculations were used initially and the total magnetic moments were identified to be zero for both un-doped Mo₂C(001) surfaces and Ni-doped Mo₂C(001) surfaces. Therefore, spin unpolarized DFT calculations were performed for both un-doped Mo₂C(001) surfaces and Ni-doped Mo₂C(001) surfaces using the Vienna *ab initio* simulation package (VASP)^{26,27} with the generalized gradient approximation PBE (GGA-PBE) functional²⁸ for exchange-correlation energy. The electron-ion interaction was described using the projector-

augmented wave (PAW) method²⁹, with a plane wave energy cutoff of 400 eV. The Brillouin-zone was sampled with $4 \times 4 \times 1$ k-point mesh for surface calculations and Γ -point mesh for gas phase calculations based on the Monkhorst-Pack scheme³⁰. The electronic occupancy was determined by the Methfessel-Paxton scheme³¹, with the width of smearing of 0.2 eV.

The orthorhombic Mo₂C phase was used in our model, henceforth abbreviated as Mo₂C. The optimized lattice constants for bulk Mo₂C are $a = 4.74 \text{ \AA}$, $b = 6.05 \text{ \AA}$, and $c = 5.23 \text{ \AA}$ which are consistent with the experimental values ($a = 4.72 \text{ \AA}$, $b = 6.01 \text{ \AA}$, $c = 5.20 \text{ \AA}$)³². A four-layer (2×4) Mo₂C(001) surface was generated with the top two layers and the adsorbates were allowed to relax, whereas the atoms from the bottom two layers were fixed at their corresponding bulk lattice positions. The Mo₂C(001) surface has two Mo terminations and one C termination. Wang et al.²⁴ calculated the surface energies of Mo₂C(001) surface with different terminations and the results show that one of the Mo termination (denoted as T_{Mo}) as shown in Figure 4.4(a) becomes more stable under weaker carburization conditions (smaller value of carbon chemical potential) and C termination (denoted as T_C) as shown in Figure 4.4(b) becomes more stable under stronger carburization conditions. In this paper, we focus on the Mo₂C(001) surface with T_{Mo} and T_C. In order to study the Ni dopant effect, only one Ni atom was added to the Mo₂C(001) surface to mimic an experimental condition, where the weight percentage of Ni is ~0.90 % (that is, one Ni for every 32 Mo₂C units).¹⁸ All surfaces simulated here had a 20 Å vacuum between the two neighboring successive slabs. The combined climbing image-Nudged Elastic Band (CI-NEB)³³ and dimer³⁴ method were used to determine the transition state (TS) structures and the activation energy barrier of the OH* and H₂O* formation at the surface.

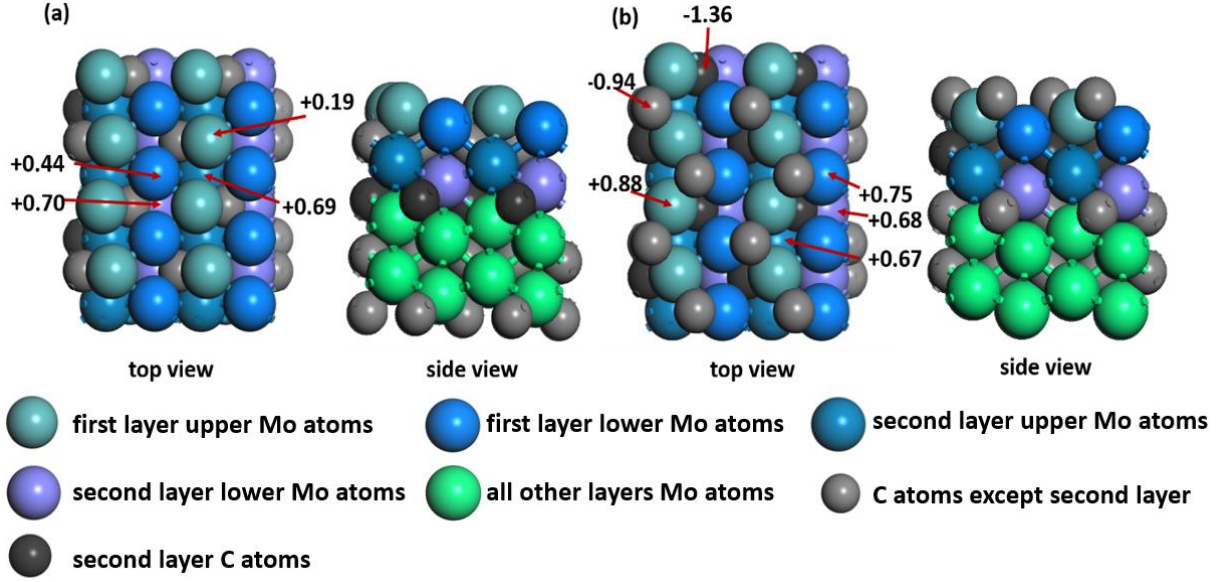


Figure 4.4. Top view and side view of optimized structures of Mo₂C(001) surfaces. (a) un-doped T_{Mo} Mo₂C(001) surface, (b) un-doped T_C Mo₂C(001) surface. The top two layers of Mo atoms are depicted in different color to differentiate Mo on different positions. Same color scheme is utilized throughout the paper.

The BEs of O*, OH*, H*, and H₂O* on the surface in this paper are defined relative to non-radical neutral gas phase species as shown in Equations (42-45) respectively:

$$BE_{O^*} = E_{O+surface} + E_{H_2(g)} - E_{surface} - E_{H_2O(g)} \quad (42)$$

$$BE_{OH^*} = E_{OH+surface} + \frac{1}{2}E_{H_2(g)} - E_{surface} - E_{H_2O(g)} \quad (43)$$

$$BE_{H^*} = E_{H+surface} - E_{surface} - \frac{1}{2}E_{H_2(g)} \quad (44)$$

$$BE_{H_2O^*} = E_{H_2O+surface} - E_{surface} - E_{H_2O(g)} \quad (45)$$

where $E_{O+surface}$, $E_{OH+surface}$, $E_{H+surface}$, and $E_{H_2O+surface}$ are the total energies of O, OH, H, and H₂O adsorbed on the Mo₂C(001) surfaces, respectively. The $E_{surface}$ is the total energy of the Mo₂C (001) surface and the $E_{H_2O(g)}$, and the $E_{H_2(g)}$ are the total energies of H₂O and H₂ in the gas phase calculated in a periodic box of 10 Å × 10 Å × 10.5 Å. The reaction energies (ΔE) for O* removal reactions were calculated by Equation (46) and the energy barriers (E_a) of OH* and H₂O* formation was calculated using the Equation (47):

$$\Delta E = E_{FS} - E_{IS} \quad (46)$$

$$E_a = E_{TS} - E_{IS} \quad (47)$$

where the E_{TS} is the total energy of the transition state structure and the E_{IS} or E_{FS} is the total energy of the initial state or final state with reactant species are treated at infinite separation.

4.3.2 O* Removal over Mo₂C(001) Surfaces

The computed thermochemistry of the adsorption of oxygen-species is discussed here, where the interactions of the substrate species and the surface can be represented in four model reactions (R) denoted as R1, R2, R3, and R4, respectively. Note that the asterisk symbol (*) described in this section represents the adsorption site on un-doped and Ni-doped Mo₂C(001) surfaces. Among the substrates, the O* species can react with the nearby H* to form OH* (R1). Subsequently, the formed OH* on surface can either react with the nearby H* to form H₂O* (R2) or react with neighboring OH* to form H₂O* and O* (R3, OH disproportionation reaction). Finally, H₂O* desorbs from the surface (R4).



The combination of R1, R2, and R4 is named direct O* removal, while the association of R1, R3, and R4 is named OH-assisted O*removal in this work.

4.3.2.1 Ni-doped Mo₂C(001) surface structures

The Mo₂C(001) surface can be either Mo-terminated (T_{Mo}) or C-terminated (T_C) as shown in [Figure 4.4\(a\)](#) and [Figure 4.4\(b\)](#). The doped Ni can be either adsorbed on the Mo₂C surface or embedded in the Mo₂C lattice in place of a Mo site from XRD ¹³ and XPS ³⁵. Thus, two different doping structures were considered on T_{Mo} and T_C Mo₂C(001) surfaces for the DFT calculations. Therefore, a total of six different Mo₂C(001) surfaces including un-doped T_{Mo} Mo₂C(001) surface, Ni-adsorbed T_{Mo} Mo₂C(001) surface, Ni-replaced T_{Mo} Mo₂C(001) surface, un-doped T_C Mo₂C(001) surface, Ni-adsorbed T_C Mo₂C(001) surface, and Ni-replaced T_C Mo₂C(001) surface. For each surface, multiple starting geometries were considered and the lowest-energy configurations were used here. The most stable Ni-adsorbed and Ni-replaced surfaces are shown in [Figure 4.5](#) with Ni loading amount corresponding to ~ 0.90 wt%. Computations suggest that Ni prefers to adsorb on the bridge site of two 1st layer lower Mo atoms on both T_{Mo} and T_C Mo₂C(001) surfaces. The most favorable site for replacing Mo with

Ni is on the top surface layer. The DFT results reveal that on T_{Mo} $Mo_2C(001)$ surface, the formation of $Ni_{adsorbed}$ and $Ni_{replaced}$ T_{Mo} $Mo_2C(001)$ is exothermic by -0.11 eV and -0.59 eV, respectively. On T_C $Mo_2C(001)$ surface, the formation of $Ni_{adsorbed}$ T_C $Mo_2C(001)$ surface is also exothermic ($\Delta E = -1.00$ eV), while the formation of $Ni_{replaced}$ T_C $Mo_2C(001)$ surface is endothermic ($\Delta E = 0.84$ eV) and not preferred.

Bader charge analysis^{10,11} results are also reported in [Figure 4.5](#), where the Mo is an electron donor and C is an electron acceptor on $Mo_2C(001)$ as expected based on their electron negativity. On the T_{Mo} $Mo_2C(001)$ surface, the charges on Ni are -0.31 and -0.16 for $Ni_{adsorbed}$ and $Ni_{replaced}$ $Mo_2C(001)$ surfaces, respectively, which indicates that the Ni accepts electrons from nearby Mo atoms. Thus, on the T_{Mo} $Mo_2C(001)$ surface, the Ni atom prefers to interact with more electropositive species while Mo atoms prefers to interact with the more electronegative species. On the contrary, on T_C $Mo_2C(001)$, the charge of Ni are +0.47 and +0.31 for $Ni_{adsorbed}$ and $Ni_{replaced}$ $Mo_2C(001)$ surfaces, respectively, which suggests that Ni is an electron donor on these surfaces. The Ni and Mo atoms favor the adsorption of electronegative molecules while C atoms favor the adsorption of electropositive species. The synergies of Ni, Mo, and C atoms affect the adsorption of various species/molecules on those surfaces.

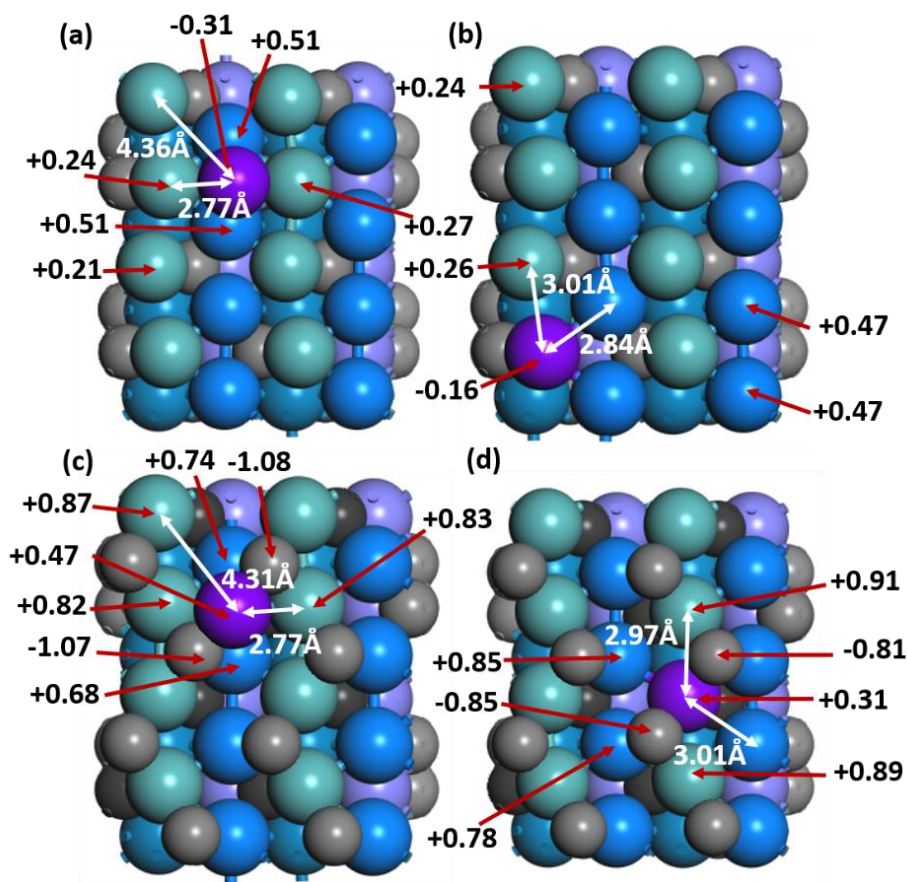


Figure 4.5. Top view of optimized structures of Mo₂C(001) surfaces. (a) Ni-adsorbed T_{Mo} Mo₂C(001), (b) Ni-replaced T_{Mo} Mo₂C(001), (c) Ni-adsorbed T_C Mo₂C(001), (d) Ni-replaced T_C Mo₂C(001). The purple sphere represents the Ni atom. The red arrow shows the Bader charges of selected atoms. The white arrow shows the distance of Ni dopant to nearby Mo atom.

4.3.2.2 Adsorption of Reaction Intermediates

The optimized structures of the reactive intermediates (O*, OH*, H*, H₂O*) on the T_{Mo} and T_C Mo₂C(001) surfaces are shown in [Figure 4.6](#) and the computed binding energies are shown in **Table 4.3**.

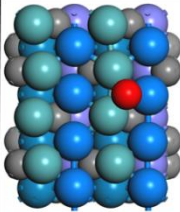
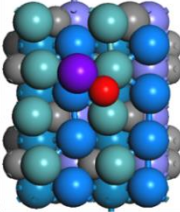
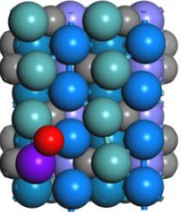
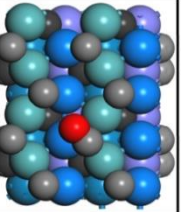
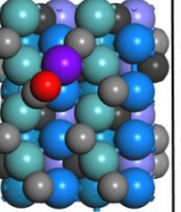
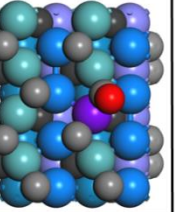
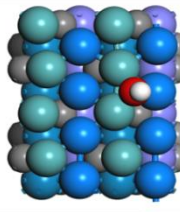
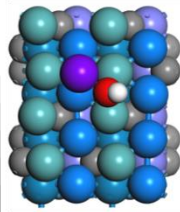
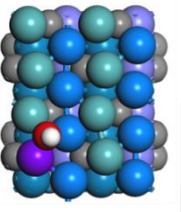
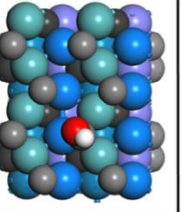
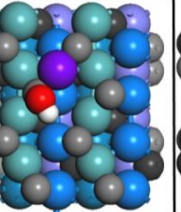
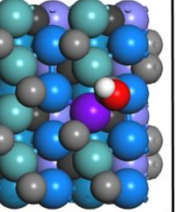
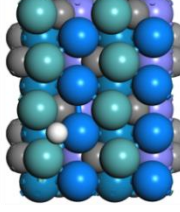
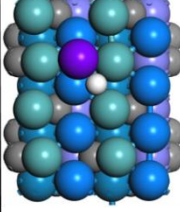
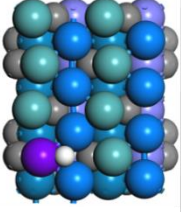
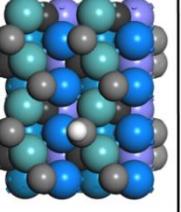
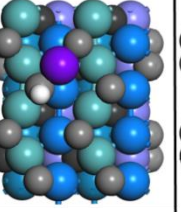
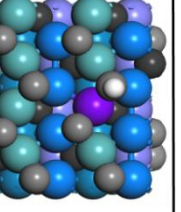
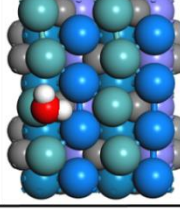
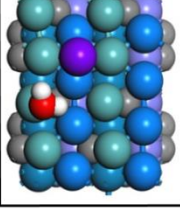
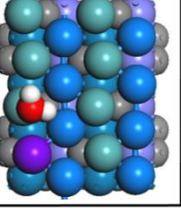
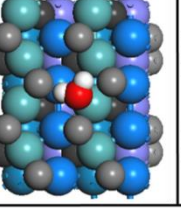
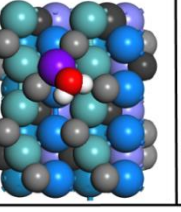
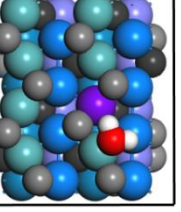
	T_{Mo} $Mo_2C(001)$			T_C $Mo_2C(001)$		
	un-doped	Ni-adsorbed	Ni-replaced	un-doped	Ni-adsorbed	Ni-replaced
O^*		Ni-O:2.02 Å 	Ni-O:1.98 Å 		Ni-O:1.89 Å 	Ni-O:2.84 Å 
OH^*		Ni-O:2.32 Å 	Ni-O:2.09 Å 		Ni-O:2.51 Å 	Ni-O:3.00 Å 
H^*		Ni-H:2.01 Å 	Ni-H:1.69 Å 		Ni-H:2.45 Å 	Ni-H:2.70 Å 
H_2O^*		Ni-O: 4.06Å 	Ni-O: 3.62Å 		Ni-O: 2.07Å 	Ni-O: 3.33Å 

Figure 4.6. Optimized structures of 4 intermediates shown in **Table 4.3** on the un-doped and Ni-doped $Mo_2C(001)$ surfaces. The purple, red, and white spheres represent Ni, O, and H, respectively. The shortest Ni-O and Ni-H distances at the surfaces are also shown.

Table 4.3. BEs (eV) of O* (Equation 42), OH*(Equation 43), H*(Equation 44), and H₂O*(Equation 45) on un-doped and Ni-doped Mo₂C(001) surfaces.

	T _{M0} Mo ₂ C(001)			T _C Mo ₂ C(001)		
	un-doped	Ni-adsorbed	Ni-replaced	un-doped	Ni-adsorbed	Ni-replaced
O*	-1.88	-1.53	-1.35	-0.12	0.21 ^a	-0.79
OH*	-1.50	-1.39	-1.16	-0.24	0.05 ^a	-0.65
H*	-0.96	-0.75	-0.97	-1.03	-0.68	-1.24
H ₂ O*	-0.97	-0.98	-1.03	-0.52	-0.78	-0.70

(^a): Note that the binding energies relative to non-radical neutral gas phase species (H₂O and H₂) as shown in Equations (42-45).

On the T_{M0} Mo₂C(001) surface, an optimum energy conformation suggests that the oxygen atom sits on a three-fold site consisting of two first layer upper Mo atoms and one first layer lower Mo atom. The BEs of O* on un-doped, Ni-adsorbed, and Ni-replaced T_{M0} Mo₂C(001) surfaces are -1.88 eV, -1.53 eV, and -1.35 eV, respectively. On the T_C Mo₂C(001) surface, the ‘O’-atom prefers to bind with the surface carbon atom, where the BEs are -0.12 eV, 0.21 eV, and -0.79 eV for un-doped, Ni-adsorbed, and Ni-replaced T_C Mo₂C(001) surfaces, respectively. The computed BE of the hydroxyl (OH*) species with the Ni-adsorbed (-1.39 eV), Ni-replaced T_{M0} Mo₂C(001) (-1.16 eV) and Ni-adsorbed T_C Mo₂C(001) (0.05 eV) are weaker compared to that of the un-doped Mo₂C(001) scenario (-1.50 eV for T_{M0} and -0.24 eV for T_C). The computed binding energy of H* binding on the Ni-adsorbed T_{M0} Mo₂C(001) is -0.75 eV

marginally (vs. -0.96) weaker compared to that on an un-doped T_{Mo} $Mo_2C(001)$ (-0.96 eV). Note that the absorption site for H^* species is similar to the adsorption sites for O^* and OH^* species. However, the site preference of H^* on Ni-replaced T_{Mo} $Mo_2C(001)$ changes from a three-fold site consisting of two first layer upper Mo atoms and one Ni atom (i.e., the preference site of O^* and OH^*) to a three-fold site consisting of two first layer inferior Mo atoms and one Ni atom with BE identical to un-doped T_{Mo} $Mo_2C(001)$ surface. On the T_C $Mo_2C(001)$ surface, the H^* prefers to bind with the carbon sites with the BEs of -1.03 eV, -0.68 eV, and -1.24 eV for un-doped, Ni-adsorbed, and Ni-replaced T_C $Mo_2C(001)$, respectively. The H_2O^* binds at the top site of first layer upper Mo atoms. For T_{Mo} , the BEs of H_2O^* are -0.98 eV and -1.03 eV on Ni-adsorbed and Ni-replaced $Mo_2C(001)$ surfaces, respectively, which are comparable to that (-0.97 eV) of un-doped $Mo_2C(001)$ surface. For T_C , the BE of H_2O^* are -0.78 eV and -0.70 eV on Ni-adsorbed and Ni-replaced $Mo_2C(001)$ surface, respectively, which are marginally stronger than that of the un-doped $Mo_2C(001)$ (-0.52 eV).

Based on the computed binding energies, the Ni dopant destabilizes the reaction intermediates (O^* , OH^*) on Ni-adsorbed, Ni-replaced T_{Mo} $Mo_2C(001)$ surface and Ni-adsorbed T_C $Mo_2C(001)$ surfaces compared to that of the un-doped $Mo_2C(001)$ surface, which may be helpful for further O^* removal reactions. Upon replacing one Mo atom by a Ni atom at the T_C $Mo_2C(001)$ surface, the presence of the dopant stabilizes the bindings of O^* , OH^* , and H^* . The Ni dopants have negligible effect on H_2O adsorption on the T_{Mo} $Mo_2C(001)$ surface. On the contrary, the Ni dopants stabilize the H_2O adsorption on the T_C $Mo_2C(001)$ surface.

4.3.2.3 Thermochemistry and reaction barriers of O^* removal

The calculated reaction energies (ΔE) and reaction barriers (E_a) of O^* removal via OH^* and H_2O^* intermediates over $Mo_2C(001)$ surfaces are tabulated in **Table 4.4** and **Table 4.5**, respectively. The transition state structures on T_{Mo} and T_C $Mo_2C(001)$ surfaces are shown in [Figure 4.7\(a\)](#) and [Figure 4.7\(b\)](#), respectively. Details regarding the computed energetics associated with the O^* removal are discussed below.

Table 4.4. Calculated reaction energies (ΔE [eV]) of O^* removal via OH^* formation and H_2O^* formation on un-doped and Ni doped $Mo_2C(001)$ surfaces.

	T_{Mo} $Mo_2C(001)$			T_C $Mo_2C(001)$		
	un-	Ni-	Ni-	un-	Ni-	Ni-
	doped	adsorbed	replaced	doped	adsorbed	replaced
(R1) $O^* + H^* \leftrightarrow OH^*$						
+ *	1.35	0.89	1.16	0.91	0.53	1.38
(R2) $OH^* + H^* \leftrightarrow$						
$H_2O^* + *$	1.49	1.16	1.09	0.75	-0.15	1.19
(R3) $OH^* + OH^* \leftrightarrow$						
$H_2O^* + O^*$	0.14	0.27	-0.07	-0.16	-0.68	-0.19

Table 4.5. Calculated energy barriers (Ea [eV]) of O* removal via OH* formation and H₂O* formation on un-doped and Ni doped Mo₂C(001) surfaces.

	T _{Mo} Mo ₂ C(001)			T _C Mo ₂ C(001)		
	un-	Ni-	Ni-	un-	Ni-	Ni-
	doped	adsorbed	replaced	doped	adsorbed	replaced
(R1) O* + H* ↔ OH* + *	1.83	1.40	1.75	1.83	1.29	1.87
(R2) OH* + H* ↔ H ₂ O* + *	1.86	1.59	1.64	1.32	0.64	1.39
(R3) OH* + OH* ↔ H ₂ O* + O*	0.71	0.45	0.07	0.22	1.29	0.44

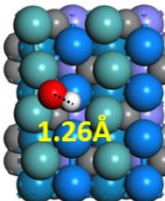
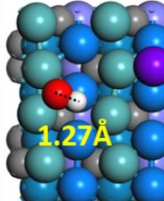
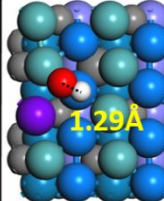
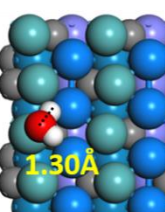
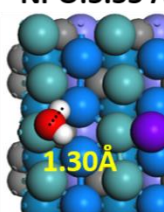
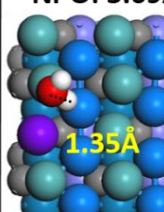
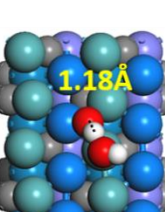
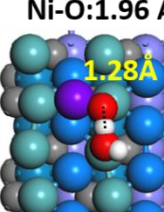
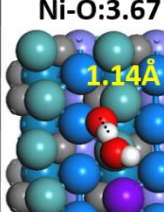
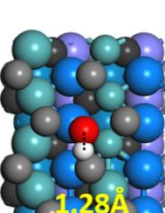
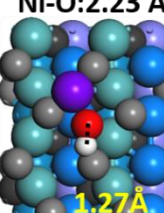
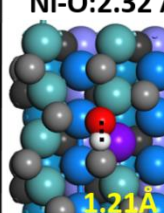
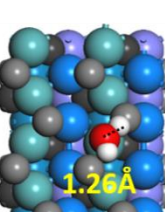
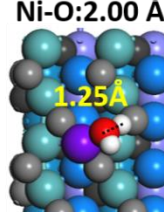
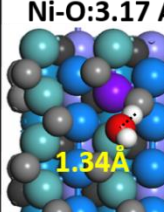
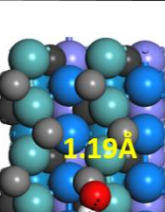
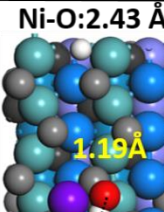
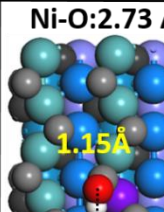
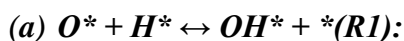
(a)	un-doped	Ni-adsorbed	Ni-replaced
$O^* + H^* \leftrightarrow OH^* + *$	 1.26Å	Ni-O: 3.79 Å  1.27Å	Ni-O: 3.08 Å  1.29Å
$OH^* + H^* \leftrightarrow H_2O^* + *$	 1.30Å	Ni-O: 3.33 Å  1.30Å	Ni-O: 3.69 Å  1.35Å
$OH^* + OH^* \leftrightarrow H_2O^* + H^*$	 1.18Å	Ni-O: 1.96 Å  1.28Å	Ni-O: 3.67 Å  1.14Å
(b)	un-doped	Ni-adsorbed	Ni-replaced
$O^* + H^* \leftrightarrow OH^* + *$	 1.28Å	Ni-O: 2.23 Å  1.27Å	Ni-O: 2.32 Å  1.21Å
$OH^* + H^* \leftrightarrow H_2O^* + *$	 1.26Å	Ni-O: 2.00 Å  1.25Å	Ni-O: 3.17 Å  1.34Å
$OH^* + OH^* \leftrightarrow H_2O^* + H^*$	 1.19Å	Ni-O: 2.43 Å  1.19Å	Ni-O: 2.73 Å  1.15Å

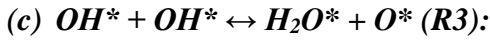
Figure 4.7. Transition state structures of elementary steps of O* removal from (a) T_{M0} Mo₂C(001) surface, (b) T_C Mo₂C(001) surface. The bond lengths of transition states are marked here for better understanding of the transition state structures. The Ni-O distances on the surface are also shown. The energetics and energy barriers associated with the reaction steps are presented in **Table 4.4** and **Table 4.5**.



Based on the energetics and energy barriers presented in **Table 4.4** and **Table 4.5**, the formation of OH* (R1) on the un-doped T_{M0} Mo₂C(001) surface is neither thermodynamically (1.35 eV) nor kinetically (1.83 eV) favorable at standard reaction conditions. The Ni dopants on T_{M0} Mo₂C(001) surface reduce the endothermicity of the reactions. For instance, the reaction energies (ΔE) of OH* formation on Ni-adsorbed site is 0.89 and on Ni-replaced site is 1.16 eV, respectively, both of which are less endothermic than that of the un-doped Mo₂C surface. The computed reaction barriers (E_a) are also smaller (by ~0.2-0.4 eV) in the presence of Ni compared to that of the clean Mo₂C catalyst surface. The OH* formation on un-doped T_C Mo₂C(001) surface is also endothermic by 0.91 eV with an energy barrier of 1.83 eV. This reaction energy and energy barrier is decreased for OH formation on the Ni-adsorbed T_C Mo₂C(001) surface (0.53 eV versus 0.91 eV for reaction energy and 1.29 eV versus 1.83 eV for energy barrier) compare with those on un-doped T_C Mo₂C(001) surface. However, on Ni-replaced T_C Mo₂C(001) surface, the OH* reaction energy and energy barrier are increased to 1.38 and 1.87 eV, respectively, marginally higher than that of the T_C Mo₂C (001) surface .



A reaction of the OH^* species on the surface is the formation of $H_2O^*(R2)$. On the un-doped T_{Mo} $Mo_2C(001)$ surface, the computed energy barrier for the H_2O^* formation is 1.86 eV and the reaction is endothermic by 1.49 eV. Based on computations (Table 2), a lower reaction energy (1.16 eV and 1.09 eV) and energy barrier (1.59 eV and 1.64 eV) are observed in the presence of Ni dopant (adsorbed and replaced) on T_{Mo} $Mo_2C(001)$ surface. The formation of H_2O on un-doped T_C $Mo_2C(001)$ surface is endothermic (0.75 eV) and require an energy barrier of 1.32 eV. In the presence of Ni dopant (adsorbed) on T_C $Mo_2C(001)$ surface, this energy barrier decreased to 0.64 eV and the formation of H_2O becomes exothermic (-0.15 eV). However, when Ni dopant replaces one Mo atom on T_C $Mo_2C(001)$ surface, the formation of H_2O^* becomes less favorable (endothermic by 1.19 eV) and require a higher energy barrier (1.39 eV).



The OH^* species can react with neighboring OH^* to form H_2O^* and O^* (OH disproportionation). This OH disproportionation reaction is marginally endothermic (0.14 eV) and the computed energy barrier is 0.71 eV. On the Ni-adsorbed T_{Mo} $Mo_2C(001)$ surface, the computed energy barrier drops to 0.45 eV, however the reaction is marginally endothermic (0.27 eV). On Ni-replaced T_{Mo} $Mo_2C(001)$ surface, the OH disproportionation reaction becomes more favorable both thermodynamically (ΔE : -0.07 eV versus 0.14 eV) and kinetically (E_a : 0.07 eV versus 0.71 eV). On un-doped T_C $Mo_2C(001)$ surface, computations indicate the OH disproportionation is exothermic (-0.16 eV) and the energy barrier required is 0.22 eV. On the Ni-doped T_C $Mo_2C(001)$, the OH disproportionation is thermodynamically favorable and the computed reaction barriers are 1.29 and 0.44 eV respectively for Ni-adsorbed and Ni-replaced Mo_2C catalyst.

Overall, water formation through OH disproportionation (R3) is thermodynamically and kinetically more favorable than R2 with lower reaction energies and energy barriers on un-doped T_{Mo} $Mo_2C(001)$, Ni-adsorbed T_{Mo} $Mo_2C(001)$, Ni-replaced T_{Mo} $Mo_2C(001)$, un-doped T_C $Mo_2C(001)$, and Ni-replaced T_C $Mo_2C(001)$ surfaces. Therefore, OH disproportionation can boost water formation on those surfaces. However, on Ni-adsorbed T_C $Mo_2C(001)$ surface, the water formation via R2 is kinetically more favorable than R3 (0.64 eV vs 1.29 eV). Therefore, a direct O^* removal likely occurs at the Ni-adsorbed T_C $Mo_2C(001)$ surface sites, while a OH-assisted O^* removal take place on other surfaces investigated here.

4.3.2.4 Potential energy surface of O^* removal

Due to the lower reaction energy and energy barrier of OH disproportion reaction on un-doped T_{Mo} $Mo_2C(001)$, Ni-adsorbed T_{Mo} $Mo_2C(001)$, Ni-replaced T_{Mo} $Mo_2C(001)$, un-doped T_C $Mo_2C(001)$, and Ni-replaced T_C $Mo_2C(001)$ surfaces, the OH-assisted O^* ($R1 \rightarrow R3 \rightarrow R4$) removal were considered on those surfaces to generate the overall potential energy surface (PES). For Ni-adsorbed T_C $Mo_2C(001)$ surface, the direct O^* removal pathway ($R1 \rightarrow R2 \rightarrow R4$) pathway and the associated thermodynamics was considered to generate the potential energy profile. The overall PES is shown in [Figure 4.8](#). The sum of the energies of a gas phase H_2O molecule and the $Mo_2C(001)$ surface is considered as the reference value (0.0 eV). From [Figure 4.8](#), it is evident that the removal of O^* intermediates to H_2O from all $Mo_2C(001)$ surfaces are endothermic. In the case of un-doped T_{Mo} $Mo_2C(001)$ surface ((solid black line in [Figure 4.8](#)), computed direct energy difference (ΔE^g , energy difference between highest and lowest point in the reaction coordinate) for the O^* removal is 3.81 eV. Computations suggest that the Ni dopant on T_{Mo} $Mo_2C(001)$ surface can assist by reducing this thermodynamic bottleneck by 0.78 eV for

adsorbed Ni on the surface and 0.53 eV for Ni replaced one Mo atom in the lattice. In the case of un-doped T_C $Mo_2C(001)$ surface, the O^* removal (solid red line in [Figure 4.8](#)) has a direct energy difference of 2.18 eV. Upon adsorbing the Ni dopant on T_C $Mo_2C(001)$ surface, the ΔE^g for O^* removal is reduced to 1.29 eV (from 2.18 eV) suggesting a relatively favorable O^* removal. Though the ΔE^g for O^* removal becomes higher with Ni_replaced $Mo_2C(001)$ surface than that of the un-doped T_C $Mo_2C(001)$ surface (3.27 eV versus 2.18 eV), the formation of this doped surface structure is endothermic reaction. Overall, O^* removal on the Ni-adsorbed T_C $Mo_2C(001)$ surface is the most favorable reaction with the lowest ΔE^g among the $Mo_2C(001)$ surfaces considered in this study.

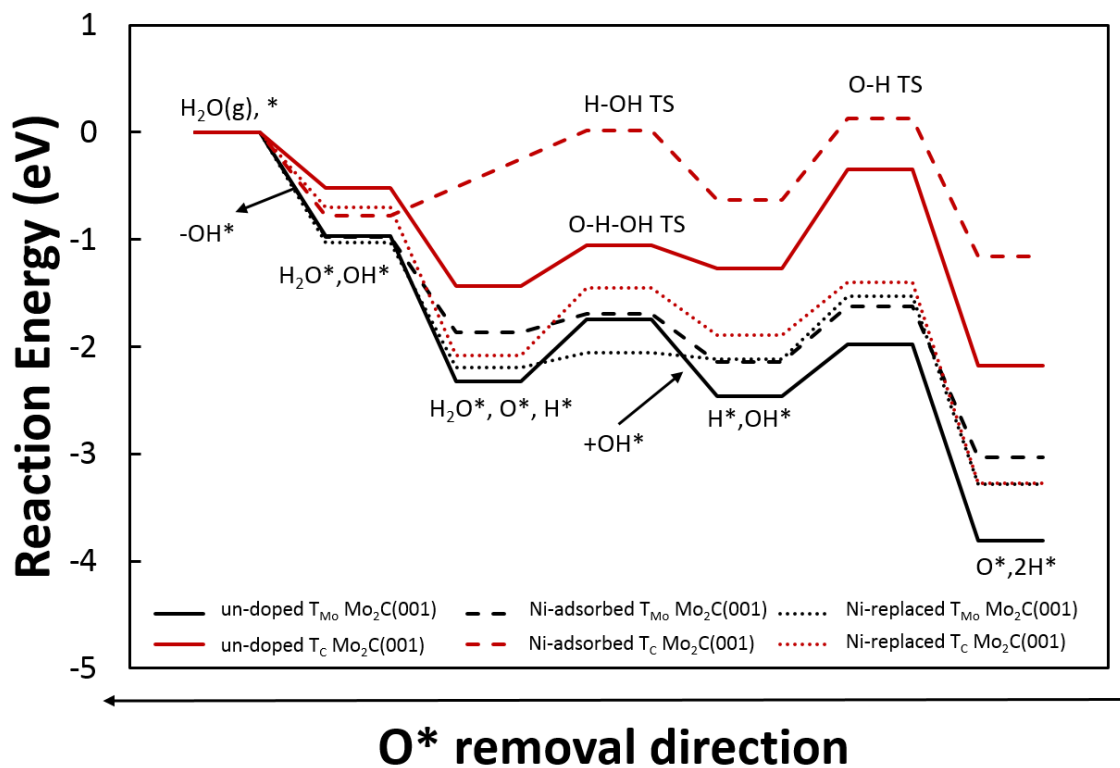


Figure 4.8. Potential energy surface of O* removal on Mo₂C(001) surface. Transition state species are marked as TS to distinguish from the intermediates. Extra OH* is added or removed to OH-assisted O* removal to balance the whole step.

4.3.2.5 Temperature programmed reduction of surface-oxidized Mo₂C and Ni-Mo₂C

As a way to assess the validity of the DFT calculation results obtained for the (001) plane of Mo₂C, temperature-programmed reduction (TPR) experiments were performed on un-doped and Ni-doped (0.2-0.4 wt.%) bulk Mo₂C catalysts. The carbide samples, passivated with a low concentration of oxygen (i.e., 1%) after synthesis, had been stored in air until the TPR experiments. The carbides were orthorhombic Mo₂C investigated for HDO of a range of oxygenated hydrocarbon compounds by several research groups³⁶. Information about the

synthesis procedure and catalytic properties related to the carbides similar to those used in the present study can be found in ref ^{16,37}.

The TPR results are presented in [Figure 4.9](#) as H₂O formation profiles as a function of reduction temperature. Since each carbide sample was dried at 100 °C in Ar prior to TPR, most of the H₂O molecules evolved during TPR can be attributed to the reduction of surface oxygen (vs. desorption of physisorbed H₂O). The fact that multiple H₂O peaks appeared over a broad temperature range for most of the catalysts indicates that several types of O* species were present on the surface of these multi-faceted Mo₂C solids. For both catalyst types (i.e., un-doped and Ni-doped), longer storage in air increased not only the amount of H₂O formed, but also the number of peaks especially at high temperatures. This means that O atom incorporation continued even after the passivation likely via adsorption of O atoms on sites more difficult to reach and formation of surface Mo oxides. Indeed, X-ray photoelectron spectroscopy of passivated Mo₂C samples often shows the presence of Mo oxide species such as MoO₃ on the surface. ^{16,38,39}

Overall, the Ni-doped Mo₂C had lower H₂O formation than the un-doped Mo₂C stored in air for a similar duration. In fact, the difference was significant; the Ni-Mo₂C stored for 12 months had a H₂O formation level (based on the area under the H₂O curves in [Figure 4.9](#)) similar to the Mo₂C stored for only 1 month. This suggests that the Ni-doped Mo₂C was less oxophilic than the un-doped counterpart. Furthermore, the reduction of Ni-Mo₂C was completed at lower temperatures than that of the un-doped Mo₂C stored for a similar duration in air. These TPR results thus are consistent with and support the validity of the DFT results obtained in the present study.

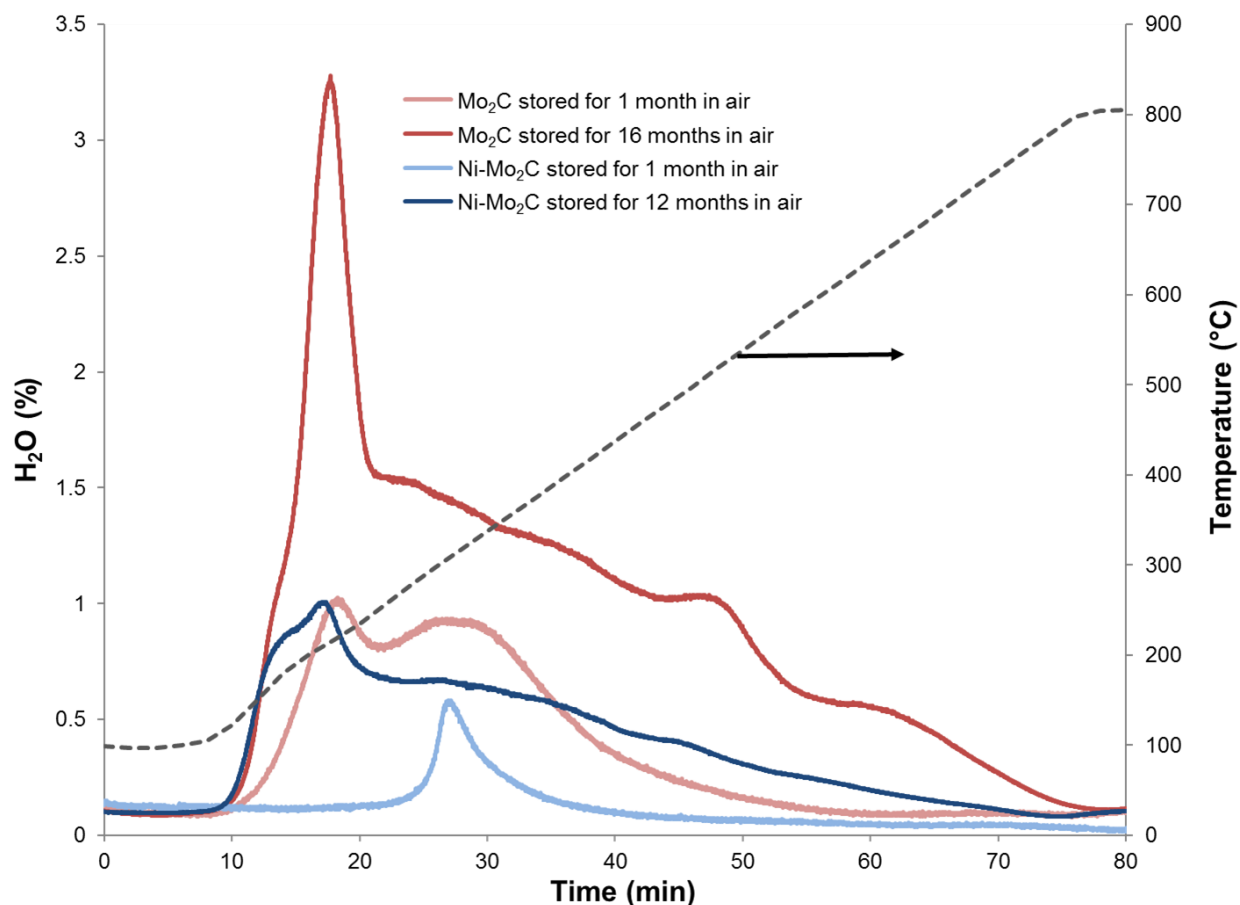


Figure 4.9. Water formation profiles obtained during temperature-programmed reduction of undoped and Ni-doped bulk Mo_2C catalysts. Prior to the experiments, the synthesized carbides were passivated with 1% O_2/N_2 and stored for different lengths of time in air. Experimental conditions: reduction gas, 70% H_2/Ar ; temperature program, stabilization at 100 °C and ramp up to 800 °C at 10 °C/min; H_2O profiles determined with a quadrupole mass spectrometer.

4.4 Conclusions

DFT calculations were performed to investigate the role of ‘K promoter to the WGS activity and selectivity on Ni(111) surface and the role of ‘Ni’ promoter towards the O^* removal from $\text{Mo}_2\text{C}(001)$ catalyst surface.

DFT calculations revealed that the K adatom enhances the adsorption of both CO and H₂O, the main reactants, and thus shifts the potential energies of the WGSR, as well as the methanation, lower. With regard to the reaction steps that determine the selectivity between the WGSR and methanation, the effectiveness of the adsorbed K species to lower the potential energies of the redox and carboxyl pathways result in the WGSR becoming even more favorable in comparison to the methanation pathways.

In addition, for O* removal reaction, the DFT results reveal that the favored Ni doping structures (e.g., Ni_adsorbed T_{M0} Mo₂C(001), Ni_replaced T_{M0} Mo₂C(001), and Ni_adsorbed T_C Mo₂C(001) surfaces) destabilize the adsorption of O* and OH* and benefit the O* removal. Among the six Mo₂C(001) surfaces considered in O* removal reaction, the Ni-adsorbed T_C Mo₂C(001) is the most favorable surface. This study shows that Ni facilitates the removal of oxygen from various Mo₂C surfaces. This computational prediction has been confirmed by the temperature programmed reduction profiles of Mo₂C and Ni doped Mo₂C catalysts that were previously passivated and stored in oxygen environment.

4.5 Acknowledgements

Case study 1 was supported in part by the Start-up fund provided by Kansas State University, the National Science Foundation under Award No. EPS-0903806, and matching support from the State of Kansas through the Kansas Board of Regents. DFT calculations were carried out thanks to the supercomputing resources and services from the Center for Nanoscale Materials (CNM) supported by the Office of Science of the US Department of Energy under the contract No. DE-AC02-06CH11357; the Beocat Research Cluster at Kansas State University,

which is funded in part by NSF grants CNS-1006860; and the National Energy Research Scientific Computing Center (NERSC) under the contract No. DE-AC02-05CH11231.

Case study 2 was conducted as part of the Computational Chemistry Physics Consortium (CCPC), which is supported by the Bioenergy Technologies Office (BETO) of Energy Efficiency & Renewable Energy (EERE). We gratefully acknowledge the computing resources provided on “Blues”, a computing cluster operated by the Laboratory Computing Resource Center at Argonne National Laboratory (ANL). This research used resources of the National Energy Research Scientific Computing Center (NERSC), which is supported by the Office of Science of the U.S. Department of Energy under Contract No. DE-AC02-05CH11231. Use of the Center for Nanoscale Materials was supported by the U.S. Department of Energy, Office of Science, Office of Basic Energy Sciences, under Contract No. DE-AC02-06CH11357. The experimental part of the manuscript has been co-authored by UT-Battelle, LLC under Contract No. DE-AC05-00OR22725 with the U.S. Department of Energy. The United States Government retains and the publisher, by accepting the article for publication, acknowledges that the United States Government retains a non-exclusive, paid-up, irrevocable, world-wide license to publish or reproduce the published form of this manuscript, or allow others to do so, for United States Government purposes. The Department of Energy will provide public access to these results of federally sponsored research in accordance with the DOE Public Access Plan (<http://energy.gov/downloads/doe-public-access-plan>). The work at ORNL was supported by the U.S. Department of Energy, Office of Energy Efficiency and Renewable Energy, Bioenergy Technologies Office through the Chemical Catalysis for Bioenergy consortium.

References

1. Liu, Z.; Hu, P. An insight into alkali promotion: A density functional theory study of CO dissociation on K/Rh(111). *J. Am. Chem. Soc.* **2001**, *123*, 12596-12604.
2. Nørskov, J. K.; Holloway, S.; Lang, N. D. Microscopic model for the poisoning and promotion of adsorption rates by electronegative and electropositive atoms. *Surf. Sci.* **1984**, *137*, 65-78.
3. Goodman, D. Catalysis - from single-crystals to the real-world. *Surf. Sci.* **1994**, *299*, 837-848.
4. Bonzel, H. P. Alkali-metal-affected adsorption of molecules on metal surfaces. *Surf Sci Rep* **1988**, *8*, 43-125.
5. Ma, W.; Jacobs, G.; Graham, U. M.; Davis, B. H. Fischer-tropsch synthesis: Effect of K loading on the water-gas shift reaction and liquid hydrocarbon formation rate over precipitated iron catalysts. *Top. Catal.* **2014**, *57*, 561-571.
6. Hwang, K.; Lee, C.; Park, J. Advanced nickel metal catalyst for water-gas shift reaction. *J. Power Sources* **2011**, *196*, 1349-1352.
7. Bornemann, T.; Steinrück, H.; Huber, W.; Eberle, K.; Glanz, M.; Menzel, D. The adsorption of H₂O on K precovered Ni(111) studied by ARUPS and TPD. *Surf. Sci.* **1991**, *254*, 105-118.
8. Bengaard, H. S.; Alstrup, I.; Chorkendorff, I.; Ullmann, S.; Rostrup-Nielsen, J. R.; Nørskov, J. K. Chemisorption of methane on Ni(100) and Ni(111) surfaces with preadsorbed potassium. *Journal of Catalysis* **1999**, *187*, 238-244.
9. Resch, C.; Zhukov, V.; Lugstein, A.; Berger, H. F.; Winkler, A.; Rendulic, K. D. Dynamics of hydrogen adsorption on promoter-and inhibitor-modified nickel surfaces. *Chem. Phys.* **1993**, *177*, 421-431.

10. Henkelman, G.; Arnaldsson, A.; Jónsson, H. A fast and robust algorithm for Bader decomposition of charge density. *Comput Mater Sci* **2006**, *36*, 354-360.
11. Tang, W.; Sanville, E.; Henkelman, G. A grid-based Bader analysis algorithm without lattice bias. *J. Phys. Condens. Matter* **2009**, *21*.
12. Ding, R.; Wu, Y.; Chen, Y.; Chen, H.; Wang, J.; Shi, Y.; Yang, M. Catalytic hydrodeoxygenation of palmitic acid over a bifunctional Co-doped MoO₂/CNTs catalyst: An insight into the promoting effect of cobalt. *Catal. Sci. Technol.* **2016**, *6*, 2065-2076.
13. Shi, C.; Zhang, A.; Li, X.; Zhang, S.; Zhu, A.; Ma, Y.; Au, C. Ni-modified Mo₂C catalysts for methane dry reforming. *Appl. Catal. A Gen.* **2012**, *431–432*, 164-170.
14. Zhao, Y.; Li, S.; Sun, Y. Ni-doping effects on carbon diffusion and oxidation over Mo₂C surfaces. *J. Phys. Chem. C* **2013**, *117*, 18936-18946.
15. Wan, C.; Leonard, B. M. Iron-doped molybdenum carbide catalyst with high activity and stability for the hydrogen evolution reaction. *Chem. Mater.* **2015**, *27*, 4281-4288.
16. Choi, J.; Zacher, A. H.; Wang, H.; Olarte, M. V.; Armstrong, B. L.; Meyer, H. M.; Soykal, I. I.; Schwartz, V. Molybdenum carbides, active and in situ regenerable catalysts in hydroprocessing of fast pyrolysis bio-oil. *Energy Fuels* **2016**, *30*, 5016-5026.
17. Zhang, W.; Zhang, Y.; Zhao, L.; Wei, W. Catalytic activities of NiMo carbide supported on SiO₂ for the hydrodeoxygenation of ethyl benzoate, acetone, and acetaldehyde. *Energy Fuels* **2010**, *24*, 2052-2059.
18. Ma, Y.; Guan, G.; Phanthong, P.; Hao, X.; Huang, W.; Tsutsumi, A.; Kusakabe, K.; Abudula, A. Catalytic activity and stability of nickel-modified molybdenum carbide catalysts for steam reforming of methanol. *J. Phys. Chem. C* **2014**, *118*, 9485-9496.

19. Ren, H.; Yu, W.; Saliccioli, M.; Chen, Y.; Huang, Y.; Xiong, K.; Vlachos, D. G.; Chen, J. G. Selective hydrodeoxygenation of biomass-derived oxygenates to unsaturated hydrocarbons using molybdenum carbide catalysts. *ChemSusChem* **2013**, *6*, 798-801.
20. Jalid, F.; Khan, T. S.; Mir, F. Q.; Haider, M. A. Understanding trends in hydrodeoxygenation reactivity of metal and bimetallic alloy catalysts from ethanol reaction on stepped surface. *J. Catal.* **2017**, *353*, 265-273.
21. Lausche, A. C.; Falsig, H.; Jensen, A. D.; Studt, F. Trends in the hydrodeoxygenation activity and selectivity of transition metal surfaces. *Catal Lett* **2014**, *144*, 1968-1972.
22. Vines, F.; Sousa, C.; Illas, F.; Liu, P.; Rodriguez, J. A. Density functional study of the adsorption of atomic oxygen on the (001) surface of early transition-metal carbides. *Journal of Physical Chemistry C* **2007**, *111*, 1307-1314.
23. dos Santos, P.; J. R.; Vines, F.; Rodriguez, J. A.; Illas, F. Atomic and electronic structure of molybdenum carbide phases: bulk and low Miller-index surfaces. *Physical Chemistry Chemical Physics* **2013**, *15*, 12617-12625.
24. Wang, T.; Luo, Q.; Li, Y.; Wang, J.; Beller, M.; Jiao, H. Stable surface terminations of orthorhombic Mo₂C catalysts and their CO activation mechanisms. *Applied Catalysis A-General* **2014**, *478*, 146-156.
25. Wang, T.; Tian, X.; Yang, Y.; Li, Y.; Wang, J.; Beller, M.; Jiao, H. Surface morphology of orthorhombic Mo₂C catalyst and high coverage hydrogen adsorption. *Surf. Sci.* **2016**, *651*, 195-202.
26. Kresse, G.; Hafner, J. Ab initio molecular-dynamics simulation of the liquid-metalamorphous- semiconductor transition in germanium. *Phys. Rev. B* **1994**, *49*, 14251-14269.

27. Kresse, G.; Furthmüller, J. Efficiency of ab-initio total energy calculations for metals and semiconductors using a plane-wave basis set. *Comput Mater Sci* **1996**, *6*, 15-50.
28. Perdew, J. P.; Burke, K.; Ernzerhof, M. Generalized gradient approximation made simple. *Phys. Rev. Lett.* **1996**, *77*, 3865-3868.
29. Kresse, G.; Joubert, D. From ultrasoft pseudopotentials to the projector augmented-wave method. *Phys. Rev. B Condens. Matter Mater. Phys.* **1999**, *59*, 1758-1775.
30. Monkhorst, H. J.; Pack, J. D. Special points for Brillouin-zone integrations. *Phys. Rev. B* **1976**, *13*, 5188-5192.
31. Methfessel, M.; Paxton, A. T. High-precision sampling for Brillouin-zone integration in metals. *Phys. Rev. B* **1989**, *40*, 3616-3621.
32. Epicier, T.; Dubois, J.; Esnouf, C.; Fantozzi, G.; Convert, P. Neutron powder diffraction studies of transition metal hemicarbides M_2C_{1-x} -II. In situ high temperature study on W_2C_{1-x} and Mo_2C_{1-x} . *Acta Metallurgica* **1988**, *36*, 1903-1921.
33. Henkelman, G.; Uberuaga, B. P.; Jónsson, H. Climbing image nudged elastic band method for finding saddle points and minimum energy paths. *J. Chem. Phys.* **2000**, *113*, 9901-9904.
34. Henkelman, G.; Jónsson, H. A dimer method for finding saddle points on high dimensional potential surfaces using only first derivatives. *J. Chem. Phys.* **1999**, *111*, 7010-7022.
35. Xiong, K.; Li, L.; Zhang, L.; Ding, W.; Peng, L.; Wang, Y.; Chen, S.; Tan, S.; Wei, Z. Ni-doped Mo_2C nanowires supported on Ni foam as a binder-free electrode for enhancing the hydrogen evolution performance. *J. Mater. Chem. A* **2015**, *3*, 1863-1867.
36. - Sullivan, M. M.; Chen, C.; Bhan, A. Catalytic deoxygenation on transition metal carbide catalysts. *Catal. Sci. Technol.* **2016**, *6*, 602-616.

37. Choi, Y.; Stenger, H. G. Water gas shift reaction kinetics and reactor modeling for fuel cell grade hydrogen. *J. Power Sources* **2003**, *124*, 432-439.
38. Choi, J.; Schwartz, V.; Santillan-Jimenez, E.; Crocker, M.; Lewis, S. A.; Lance, M. J.; Meyer, Harry M., III; More, K. L. Structural evolution of molybdenum carbides in hot aqueous environments and impact on low-temperature hydroprocessing of acetic acid. *Catalysts* **2015**, *5*, 406-423.
39. Schaidle, J. A.; Blackburn, J.; Farberow, C. A.; Nash, C.; Steirer, K. X.; Clark, J.; Robichaud, D. J.; Ruddy, D. A. Experimental and computational investigation of acetic acid deoxygenation over oxophilic molybdenum carbide: surface chemistry and active site identity. *ACS Catalysis* **2016**, *6*, 1181-1197.

Chapter 5 - Structure and Size Effects of Ni Nanocatalysts for Hydrogen Production via WGSR

Chapter 5 is adapted with permission from:

Zhou, M.; Le, T.; Huynh, L.; Liu, Bin. Effects of Structure and Size of Ni nanocatalysts on Hydrogen Selectivity via Water-gas-shift Reaction – A First-principles-based Kinetic Study. *Catalysis Today* **2017**, 280, 210-219.

5.1 Introduction

This chapter aims to elucidate the hydrogen selectivity on different Ni surface, where the adverse effect of methanation cannot be neglected. WGSR and methanation are both sensitive to catalyst surface structures¹⁻³. Stamatakis et al.³ performed kinetic Monte Carlo modeling of WGSR on Pt(111), Pt(211), and Pt(322) at 180 ~ 345°C and 1 atm, and proposed that at low CO:H₂O ratios (e.g., 10⁻³), the step sites are much more active than the terraces sites; but at the CO:H₂O ratios of 0.5, the coverages of CO and H and (turnover frequency) TOF of H₂ show less sensitivity to the surface structures. Catapan et al.¹ compared the WGSR and coke formation on Ni(111) and Ni(211) and concluded that the Ni(211) facet is more active for C-O bond scissions than Ni(111). Low-coordination surface atoms, i.e., at the step sites, are able to enhance the binding of H₂O⁴ and CO and dissociate the adsorbates. The facilitated H₂O dissociation is beneficial toward WGSR, however, the enhanced C-O bond scission will also increase the selectivity to methanation. Therefore, a mechanistic understanding of the competition between WGSR and methanation and its structure-dependence will help address a fundamental heterogeneous catalysis issue.

Modern nanotechnologies have tremendously advanced the preparation of tailored nanocatalysts.^{5,6} Control of nanoparticle shape and size will ultimately determine the dominant surface active terrace, edge, and corner sites. One prominent example of CO oxidation on gold demonstrated by Haruta et al.⁷ suggests that catalytic activity and selectivity can be dramatically enhanced on highly dispersed nanoparticles (< 5 nm). In WGSR, it has been found by Shekhar et al. that the low-coordinated corner Au sites can be seven times more active than the perimeter Au sites⁸, both of which also depend on Au nanoparticle sizes. CO methanation is also found to be strongly dependent on the Ni nanoparticle sizes (0.5 ~ 13 nm).⁹ A systematic investigation on the effect of Ni nanoparticle sizes (5 ~ 10, 10 ~ 20, and 20 ~ 35 nm) in Ni/ α -Al₂O₃ on CO methanation by Gao et al. showed that nanoparticle size of 1 ~ 20 nm results in the highest CO turnover frequency (TOF) and CH₄ yield.¹⁰

In this chapter, the competition between WGSR and methanation was investigated to elucidate the key factors, i.e., temperature, surface coverage on hydrogen selectivity on nanoscale Ni catalysts using a uniform computational framework that consolidates periodic, spin-polarized DFT calculated thermochemistry and kinetics and the mean field kinetic modeling. A mechanism consisting of only the dominant WGSR (i.e., redox and carboxyl pathways), and methanation pathways (i.e., CHO and HCOH pathways) on Ni(111) was constructed (as shown in Section 3.3) to simplify the reactions.¹¹ The universal kinetic Brønsted-Evans-Polanyi (BEP) relationships describing elementary steps involving C–H, O–H, and C–O bonds have also been established on Ni(111), Ni(100), and Ni(211) facets.

5.2 Computational Methods

5.2.1 DFT Calculations

The (111), (100), and (211) facets of single Ni crystal were used to represent the close-packed, open-packed, and step sites that are common in supported spherical or hemispherical face-centered cubic (FCC) transition metal nanoparticle surface.¹² Specifically, the Ni(111) surface is represented by a three-layer slab in a 3×3 hexagonal supercell; the Ni(100) surface represented by a three-layer 3×3 orthogonal supercell, and the Ni(211) surface represented by a three-layer 1×3 supercell, respectively. All other computational details are same as section 3.2 in Chapter 3.

Vibrational frequency analysis was also performed on all reaction intermediates as shown in **Appendix A** to approximate thermodynamic properties (e.g., entropy (S), enthalpy (H), and Gibbs free energy (G)). Here, the thermodynamic properties were calculated using the SurfKin package¹³, where the translational, rotational, and vibrational entropies of gas phase and surface intermediates were calculated based on the standard statistical mechanical approach.¹⁴ The detailed approach for calculating thermodynamic properties are presented in Chapter # section #.

5.2.2 Micro-kinetic Modeling

The descriptor-based Catalysis Micro-kinetic Analysis Package (CatMAP)¹⁵, developed by Medford et al. for kinetic modelings of heterogeneous catalysis and electrocatalysis systems, was used to calculate the rates of WGS and methanation and the surface coverages of reaction intermediates based on the mean field theory. The micro-kinetic model used in this study consists of 14 reaction steps, and 10 reaction intermediates. The flat Ni(111) and Ni(100) facets were modeled using two different surface sites: a “hydrogen reservoir” site¹⁶, and site for all

other intermediates. The stepped Ni(211) facet was modeled by considering three different sites: a “hydrogen reservoir” site, a “four-fold hollow” site and a site for all other intermediates. An example of starting files for micro-kinetic modeling is provided in **Appendix B**.

A temperature range of 423 ~ 723 K, and a pressure of 1bar were selected¹⁷⁻¹⁹. The formation energies of each reaction intermediate in the mechanism are calculated via explicit DFT calculations. H in gas phase H₂, O in gas phase H₂O and C in gas phase CH₄ were used as the reference for H, O, and C species respectively. The energy barriers were taken from DFT calculations. The lateral interactions between adsorbates were not included in current modeling.

5.2.3 Generation of Ni Nanoparticles

The Ni nanoparticle is assumed to have the shape of a truncated cuboctahedrons with predominant close-packed sites (i.e., (111)-like facet), open-packed sites (i.e., (100)-like facet), and step sites (i.e., (211)-like facet).¹² To investigate the size-dependence, cuboctahedra consisting of various numbers of Ni atoms were generated, corresponding to diameters ranging from 1 ~ 8 nm, measured as the distance between two opposite Ni(100) facets. The optimal (111), (100) and (211) fractions for each octahedron are determined according to the Wulff theorem²⁰ so that the overall surface energies can be minimized.

5.3 WGSR and Methanation on Ni(111), Ni(100), and Ni(211)

5.3.1 Adsorptions of Reaction Intermediates

Fourteen intermediate species were studied using periodic DFT calculations on the open-packed Ni(100) and stepped Ni(211) facets. The binding energies were then calculated based on their most stable configurations on respective surfaces. These binding energies and the preferred

adsorption sites for all intermediates included in this study are listed in **Table 5.1**. The binding energies on close-packed Ni(111) have been reported in **Table 3.1** in Chapter 3. The adsorption structures on Ni(100) and Ni(211) are illustrated in [Figure 5.1\(a\)](#) and [Figure 5.1\(b\)](#), respectively.

Table 5.1. Binding energies (BE), site preferences of reaction intermediates on Ni(111), Ni(100), and Ni(211) surfaces.

	Ni(111) [†]		Ni(100)		Ni(211)	
	BE	site	BE	site	BE	site
	[eV]		[eV]		[eV]	
H ₂ O	-0.27	top	-0.36	top	-0.55	top
CO	-1.93	hcp	-1.88	4-fold hollow	-1.97	hcp
CO ₂	-0.01	physisorption	-0.25	4-fold hollow	-0.38	top-top
HCOH	-3.88	fcc	-4.19	bridge	-4.53	bridge
CH ₂ OH	-1.56	fcc	-1.63	bridge	-2.05	bridge
H	-2.80	fcc	-2.73	4-fold hollow	-2.82	hcp
OH	-3.27	fcc	-3.43	4-fold hollow	-3.78	bridge
COOH	-2.25	bridge	-2.69	4-fold hollow	-2.18	top-top
CHO	-2.27	fcc, hcp	-2.81	bridge	-2.53	bridge
CH ₂	-4.03	fcc	-4.27	4-fold	-4.11	bridge

				hollow		
COH	-4.39	fcc, hcp	-4.67	4-fold	-4.43	hcp
				hollow		
O	-5.39	fcc	-5.61	4-fold	-5.57	hcp
				hollow		
CH	-6.41	fcc	-6.95	4-fold	-6.67	4-fold
				hollow		hollow
C	-6.89	hcp	-8.22	4-fold	-7.91	4-fold
				hollow		hollow

[†] Data taken from **Table 3.1** in Chapter 3

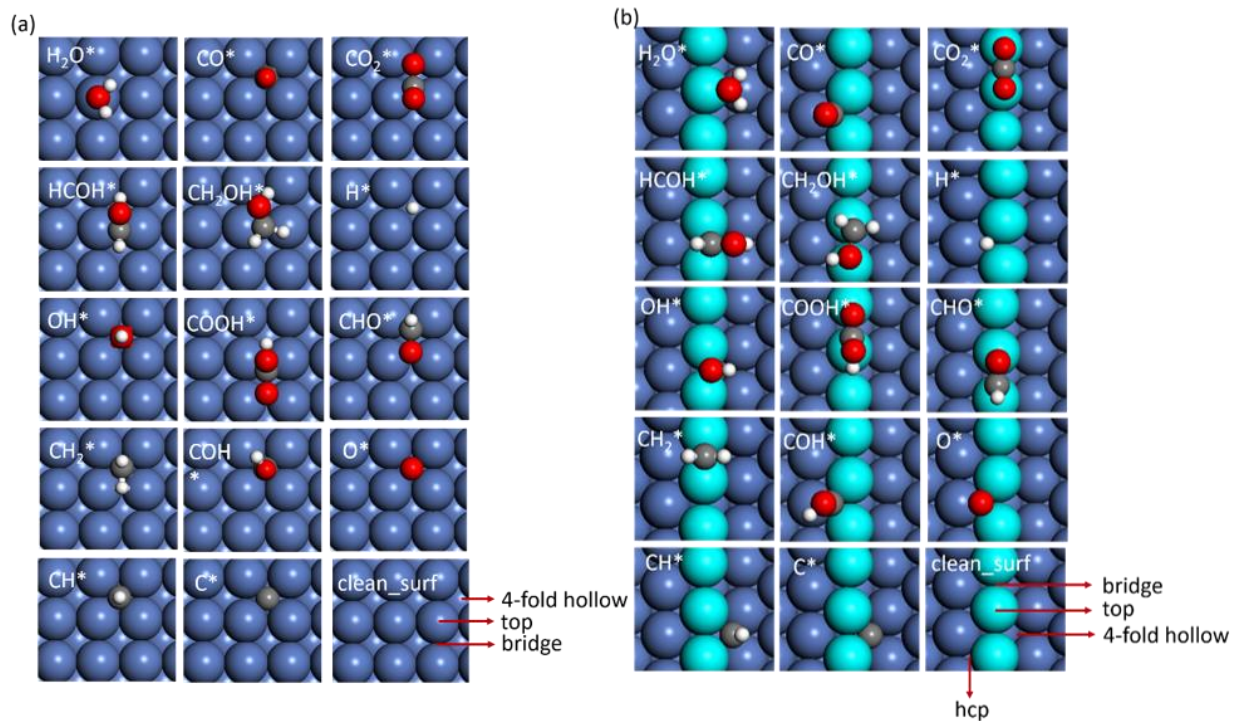


Figure 5.1. Optimized structures of the clean surface and the 14 intermediates in **Table 5.1** on (a) Ni(100), and (b) Ni(211). The grey, red, white, and blue spheres represent C, O, H, and Ni, respectively. The edge Ni atoms in Ni(211) are highlighted in turquoise. The adsorption sites on Ni(100) and Ni(211) are marked on the clean surface (clean_surf).

A brief overview of the binding energies and their preferred binding sites of the studied intermediates will help explain the thermodynamics and surface coverages in subsequent modelings. On Ni(100) and Ni(211), H₂O adsorbs on the top site, and the respective binding energies are -0.55 eV and -0.36 eV, versus -0.27 eV on Ni(111). CO binds on the 4-fold hollow site and the hcp site of the respective Ni(100) and Ni(211) facets. The CO binding energies are -1.88 eV and -1.97 eV, which are comparable to that on the Ni(111). CO₂ binds much stronger on the 4-fold hollow site and the top-top site of Ni(100) and Ni(111) facets, at -0.25 eV and -0.38 eV, respectively, versus that of -0.01 eV on Ni(111). HCOH also binds stronger, at respective -

4.19 eV and -4.53 eV, at the bridge sites of respective Ni(100) and Ni(211) facets than on Ni(111). CH₂OH binds stronger on Ni(100) and Ni(211) at the bridge sites, with binding energies of -1.63 eV and -2.05 eV, respectively, as well. H binds at the 4-fold hollow site and the hcp site on Ni(100) and Ni(211). The binding energy of H on Ni(100) is -2.73 eV, slightly weaker than that on the Ni(111), while H binds slightly stronger at -2.82 eV than that on the Ni(111). OH binds stronger than that on Ni(111) at the 4-fold hollow site and the bridge site of Ni(100) and Ni(211) at -3.43 eV and -3.78 eV, respectively. COOH binds much stronger at the 4-fold hollow at -2.69 eV (versus -2.25 eV on Ni(111)), however, the binding is weaker on Ni(211) at -2.18 eV at the top-top site. CHO also binds much stronger on the bridge site of Ni(100) at -2.81 eV (versus -2.27 eV on Ni(111)). CHO also prefers to bind at the bridge site of Ni(211) at -2.53 eV, again stronger than on Ni(111). CH₂ binds at the 4-fold hollow site and bridge site of respective Ni(100) and Ni(211) at -4.27 eV and -4.11 eV compared to -4.08 eV on Ni(111). COH binds at the 4-fold hollow site of Ni(100) and the hcp site of Ni(211), at -4.67 eV and -4.43 eV respectively compared to -4.39 eV on Ni(111). O binds at the 4-fold hollow site of Ni(100) and the hcp site of Ni(211) surface with respective binding energies of -5.61 eV and -5.57 eV, both of which are stronger than on the Ni(111) surface. CH binds at the 4-fold hollow of Ni(100) and the 4-fold hollow of the step on Ni(211) with binding energies of -6.95 eV and -6.67 eV, respectively. Similar to CH, C also binds on the 4-fold hollow sites of Ni(100) and Ni(211) with much stronger (> 1.0 eV) bind energies at -8.22 eV and -7.91 eV in comparison to -6.89 eV on Ni(111).

All intermediates bind stronger on Ni(100) and Ni(211) facets in general, except for CO and H on the (100) facet, and COOH on Ni(211). CO and H still prefer the hcp 3-fold sites on Ni(211), where the low-coordination edge Ni atoms play negligible role in enhancing the binding

of CO and H. However, the intermediates participating in CO methanation – e.g., CHO, CH, O – bind much stronger on Ni(211) and Ni(100).

5.3.2 BEP Relationship

A BEP relationship can reveal a linear correlation between the transition state energy and the corresponding reaction energy of an elementary step.^{21,22} Consequently, BEP relationships provide a means for fast estimation of reaction kinetics.²³⁻²⁵ In this study, the elementary steps involving C–H, O–H bonds and C–O bonds on the (111), (100), and (211) facets were investigated. The transition state energies (E_{TS}) and final state energies (E_{FS}) relative to gas phase initial state energies were used to obtain the BEP relationship (Figure 5.2 (a) and (b)). The transition state structures are shown in Figure 5.3.

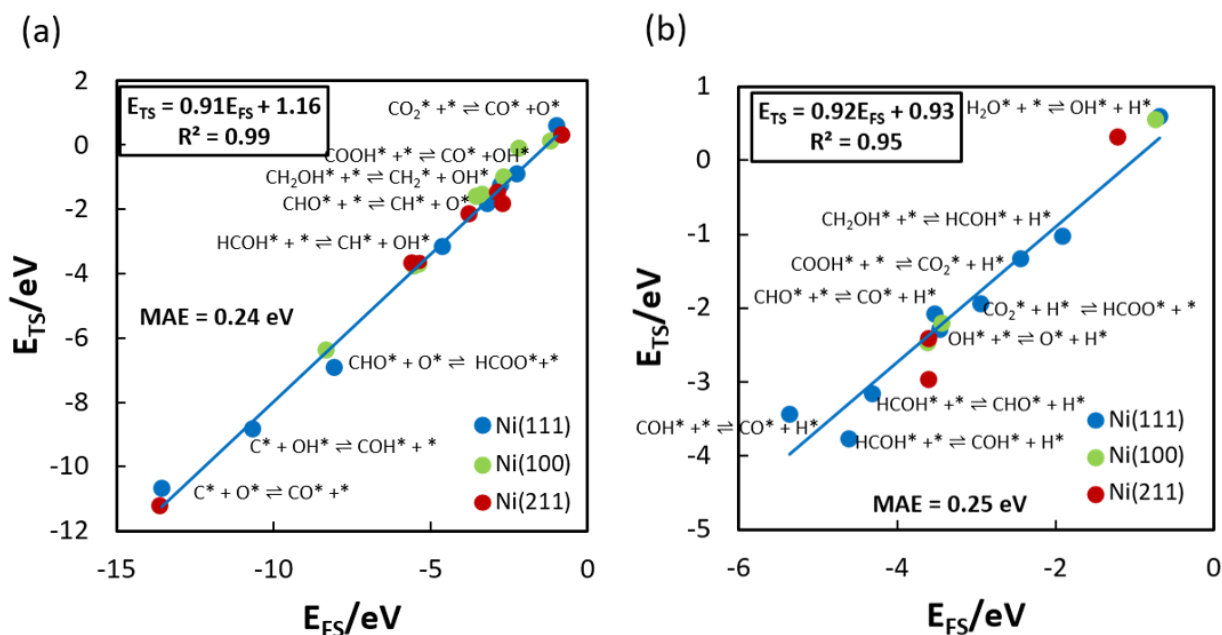


Figure 5.2. (a) BEP relationship for C–O bond forming/scission; (b) BEP relationship for C–H/O–H bond forming/scission. The elementary steps are expressed in the exothermic direction. E_{FS} and E_{TS} are relative energies to gas phase initial state energies.

Using the results obtained from DFT calculations on the (111) facet (blue dots), a linear relationship for both C-O bond forming/scission or C-H/O-H bond forming/scission clearly exist as described by [Figure 5.2\(a\) and \(b\)](#), with the mean absolute error (MAE) of 0.24 eV and 0.25 eV for C-O bond scission and C-H/O-H bond scission reactions, respectively. The slope and intercept for C-O bond cleavage/forming reaction are 0.91 and 1.16 eV while the corresponding values for C-H/O-H bond cleavage/forming reaction are 0.92 and 0.93 eV on Ni(111). The slope of C-H/O-H bond relationship (0.92) is in good agreement with that (0.96) developed by Mohsenzadeh et al.²⁶ using a dataset that combines Ni(111), Ni(100) and Ni(110) facets; and 0.86 obtained by Catapan et al. for just Ni(111)¹. The C-O bond BEP relationship is in good agreement with that developed by Catapan as well¹.

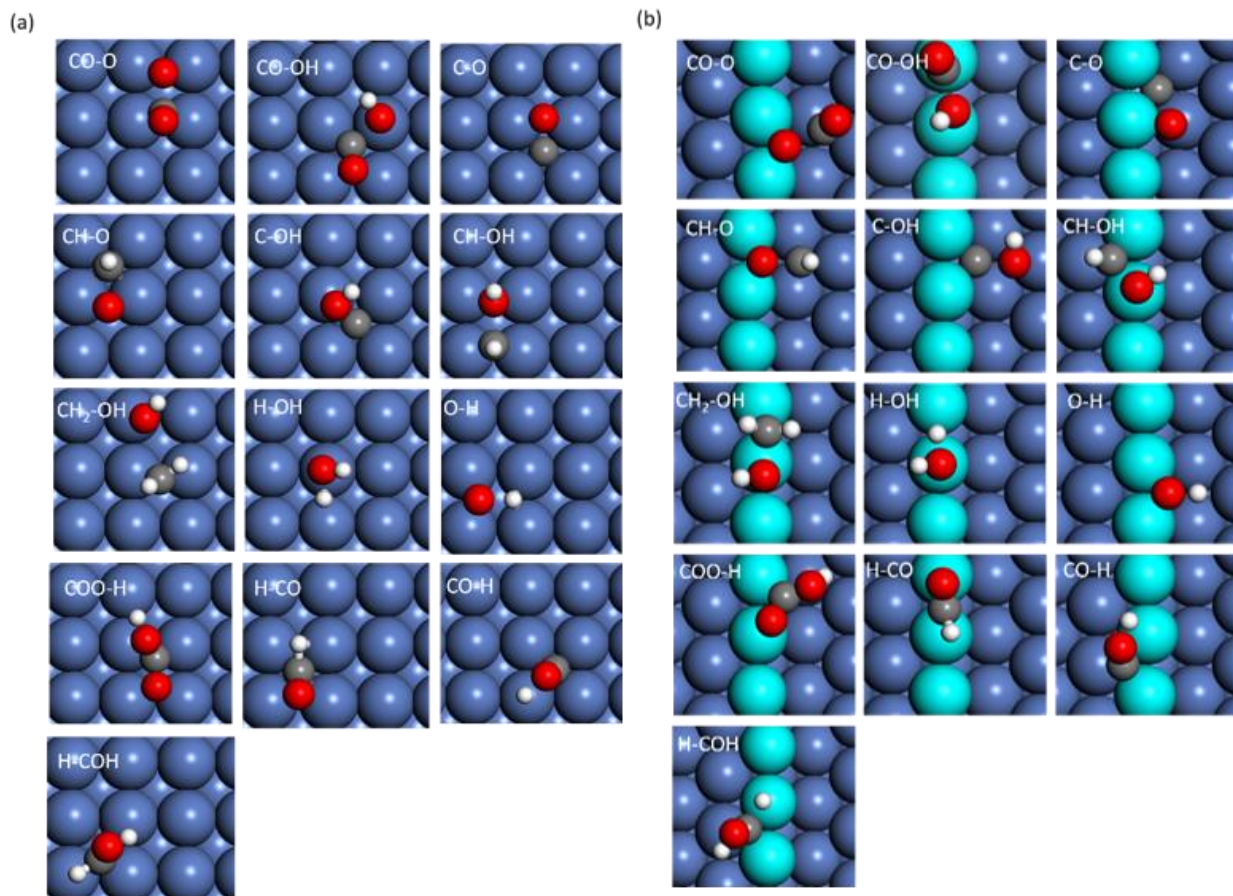


Figure 5.3. Optimized transition state structures on (a) Ni(100); and (b) Ni(211). The grey, red, white, and blue spheres represent C, O, H, and Ni, respectively. The edge Ni atoms in Ni(211) are highlighted with the turquoise color.

It should be noted that, unlike the BEP developed in other literature, this work intends to test the generality of the BEP relationship using only a subset of kinetic data, i.e., Ni(111). We believe that the BEP relationship developed on Ni(111) has the predictive power for Ni(211) and Ni(100). In order to further demonstrate the applicability of such linear relationships on Ni(100) and Ni(211), additional DFT calculations on a subset of the elementary steps on Ni(100) (green dots) and Ni(211) (red dots) were included in [Figure 5.2 \(a\) and \(b\)](#). Seven elementary steps are calculated for testing C-O bond cleavage/forming reaction, including: $\text{CO}^* + \text{O}^* \leftrightarrow \text{CO}_2^* + *$,

$\text{CO}^* + \text{OH}^* \leftrightarrow \text{COOH}^* + *$, $\text{CO}^* + * \leftrightarrow \text{C}^* + \text{O}^*$, $\text{CHO}^* + * \leftrightarrow \text{CH}^* + \text{O}^*$, $\text{COH}^* + * \leftrightarrow \text{C}^* + \text{OH}^*$, $\text{HCOH}^* + * \leftrightarrow \text{CH}^* + \text{OH}^*$, and $\text{CH}_2\text{OH}^* + * \leftrightarrow \text{CH}_2^* + \text{OH}^*$. In the meantime, five elementary steps are calculated for testing C-H/O-H bond cleavage/forming, including $\text{H}_2\text{O}^* + * \leftrightarrow \text{H}^* + \text{OH}^*$, $\text{OH}^* + * \leftrightarrow \text{O}^* + \text{H}^*$, $\text{COOH}^* + * \leftrightarrow \text{CO}_2^* + \text{H}^*$, $\text{CO}^* + \text{H}^* \leftrightarrow \text{CHO}^* + *$, $\text{CO}^* + \text{H}^* \leftrightarrow \text{COH}^* + *$. It can be seen that the same steps on the less-packed terrace sites and steps sites indeed follow the same linear relationships reasonably well. The energy barriers of the elementary steps are listed in **Table 5.2**.

Table 5.2. Energy barriers of the elementary steps for C-O bond formation/scission and C-H/O-H bond formation/scission on Ni(111), Ni(100), and Ni(211) surfaces.

	Ni(111) [‡]		Ni(100)		Ni(211)	
	$\Delta E/\text{eV}$	E_a/eV	$\Delta E/\text{eV}$	E_a/eV	$\Delta E/\text{eV}$	E_a/eV
$\text{CO}^* + \text{O}^* \leftrightarrow \text{CO}_2^* + *$	0.97	1.56	1.15	1.31	0.84	1.53
$\text{CO}^* + \text{OH}^* \leftrightarrow \text{COOH}^* + *$	0.96	1.40	0.88	1.83	1.60	1.66
$\text{CO}^* + * \leftrightarrow \text{C}^* + \text{O}^*$	1.28	2.88	-0.3	1.79	0.15	2.40
$\text{COH}^* + * \leftrightarrow \text{C}^* + \text{OH}^*$	0.52	1.86	-0.65	0.97	-0.97	0.74
$\text{CHO}^* + * \leftrightarrow \text{CH}^* + \text{O}^*$	-0.50	1.04	-1.25	1.22	-0.69	0.71
$\text{HCOH}^* + * \leftrightarrow \text{CH}^* + \text{OH}^*$	-0.74	0.72	-1.30	0.44	-1.07	0.87
$\text{CH}_2\text{OH}^* + * \leftrightarrow \text{CH}_2^* + \text{OH}^*$	-0.70	0.65	-0.99	0.63	-0.81	0.58
$\text{CHO}^* + * \leftrightarrow \text{HCOO}^* + *$	-0.41	0.73	--	--	--	--
$\text{COOH}^* + * \leftrightarrow \text{CO}_2^* + \text{H}^*$	-0.19	0.93	0.04	1.06	-0.65	0.44
$\text{CO}^* + \text{H}^* \leftrightarrow \text{COH}^* + *$	0.96	1.91	0.59	1.67	0.95	1.93
$\text{CO}^* + \text{H}^* \leftrightarrow \text{CHO}^* + *$	1.25	1.44	1.13	1.23	1.08	1.14
$\text{COH}^* + \text{H}^* \leftrightarrow \text{HCOH}^* + *$	0.73	0.83	0.83	1.22	0.34	0.69
$\text{OH}^* + * \leftrightarrow \text{O}^* + \text{H}^*$	-0.20	0.98	-0.23	0.96	0.11	1.03
$\text{H}_2\text{O}^* + * \leftrightarrow \text{OH}^* + \text{H}^*$	-0.41	0.86	-0.37	0.91	-0.66	0.87
$\text{HCOH}^* + \text{H}^* \leftrightarrow \text{CH}_2\text{OH}^* + *$	0.34	0.87	--	--	--	--
$\text{HCOO}^* + * \leftrightarrow \text{CO}_2^* + \text{H}^*$	0.13	0.99	--	--	--	--
$\text{CHO}^* + \text{H}^* \leftrightarrow \text{HCOH}^* + *$	0.43	1.14	--	--	--	--

[‡] Data taken from **Table 3.2** in Chapter 3

5.3.3 Free Energy Diagrams of WGSR and Methanation on Ni(111), Ni(100), and Ni(211)

WGSR is a moderately exothermic reaction (as shown in Equation (3) in Chapter 1), and the thermochemistry favors CO conversion at low temperatures (in the range of 423K ~ 513K). Nevertheless, WGSR at intermediate and high temperatures (up to 1000K under steam reforming conditions) are still relevant in many applications.^{27,28} Figure 5.4 presents the DFT-based free energies of WGSR redox and carboxyl pathways on the (111), (100), and (211) facets. The free energies were estimated at 600 K and 1 bar, using gas phase CO, H₂O and clean surface as the energy reference.

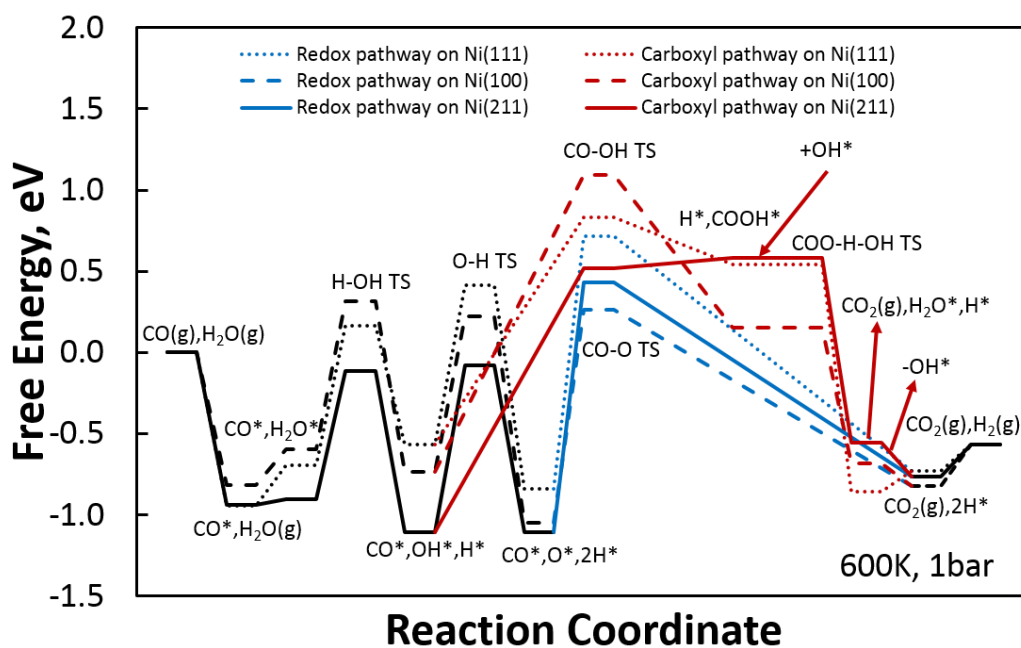


Figure 5.4. Free energy diagrams representing the redox and carboxyl pathways on Ni(111), Ni(100), and Ni(211) surface at 600 K and 1 bar. The black path represents CO adsorption, H₂O adsorption, dissociation, and H₂ formation.

Water dissociation is enhanced on Ni(211) (black solid paths in [Figure 5.4](#)).²⁹ On Ni(100), the OH dissociation step forming O becomes even more exothermic (black dashed path), which is consistent with the findings by Mohsenzadeh et al.³⁰ The enhanced water dissociation is expected to boost WGSR and hydrogen production by supplying the essential H, O, and OH species.

Direct CO oxidation by O from water dissociation occurs in the redox pathways forming CO₂, represented by the solid, dashed, and dotted paths for (211), (100), and (111) in [Figure 5.4](#), respectively. It can be seen in [Figure 5.4](#) that the CO oxidation step remains the rate-limiting step on all three facets studied. The redox pathways corresponding to the Ni(100) and Ni(211) facets shift downward in the free energy diagram compared to the closed-packed Ni(111), due to the enhanced water dissociation and CO oxidation thermochemistry.

The carboxyl pathway is another competitive WGSR route, and CO reacts with OH forming COOH is the rate-limiting step. On Ni(100) and Ni(211), the carboxyl pathway remains competitive, with COOH formation step being rate-limiting. The free energies of the carboxyl pathway on Ni(211) shift downward when compared to the Ni(111) facet, due to the enhanced water dissociation that produces the OH species. It is also intriguing to note that the rate-limiting step on Ni(100) shifts upward, due to the increased energy barrier of COOH formation, making the carboxyl pathway the least kinetically favorable.

The free energy diagrams depicting CO methanation via the formyl and HCOH pathways on Ni(111), Ni(100), and Ni(211) at 600 K and 1 bar are shown in [Figure 5.5](#). Gas phase CO and adsorbed H are chosen as the zero energy reference. The C–O bond scissions of the CHO and HCOH intermediates are the rate-limiting steps of respective pathways. The formation of CHO* are exothermic on all facets, and Ni(211) enables the lowest energy barrier for CO

hydrogenation. The energy barriers of the C–O bond scission in CHO are lower on Ni(211) and Ni(100) facets. The formyl pathway on Ni(211) has the lowest overall free energies, mainly due to the much lower energy barrier for C–O bond scission in CHO.

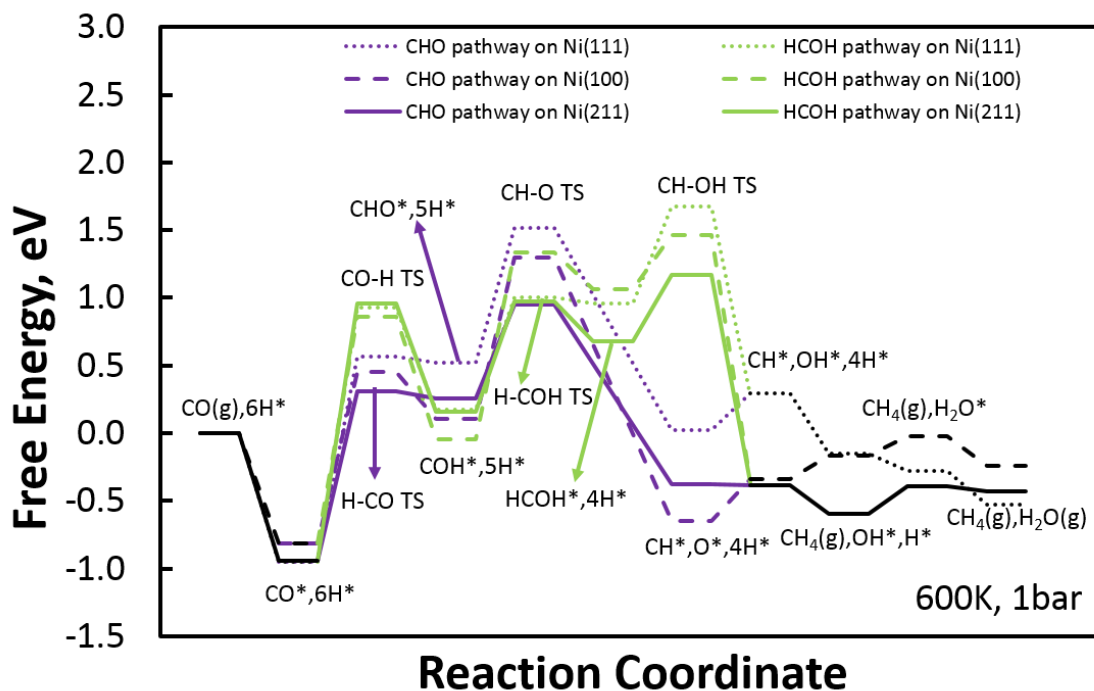


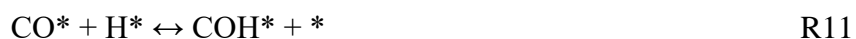
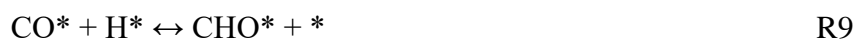
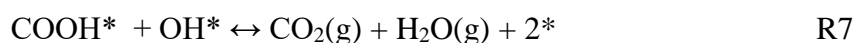
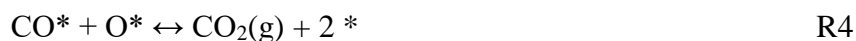
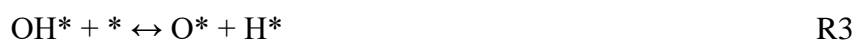
Figure 5.5. Free energy diagrams of the formyl (purple) and HCOH (green) pathway on Ni(111), Ni(100), and Ni(211) facets at 600 K and 1 bar. The black path represents CO adsorption, H₂O adsorption, dissociation, and CH₄ formation steps.

HCOH pathway involves COH as an intermediate species. CO hydrogenation pathways forming COH* are endothermic on all facets and Ni(100) has lowest energy barrier. The formation of HCOH* is still endothermic and Ni(211) has lowest energy barrier. The C – O bond scission from HCOH* is exothermic on all facets and the energy barriers decrease in order of Ni(111) > Ni(100) > Ni(211). Overall, the formyl pathway and the HCOH pathway are both competitive pathways on Ni(211).

5.4 Micro-kinetic Modeling of WGSR and Methanation

5.4.1 First-principles Based Mechanism for Micro-kinetic Modeling

The influence of CO methanation on hydrogen selectivity and the structure and size-dependence on Ni nanocatalysts have been investigated by carrying out mean-field theory-based micro-kinetic modelings. A mechanism consisting of 14 reaction steps, including the redox and carboxyl pathways (R4~R7, for WGSR), the formyl and HCOH pathways (R9 ~ R13, for methanation), CO adsorption (R1), H₂O dissociation (R2, R3), H₂ and CH₄¹¹ formation steps (R8, R14) for micro-kinetic modeling are constructed:



The asterisk (*) represents the open site on Ni(111), Ni(100), or Ni(211), and will be differentiated in the kinetic modeling. Particularly, ‘H reservoir’ sites were created, as implemented by Medford et al.¹⁶. The detailed mechanisms for respective Ni(111), Ni(100), and Ni(211) facets and Ni nanocatalysts are shown in **Appendix C**. R4 and R5 are identified as the rate-limiting steps for WGSR as discussed in Section 3.3.2 in Chapter 3.

There are still debates regarding the actual rate-limiting steps for micro-kinetic modeling of CO methanation.³¹ In this kinetic modeling, C-O bond dissociation steps (R10 and R13) are both treated as the rate-limiting steps based on the first-principles calculations. The energy barriers for water dissociation, i.e., R2 and R3, are also explicitly included due to its sensitivity of these steps to surface structures (as shown in [Figure 5.4](#)). In addition, the energy barriers of CO hydrogenation steps were also included.

Gas phase H₂ and H* are in thermodynamic equilibrium, an assumption that has been adopted by Sehested et al.³¹. CH* is also assumed to proceed quickly and in thermodynamic equilibrium with gas phase CH₄, which is same with the mechanism proposed by Vannice³² that CH_y hydrogenation step proceeds very quickly and does not influence the kinetics of the whole methane formation reaction³². In our kinetic modeling, the energy barriers for both H₂ and CH₄ formations have been neglected.

5.4.2 Ni Nanocatalyst Facets and Size Effects on Reactivity and Selectivity

Dependence

[Figure 5.6](#) shows the H₂ and CH₄ production rates based on the micro-kinetic modeling conducted at a temperature range of 423 ~ 723 K and the pressure of 1 bar on Ni(111), Ni(100), and Ni(211) facets. The simulated feed composition, with a representative molar ratio of CO :

$\text{H}_2\text{O} = 1:2^{33}$, was used. The production rates on different single Ni crystal facets are represented in terms of the turnover frequency (TOF in s^{-1}). The TOF order for both H_2 and CH_4 , corresponding to the rates of WGSR and methanation, are in good agreement with the free energy diagram (Figures 5.4 and 5.5). The vertical dashed line indicates the TOF for the temperature of 600 K.

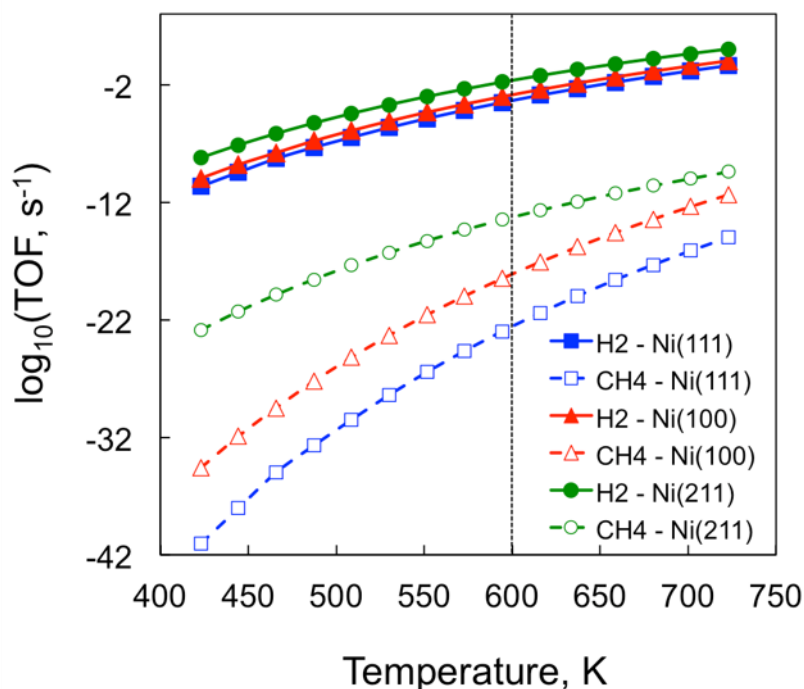


Figure 5.6. Turnover frequencies (s^{-1}) of H_2 and CH_4 production on Ni(111), Ni(100), and Ni(211) at 1 bar, respectively. The feed composition has a molar ratio of $\text{CO} : \text{H}_2\text{O} = 1:2$. Vertical black dash line marks the reaction conditions of free energy diagram being generated in section 5.3.3.

In Figure 5.6, both the H_2 and CH_4 production rates increase with the temperature, which suggest that the reaction system is still kinetically controlled. In principle, this could be due to

the lack of explicit consideration of the adsorbate-adsorbate interactions in our micro-kinetic models. In fact, the CO surface coverage as shown in Figure 5.7 has been found to be over-estimated to around nearly 1 ML and would be likely to hinder the surface to reach thermodynamic equilibrium. Further studies with considering adsorbate-adsorbate interactions in micro-kinetic models will be discussed in Chapter 6.

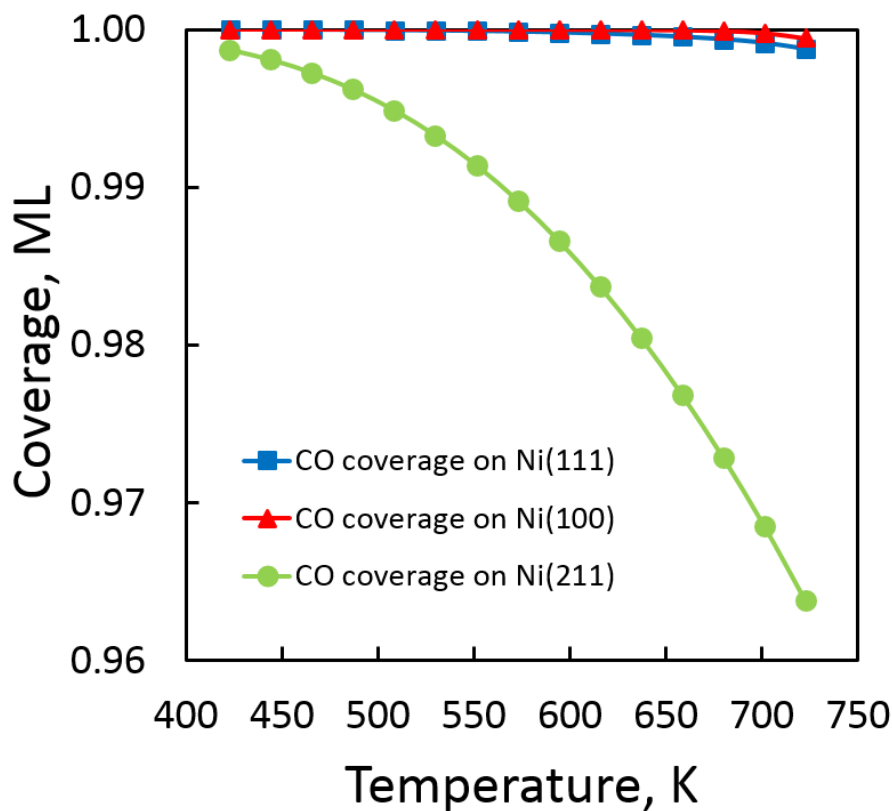


Figure 5.7. Surface coverage of CO* on (a) Ni(111) and Ni(100) and surface coverage of CO* and O* on (b) Ni(211) with feed composition of molar ratio of CO : H₂O = 1:2 at 1bar.

Figure 5.6 shows that the H₂ production rate decreases in the order of Ni(211) > Ni(100) > Ni(111), and the same trend has been observed for CH₄ production rate. At feed composition

of $\text{CO} : \text{H}_2\text{O} = 1:2$, the H_2 production rate is much higher on all Ni facets than the CH_4 production rate. Among the Ni(111), Ni(100), and Ni(211) facets, the difference in TOFs for H_2 productions (solid lines) is much smaller than that for CH_4 productions (dashed lines). Qualitatively, the modeling suggests that although reaction rates are higher on the Ni(211) step edge sites, methanation is much more sensitive to these low-coordination Ni atoms that facilitate the C–O bond scission rate-limiting steps.

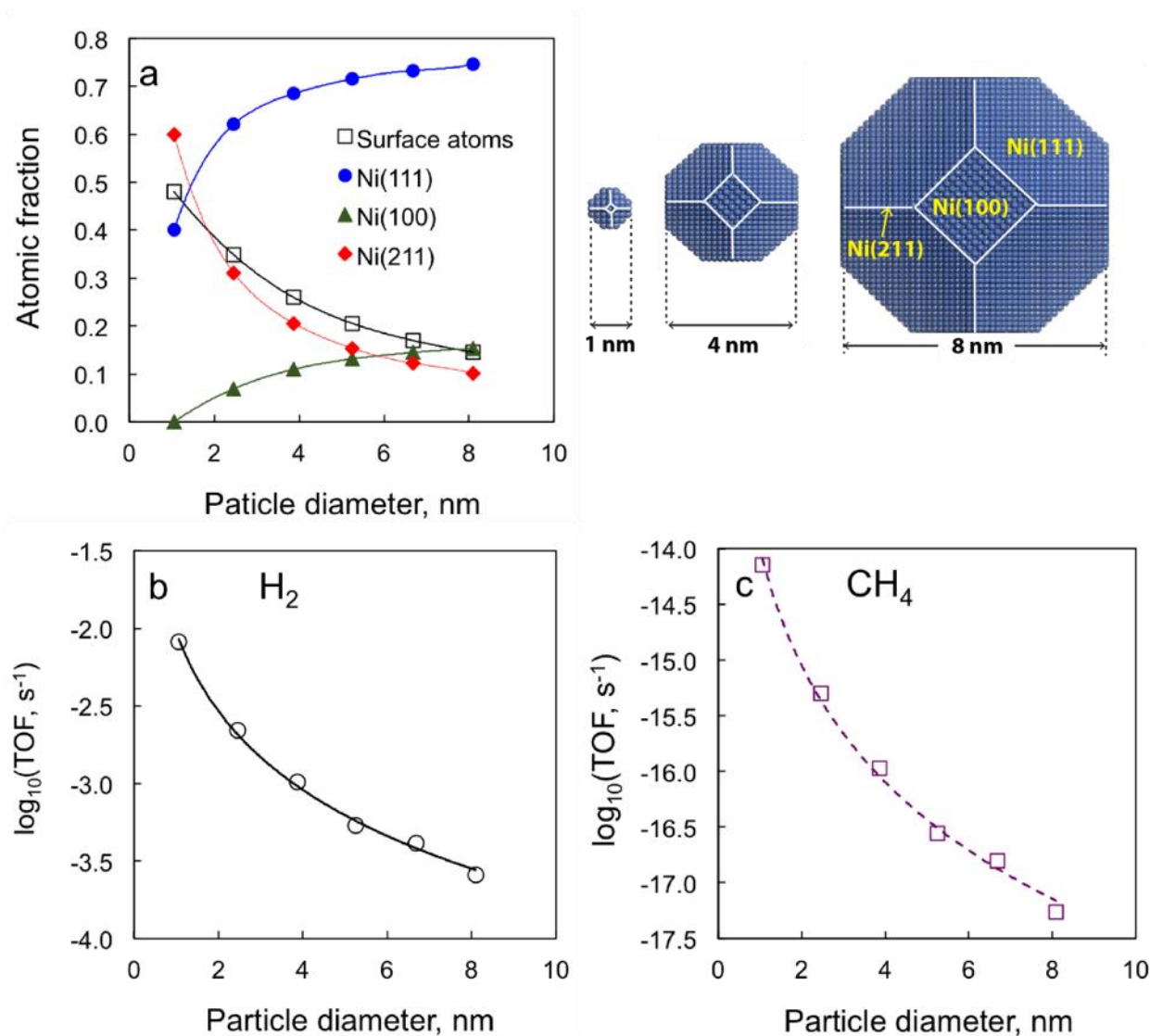


Figure 5.8. (a) Atomic fractions of surface Ni atoms (black square), and fractions of Ni atoms at close-packed (solid orange circle), open-packed (solid green circle), and step edge sites (solid red circle) for unsupported cuboctahedral Ni nanoparticles with diameter from 1 nm ~ 8 nm. The schematic representations of cuboctahedra of 1, 4, and 8 nm diameters are also shown; (b) TOF (s^{-1}) of H_2 ; and (c) CH_4 production at 600 K and 1 bar. The TOF is the sum of TOF on Ni(111), Ni(100) and Ni(211). The feed composition has a molar ratio of $\text{CO} : \text{H}_2\text{O} = 1:2$. The solid and dashed lines are simply to guide the trend of modeling results.

The particle size effect on WGS and methanation competitions is also investigated by integrating individual Ni single crystal facets, i.e., Ni(111), Ni(100), and Ni(211), to reflect representative fractions of each Ni atom site on a single Ni catalyst nanoparticle. The crystal facets can be conveniently combined into truncated cuboctahedra, and the fraction of each facet is dependent on the diameter of the nanoparticle, as shown in [Figure 5.8 \(a\)](#). With increasing particle sizes (diameter varying from 1 nm to 8 nm), the fraction of surface atoms decreases from 0.48 to 0.1 (black squares). Correspondingly, the fractions of Ni atom at the close-packed sites increases from 0.4 to 0.75 (solid orange circles) and the Ni atoms at the open-packed sites increases from 0 to 0.15. However, the Ni atoms at the nanoparticle edges decreases from 0.6 to 0.1.

For instance, the fractions of surface Ni atoms on Ni(111), Ni(100) and Ni(211) are 0.68, 0.11, and 0.21, respectively ([Figure 5.8 \(a\)](#)), corresponding to a Ni particle of a diameter of 4 nm. The open sites for each facet are defined as different reaction species within the mechanism, which is demonstrated in the **Appendix C**. The TOFs for H₂ and CH₄ productions as a function of particle diameter (in nm) are shown in [Figure 5.8 \(b\) and \(c\)](#), for a given temperature and pressure (i.e. 600 K and 1 bar). In [Figure 5.8 \(b\) and \(c\)](#), the production rate of H₂ and CH₄ both decrease with increasing particle sizes. It can also be noted that, at 600 K and 1 bar, both the H₂ and CH₄ production TOFs follow a similar trend of the atomic fraction of Ni atoms at the (211) sites. For H₂ production, the rate (in log₁₀ of TOF) decreases from -2.0 to -3.5 as the nanoparticle diameter increase to 8 nm, while the rate for CH₄ changes from -14.0 to -17.5. Therefore, it can also be concluded that the methanation reaction, which depends more on the edge site for C–O bond scission, will be more sensitive to the cluster sizes as well.

5.4.3 Feed Composition Effect on WGSR and Methanation

As discussed in Section 5.4.2, at high CO concentration without H₂ in the feed, the open sites on Ni surface are dominated by CO. As indicated by Figure 5.6, the selectivity for hydrogen production should remain high on all Ni facets. Typically, the CO concentration in the reforming product stream will be much lower than the CO: H₂O = 1:2 ratio used in Section 4.2. Instead, substantial H₂ is also present.^{34,35} Feed composition will affect the equilibrium and product selectivity. A different feed composition is used for the micro-kinetic modeling on the respective Ni(111), Ni(100), and Ni(211). The selected composition, i.e., 2.5% CO, 25% H₂O, 12.5% CO₂, 37.5% H₂, and balance N₂, is based on the values reported in Ref. ¹⁹. Similar to Section 5.4.2, Figure 5.9 shows the H₂ and CH₄ production rate as a function of temperature. H₂ production rates on Ni(100) and Ni(211) are not shown, as H₂ production rates are negative at the temperature below 573 K on Ni(100), and on Ni(211) for the entire temperature range considered. The negative H₂ production rates can be explained as hydrogen is consumed in CO methanation at a faster rate than that produced via WGSR on Ni(100) and Ni(211) facets. It can be seen from Figure 5.9 that the CH₄ production rate decreases in the order of Ni(211) > Ni(100) > Ni(111). Comparison of the CH₄ production rates in Figures 5.9 and 5.6 show that the CH₄ production rates dramatically increase at the new feed composition. Throughout the temperature range, the CH₄ production rates on Ni(211) and Ni(100) are higher than that of H₂ production on Ni(111). This finding reveals that, at low CO concentration and high H₂ concentration, methanation will become a significant competition and lower hydrogen selectivity by consuming CO and H₂, particularly on the low-coordinated step edge sites and open-packed sites.

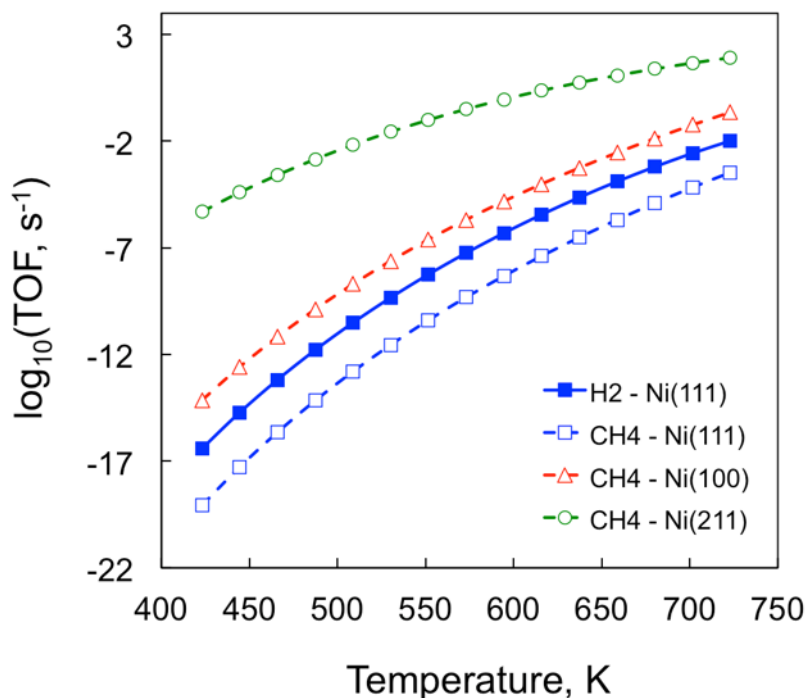


Figure 5.9. Turnover frequencies (s^{-1}) of CH_4 production on Ni(111), Ni(100), and Ni(211) at 1bar, respectively. The feed gas molar composition is 2.5% CO, 25% H_2O , 12.5% CO_2 , 37.5% H_2 , and balance N_2 .

5.5 Conclusions

DFT, statistical mechanical calculations, and micro-kinetic modeling were carried out for WGS and methanation on different Ni facets to understand the surface structure and particle size effect for reaction selectivity. Free energy diagrams were generated at 600 K and 1 bar to study WGS and methanation reaction thermodynamically and kinetically. The energetics of WGS and methanation point out that the most favorable facet of redox pathway is Ni(100) and for carboxyl pathway is Ni(211). For methanation pathway, Ni(211) favors both formyl pathway and HCOH pathway.

Detailed micro-kinetic modelings contain favorable pathways for WGSR and methanation on different facets were used to calculate reaction rates under the temperature range of 423 to 723 K. The results of the micro-kinetic model indicate that temperature, catalyst structure, particle size and feed composition can affect WGSR and methanation. With feed composition of $\text{CO} : \text{H}_2\text{O} = 1:2$, trends for H_2 and CH_4 production rates show an increase with increasing temperature on all facets, and decrease in the same order as: $\text{Ni}(211) > \text{Ni}(100) > \text{Ni}(111)$. Also, the TOFs of H_2 and CH_4 production decrease with increasing Ni particle sizes, whereas methanation is more dependent on the step edge sites on the nanoparticle surfaces. Furthermore, feed composition can also influence H_2 and CH_4 production rate. The presence of H_2 in feed gas favors methanation reaction and can dramatically increase the CH_4 production rate.

This work presents the detailed information of WGSR and methanation on different Ni facet and particle size. The finding of this work provides fundamental insight of the activity and competition between WGSR and methanation on different facets. The structure sensitivity and particle size effect supply explanation for different catalytic performance. This first-hand information can be used to tune and predict catalyst performance for WGSR and methanation.

5.6 Acknowledgements

This work is supported in part by the Start-up fund provided by Kansas State University, the National Science Foundation under Award No. EPS-0903806, and matching support from the State of Kansas through the Kansas Board of Regents. DFT calculations were carried out thanks to the supercomputing resources and services from the Center for Nanoscale Materials (CNM) supported by the Office of Science of the US Department of Energy under the contract No. DE-

AC02-06CH11357; the Beocat Research Cluster at Kansas State University, which is funded in part by NSF grants CNS-1006860; and the National Energy Research Scientific Computing Center (NERSC) under the contract No. DE-AC02-05CH11231. The authors also great appreciate the valuable inputs from Dr. Andrew Medford and the CatMAP support team.

References

1. Catapan, R. C.; Oliveira, A. A. M.; Chen, Y.; Vlachos, D. G. DFT study of the water-gas shift reaction and coke formation on Ni(111) and Ni(211) surfaces. *J. Phys. Chem. C* **2012**, *116*, 20281-20291.
2. Andersson, M. P.; Abild-Pedersen, F.; Remediakis, I. N.; Bligaard, T.; Jones, G.; Engbæk, J.; Lytken, O.; Horch, S.; Nielsen, J. H.; Sehested, J.; Rostrup-Nielsen, J. R.; Nørskov, J. K.; Chorkendorff, I. Structure sensitivity of the methanation reaction: H₂-induced CO dissociation on nickel surfaces. *J. Catal.* **2008**, *255*, 6-19.
3. Stamatakis, M.; Chen, Y.; Vlachos, D. G. First-principles-based kinetic Monte Carlo simulation of the structure sensitivity of the water-gas shift reaction on platinum surfaces. *J. Phys. Chem. C* **2011**, *115*, 24750-24762.
4. Mohsenzadeh, A.; Bolton, K.; Richards, T. DFT study of the adsorption and dissociation of water on Ni(111), Ni(110) and Ni(100) surfaces. *Surf. Sci.* **2014**, *627*, 1-10.
5. Cuenya, B. R. Synthesis and catalytic properties of metal nanoparticles: Size, shape, support, composition, and oxidation state effects. *Thin Solid Films* **2010**, *518*, 3127-3150.
6. Xiong, Y.; Wiley, B. J.; Xia, Y. Nanocrystals with unconventional shapes - A class of promising catalysts. *Angewandte Chemie-International Edition* **2007**, *46*, 7157-7159.

7. Haruta, M. Size- and support-dependency in the catalysis of gold. *Catalysis Today* **1997**, *36*, 153-166.
8. Shekhar, M.; Wang, J.; Lee, W.; Williams, W. D.; Kim, S. M.; Stach, E. A.; Miller, J. T.; Delgass, W. N.; Ribeiro, F. H. Size and support effects for the water-gas shift catalysis over gold nanoparticles supported on model Al₂O₃ and TiO₂. *J. Am. Chem. Soc.* **2012**, *134*, 4700-4708.
9. van Meerten, R. Z. C.; Beaumont, A. H. G. M.; van Nesselrooij, P. F. M. T.; Coenen, J. W. E. Structure sensitivity and crystallite size change of nickel during methanation of CO/H₂ on nickel-silica catalysts. *Surface Science* **1983**, *135*, 565-579.
10. Gao, J.; Liu, Q.; Gu, F.; Liu, B.; Zhong, Z.; Su, F. Recent advances in methanation catalysts for the production of synthetic natural gas. *RSC Adv.* **2015**, *5*, 22759-22776.
11. Zhou, M.; Liu, B. DFT Investigation on the competition of the water-gas shift reaction versus methanation on clean and potassium-modified nickel(111) surfaces. *ChemCatChem* **2015**.
12. Henry, C. R. Morphology of supported nanoparticles. *Prog Surf Sci* **2005**, *80*, 92-116.
13. Le, T. N.; Liu, B.; Huynh, L. K. SurfKin: An ab initio kinetic code for modeling surface reactions. *J. Comput. Chem.* **2014**, *35*, 1890-1899.
14. McQuarrie, D. A. *Statistical Mechanics*; University Science Books: Sausalito, 2000; .
15. Medford, A. J.; Shi, C.; Hoffmann, M. J.; Lausche, A. C.; Fitzgibbon, S. R.; Bligaard, T.; Nørskov, J. K. CatMAP: A software package for descriptor-based micro-kinetic mapping of catalytic trends. *Catal Lett.* **2015**, *145*, 794-807.
16. Yang, N.; Medford, A. J.; Liu, X.; Studt, F.; Bligaard, T.; Bent, S. F.; Nørskov, J. K. Intrinsic selectivity and structure sensitivity of rhodium catalysts for C₂₊ oxygenate production. *J. Am. Chem. Soc.* **2016**, *138*, 3705-3714.

17. Huang, S.; Lin, C.; Wang, J. Trends of water gas shift reaction on close-packed transition metal surfaces. *J. Phys. Chem. C* **2010**, *114*, 9826-9834.
18. Newsome, D. S. Water-gas shift reaction. *Catal. Rev. Sci. Eng.* **1980**, *21*, 275-281.
19. Schumacher, N.; Boisen, A.; Dahl, S.; Gokhale, A. A.; Kandoi, S.; Grabow, L. C.; Dumesic, J. A.; Mavrikakis, M.; Chorkendorff, I. Trends in low-temperature water-gas shift reactivity on transition metals. *J. Catal.* **2005**, *229*, 265-275.
20. Wulff, G. On the question of the rate of growth and dissolution of crystal surfaces. *Z. Krystallogr* **1901**, *34*, 449-530.
21. Bligaard, T.; Nørskov, J. K.; Dahl, S.; Matthiesen, J.; Christensen, C. H.; Sehested, J. The Brønsted-Evans-Polanyi relation and the volcano curve in heterogeneous catalysis. *J. Catal.* **2004**, *224*, 206-217.
22. Nørskov, J. K.; Bligaard, T.; Logadottir, A.; Bahn, S.; Hansen, L. B.; Bollinger, M.; Bengaard, H.; Hammer, B.; Sljivancanin, Z.; Mavrikakis, M.; Xu, Y.; Dahl, S.; Jacobsen, C. J. H. Universality in heterogeneous catalysis. *J. Catal.* **2002**, *209*, 275-278.
23. Liu, B.; Zhou, M.; Chan, M. K. Y.; Greeley, J. P. Understanding polyol decomposition on bimetallic Pt-Mo catalysts - A DFT study of glycerol. *ACS Catal.* **2015**, *5*, 4942-4950.
24. Liu, B.; Cheng, L.; Curtiss, L.; Greeley, J. Effects of van der Waals density functional corrections on trends in furfural adsorption and hydrogenation on close-packed transition metal surfaces. *Surf. Sci.* **2014**, *622*, 51-59.
25. Liu, B.; Greeley, J. Decomposition pathways of glycerol via C-H, O-H, and C-C bond scission on Pt(111): A density functional theory study. *J. Phys. Chem. C* **2011**, *115*, 19702-19709.

26. Mohsenzadeh, A.; Richards, T.; Bolton, K. DFT study of the water gas shift reaction on Ni(111), Ni(100) and Ni(110) surfaces. *Surf. Sci.* **2016**, *644*, 53-63.
27. Xu, J.; Froment, G. Methane steam reforming, methanation and water-gas shift .1. Intrinsic kinetics. *AIChE J.* **1989**, *35*, 88-96.
28. Zhang, Z.; Baerns, M. Hydrogen formation by steam-reforming and water gas shift reaction in the oxidative methane coupling reaction over calcium-oxide cerium dioxide catalysts. *Applied Catalysis.* **1991**, *75*, 299-310.
29. Huang, Y.; Ling, C.; Jin, M.; Du, J.; Zhou, T.; Wang, S. Water adsorption and dissociation on Ni surface: Effects of steps, dopants, coverage and self-aggregation. *Phys. Chem. Chem. Phys.* **2013**, *15*, 17804-17817.
30. Mohsenzadeh, A.; Richards, T.; Bolton, K. DFT study of the water gas shift reaction on Ni(111), Ni(100) and Ni(110) surfaces. *Surf. Sci.* **2016**, *644*, 53-63.
31. Sehested, J.; Dahl, S.; Jacobsen, J.; Rostrup-Nielsen, J. R. Methanation of CO over nickel: Mechanism and kinetics at high H₂/CO ratios. *J Phys Chem B.* **2005**, *109*, 2432-2438.
32. Vannice, M. A. The catalytic synthesis of hydrocarbons from H₂/CO mixtures over the group VIII metals. II. The kinetics of the methanation reaction over supported metals. *J. Catal.* **1975**, *37*, 462-473.
33. Lin, J.; Biswas, P.; Gulianti, V. V.; Misture, S. Hydrogen production by water-gas shift reaction over bimetallic Cu-Ni catalysts supported on La-doped mesoporous ceria. *Appl. Catal. A. Gen.* **2010**, *387*, 87-94.
34. Wawrzetz, A.; Peng, B.; Hrabar, A.; Jentys, A.; Lemonidou, A. A.; Lercher, J. A. Towards understanding the bifunctional hydrodeoxygenation and aqueous phase reforming of glycerol. *J. Catal.* **2010**, *269*, 411-420.

35. Comas, J.; Marino, F.; Laborde, M.; Amadeo, N. Bio-ethanol steam reforming on Ni/Al₂O₃ catalyst. *Chem. Eng. J.* **2004**, 98, 61-68.

Chapter 6 - Adsorbate-adsorbate Interaction Effects for Hydrogen

Production via WGSR

Chapter 6 is reproduced with permission from:

Zhou, M.; Liu, B. First-principles Investigation of Adsorbate-Adsorbate Interactions on Ni(111), Ni(211), and Ni(100) Surfaces. *Ind. Eng. Chem. Res.* **2017**, 56, 5813-5820.

6.1 Introduction

DFT-based molecular modeling typically only considers adsorption and chemical reactions at low surface coverage conditions. However, under realistic reaction conditions, adsorbate-adsorbate interactions directly impact chemisorptions and reaction energy barriers.¹⁻⁴ The influence cannot be neglected if key reaction intermediates are involved. According to the mean field micro-kinetic modeling discussed in Chapter 5 section 5.4.2, the rate of H₂ production via WGSR follows an order of Ni(111) < Ni(100) < Ni(211). Although this is a qualitatively anticipated behavior, where stepped and low-coordination sites are more active, the coverage of CO has been severely overestimated (as shown in [Figure 5.7](#) in Chapter 5) and may hinder the accuracy of quantitative analyses.

We hypothesize that adsorbate-adsorbate interactions vary on different single crystal facets, and thus a function of particle shape and size. Furthermore, the inclusion of such molecular behavior will alter catalyst selectivity. Here, the objective is to elucidate the nature of adsorbate-adsorbate interactions on different catalyst facets. In a broader context, the different behaviors of adsorbate molecules interact with its neighbors in a local environment would offer

insights into the development of the capability of modeling the heterogeneity of a catalyst surface.

In literature, several means have been developed to quantitatively describe the CO-CO lateral interaction, which is repulsive. Empirical correlations, in the forms of polynomial functions of CO coverage (θ_{CO}) on copper Equation (48),⁵ and platinum Equation (49),⁶ fitted to DFT calculations, have been employed.

$$BE_{CO*}(\theta_{CO}) = 6.81\theta_{CO}^2 - 3.14\theta_{CO} - 0.53 \quad (48)$$

$$BE_{CO*}(\theta_{CO}) = -1.78 + 0.0065 \exp(4.79\theta_{CO}) + 0.031135\theta_{CO}\exp(4.79\theta_{CO}) \quad (49)$$

The binding energies of other adsorbate species, such as O, H, OH, and COOH, can then be approximated through a simple correction using either Equation (50) or Equation (51), as a function of θ_{CO} .

$$BE(\theta_{CO}) = BE_0 + \frac{a}{1 + \exp[b(\theta_0 - \theta_{CO})]} \quad (50)$$

$$BE(\theta_{CO}) = BE_0 + a\exp(b\theta_{CO}) \quad (51)$$

where a , b , θ_0 , are fitting parameters, and BE_0 is the binding energy of the adsorbate calculated without the presence of CO.

Recent work has suggested that the binding energy of an adsorbate, such as CO, remains relatively constant below a threshold coverage (θ_0). Above θ_0 , the influence of lateral interaction becomes pronounced quickly.^{1,3,4} This pattern can be generalized by the *piece-wise* integral binding energy (BE^{int}), as shown in Equation (52),

$$BE^{int}(\theta_{CO}) = \begin{cases} BE_0\theta_{CO}, & \theta_{CO} \leq \theta_0 \\ BE_0\theta_{CO} + \varepsilon(\theta_{CO} - \theta^*)^2, & \theta_{CO} > \theta_0 \end{cases} \quad (52)$$

where $dE^{int}(\theta) = E^{diff}(\theta)d\theta$ and ε (in eV/ML) represent a measure of the interaction strength between adsorbates, known as the self-interaction parameters.

In this chapter, WGSR sequences consisting of the favorable redox and carboxyl pathways (R1 – R8) in Chapter 5 Section 5.4 will be used as a model reaction once again on Ni surfaces to gain understanding on this topic. Periodic DFT calculations were performed to determine the CO chemisorption structures and adsorption energies over a range of surface coverage on Ni(111), Ni(100), and Ni(211) facets. Molecular structures and corresponding binding energies for H₂O, OH, O, H, and COOH coadsorbed at the 4/9 ML coverage were also obtained.

Particularly, the CO–CO self-interactions were explicitly incorporated in the analysis of WGSR pathways for hydrogen production on single-crystal facets of Ni and other transitional metals like Cu, Pt, and Au. The carboxyl pathway is found to be the dominant pathway on Cu(111), Pt(111), and Au(111)⁵⁻⁸ from DFT calculations. Thus, a general trend for WGSR activity with only considering carboxyl pathways on transition metals is predicted through micro-kinetic modeling and compared with experimental results.

6.2 Computational Methods

The computational details are same as section 3.2 in Chapter 3 and section 5.2.1 in Chapter 5. The optimal configurations of CO co-adsorptions at 1/9, 2/9, 1/3, 4/9, 5/9, 2/3, 7/9, 8/9, and 1 ML coverages were determined through geometrical optimizations. In this study, we

adopted the conventional definition for surface coverage, i.e., each surface Ni atom is counted as one adsorption site. Hence, the corresponding number of adsorbed CO molecules will be 1–9 on each facet. The interactions of CO with H₂O, OH, O, H, and COOH were considered specifically at the 4/9 ML coverage, using the optimized CO configuration (at 4/9 ML coverage) as a starting point. The adsorbate (i.e., H₂O, OH, O, H, and COOH) was then introduced to the open site for further optimization.

At the low coverage limit (i.e., 1/9 ML), the binding energy (BE_A) of adsorbate A , representing H₂O, H, OH, O, and COOH, is defined as Equation (53),

$$BE_A = E_{A+slab} - E_{clean\ slab(N)} - E_{(A)} \quad (53)$$

where E_{A+slab} is the total energy of the adsorbate (A), $E_{(A)}$ is the total energy of the adsorbate (A) in gas phase calculated in a large vacuum box ($10 \text{ \AA} \times 10 \text{ \AA} \times 10.5 \text{ \AA}$), and $E_{clean\ slab(N)}$ is the total energy of the clean slab. N is the number of surface sites in the unit cell (i.e., $N=9$ for all the Ni surfaces considered here)

The differential binding energy (BE^{diff}), representing the additional energy needed to insert one more CO molecule on the surface, is calculated from Equation (54),

$$BE^{diff}(\theta) = E_{n-CO+slab(N)} - E_{CO_gas} - E_{n-1-CO+slab(N)} \quad (54)$$

where n is the number of CO adsorbed on slab, $E_{n-CO+slab(N)}$ is the total energy of the surface with $n-1$ adsorbed CO, E_{CO_gas} the total energy of gas phase CO.

The binding energies of adsorbate A at $4/9$ ML coverage (BE_{A-4co}) is defined by Equation (55),

$$BE_{A-4co} = E_{A-4CO+slab} - E_{4CO+slab} - E_{A_{gas}} \quad (55)$$

where the $E_{4CO+slab}$ is the total energy of adsorbate A with 4 co-adsorbed CO, and $E_{4CO+slab}$ is the total energy of the slab with four adsorbed CO molecules.

The differential CO free energy difference ($G^{diff}(\theta)$) is defined by Equation (56),

$$G^{diff}(\theta) = G_{n-CO+slab(N)} - G_{CO_{gas}} - G_{n-1-CO+slab(N)} \quad (56)$$

where $G_{n-CO+slab(N)}$ is the total free energy of the surface with n adsorbed CO, $G_{CO_{gas}}$ the total free energy of gas phase CO, and $G_{n-1-CO+slab(N)}$ is the total free energy of the surface with $n-1$ adsorbed CO.

6.3 Chemisorptions on Ni(111), Ni(100), and Ni(211) at Higher Coverages

6.3.1 CO Adsorption

CO chemisorptions take place in a monodentate fashion, i.e., each molecule occupies one site. The structures of CO chemisorption on Ni(111), Ni(100) and Ni(211) at nine different coverages ($1/9$ ML – 1 ML) corresponding to the respective lowest ground state energy at each coverage are illustrated in [Figure 6.1](#).

On Ni(111), the available binding sites are the hcp, fcc, and top site, indicated by red arrows in [Figure 6.1\(a\)](#). The BE_{CO} at the 1/9 ML coverage, according to Equation (53), is -1.93 eV, -1.92 eV, and -1.55 eV, respectively. Up to 1/3 ML, each CO is still able to bind at their preferred hcp site on Ni(111). At higher coverages, i.e., 4/9 ML, 5/9 ML, and 2/3 ML, some CO molecules are found to bind at the fcc site, which is regarded as a slightly metastable site according to the single molecule calculation. At 7/9 ML, CO begins to occupy the top site, 0.38 eV metastable, in addition to the hcp and fcc sites. At even higher coverages, i.e., 8/9 ML and 1 ML, the configurations of CO chemisorption become ordered again, and each CO binds at the hcp site. As shown in [Figure 6.1\(a\)](#), each CO molecule tends to maximize the intermolecular distances with its neighbors, thus sacrificing their preferred binding sites if necessary to maintain a rather uniform distribution on Ni(111) in order to minimize the repulsive forces.³

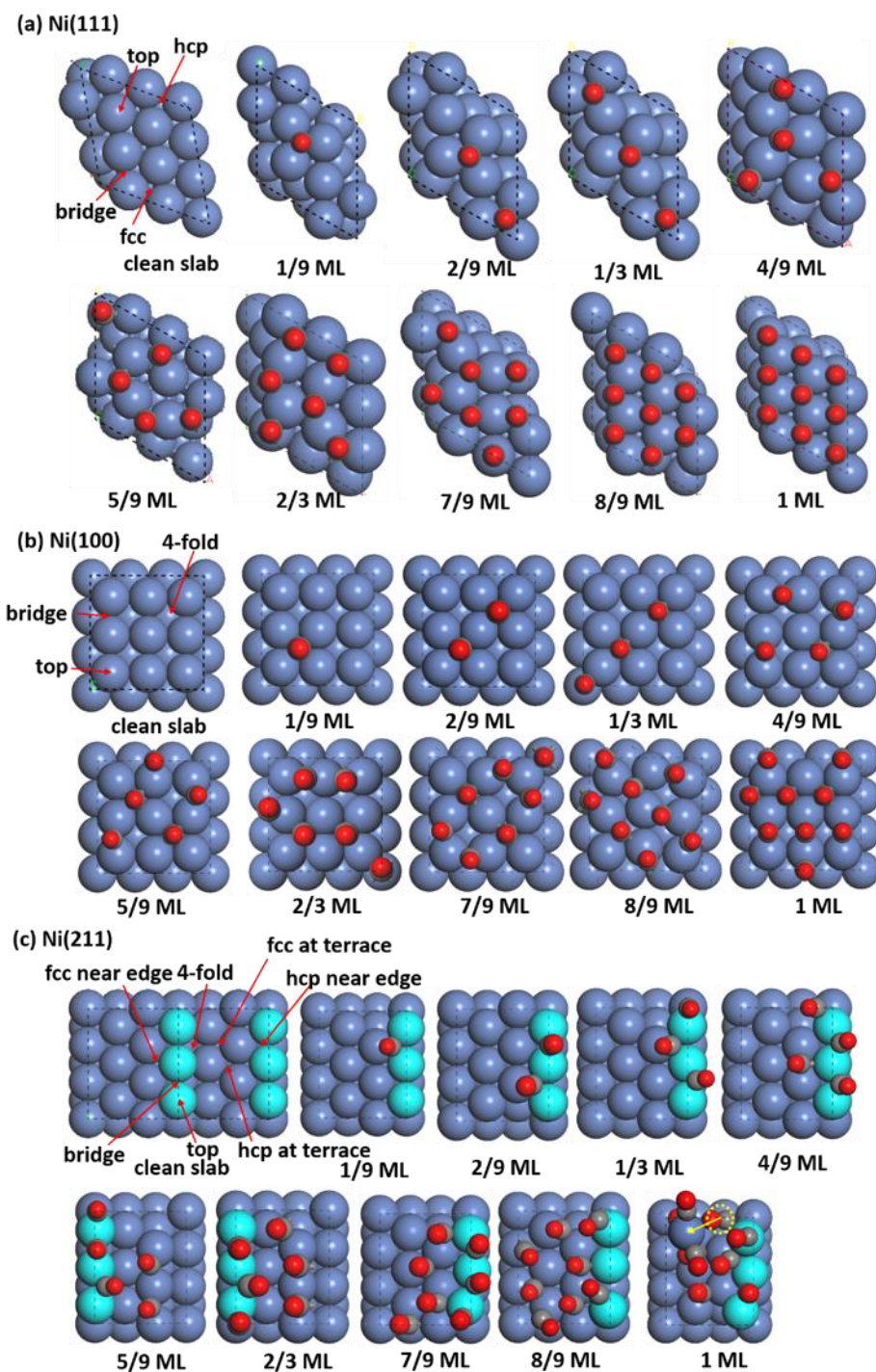


Figure 6.1. Optimized CO chemisorption geometries on (a) Ni(111), (b) Ni(100), and (c) Ni(211) at different coverages. Adsorption sites are labeled on each clean slab. The clean Ni(211) surface in (c) is further expanded to show the 4-fold site. Ni, C, O, and H are depicted

in blue, grey, red, and white, respectively. The edge Ni atoms in Ni(211) are highlighted in turquoise. The dashed yellow circle indicates the original location of Ni atom and the yellow arrow indicates the direction of Ni dislocation with high CO coverage on Ni(211). The dashed black lines indicate the boundaries of the supercell.

Ni(100) is the most open facet, with the Ni-Ni distance being 2.49 Å. On Ni(100), the available binding sites include the 4-fold, bridge, and top site (as indicated by the red arrows in [Figure 6.1\(b\)](#)), and the corresponding BE_{CO} is -1.88 eV, -1.83 eV, and -1.65 eV, respectively, at the 1/9 ML coverage. The optimized geometries on Ni(100) are illustrated in Figure 1(b). For 1/9 – 1/3 ML, each CO binds at its preferred 4-fold site. From 4/9 – 1 ML, CO binds at both the bridge and the 4-fold sites. For instance, at 4/9 ML, three of the four CO molecules actually bind at the bridge site. It has also been noted that the surface Ni can dislocate at high CO chemisorption coverage; for example, at 8/9 ML CO coverage, the Ni-Ni distance for Ni(100) facets vary between 2.45 Å and 2.62 Å.

On Ni(211), the available binding sites are the hcp near edge, fcc near edge, bridge, top, and 4-fold sites. The corresponding BE_{CO} is -1.97 eV, -1.85 eV, -1.94 eV, -1.78 eV, and -1.64 eV, respectively, at the 1/9 ML coverage. As shown in [Figure 6.1\(c\)](#), initially, CO would bind at the hcp site near edge. Then, the second CO is adsorbed at the bridge site. Such a zigzag pattern continues until the 4/9 ML coverage, where CO molecules adsorb alternately at the bridge, hcp or fcc near edge sites. Once these sites are occupied, additional CO molecules bind at the terrace of Ni(211) facet at the 5/9 – 7/9 ML coverages. These calculations indicate the Ni(211) step site can accommodate four CO molecules at maximum. The adsorption pattern on Ni(211) provides another clear example suggesting that adsorbed CO molecules can sacrifice their preferred

binding site in order to minimize a repulsive lateral interaction, in this case, by occupying the metastable terrace sites. At even higher coverages, i.e., 8/9 ML and 1 ML, noticeable surface reconstructs can be observed, as indicated in [Figure 6.1\(c\)](#).

The CO differential binding energies were obtained in order to quantitatively understand the trends for the CO-CO lateral interactions on the single crystal facets. [Figure 6.2\(a\)](#) shows the variations of CO differential binding energies, BE^{diff} based on Equation (54), with the CO coverage. The black dash line indicates BE^{diff} at 0 eV, meaning that further CO adsorption will be thermodynamically unfavorable, or the surface is *saturated* with CO.

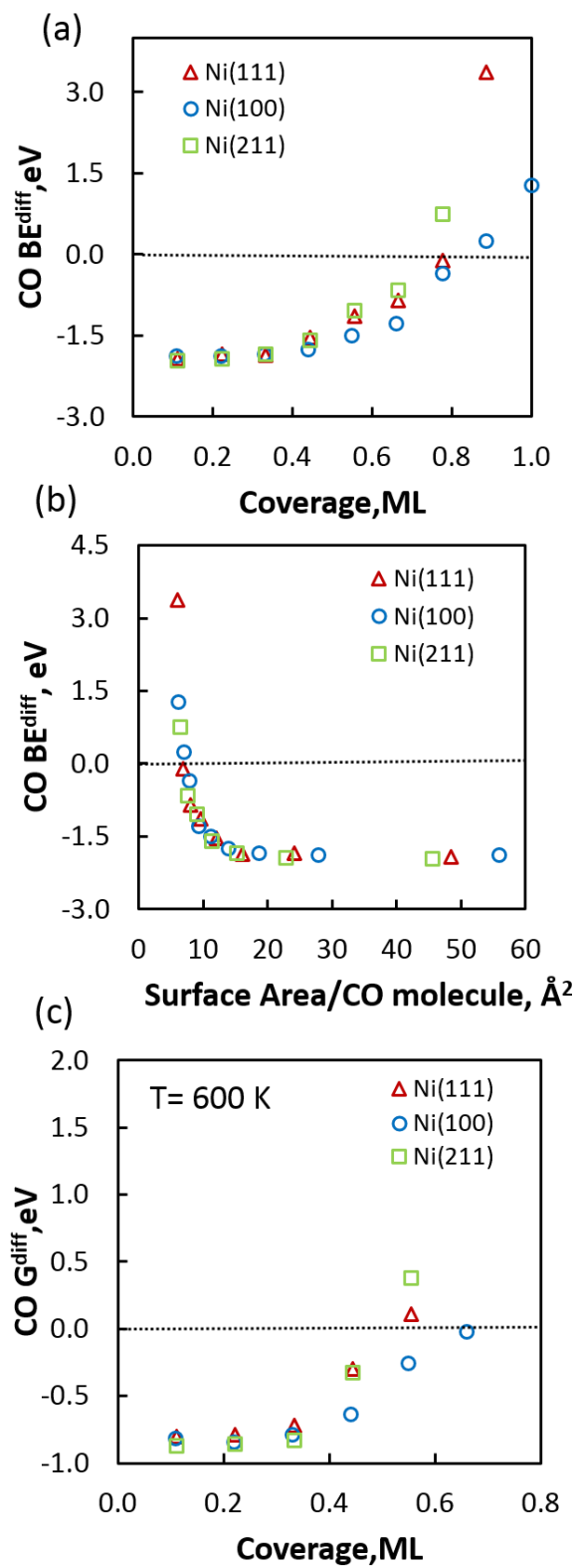


Figure 6.2. (a) Coverage-dependent CO differential binding energies (BE^{diff}) on Ni(111),

Ni(100), and Ni(211) surfaces. (b) CO BE^{diff} as a function of surface area per CO molecule on Ni(111), Ni(100), and Ni(211) surfaces. (c) Coverage-dependent differential CO free energy difference ($G^{diff}(\theta)$) on Ni(111), Ni(100), and Ni(211) surface. The dashed line indicates that the BE^{diff} or G^{diff} is at 0 eV, corresponding to the *saturation* coverage.

On Ni(111), BE^{diff} (in red triangles) remains flat up to the 1/3 ML coverage, and each CO is able to adsorb at their preferred hcp site. This indicates that CO experiences little repulsion from its neighboring CO molecules. Starting from the 4/9 ML coverage, BE^{diff} shows a noticeable indication that the thermodynamic driving force for additional CO adsorption becomes weaker due to the repulsive lateral interactions from the pre-adsorbed CO. This behavior has been captured with empirical relationships, such as Equations (48) and (49), in the literature,^{5,6} and confirms the *piece-wise* behavior of adsorption energy discussed previously.^{1,3} In principle, it is also possible to understand the range of the CO lateral repulsive force this way. At 8/9 ML, the BE^{diff} becomes positive, which suggests the CO adsorption at this high coverage becomes unfavorable.

On Ni(100), the BE^{diff} of CO (in blue circles in [Figure 6.2\(a\)](#)) remains relatively flat up until the 4/9 ML coverage, then increases at higher coverages. However, BE^{diff} increases at a slower pace than that on Ni(111), suggesting that the CO adsorbate-adsorbate interaction is not as repulsive as on the most close-packed nickel single crystal facet. This can be rationalized by the fact that, on a more open surface, the geometric locations of adsorbed CO molecules, determined by their chemisorption sites (4-fold, bridge), can facilitate the mitigation of the repulsive CO-CO interaction. The BE^{diff} maintains negative until the 8/9 ML coverage.

On Ni(211), the BE^{diff} of CO (in green squares in [Figure 6.2\(a\)](#)) increases discernibly starting from the 1/3 ML coverage. At the step edge of Ni(211), the unique alternating zigzag pattern helps effectively minimize the lateral interaction, even though the CO intermolecular distance (2.96 Å) is shorter than that (4.33 Å) on Ni(111). Above the 1/3 ML coverage threshold, BE^{diff} increases quickly, suggesting a rapid increase of the repulsive interactions similar to the trend on Ni(111). In this case of Ni(211), CO will have to adsorb at the much less stable (211) terrace sites once the edge sites have been occupied. On Ni(211), beyond 7/9 ML, additional CO adsorption will then destabilize the slab surface, therefore, the BE^{diff} corresponding to the 8/9 and 1 ML coverages are not included.

The CO self-interaction parameters are obtained by fitting the calculated DFT results to Equation (52) on Ni(111), Ni(100), and Ni(211) surfaces. In this case, the CO self-interaction parameters are 1.54 on Ni(111), 1.16 on Ni(100), and 2.09 on Ni(211). These CO self-interaction parameters are used in the micro-kinetic modeling in section 6.4 and section 6.5 to study the effect of considering CO self-interaction for hydrogen production.

The entropies of CO chemisorptions have also been considered, and the differential CO adsorption energies (G^{diff}) at 600 K are shown in [Figure 6.2\(c\)](#). At 600 K, CO chemisorption at 5/9 ML coverage on Ni(111) and Ni(211) become thermodynamically unfavorable, therefore, the 4/9 ML coverage was adopted for the analyses of H₂O-CO, H-CO, O-CO, OH-CO, and COOH-CO pair interaction in Section 6.3.2.

As in [Figure 6.2\(a\)](#), it can be seen that the coverage dependence of CO-CO lateral interactions are intrinsically weaker on Ni(100) compared to that on Ni(111) and Ni(211). This can be intuitively understood from the fact that Ni(100) enables larger CO separation from its neighbors due to its open surface structure. In [Figure 6.2\(b\)](#), BE^{diff} is plotted against the surface

area per adsorbed CO molecule ($\text{\AA}^2/\text{CO}$). It can be noted that BE^{diff} collapses into a single trend, where BE^{diff} quickly decreases first and then approaches an asymptotic value at c.a. 15 $\text{\AA}^2/\text{CO}$ molecule. This pattern suggests a universal chemical nature for CO-CO repulsion.

6.3.2 Lateral Interactions between CO and Other Species

In this section, the adsorption structures and energies of reaction intermediates involved in the relevant WGS redox and carboxyl pathways, i.e., H_2O , H, OH, O, and COOH on the (111), (100), and (211) facets, were obtained at the 4/9 ML CO coverage, as shown in [Figure 6.3](#).

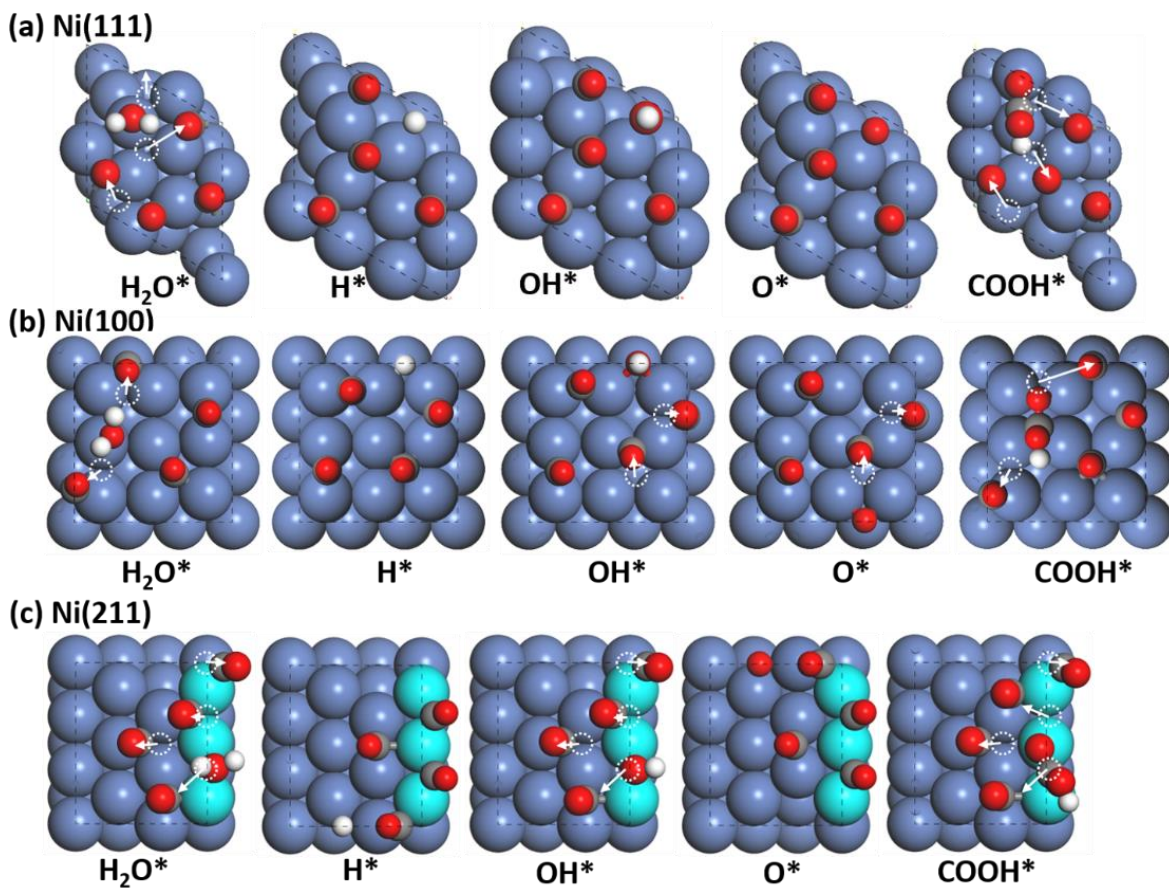


Figure 6.3. Top views of optimized H_2O , H , OH , O , and COOH on (a) $\text{Ni}(111)$, (b) $\text{Ni}(100)$, and (c) $\text{Ni}(211)$ at $4/9$ ML CO coverage. The white dash circles indicate the original CO locations, and the white arrows indicate the moving direction of CO to the new locations once co-adsorbed H_2O , H , OH , O , and COOH are introduced.

On $\text{Ni}(111)$, H_2O adsorbs at the top site (Figure 6.3(a)), which is the preferred site at low coverage limit (i.e., $1/9$ ML) as shown in Chapter 3 section 3.3. One of its O–H bonds points at one neighboring CO molecule, the distance between the H and O atoms is 1.86 \AA , and thus suggesting an intermolecular hydrogen bond-type structure, usually at a distance of $1.97\text{--}1.98 \text{ \AA}$. In addition, three surrounding CO molecules have been pushed away to new locations in order to

accommodate this H₂O molecule, as illustrated by the white dashed circles and arrows in [Figure 6.3\(a\)](#). H, OH, and O bind at the 3-fold fcc site, also their preferred site. However, the neighboring CO molecules remain at their original positions. COOH also binds at the bridge site. Among the reaction intermediates, COOH is the most bulky molecule. As illustrated in [Figure 6.3\(a\)](#), three CO molecules have been displaced. As a result, the OH group of COOH points at one neighboring CO molecule, the distance between the H and O atoms is 2.05 Å, again suggesting the existence of intermolecular hydrogen bonding.

On Ni(100), H₂O adsorbs on the top site, with two CO molecules near H₂O are simultaneously displaced to new sites, as indicated in [Figure 6.3\(b\)](#). The intermolecular hydrogen bond structure is formed with one H atom in H₂O to O atom in neighboring CO separated at 2.09 Å. H, OH, and O are still able to bind at their preferred 4-fold site. However, for OH and O, two CO molecules are displaced to new locations, i.e., the bridge and 4-fold sites. COOH adsorbs at the 4-fold site by dislocating two CO molecules from their current bridge sites to a new bridge and 4-fold site, respectively.

On Ni(211), H₂O binds at the bridge site near edge, by displacing one CO to the fcc site near edge site, as shown in [Figure 6.3\(c\)](#). It can also be noted that the distance between the H atom in H₂O and the O atom in one nearby CO molecule is 1.61 Å, indicating possible intermolecular hydrogen bonding. H now binds at the fcc site at the Ni(211) terrace, instead of competing against the CO molecules for their preferred hcp site near edge. Also, there is no CO molecule that has been displaced by the H atom. The same pattern has been observed for O, which also binds at the fcc site on the Ni(211) terrace. Both OH and COOH are able to bind at their preferred bridge site. The H atom in COOH points to one of the nearby CO molecules, and the distance between H and O atoms is 1.75 Å indicating a hydrogen bond-like structure.

The comparisons of the binding energies of H₂O, OH, H, O, and COOH on Ni(111), Ni(100), and Ni(211) surface at 4/9 ML CO coverage and those without pre-adsorbed CO are listed in **Table 6.1**. The nature of the pair interactions is repulsive on Ni(111) at the CO coverage of 4/9 ML, as shown in the comparisons summarized in **Table 6.1** between BE_{A-4CO} and corresponding BE_A , for reaction intermediates except H₂O. In addition, CO, O, and COOH experience the most repulsive interactions (~0.80 eV). OH also experiences moderate repulsive interactions, which decreases the OH binding energy by approximately 0.55 eV. The BE_H is least affected due to its small atomic size, as proven in previous literature,² and is weakened by only approximately 0.06 eV. The adsorption of H₂O is instead enhanced by 0.05 eV in the presence of pre-adsorbed CO molecules due to the intermolecular hydrogen bonding.

Table 6.1. Binding energies (in eV) of CO, H₂O, OH, H, O, and COOH on Ni(111), Ni(100) and Ni(211) without pre-adsorbed CO and at 4/9 ML CO coverage. The italicized numbers highlight the BE_{A-4CO} enhanced by co-adsorbed CO molecules.

	Ni(111)		Ni(100)		Ni(211)	
	BE_A	BE_{A-4CO}	BE_A	BE_{A-4CO}	BE_A	BE_{A-4CO}
CO	-1.93	-1.15	-1.88	-1.45	-1.97	-1.04
H ₂ O	-0.27	-0.32	-0.36	<i>-0.46</i>	-0.55	-0.39
OH	-3.27	-2.72	-3.43	-3.16	-3.78	-2.94
H	-2.80	-2.74	-2.73	-2.76	-2.82	-2.74
O	-5.39	-4.58	-5.61	-5.11	-5.57	-4.81
COOH	-2.25	-1.43	-2.69	-2.14	-2.18	-1.37

On Ni(100), the adsorbate-adsorbate interactions are also repulsive, except for H₂O and H, with their binding energies increased by 0.1 eV and 0.03 eV, respectively. Similar to the CO-CO lateral interactions, the repulsions between CO and each considered reaction intermediates are to a smaller extent compared to those on Ni(111). The BE_O and BE_{COOH} are weakened the most, by 0.5 and 0.55 eV, respectively, which is followed by CO-CO interactions, which has decreased by 0.43 eV. The BE_{OH} decreases the least, by 0.27 eV.

On Ni(211), the diminished binding energies indicate that all the repulsive nature of CO with the considered reaction intermediates. In particular, the adsorption of H₂O is also weakened 0.16 eV. CO, OH, O and COOH follow this trend with the binding energy decreasing by 0.93 eV, 0.84 eV, 0.76, and 0.81 eV, respectively. The adsorption of H is weakened by 0.08 eV, which is the least affected.

6.4 Impact on Hydrogen Production on Ni(111), Ni(100), and Ni(211) at 4/9ML CO Coverage

6.4.1 Free Energy Diagrams of WGSR

In order to understand how previously established knowledge of the interactions of the WGSR reaction intermediate pairs will affect the reaction activity on these single crystal facets, the free energy diagrams of WGSR incorporating the calculated adsorbate-adsorbate interactions at 600 K, are shown in [Figure 6.4 \(a-c\)](#), respectively. The pre-adsorbed four CO molecules on Ni facets with gas phase H₂O and CO are used as the energy reference (i.e., 0 eV). In this analysis, we primarily focus on the reaction energetics, while assuming the energy barriers of each elementary step remain unchanged, as a first approximation.

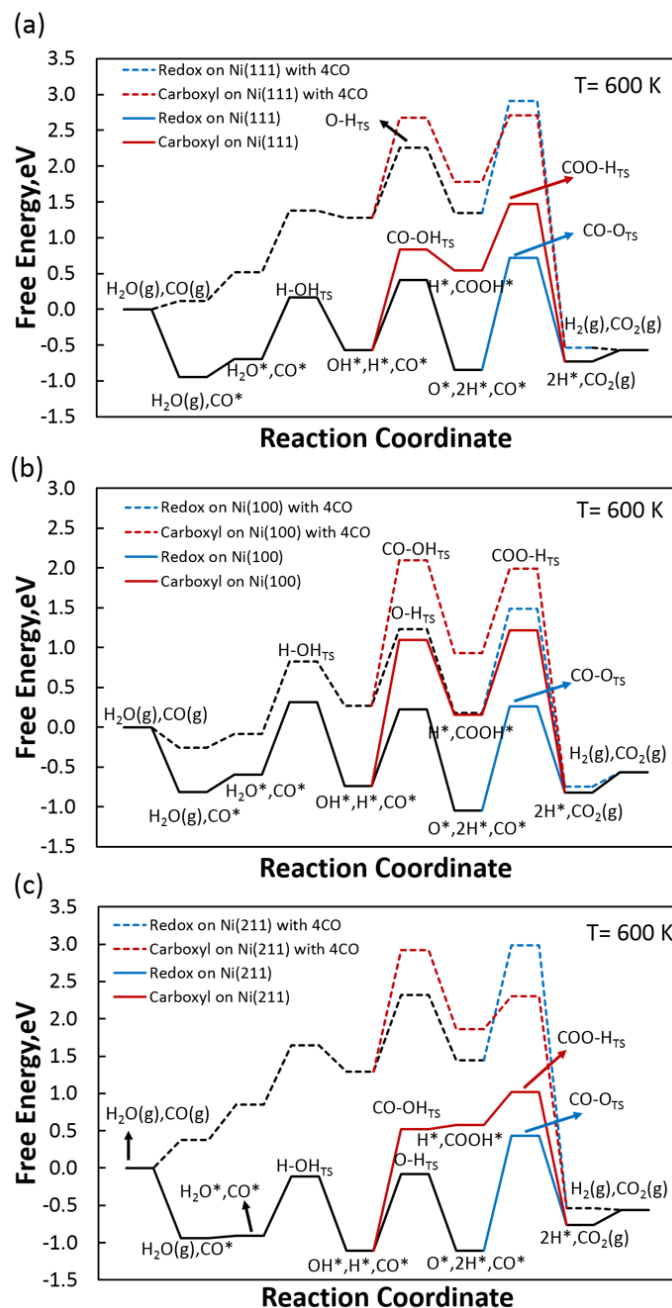


Figure 6.4. Free energy diagrams for redox and carboxyl pathways at 4/9 ML CO coverage on (a) Ni(111), (b) Ni(100), and (c) Ni(211). The solid lines are the original free energies with no pre-adsorbed CO, and the dashed lines corresponding to co-adsorbed 4/9 ML CO. The blue path represents the redox pathway; the red path represents the carboxyl pathway, and the black path represents CO, H₂O adsorption and activation steps, and H₂ formation steps.

As shown in Figure 6.4(a), on Ni(111), the overall free energy surfaces for both redox and carboxyl pathways have become much more endothermic due to the weakened adsorptions of CO and H₂O. Further activations of H₂O, forming OH and O, are also adversely affected (i.e., becoming more endothermic). As a result, the redox pathway loses its competition to become less competitive compared to the carboxyl pathway due to the H₂O activation. On Ni(100), as shown in Figure 6.4(b), the overall free energy upshift as the weakened CO, OH, O, and COOH adsorptions. Nevertheless, the redox pathway still remains competitive against the carboxyl pathway. On Ni(211), the free energies of hydrogen production via the redox and carboxyl pathways again resemble to that on Ni(111). However, unlike Ni(111), though the redox pathways becomes much less competitive compared to the low coverage limit situation represented by the solid lines shown in Figure 6.4(c), it is still competitive with carboxyl pathway.

The above analysis can be used as a basic guideline to understand the activity and selectivity of hydrogen production influenced by the idealized nickel single crystal surface lattice structures. In the next section, micro-kinetic modeling was performed to obtain the turnover frequency (TOF) of H₂ to investigate the role of adsorbate-adsorbate interaction.

6.4.2 Micro-kinetic Modeling

Without consideration of CO lateral interactions, it is predicted that CO will occupy nearly all the open sites on all three single crystal facets. This behavior prevents the surface to reach thermodynamic equilibrium. From DFT calculations, the CO self-interaction parameters on Ni(111), Ni(100), and Ni(211) are found to be 1.54, 1.16, and 2.09, respectively, using Equation (52). These self-interaction parameters were then applied in the micro-kinetic models to compute

hydrogen production rates. A temperature range of 423 ~ 723 K, and a pressure of 1bar with CO and H₂O molar ratio of 1:2 were considered,⁹⁻¹¹ which is the same reaction conditions as the micro-kinetic modeling in Chapter 5 section 5.4.2. A mechanism, consisting of R1–R8 (see Section 5.4.2), was used.

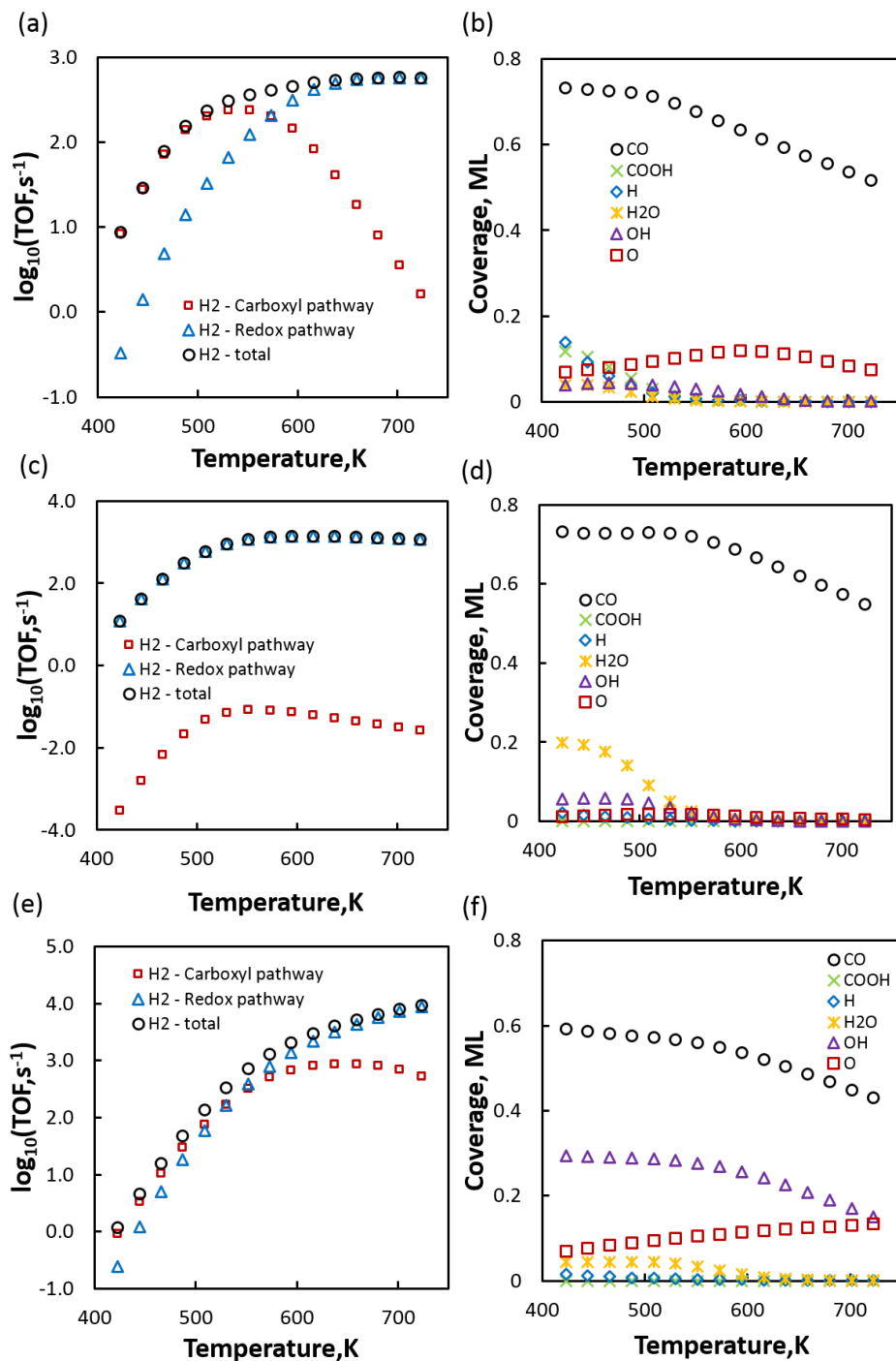


Figure 6.5. The TOF of H₂ production on (a) Ni(111), (c) Ni(100), and (e) Ni(211) at 1 bar. The predicted reaction intermediates coverages on (b) Ni(111), (d) Ni(100), and (f) Ni(211). The feed has a molar ratio of CO:H₂O = 1:2.

The H_2 production TOF (in s^{-1}) of and surface coverage of main intermediates on Ni(111), Ni(100), and Ni(211) are shown in Figure 6.5. The most significant change is that, with CO self-interaction, CO coverages are revised and lowered down to a range of 0.4 - 0.75 ML on Ni(111), Ni(100), and Ni(211) surfaces. On Ni(111), as shown in Figure 6.5(a), the carboxyl pathway contributes to nearly all the H_2 production when the temperature is below 550 K. Above this temperature, the redox pathway becomes more competitive quickly, and dominates H_2 production after reaching 570 K. This behavior can be understood by examining Figure 6.5(b), where COOH and O coverage (other than CO) are the main surface species at the low and high temperature regimes, corresponding to carboxyl and redox pathways, respectively.

A different trend is noted on Ni(100), where redox remains as the main route for H_2 production throughout the temperature range, as shown in Figure 6.5(c). From Figure 6.5(d), it is shown that H_2O adsorption and activation should be strengthened.

Thirdly, on Ni(211) surface, the trend resembles more to Ni(111), where the carboxyl pathway is slightly more favored at temperatures below 530 K. Above 530 K, the redox pathway becomes more favorable. This observation can be explained by Figure 6.5(f) that OH (other than CO) coverage becomes abundant surface species at low temperature, which takes part in the carboxyl pathway. Figure 6.6 compares the total H_2 production rate on Ni(111), Ni(100), and Ni(211) surfaces. At the temperature below about 570 K, the H_2 production rate is higher on the open flat surface, such as Ni(100), than on the stepped surface, e.g., Ni(211). Above 570 K, this trend is reversed. The possible reason is CO self-interaction parameter on Ni(211) surface is larger than that on Ni(111) and Ni(100) surfaces, which weakens the CO binding strength too much on Ni(211) surface and leads to insufficient CO adsorbed on the surface. Therefore, the WGS activity on Ni(211) activity is lowered at low temperatures.

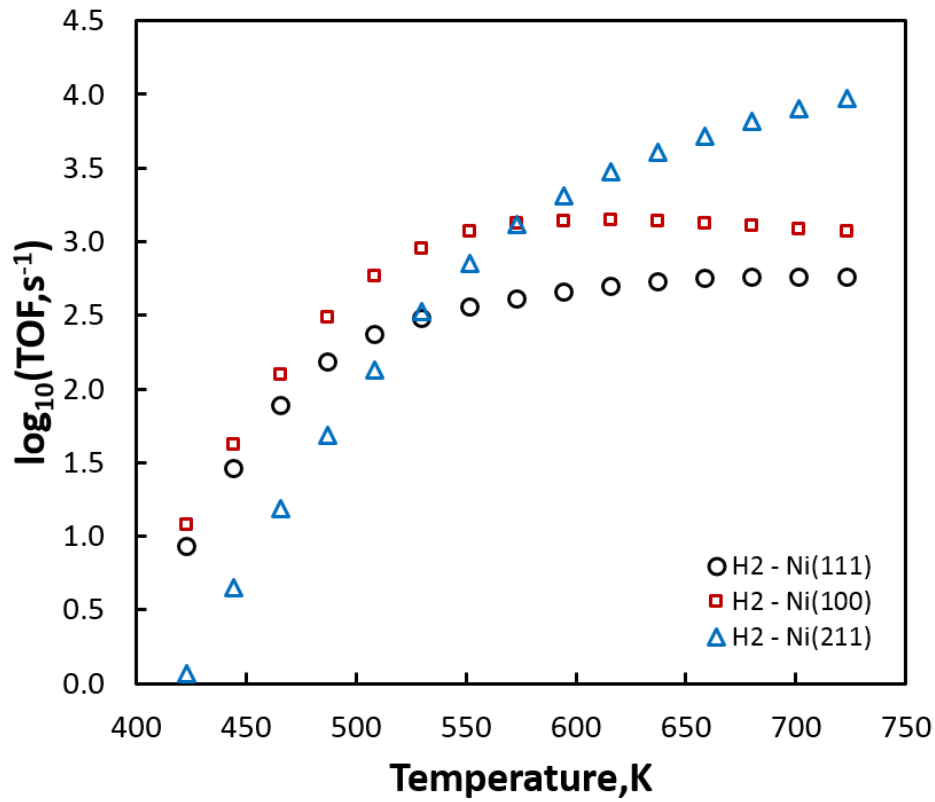


Figure 6.6. Comparison of H₂ production TOFs on Ni(111), Ni(100), and Ni(211). The feed has a molar ratio of CO: H₂O = 1:2.

6.4.3 Reaction Orders from Micro-kinetic Modeling

The reaction rate of WGSR can be expressed with Equation (57)¹²:

$$r = k P_{CO}^a P_{H_2O}^b P_{CO_2}^c P_{H_2}^d, \quad (57)$$

where a, b, c, and d are the reaction orders of CO, H₂O, CO₂ and H₂, respectively. k is the rate coefficient. P_{CO} , P_{H_2O} , P_{CO_2} , and P_{H_2} are the pressure of CO, H₂O, CO₂, and H₂.

The reaction orders of CO, H₂O, CO₂ and H₂ are calculated through micro-kinetic modeling. When calculating the reaction order of CO, the pressure of CO varies with fixed pressures of other species (i.e. H₂O, CO₂, and H₂) at 600 K. Similar procedures are performed to calculate the reaction orders of H₂O, CO₂, and H₂. **Table 6.2** shows the reaction orders of CO, H₂O, CO₂ and H₂ on Ni(111), Ni(100), and Ni(211) surfaces. The Ni(111) surface shows a CO reaction order of 0.05, a H₂O reaction order of 0.77, a CO₂ reaction order of 0, and a H₂ reaction order of -0.60. The Ni(100) surface shows a CO reaction order of -0.12, a H₂O reaction order of 0.53, a CO₂ reaction order of -0.01, and a H₂ reaction order of -0.57. The Ni(211) surface shows a CO reaction order of 0.21, a H₂O reaction order of 0.05, a CO₂ reaction order of 0, and a H₂ reaction order of -0.42. The CO reaction order is somewhat positive on Ni(111) and Ni(211) from micro-kinetic modeling unlike the CO reaction order of -0.14 ± 0.05 from experimental study¹³, which is likely due to the larger calculated CO self-interaction parameters on Ni(111) and Ni(211) surfaces with predicting too low CO coverage. A good agreement of H₂O reaction order between experiment results (0.62 ± 0.11)¹³ and our DFT-based micro-kinetic model on all Ni surfaces are observed.

Table 6.2. Reaction orders of CO, H₂O, CO₂ and H₂ (*a*, *b*, *c*, *d*) obtained from micro-kinetic modeling on Ni(111), Ni(100), and Ni(211), respectively.

Surface	<i>a</i>	<i>b</i>	<i>c</i>	<i>d</i>
Ni(111)	0.05	0.77	0	-0.60
Ni(100)	-0.12	0.53	-0.01	-0.57
Ni(211)	0.21	0.05	0	-0.42

6.5 Hydrogen Productions on Other Transition Metals

Besides Ni, other transition metals (e.g., Cu, Au, Pt) also show reasonable activities for WGSR. In this section, we also studied the WGSR on Cu(111), Cu(211), Au(111), Pt(111) surfaces. A general trend (volcano plot) of WGSR activity on different transition metals will be generated using CO and H₂O as descriptor. These theoretical results will finally compare with Grenoble's experimental results¹³. As the carboxyl pathway is found to be the dominant pathway on Cu(111), Pt(111), and Au(111),⁵⁻⁸ R1, R2, R5, R6, R7, and R8 (carboxyl pathway) as shown in Chapter 5 section 5.4.2 are included in the micro-kinetic modeling.

Three-layer Pt(111), Cu(111) and Au(111) with $p(3 \times 3)$ unit cells were used. A three-layer (1×3) supercell was used to model the Cu(211) facet. The other computational details remain the same as for Ni(111) and Ni(211) facets shown in section 6.2.

6.5.1 Adsorption of Reaction Intermediates on Other Transition Metals

The binding energies (BEs) and preferred binding sites of H₂O, CO, OH, H, and COOH are summarized in **Table 6.3** and [Figure 6.7](#). On Pt(111) surface, H₂O, OH, H, and COOH prefer to bind at the top site with respective BEs of -0.23 eV, -2.28 eV, -2.79 eV, and -2.39 eV. CO binds at the fcc site with BE of -1.86 eV. The preferred binding sites for H₂O, CO, OH, H, and COOH on Pt(111) are consistent with ref⁶. On Cu(111) surface, H₂O adsorbs at top site with BE of -0.16 eV, while COOH binds at the off-top site with BE of -1.53 eV. CO*, OH*, and H* prefer to bind at the fcc sites with respective BEs of -0.78 eV, -2.99 eV, and -2.44 eV. The most stable binding sites for H₂O, CO, OH, H, and COOH on Pt(111) are in accordance with ref⁵. On Cu(211) surface, H₂O binds at the top site with BE -0.38 eV and H* binds at the hcp near edge site with BE of -2.60 eV. The most stable adsorption site for other species (i.e. CO*, OH*, and

COOH*) are bridge site on Cu(211) surface. On Au(111) surface, H₂O and COOH bind at the top site with respective BEs of -0.08 eV and -1.28 eV. The most stable binding site for CO on Au(111) is bridge site, which is consistent with ref⁸. And OH prefers to bind at bridge site on Au(111) surface with BE of -1.74 eV. H adsorbs at fcc site on Au(111) surface with BE of -1.98 eV.

Table 6.3. Binding energies (BEs) and site preference of WGSR reaction intermediates on Pt(111), Cu(111), Cu(211), and Au(111) surfaces.

	Pt(111)		Cu(111)		Cu(211)		Au(111)	
	BE [eV]	site	BE [eV]	site	BE [eV]	site	BE [eV]	site
H ₂ O*	-0.23	top	-0.16	top	-0.38	top	-0.08	top
CO*	-1.86	fcc	-0.78	fcc	-1.01	bridge	-0.07	bridge
OH*	-2.28	top	-2.99	fcc	-3.43	bridge	-1.74	bridge
H*	-2.79	top	-2.44	fcc	-2.60	hcp	-1.98	fcc
COOH*	-2.39	top	-1.53	off-top	-1.98	bridge	-1.28	top

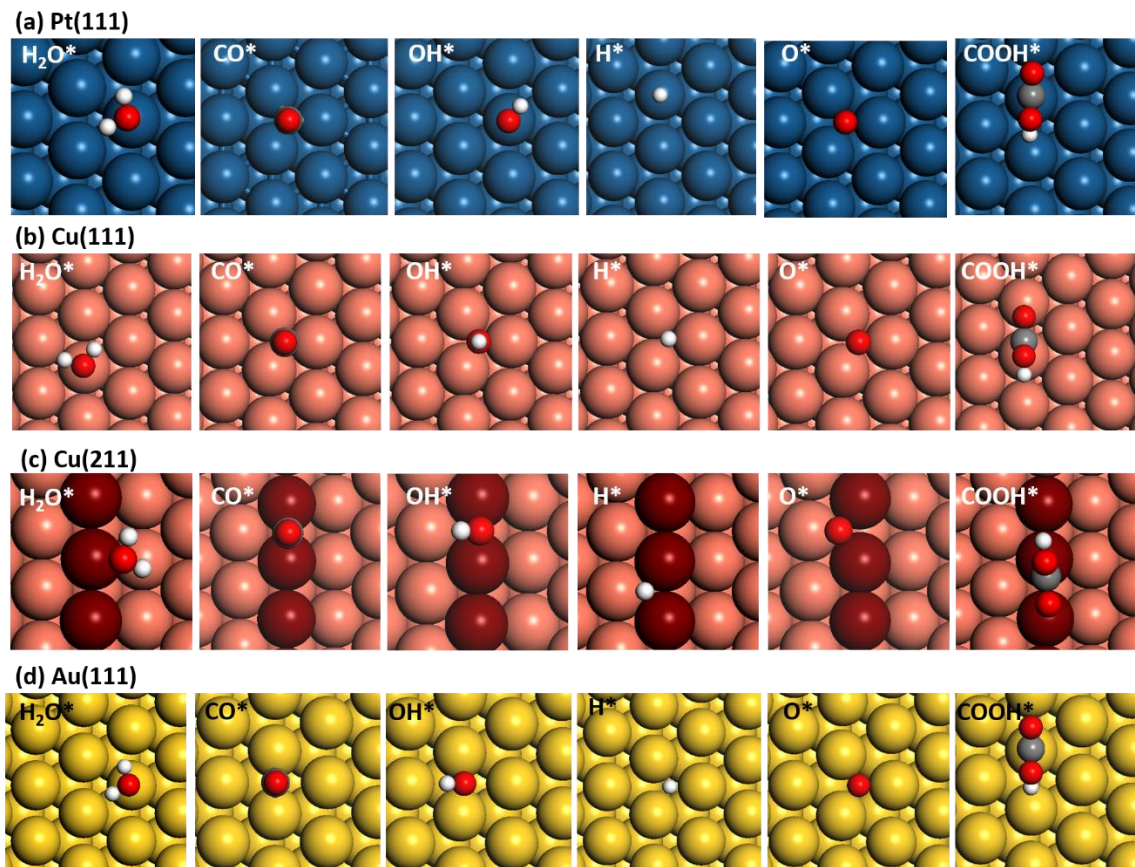


Figure 6.7. Optimized structure of the 6 intermediates for WGSR in **Table 6.3** on (a) Pt(111) surface, (b) Cu(111) surface, (c) Cu(211) surface, and (d) Au(111) surface. The dark blue, pink, and gold atoms represent Pt, Cu, and Au atoms respectively. The edge Cu atoms in Cu(211) surface are highlighted in dark red.

6.5.2 Micro-kinetic Modeling on Transition Metals

The modeling was performed at 573 K, and CO and H_2O partial pressures at 24.3 kPa and 31.4 kPa. This temperature and pressure selection is the same as Grenoble's experimental condition¹³. BEP correlations obtained from Ni(111) (see Chapter 5 section 5.3.2) were employed to estimate transition state energies of C-O bond formation/cleavage and O-H bond formation/cleavage steps on Pt(111), Cu(111), Cu(211), and Au(111) surfaces. [Figure 6.8](#) shows

the two-dimensional volcano plots of TOF of hydrogen without considering CO self-interaction, and [Figure 6.9 presents](#) the predicted CO surface coverage.

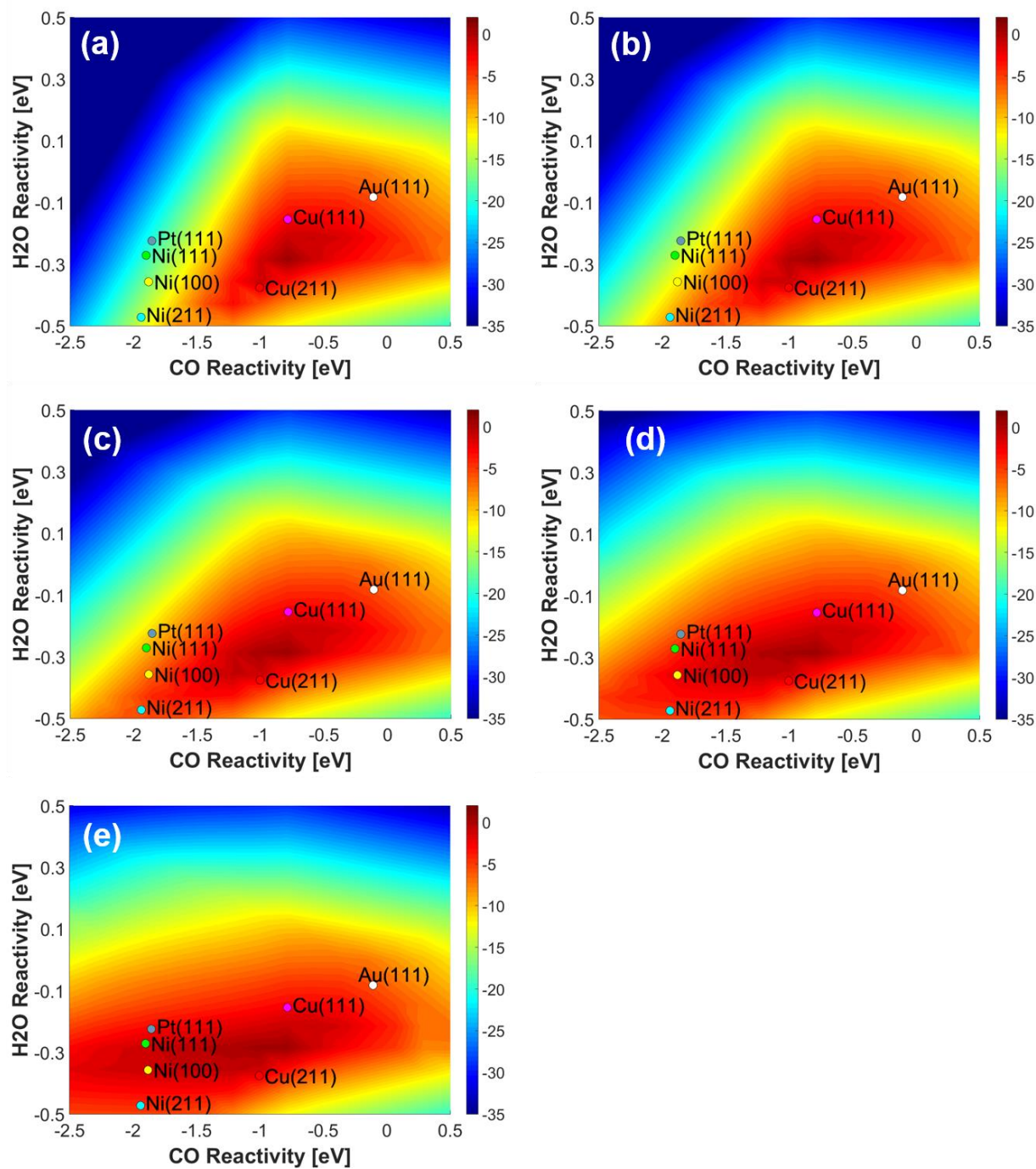


Figure 6.8. The TOF of hydrogen at varying binding energies of CO and H₂O with (a) no CO self-interaction, (b) $\frac{1}{4}$ CO self-interaction, (c) $\frac{1}{2}$ CO self-interaction, (d) $\frac{3}{4}$ CO self-interaction, and (e) full CO self-interaction included at T = 573 K, P_{CO} = 24.3 kPa and P_{H₂O} = 31.4 kPa.

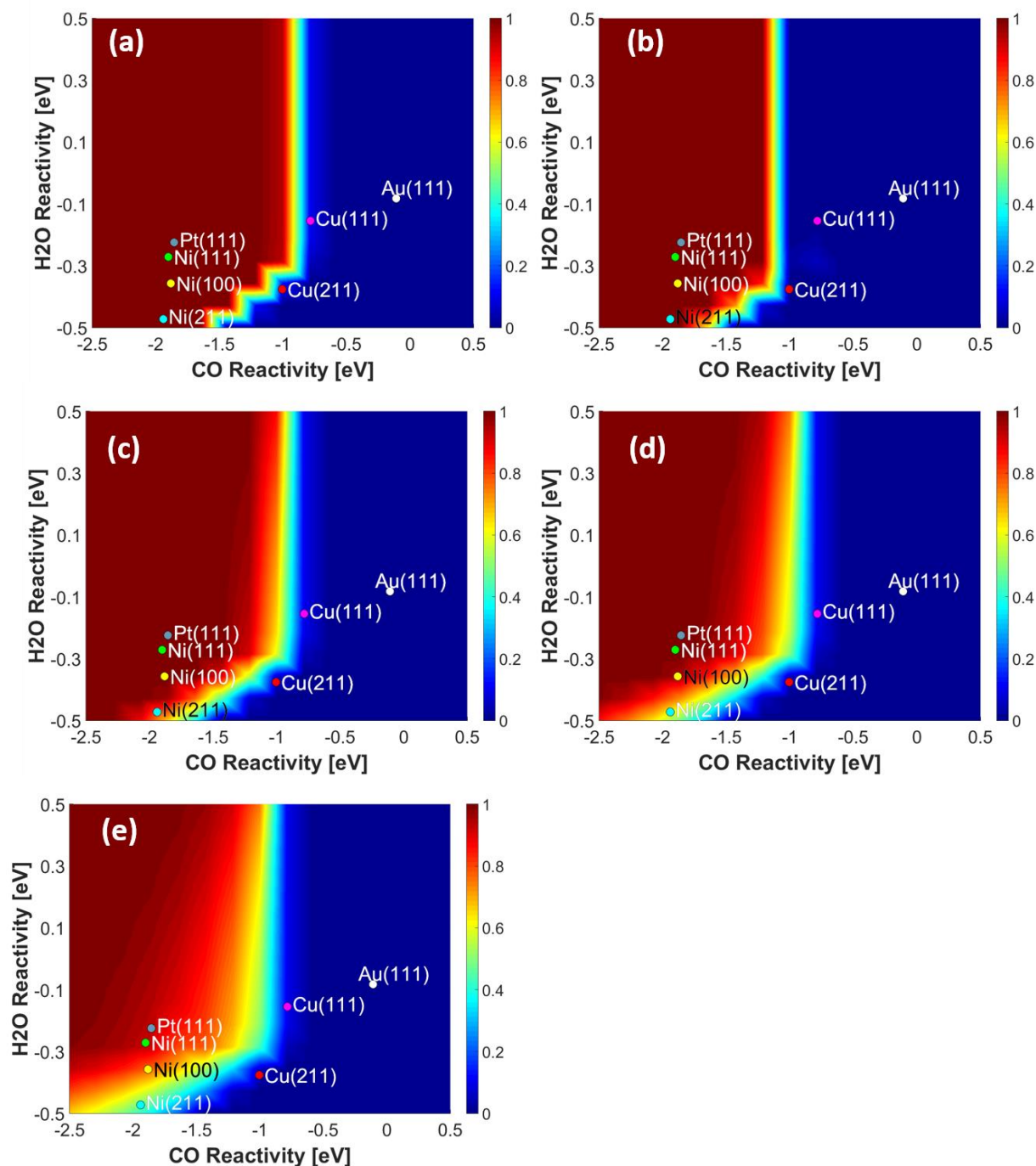


Figure 6.9. The predicted CO coverage as a function of CO and H₂O binding energies, with (a) no CO self-interaction, (b) $\frac{1}{4}$ CO self-interaction, (c) $\frac{1}{2}$ CO self-interaction, (d) $\frac{3}{4}$ CO self-interaction, and (e) full CO self-interaction included at $T = 573$ K, $P_{\text{CO}} = 24.3$ kPa and $P_{\text{H}_2\text{O}} = 31.4$ kPa.

From Figure 6.8(a), both too strong and too weak CO BE to catalysts show low TOF of H₂ production. An optimal strength of CO interaction with surface is required. The trend of activity of the transition metals for WGSR with no CO self-interaction parameter included in micro-kinetic modeling is predicted to be Cu(211) > Cu(111) > Au(111) > Ni(211) > Ni(100) > Ni(111) > Pt(111). The predicted CO coverage on Pt(111), Ni(111), Ni(100), and Ni(211) surfaces in Figure 6.9(a) are nearly 1 ML that poison those surfaces with low WGSR activity. Therefore, CO self-interaction parameters for Pt(111), Ni(111), Ni(100), and Ni(211) surfaces are necessary for the micro-kinetic modeling. The CO self-interaction parameters on Au(111), Cu(111), and Cu(211) surface can be neglected as the low CO coverages observed in Figure 6.9(a).

DFT calculations were performed with different CO coverages on Pt(111) surface to calculate the only unknown CO self-interaction parameter on Pt(111). The results are shown in **Appendix D**. Through fitting to the DFT data using Equation (52), the CO self-interaction parameter is 1.70 on Pt(111) surface, which is added to the micro-kinetic modeling.

Figure 6.8(e) shows the TOF of hydrogen with considering full CO self-interaction on Pt(111), Ni(111), Ni(100), and Ni(211) surfaces, and Figure 6.9(e) are the corresponding CO coverages. When considering full CO self-interactions, the estimated trend of the WGSR activity for transition metals is predicted to be Ni(100) > Ni(111) > Cu(211) > Cu(111)~Pt(111) > Ni(211) > Au(111). The catalyst reactivity of Ni and Pt surfaces increase and the predicted CO coverage decrease when considering full CO self-interaction, which means that Ni and Pt can be active WGSR catalyst if CO poison can be relieved.

However, in reality, the CO coverage on catalyst surface is unlikely to be uniform. Some locations may have high CO density, where consideration of CO self-interactions is

necessary. Thus, the CO self-interaction parameter on a real catalyst surface can vary in an experimental condition. To mimic experiment conditions, CO self-interaction parameters can vary (not a constant value) in micro-kinetic modelings for quantitative analysis of WGSR reactivity trend on different transition metals. Figure 6.8(b-d) present the TOFs of hydrogen production with varying CO self-interaction parameters, and the predicted CO coverages are shown in Figure 6.9(b-d). At $\frac{1}{4}$ of the original CO self-interaction parameter, micro-kinetic predicted WGSR activity trend on transition metals follows $\text{Cu}(211) > \text{Cu}(111) > \text{Au}(111) > \text{Ni}(211) > \text{Ni}(100) > \text{Ni}(111) > \text{Pt}(111)$, the same trend as that without considering CO self-interaction. When $\frac{1}{2}$ of the original CO self-interaction parameter was used, the predicted WGSR activity order changed to: $\text{Cu}(211) > \text{Cu}(111) > \text{Au}(111) \sim \text{Ni}(211) > \text{Ni}(100) > \text{Ni}(111) > \text{Pt}(111)$. With $\frac{3}{4}$ of the original CO self-interaction parameter used, the WGSR trend change to $\text{Cu}(211) \sim \text{Ni}(100) > \text{Cu}(111) > \text{Ni}(111) > \text{Ni}(211) \sim \text{Pt}(111) > \text{Au}(111)$. Overall, the strong CO binding sites become more active when more pronounced CO self-interactions are considered.

Experimentally, Grenoble et al.¹³ proposed that the trend of WGSR activity on transition metals to be $\text{Cu} > \text{Ni} > \text{Pt} > \text{Au}$ at 573 K with a feed gas containing $P_{\text{CO}} = 24.3$ kPa and $P_{\text{H}_2\text{O}} = 31.4$ kPa. The micro-kinetic models predict a better WGSR trend when considering larger fraction of CO self-interaction up to $\frac{3}{4}$ CO self-interaction.

In this work, only CO self-interactions were considered in the micro-kinetic model. Other lateral interactions, such as self-interactions of OH species, or cross-interaction between CO and OH are believed to influence the prediction from micro-kinetic modeling. Further studies focused on this topic will further advance the capability and accuracy of kinetic modeling techniques.

6.6 Conclusions

Periodic density functional theory calculations have been performed in this study to investigate the adsorbate–adsorbate interactions between the CO–CO, CO–H₂O, CO–OH, CO–H, CO–O, and CO–COOH pairs on Ni(111), Ni(100), and Ni(211). The nature of these pair interactions is repulsive except for H₂O and H. In these exceptions, H₂O adsorptions on Ni(111) and Ni(100) are enhanced by approximately 0.05– 0.1 eV because of the intermolecular hydrogen bonding, and H binding energy increases by 0.03 eV on Ni(100). On Ni(111) and Ni(211), it has been found that the CO–CO, CO–O, CO–OH, and CO–COOH pair interactions are strongly repulsive, where the binding energies are destabilized by 0.5– 1.0 eV, while the CO–H interaction is the least repulsive. On Ni(100), the adsorbate–adsorbate interaction is comparably weaker because of the open lattice structure. When the CO BE^{diff} is plotted as a function of the surface area per adsorbed CO molecule, BE^{diff} on all facets collapse into a single trend, suggesting a universal chemical nature for CO–CO interactions.

The adsorbate–adsorbate interaction is also considered in the micro-kinetic modeling at 1 bar and feed composition of CO: H₂O = 1:2. A reaction mechanism transfer from carboxyl pathway to redox pathway is observed with elevated temperature on Ni(111) and Ni(211) surfaces. On Ni(100) surface, the redox pathway remains competitive against the carboxyl pathway. Overall, the H₂ production rate is the highest on Ni(100) at the temperature below ~570 K and above ~570 K, Ni(211) surface has the highest H₂ production rate. The calculated reaction order of CO and H₂O are in good agreement with the experimental results, as well.

Adsorbate-adsorbate effect to catalytic activity of various transition metals to WGSR was also studied. The results show that the WGSR activity increasing at the strong CO binding metals

when considering CO self-interaction. In addition, Ni and Pt catalysts can become active if the CO poison can be relieved.

This study once again confirmed the effect of intermolecular interactions of surface adsorbates to catalyst activity. We also note that more sophisticated intermolecular interactions can be developed to generate an unblemished volcano plot for predicting WGS catalyst activity and designing new WGS catalyst with high precision.

6.7 Acknowledgments

This contribution was identified by Session Chair, Hongliang Xin (Virginia Tech), as the Best Presentation in the “Computational Chemistry for Energy Production” session of the ENFL Division at the 2016 ACS Fall National Meeting in Philadelphia, PA. M.Z. and B.L. acknowledge the start-up fund provided by Kansas State University, the National Science Foundation under Award No. EPS-0903806, and matching support from the State of Kansas through the Kansas Board of Regents for financial support. The authors are also grateful for the supercomputing resources and services from the Center for Nanoscale Materials (CNM) supported by the Office of Science of the U.S. Department of Energy under Contract No. DE-AC02-06CH11357; the Beocat Research Cluster at Kansas State University, which is funded in part by NSF Grant CNS-1006860; and the National Energy Research Scientific Computing Center (NERSC) under Contract No. DE-AC02-05CH11231.

References

1. Grabow, L. C.; Hvolbæk, B.; Nørskov, J. K. Understanding trends in catalytic activity: the effect of adsorbate-adsorbate interactions for Co oxidation over transition metals. *Top. Catal.* **2010**, *53*, 298-310.
2. Lausche, A. C.; Medford, A. J.; Khan, T. S.; Xu, Y.; Bligaard, T.; Abild-Pedersen, F.; Nørskov, J. K.; Studt, F. On the effect of coverage-dependent adsorbate-adsorbate interactions for CO methanation on transition metal surfaces. *J. Catal.* **2013**, *307*, 275-282.
3. Yang, N.; Medford, A. J.; Liu, X.; Studt, F.; Bligaard, T.; Bent, S. F.; Nørskov, J. K. Intrinsic selectivity and structure sensitivity of rhodium catalysts for C₂₊ oxygenate production. *J. Am. Chem. Soc.* **2016**, *138*, 3705-3714.
4. Miller, S. D.; Kitchin, J. R. Relating the coverage dependence of oxygen adsorption on Au and Pt fcc(1 1 1) surfaces through adsorbate-induced surface electronic structure effects. *Surf. Sci.* **2009**, *603*, 794-801.
5. Gokhale, A. A.; Dumesic, J. A.; Mavrikakis, M. On the mechanism of low-temperature water gas shift reaction on copper. *J. Am. Chem. Soc.* **2008**, *130*, 1402-1414.
6. Grabow, L. C.; Gokhale, A. A.; Evans, S. T.; Dumesic, J. A.; Mavrikakis, M. Mechanism of the water gas shift reaction on Pt: First principles, experiments, and micro-kinetic modeling. *J. Phys. Chem. C* **2008**, *112*, 4608-4617.
7. Tang, Q.; Chen, Z.; He, X. A theoretical study of the water gas shift reaction mechanism on Cu(1 1 1) model system. *Surf. Sci.* **2009**, *603*, 2138-2144.
8. Zhao, Z. -.; Li, Z.; Cui, Y.; Zhu, H.; Schneider, W. F.; Delgass, W. N.; Ribeiro, F.; Greeley, J. Importance of metal-oxide interfaces in heterogeneous catalysis: A combined DFT, micro-kinetic, and experimental study of water-gas shift on Au/MgO. *J. Catal.* **2017**, *345*, 157-169.

9. Huang, S.; Lin, C.; Wang, J. Trends of water gas shift reaction on close-packed transition metal surfaces. *J. Phys. Chem. C* **2010**, *114*, 9826-9834.
10. Newsome, D. S. Water-gas shift reaction. *Catal Rev Sci Eng* **1980**, *21*, 275-281.
11. Schumacher, N.; Boisen, A.; Dahl, S.; Gokhale, A. A.; Kandoi, S.; Grabow, L. C.; Dumesic, J. A.; Mavrikakis, M.; Chorkendorff, I. Trends in low-temperature water-gas shift reactivity on transition metals. *J. Catal.* **2005**, *229*, 265-275.
12. Goodridge, F.; Quazi, H. Water-gas shift reaction - a comparison of industrial catalysts. *Transactions of the Institution of Chemical Engineers and the Chemical Engineer* **1967**, *45*, T274.
13. Grenoble, D. C.; Estadt, M. M.; Ollis, D. F. The chemistry and catalysis of the water gas shift reaction. 1. The kinetics over supported metal catalysts. *J. Catal.* **1981**, *67*, 90-102.

Chapter 7 - Insights into Catalysis at Catalyst-Support Interfaces

Case study 2 is reproduced in part with permission from:

Zhu, W.; Wu, Z.; Foo, G.; Gao, X.; Zhou, M.; Liu, B.; Veith, G.; Wu, P.; Browning, K.; Lee, H.; Li, H.; Dai, S.; and Zhu, H. “Taming interfacial electronic properties of Pt nanoparticles on vacancy-abundant boron nitride nanosheets for enhanced catalysis”, *Nature Communications*, **2017**, DOI: 10.1038/ncomms15291.

7.1 Introduction

The importance of an appropriate support to catalyst has sparked great interest among researchers. The usage of support should help decrease the total catalyst expense by maintaining the stability and dispersion of main catalyst component, decreasing the amount of costly materials used, and tuning catalytic performance.^{1,2}

Catalyst supports can participate catalytic processes. They may be catalytically active themselves or they may modulate catalyst particle properties. More importantly, new active sites are generated between the metal/support interfaces, which introduce new catalytic properties. These properties can significantly enhance catalyst performance, and should be exploited and taken into consideration in catalyst design.

In this chapter, two reaction models are performed: (a) WGS over Cu/CeO₂ and Ni/CeO₂ catalysts, and (b) CO oxidation over vacancy abundant hexagonal boron nitride nanosheets (h-BNNS) supported Pt nanoparticle to analyse the critical catalytic role of support in the reactions. The adsorptions associated with the reactive intermediates were calculated using DFT to address how the metal/support interface influence the binding of reactive intermediates and therefore affect the catalyst activity.

7.2 Case Study 1: WGS over Cu/CeO₂ and Ni/CeO₂ catalysts

Ceria (CeO₂) is considered to be a beneficial support material for WGS due to its high oxygen storage capacity, rich oxygen vacancy, and the ability to form strong interactions with metal catalyst particles.³ As discussed earlier, water dissociation is a critical step for WGS. Rodriguez et al.⁴ found that ceria is able to enhance WGS activity of Au and Cu nanoparticles dramatically by facilitating water dissociation on its reduced surface. Wang et al.⁵ proposed that water dissociation takes place at the Ov site or at the Cu-Ov interface over the Cu/CeO₂ catalyst. Senanayake et al.⁶ indicated that CeO₂-supported Ni catalysts display higher WGS activity than common industrial WGS catalyst (ZnO supported Cu catalyst), and small Ni coverage (below 0.25 ML) on CeO₂ is particularly efficient for water dissociation of water and catalyzing the carboxyl pathway. Studies by Carrasco et al.⁷ showed that Ni²⁺ sites are generated due to strong metal-oxide support interactions. The presence of Ni²⁺ sites favors water dissociation, which affects the overall WGS activity.

In this section, the behaviors of Cu/CeO₂ and Ni/CeO₂ catalysts to WGS pathways (redox pathway and carboxyl pathway) were investigated using periodic DFT calculations. Adsorptions of reactive intermediates are calculated to generate the potential energies of WGS pathways. The obtained potential energies can be compared with the potential energies on pure Cu(111) surface and Ni(111) surface generated by the data in Chapter 3 and Chapter 6 to find out the critical role of CeO₂ support on Cu and Ni catalysts.

7.2.1 Computational Methods

Spin polarized DFT calculations were performed with the Vienna *ab initio* simulation package (VASP).⁸⁻¹¹ The generalized gradient approximation PBE (GGA-PBE) functional¹² was

employed to describe the electron exchange-correlation energy. The projector augmented wave (PAW) pseudopotential method accounting for O-2s²2p⁴, Ce-5s²5p⁶4f¹5d¹6s², Cu-3d¹⁰4s¹, and Ni-3d⁸4s¹ valence electrons was used. The cutoff energy was set to be 385 eV. The Gaussian smearing technique was utilized to assist numerical convergence with smearing parameter of 0.2. The system was sampled with the single gamma k-point.¹³ In addition, a local on-site Coulomb repulsion term (GGA + U) according to the formulation by Dudarev et al.¹⁴ was employed to account for the strong on-site Coulomb interaction of the Ce 4f electrons. The difference between the Coulomb U and exchange J parameters ($U_{\text{eff}} = U - J$) was set to be 4.5 eV¹⁵ for geometric optimizations, which was calculated self-consistently by Fabris et al.¹⁵ using the linear response approach¹⁶.

Ceria supported Cu and Ni catalysts were modeled with a quasi-one dimensional Cu or Ni ‘nanowire’ supported on a terrace CeO₂ (111) surface, the optimized structures are shown in [Figure 7.1](#). This nanowire configuration provides a rather realistic representation of large (~ several nanometers) catalyst particles with much better-defined step, facet, and peripheral structures near the catalyst-support interface. This concept has been implemented in several recent studies for supported metal catalysts.^{17,18} Due to the quasi-periodic nature, this approach can also be computationally convenient. A three-layer $p(4 \times 2)$ unit cell was used to represent the CeO₂ support. The metal nanowire that is three layers thick and two or three atoms wide is placed on CeO₂ (111) surface.

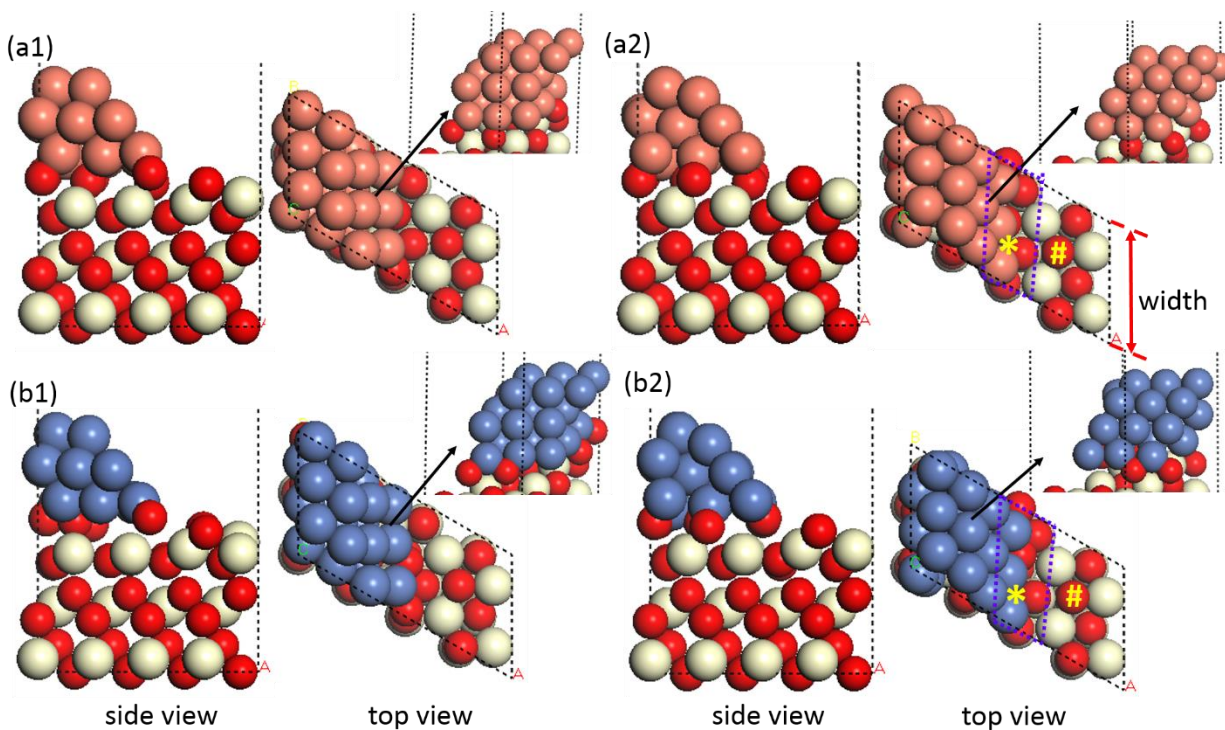


Figure 7.1. Optimized structures of (a1) Cu/CeO₂ and (b1) Ni/CeO₂, and (a2) reconstructed Cu/CeO₂ and (b2) reconstructed Ni/CeO₂. The * and # indicate the two type of adsorption sites considered in the analysis (see details in text). Dashed black lines indicate the boundaries of the supercell. Areas enclosed by purple dashed lines indicate the metal/oxide interface. The red arrow indicates the width of the super cell. Ce, O, Cu, and Ni atoms are depicted in white, red, pink, and blue, respectively.

The right side Cu/CeO₂ or Ni/CeO₂ interface was chosen for reaction modeling. The top layer of CeO₂, the entirety of nanowire, and adsorbate were allowed to relax during optimizations, whereas the bottom two layers of CeO₂ were fixed at the bulk ceria lattice value.

7.2.2 The Structure of Cu/CeO₂ and Ni/CeO₂ Catalysts

After optimizing the pure CeO₂(111) surface, the calculated Ce-Ce distance on the CeO₂(111) surface is 3.826 Å. Thus, for the $p(4 \times 2)$ CeO₂ unit cell, the width of CeO₂ unit cell (defined at Figure 7.1(a2)) is 7.653 Å. After optimizing the pure Cu and Ni nanowires, the calculated Cu-Cu and Ni-Ni distances are 2.556 Å and 2.492 Å, respectively. The widths of Cu and Ni nanowire (defined at Figure 7.1(a2)) for each unit cell will be 7.668 Å and 7.476 Å, respectively. When Cu or Ni nanowire is supported on CeO₂(111) surface, both Cu and Ni nanowires have a size mismatch of about 2.5% with CeO₂(111) surface, indicating a small compressive strain within Cu nanowire, while a small tensile strain in the adsorbed Ni nanowire.

The Cu/CeO₂ and Ni/CeO₂ catalysts were relaxed then without adsorbates, and the optimized structures are shown in Figure 7.1(a1) and Figure 7.1(b1), respectively. However, after adsorption of reaction intermediates, the Cu and Ni nanowires both reconstructed. The most notable difference between the original and reconstructed structure is that the reactive facet of metal wire has shifted from the (100) facet to the close-packed (111) facet. After removing the adsorbate, both Cu/CeO₂ and Ni/CeO₂ retained their new structures. The reconstructed Cu/CeO₂ and Ni/CeO₂ models, shown in Figure 7.1(a2) and Figure 7.1(b2), respectively, are -1.05 eV and -0.67 eV more stable. For the remaining analysis, the reconstructed Cu/CeO₂ and Ni/CeO₂ catalyst models will be used.

When reduced, CeO₂ loses lattice oxygen and produces vacancy sites (Ov). Figure 7.2 shows the optimized structure of Cu/CeO₂ and Ni/CeO₂ catalysts with one Ov. Many studies suggested that Ov in CeO₂ surface promote water dissociations,^{5,19,20} a beneficial effect in WGS. Here, WGS occurring on reduced Cu/CeO₂ and Ni/CeO₂ catalysts will be focused.

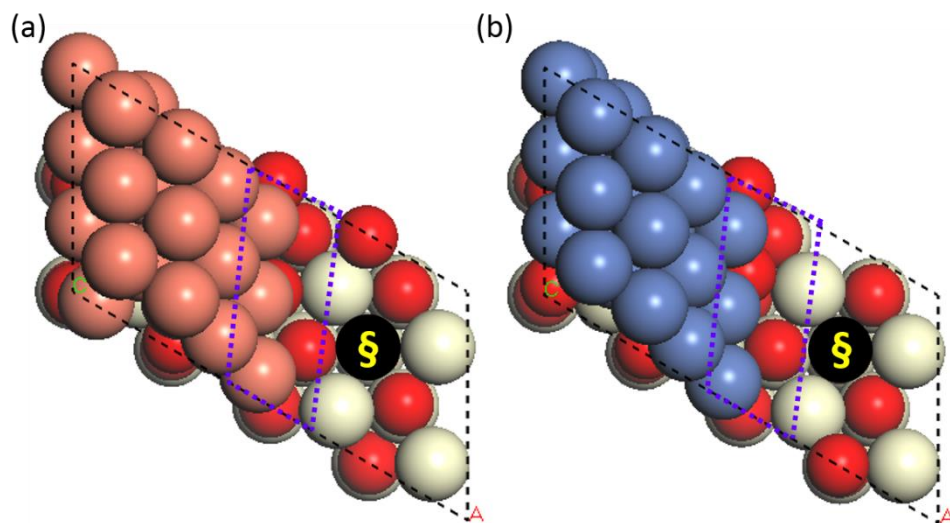


Figure 7.2. Optimized structures of (a) Cu/CeO₂ with Ov and (b) Ni/CeO₂ with Ov. The Ov is highlighted as black dots. The § indicates one type of adsorption sites considered in the analysis (see details in text). Black dashed lines indicate the boundaries of the supercell. Areas enclosed in purple dashed lines indicate the metal/oxide interface.

7.2.3 Adsorption of Reaction Intermediates

Kitchin et al.²¹ and Mehta et al.²² proposed that strain shifts the d-band centers of the metal atoms along the boundary to higher energies, which strength the binding of adsorbates. Besides strain, ligand (bond interactions between metal and support), reorientation of adsorbate, supplementary bonding provided by support can also influence the adsorption energetics, which vary systematically on their own.²² The influence of catalyst support to adsorption energetics are variable, which need to calculate individually for each adsorbate.

Three different sites were employed in Cu/CeO₂ and Ni/CeO₂ catalysts model, where the metal/support interface sites (top, bridge, and 3-fold sites of perimeter Cu or Ni sites, and metal-metal-O hollow sites) are indicated by a ‘*’ symbol in [Figure 7.1\(a2\)](#) and [Figure 7.1\(b2\)](#). The top

site of O atoms on CeO₂ close to the interface is depicted by a ‘#’ symbol in [Figure 7.1\(a2\)](#) and [Figure 7.1\(b2\)](#). The Ov site on CeO₂ close to interface is noted as a ‘§’ symbol in [Figure 7.2](#).

The WGSR mechanism consists of five reaction intermediates (CO*, H₂O§, H#, OH*, COOH*). The binding energies (BEs) of each species adsorbed at preferred sites on Cu/CeO₂ and Ni/CeO₂ are listed in **Table 7.1**, and the respective adsorption structures are shown in [Figure 7.3](#) and [Figure 7.4](#). The BEs of these species on unsupported Cu(111) and Ni(111) surfaces are also listed in **Table 7.1** for comparison.

Table 7.1. Binding energies (BEs) of reaction intermediates on Cu/CeO₂, Ni/CeO₂ catalysts and unsupported Cu(111), Ni(111) surfaces.

	Cu/CeO ₂	Cu(111) [†]	Ni/CeO ₂	Ni(111) [‡]
CO*	-0.85	-0.78	-2.03	-1.93
H ₂ O§	-0.91	-0.16	-0.55	-0.27
H#	-4.83	-2.44	-3.39	-2.80
OH*	-3.22	-2.99	-3.35	-3.27
COOH*	-1.90	-1.53	-1.97	-2.25

[†]Data taken from **Table 6.3** in Chapter 6, and [‡]Data taken from **Table 3.1** in Chapter 3.

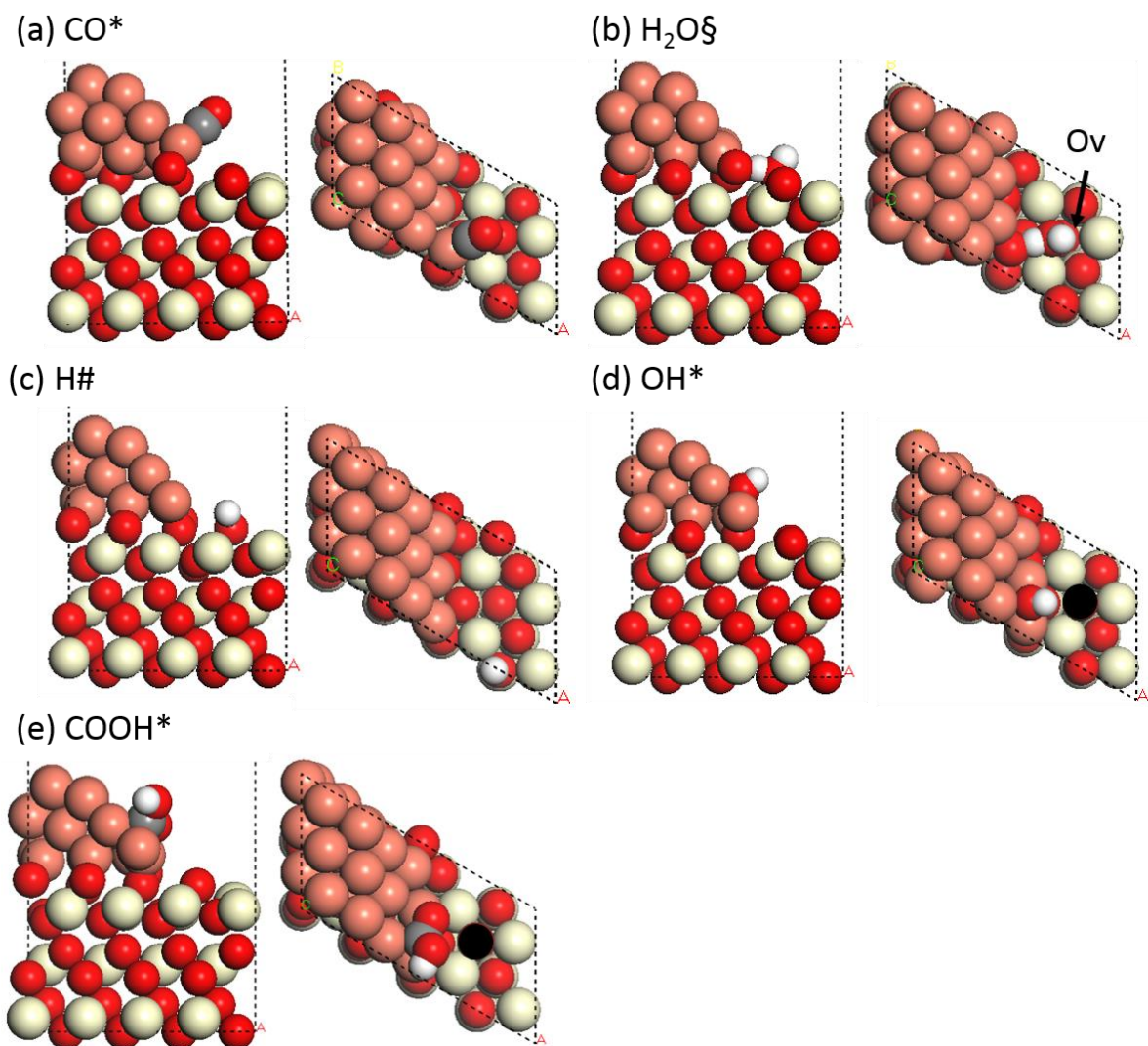


Figure 7.3. Optimized structures of reaction intermediates (a) CO*, (b) H₂O§, (c) H#, (d) OH*, and (e) COOH* (in **Table 7.1**) on Cu/CeO₂ surface. H and C atoms are depicted in white and grey, respectively. The black arrow indicates the position of Ov, which cannot recognize as being overlapped by the adsorbate in (b).

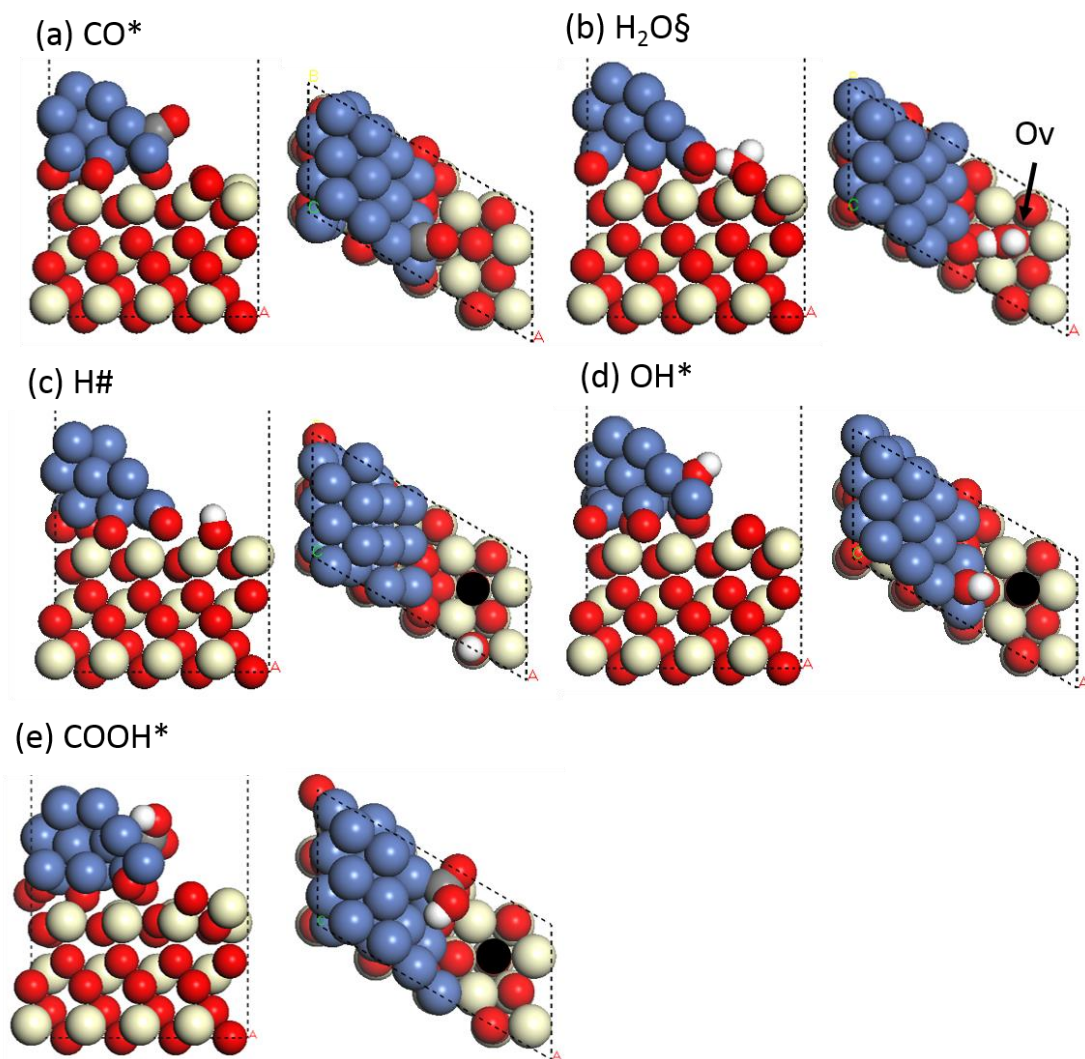


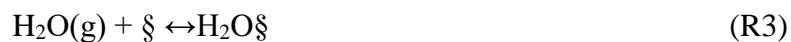
Figure 7.4. Optimized structures of reaction intermediates (a) CO*, (b) H₂O_δ, (c) H#, (d) OH*, and (e) COOH* (in **Table 7.1**) on Ni/CeO₂ surface. The black arrow indicates the position of Ov, which cannot recognize as being overlapped by the adsorbate in (b).

As shown in [Figure 7.3 \(a\)](#) and [Figure 7.4\(a\)](#), CO prefers to bind at the top and 3-fold sites near Cu- and Ni-CeO₂ interfaces, respectively. The calculated CO* BEs are -0.85 eV and -2.03 eV, which are about 0.1 eV stronger than those on unsupported Cu(111) and Ni(111) surfaces. H₂O binds preferentially through its oxygen at the bridge site between two Ce atoms

next to the Ov on both Cu/CeO₂ and Ni/CeO₂ catalysts, as illustrated in [Figure 7.3 \(b\)](#) and [Figure 7.4\(b\)](#). H₂O binds much stronger on Cu/CeO₂ and Ni/CeO₂ than on unsupported Cu(111) and Ni(111), with BEs of -0.91 eV and -0.55 eV, respectively. H prefers to bind at the top of O on CeO₂ surface, with BEs of -4.83 eV and -3.39 eV over Cu/CeO₂ and Ni/CeO₂ catalysts, respectively. The BEs of OH are -3.22 eV and -3.35 eV at the respective interface of Cu/CeO₂ and Ni/CeO₂. COOH prefers to bind at the 3-fold site at the interfaces of reduced Cu/CeO₂ and Ni/CeO₂ catalysts with its C atom located at the 3-fold site. The BEs of COOH are -1.90 eV and -1.97 eV, respectively.

7.2.4 WGSR Pathways on Cu/CeO₂ and Ni/CeO₂ Catalysts

The CeO₂ support can store or release oxygen under oxidizing and reducing conditions. Both experimental and theoretical studies proposed the adsorbed CO on metal/support (e.g., Au/CeO₂^{23,24}, Pt/CeO₂²³, Pd/CeO₂²⁵) can oxidize by lattice O on CeO₂, known as redox pathway, followed by re-oxidation of the support by H₂O re-oxidizes the reduced CeO₂. However, re-oxidation of the CeO₂ support are difficult with large energy barrier (above 1 eV) from DFT study on Au/CeO₂.²⁶ Instead of re-oxidizing CeO₂ support, the adsorbed OH produced through H₂O activation can react with adsorbed CO to form COOH, known as carboxyl pathway, followed by COOH dissociation.^{24,27} No significant amount of formate (HCOO) was observed over Cu/CeO₂. Hence, it is believed that formate should play a minor role in the reaction mechanism.⁵ Moreover, the formate is also found to be just a spectator species over Pt/CeO₂ from FTIR analyses.²⁸ Therefore, only redox pathway and carboxyl pathway are considered, as shown below:



The calculated reaction energetics associated with reaction pathways are listed in **Table 7.2**. In the redox pathway, surface lattice oxygen readily reacts with CO, forming CO₂ (R2). This step is very exothermic with a reaction energy of -2.93 eV and -1.53 eV on Cu/CeO₂ and Ni/CeO₂, respectively. Then H₂O adsorbs next to the Ov site (as shown in [Figure 7.3 \(b\)](#) and [Figure 7.4\(b\)](#) on Cu/CeO₂ and Ni/CeO₂ catalysts), followed by H₂O activation. The O-H bond in water breaks to form OH* and H# (R4) with respective reaction energies of -1.74 eV and -0.85 eV on Cu/CeO₂ and Ni/CeO₂. Instead re-oxidize the CeO₂ support, carboxyl pathway happens with OH* react with CO* (R5) forming COOH*. This step is endothermic by 0.20 eV and 1.48 eV on Cu/CeO₂ and Ni/CeO₂ catalysts, respectively. Then, COOH dissociates to form CO₂ and H# in the R6 step. This step is exothermic with respective reaction energies of -2.56 eV and -1.05 eV on Cu/CeO₂ and Ni/CeO₂. Lastly, two H atoms that bind at the O site on CeO₂ recombine to form H₂.

Table 7.2. DFT calculated reaction energies (ΔE [eV]) of the elementary steps on Cu/CeO₂ and Ni/CeO₂ catalysts.

		Cu/CeO ₂	Ni/CeO ₂
(R1)	$\text{CO(g)} + * \leftrightarrow \text{CO}^*$	-0.85	-2.03
(R2)	$\text{CO}^* \leftrightarrow \text{CO}_2\text{(g)} + \S$	-2.93	-1.53
(R3)	$\text{H}_2\text{O(g)} + \S \leftrightarrow \text{H}_2\text{O}\S$	-0.91	-0.55
(R4)	$\text{H}_2\text{O}\S + * \leftrightarrow \text{H}\# + \text{OH}^*$	-1.74	-0.85
(R5)	$\text{CO}^* + \text{OH}^* \leftrightarrow \text{COOH}^* + *$	0.20	1.48
(R6)	$\text{COOH}^* + \# \leftrightarrow \text{CO}_2\text{(g)} + \text{H}\#$	-2.56	-1.05
(R7)	$\text{H}\# + \text{H}\# \leftrightarrow \text{H}_2\text{(g)} + 2\#$	5.14	2.27

By combining the calculated energetics of the above reaction sequence, the overall potential energy surface describing WGSr carboxyl pathway can be summarized in [Figure 7.5](#). Potential energy surfaces on unsupported Cu(111) and Ni(111) are also shown (in respective black and red dashed lines) in [Figure 7.5\(a\)](#) and [Figure 7.5\(b\)](#). Due to stronger binding of CO and H₂O and more favorable dissociation of H₂O on Cu/CeO₂ and Ni/CeO₂ catalysts, initial potential energies shift downward on Cu/CeO₂ catalyst (black solid line) compare to unsupported Cu(111) (black dashed line) and Ni/CeO₂ catalyst (red solid line) compare to unsupported Ni(111) (red dashed line).

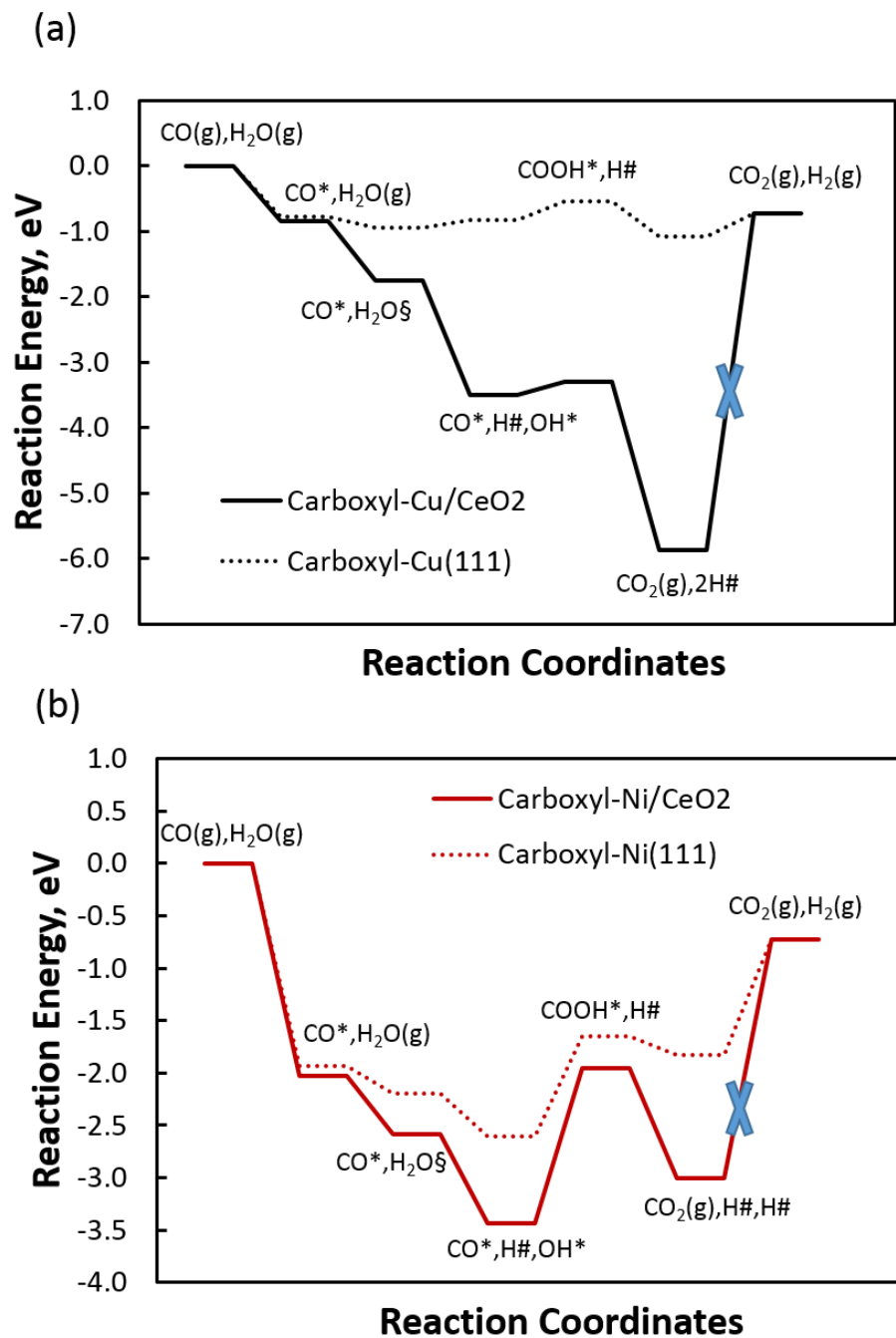


Figure 7.5. Potential energy surfaces of the WGS carboxyl pathway on (a) Cu/CeO₂ (black solid line), and unsupported Cu(111) (black dashed line), (b) Ni/CeO₂ (red solid line) and Ni(111) (red dashed line).

However, when COOH forms and dissociates to CO₂ and H#, the H# structures are very stable on Cu/CeO₂ and Ni/CeO₂ catalysts, which make the final H₂ formation steps from two H# impossible. These findings reveal that the CeO₂ support on Cu/CeO₂ and Ni/CeO₂ catalysts is likely hydroxylated, indicating that the model representing CeO₂ support needs to be revised to capture this character. In fact, a recent published Science paper ²⁹ presented that CO oxidation happens on steam-treated Pt/CeO₂ catalyst, in which the Pt/CeO₂ catalyst has surface O_{lattice} [H] species (same with H# here).

7.3 Case Study 2: CO Oxidation over Pt/h-BNNS

Supported Pt nanoparticle catalysts have continuously drawn broad and increasing attention because of their unique catalytic activity for a large number of important chemical reactions, such as CO oxidation^{30,31}. Due to the strong binding of CO, the O₂ activation is usually blocked on Pt catalyst for CO oxidation.

The h-BNNS can have high surface area and abundant edges and B/N vacancies,³² which could serve as an ideal non-redox active support for Pt NPs. Enhanced Pt nanoparticle activity to CO oxidation are found when supported with vacancy abundant h-BNNS. It is hypothesized that the interfacial charge transfer between Pt nanoparticle and h-BNNS support favor the adsorption of O₂, alleviating CO poisoning and promoting catalysis.

Figure 7.6 shows the schematic illustration of h-BNNS with B-vacancy (B_v) and N-vacancy (N_v). The interfacial electronic effect was primarily stemmed from the interaction between Pt and B_v as well as Pt and N_v. DFT calculations suggest that there exists a strong interaction between Pt and B/N vacancies, which is consistent with electron energy loss spectroscopy results. Therefore, in this section, the vacancy abundant h-BNNS support effect,

especially the interfacial electronic effect, on CO oxidation activity over Pt nanoparticle is discussed through DFT calculations.

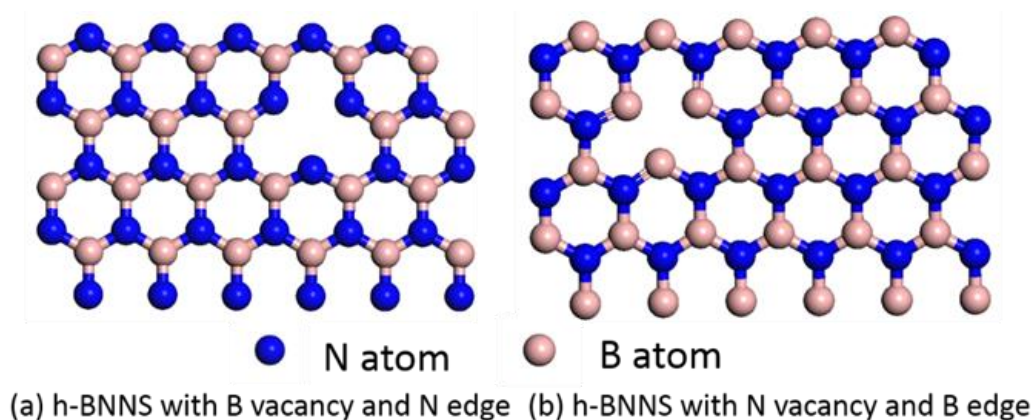


Figure 7.6. Schematic illustration of h-BNNS with B_v and N_v. (a) h-BNNS with B vacancy and N-terminated edge. (b) h-BNNS with N vacancy and B-terminated edge.

7.3.1 Computational Details

Spin-polarized periodic DFT calculations were performed using the Vienna Ab initio Simulation Package (VASP)^{9,33} to optimize the Pt₄ clusters, CO, O₂ adsorptions, and analyze the Bader charge of Pt/h-BNNS models. The h-BNNS was modeled using a $p(5 \times 5)$ supercell, with a vacuum of 20 Å along the direction perpendicular to the substrate. The Generalized Gradient Approximation (GGA)-PBE functional¹² was used for electronic exchange-correlation effect. The projector wave augmentation (PAW) method³⁴ was used to describe the electron-ion interaction, with a plane wave cutoff energy of 400 eV. A $4 \times 4 \times 1$ k-points mesh based on the Monkhorst-Pack scheme¹³ was used for Brillouin-Zone integration. Binding energies (BEs) on clean h-BN were calculated as: $BE = E_{\text{Pt4/h-BNNS}} - E_{\text{Pt4}} - E_{\text{clean h-BN}}$; BE on N_v/B_v on h-BNNS are

calculated as: $BE = E_{Pt4 \text{ on } N_V/B_V(h-BNNS)} - E_{Pt4} - E_{N_V/B_V(h-BNNS)}$. Respective binding energies of CO and O₂ were calculated according to: $BE_{CO/O_2^*} = E_{CO/O_2^*} - E_{Pt4 \text{ on } BNNS} - E_{CO/O_2(g)}$

7.3.2 Results and Discussion

Periodic DFT calculations and Bader charge analysis³⁵⁻³⁸ were performed to optimize the molecular structures, and analyze the effective charges on the Pt cluster in Pt/h-BNNS. First, optimized structures of a Pt₄ cluster on respective periodic h-BNNS, with clean, B_V and N_V, were obtained, with the corresponding Bader charge on Pt, B and N atoms presented in [Figure 7.7](#). It has been found that the Pt₄ cluster prefers the 3D pyramidal geometry on the h-BNNS support, and without any vacancy, the charge transfer between Pt and h-BNNS is negligible on the clean h-BNNS ([Figure 7.7\(a\)](#)). As shown in [Figure 7.7 \(b\) and \(c\)](#), the Pt atom (#1, #4) forms respective Pt-B and Pt-N bonds at the N_V and B_V sites, and the BEs in both cases increase significantly, which is consistent with experimental findings that strong interaction exists between Pt and the vacancies of h-BNNS. Bader charge analyses also confirmed that there exists an interfacial charge transfer between the Pt₄ cluster and h-BNNS. At the N_V site (B termination, [Figure 7.7\(b\)](#)), charge transfers from h-BNNS to Pt, resulting in a net gain of 0.8 e on Pt #1; while at B_V site (N termination, [Figure 7.7\(c\)](#)), charge transfers away from Pt, resulting in a net loss of 0.72 e on Pt #4.

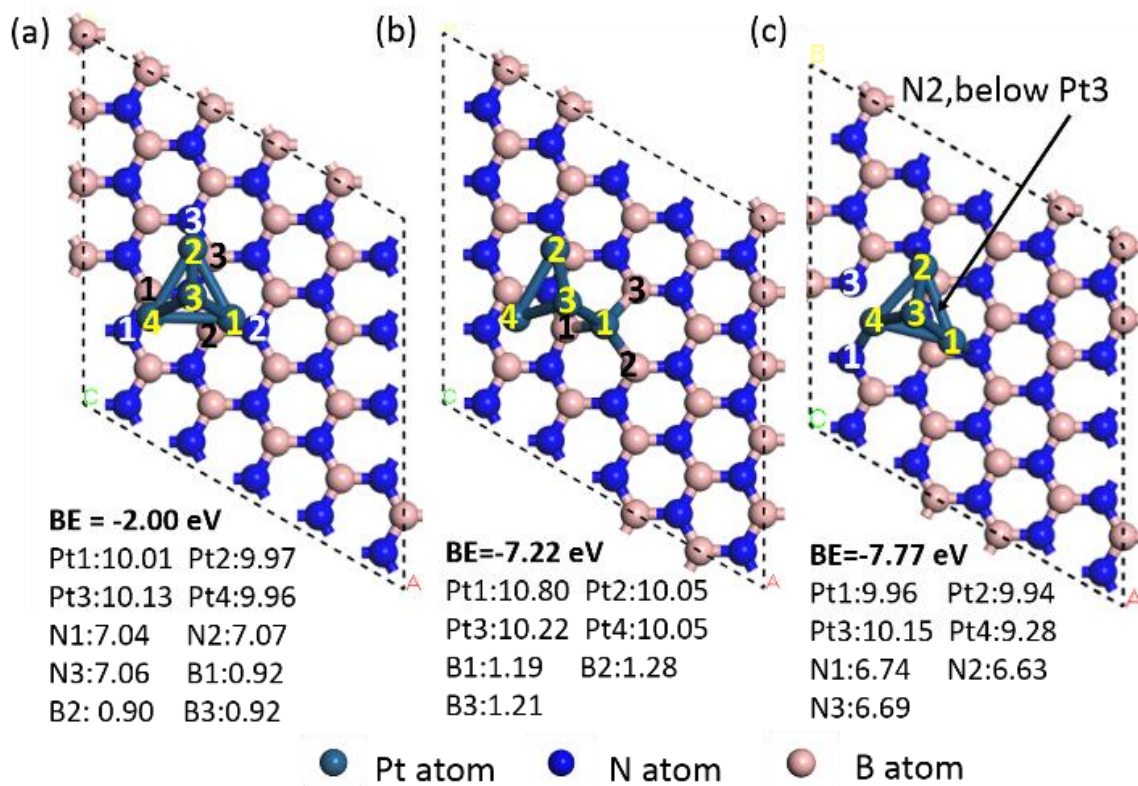


Figure 7.7. Optimized structures and Bader charges of pyramidal Pt₄ cluster on h-BNNS. (a) Pt₄ cluster on clean, vacancy-free h-BNNS, (b) Pt₄ cluster h-BNNS with N_v, and (c) Pt₄ cluster on h-BNNS with B_v.

In the presence of B_v, the adsorbing CO binding energy on Pt in its most stable configuration is -2.59 eV (Figure 7.8(b)), weaker than on the Pt with vacancy-free h-BNNS (-2.65 eV, Figure 7.8(a)), indicating the alleviation of strong CO adsorption on Pt/h-BNNS. On the other hand, the adsorbing CO binding energy on Pt increased slightly after charge transferred from N_v to Pt (Figure 7.8(c)). Moreover, BEs of O₂ on the Pt₄ cluster are stronger with both B_v (-2.90 eV) (Figure 7.8(e)) and N_v (-3.08 eV) (Figure 7.8(f)) than that on the vacancy-free Pt/h-BNNS (-2.26 eV) (Figure 7.8(d)), and also stronger than the BEs of CO (Figure 7.8(b) and (c)). This suggests that the effects on Pt induced by vacancy-abundant h-BNNS could facilitate O₂

adsorption and activation, and enhance CO oxidation, which is in accord with other theoretical studies^{39,40}. This observation also explains why bulk h-BN (with fewer edges and vacancies, performs inferior to h-BNNS (abundant of vacancies and edges).

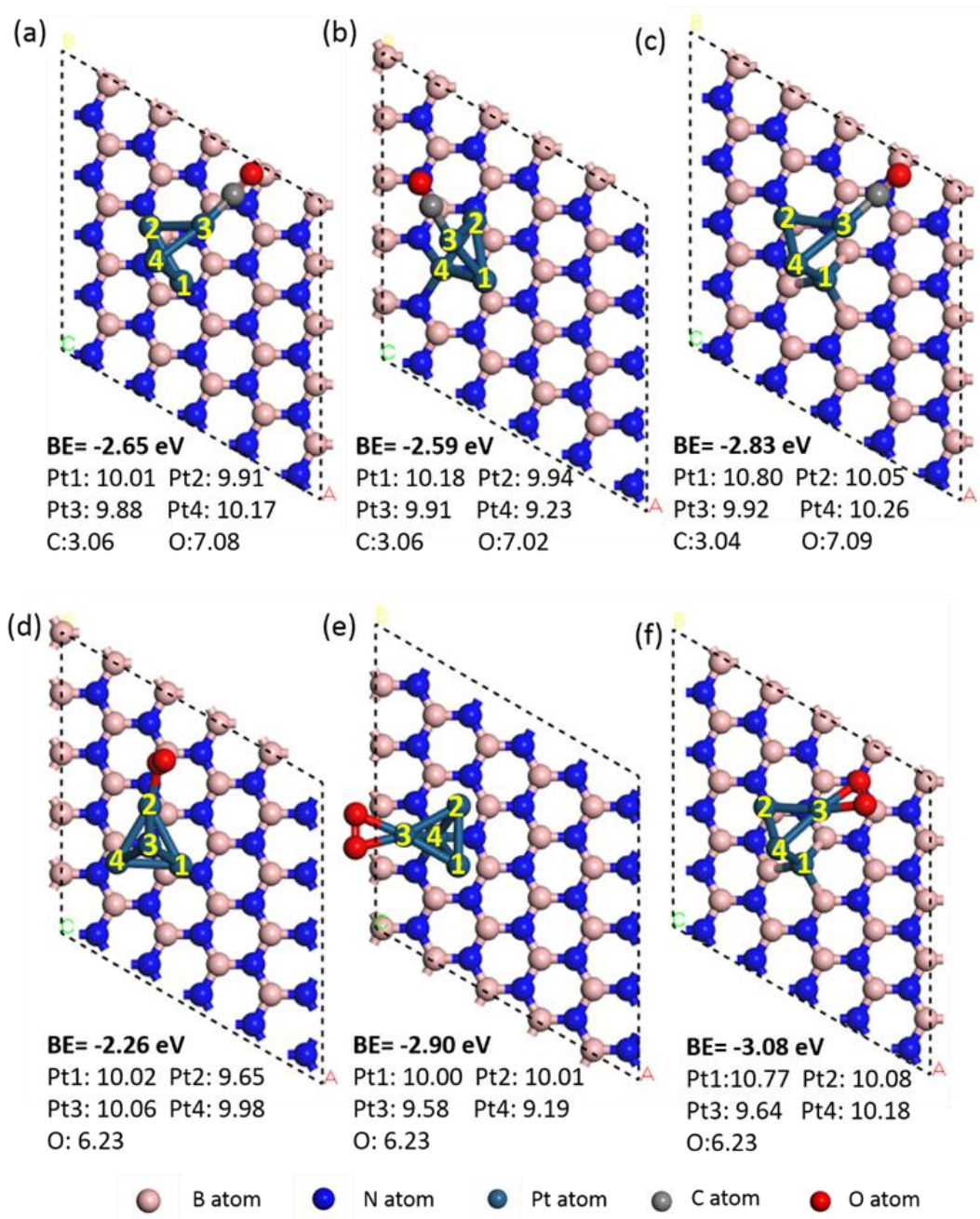


Figure 7.8. The most stable configuration of CO (a-c) and O₂ (d-f) adsorption and BEs on Pt₄ cluster. (a) Pt₄ cluster on clean, vacancy-free h-BNNS, (b) Pt₄ cluster h-BNNS with Bv, and (c) Pt₄ cluster on h-BNNS with Nv, (d) Pt₄ cluster on clean, vacancy-free h-BNNS, (e) Pt₄ cluster h-BNNS with Bv, and (f) Pt₄ cluster on h-BNNS with Nv.

7.4 Conclusions

DFT calculations were performed on both WGS over CeO_2 supported Cu or Ni catalysts and CO oxidation over vacancy abundant h-BNNS supported Pt nanoparticles to investigate support effect to catalysts activities. The new active sites at metal/support interface change the binding of reactants to the catalyst. The Cu/ CeO_2 and Ni/ CeO_2 catalysts are hydroxylated first for WGS, which needs further calculations to reaction energetics and kinetics to investigate CeO_2 support effect. The O_2 binds stronger than CO molecules on vacancy abundant h-BNNS supported Pt nanoparticles, alleviating the CO poisoning and promoting CO oxidation reaction.

The energetics of support effect to reactions have been studied in this chapter. Future study could focus on the support effect to energy barriers of each reaction steps. Then micro-kinetic modeling with inter-atomic interaction can be performed to have a completed understanding of support effect.

7.5 Acknowledgements

Case study 1 was supported in part by the Start-up fund provided by Kansas State University, the National Science Foundation under Award No. EPS-0903806, and matching support from the State of Kansas through the Kansas Board of Regents. The authors are also grateful for the supercomputing resources and services from the Center for Nanoscale Materials (CNM) supported by the Office of Science of the U.S. Department of Energy under Contract No. DE-AC02-06CH11357; the Beocat Research Cluster at Kansas State University, which is funded in part by NSF Grant CNS-1006860; and the National Energy Research Scientific Computing Center (NERSC) under Contract No. DE-AC02-05CH11231.

Case study 2 was supported by the Start-up fund provided by Kansas State University; the National Science Foundation under Award No. EPS-0903806, and matching support from the State of Kansas through the Kansas Board of Regents for financial support. M.X.Z. and B.L. also acknowledge the supercomputing resources provided by the Center for Nanoscale Materials (CNM) of the Office of Science of the US Department of Energy under the contract No. DE-AC02-06CH11357; the Beocat Research Cluster at Kansas State University, which is funded in part by NSF grants CNS-1006860; and the National Energy Research Scientific Computing Center (NERSC) under the contract No. DE-AC02-05CH11231.

References

1. Shibasaki-Kitakawa, N.; Honda, H.; Kuribayashi, H.; Toda, T.; Fukumura, T.; Yonemoto, T. Biodiesel production using anionic ion-exchange resin as heterogeneous catalyst. *Bioresour. Technol.* **2007**, *98*, 416-421.
2. Bagheri, S.; Muhd Julkapli, N.; Bee Abd Hamid, S. Titanium dioxide as a catalyst support in heterogeneous catalysis. *Sci. World J.* **2014**, *2014*.
3. Gorte, R. J. Ceria in catalysis: From automotive applications to the water-gas shift reaction. *AIChE J.* **2010**, *56*, 1126-1135.
4. Rodriguez, J. A.; Liu, P.; Hrbek, J.; Evans, J.; Pérez, M. Water gas shift reaction on Cu and Au nanoparticles supported on CeO₂(111) and ZnO(0001): Intrinsic activity and importance of support interactions. *Angew. Chem. Int. Ed.* **2007**, *46*, 1329-1332.
5. Wang, X.; Rodriguez, J.; Hanson, J.; Gamarra, D.; Martinez-Arias, A.; Fernandez-Garcia, M. In situ studies of the active sites for the water gas shift reaction over Cu-CeO₂ catalysts:

Complex interaction between metallic copper and oxygen vacancies of ceria. *J Phys Chem B* **2006**, *110*, 428-434.

6. Senanayake, S. D.; Evans, J.; Agnoli, S.; Barrio, L.; Chen, T. ; Hrbek, J.; Rodriguez, J. A. Water-gas shift and CO methanation reactions over Ni-CeO₂(111) catalysts. *Top. Catal.* **2011**, *54*, 34-41.

7. Carrasco, J.; Lopez-Duran, D.; Liu, Z.; Duchon, T.; Evans, J.; Senanayake, S. D.; Crumlin, E. J.; Matolin, V.; Rodriguez, J. A.; Veronica Ganduglia-Pirovano, M. In situ and theoretical studies for the dissociation of water on an active Ni/CeO₂ catalyst: importance of strong metal-support interactions for the cleavage of O-H bonds. *Angewandte Chemie-International Edition* **2015**, *54*, 3917-3921.

8. Kresse, G.; Furthmüller, J. Efficient iterative schemes for ab initio total-energy calculations using a plane-wave basis set. *Phys. Rev. B Condens. Matter Mater. Phys.* **1996**, *54*, 11169-11186.

9. Kresse, G.; Furthmüller, J. Efficiency of ab-initio total energy calculations for metals and semiconductors using a plane-wave basis set. *Comput Mater Sci* **1996**, *6*, 15-50.

10. Kresse, G.; Hafner, J. Ab initio molecular-dynamics simulation of the liquid-metalamorphous- semiconductor transition in germanium. *Phys. Rev. B* **1994**, *49*, 14251-14269.

11. Kresse, G.; Hafner, J. Ab initio molecular dynamics for liquid metals. *Phys. Rev. B* **1993**, *47*, 558-561.

12. Perdew, J. P.; Burke, K.; Ernzerhof, M. Generalized gradient approximation made simple. *Phys. Rev. Lett.* **1996**, *77*, 3865-3868.

13. Monkhorst, H. J.; Pack, J. D. Special points for Brillouin-zone integrations. *Phys. Rev. B* **1976**, *13*, 5188-5192.

14. Dudarev, S. L.; Botton, G. A.; Savrasov, S. Y.; Humphreys, C. J.; Sutton, A. P. Electron-energy-loss spectra and the structural stability of nickel oxide: An LSDA+U study. *Phys. Rev. B Condens. Matter Mater. Phys.* **1998**, *57*, 1505-1509.
15. Fabris, S.; De Gironcoli, S.; Baroni, S.; Vicario, G.; Balducci, G. Taming multiple valency with density functionals: A case study of defective ceria. *Phys. Rev. B Condens. Matter Mater. Phys.* **2005**, *71*.
16. Cococcioni, M.; De Gironcoli, S. Linear response approach to the calculation of the effective interaction parameters in the LDA+U method. *Phys. Rev. B Condens. Matter Mater. Phys.* **2005**, *71*.
17. Zhao, Z.; Li, Z.; Cui, Y.; Zhu, H.; Schneider, W. F.; Delgass, W. N.; Ribeiro, F.; Greeley, J. Importance of metal-oxide interfaces in heterogeneous catalysis: A combined DFT, micro-kinetic, and experimental study of water-gas shift on Au/MgO. *J. Catal.* **2017**, *345*, 157-169.
18. Molina, L.; Hammer, B. Active role of oxide support during CO oxidation at Au/MgO. *Phys. Rev. Lett.* **2003**, *90*, 206102.
19. Vecchietti, J.; Bonivardi, A.; Xu, W.; Stacchiola, D.; Delgado, J. J.; Calatayud, M.; Collins, S. E. Understanding the role of oxygen vacancies in the water gas shift reaction on ceria-supported platinum catalysts. *ACS Catalysis* **2014**, *4*, 2088-2096.
20. Chen, B.; Ma, Y.; Ding, L.; Xu, L.; Wu, Z.; Yuan, Q.; Huang, W. Reactivity of hydroxyls and water on a CeO₂(111) thin film surface: the role of oxygen vacancy. *Journal of Physical Chemistry C* **2013**, *117*, 5800-5810.
21. Kitchin, J.; Norskov, J.; Barteau, M.; Chen, J. Role of strain and ligand effects in the modification of the electronic and chemical properties of bimetallic surfaces. *Phys. Rev. Lett.* **2004**, *93*, 156801.

22. Mehta, P.; Greeley, J.; Delgass, W. N.; Schneider, W. F. Adsorption energy correlations at the metal-support boundary. *ACS Catalysis* **2017**, *7*, 4707-4715.
23. Fu, Q.; Saltsburg, H.; Flytzani-Stephanopoulos, M. Active nonmetallic Au and Pt species on ceria-based water-gas shift catalysts. *Science* **2003**, *301*, 935-938.
24. Song, W.; Hensen, E. J. M. Mechanistic aspects of the water-gas shift reaction on isolated and clustered Au atoms on CeO₂(110): A density functional theory study. *ACS Catal.* **2014**, *4*, 1885-1892.
25. Bunluesin, T.; Gorte, R.; Graham, G. Studies of the water-gas-shift reaction on ceria-supported Pt, Pd, and Rh: implications for oxygen-storage properties. *Applied Catalysis B-Environmental* **1998**, *15*, 107-114.
26. Chen, Y.; Cheng, J.; Hu, P.; Wang, H. Examining the redox and formate mechanisms for water-gas shift reaction on Au/CeO₂ using density functional theory. *Surf. Sci.* **2008**, *602*, 2828-2834.
27. Liu, Z.; Jenkins, S. J.; King, D. A. Origin and activity of oxidized gold in water-gas-shift catalysis. *Phys. Rev. Lett.* **2005**, *94*.
28. Tibiletti, D.; Goguet, A.; Meunier, F.; Breen, J.; Burch, R. On the importance of steady-state isotopic techniques for the investigation of the mechanism of the reverse water-gas-shift reaction. *Chemical Communications* **2004**, 1636-1637.
29. Nie, L.; Mei, D.; Xiong, H.; Peng, B.; Ken, Z.; Hernandez, X. I. P.; DeLariva, A.; Wang, M.; Engelhard, M. H.; Kovarik, L.; Datye, A. K.; Wang, Y. Activation of surface lattice oxygen in single-atom Pt/CeO₂ for low-temperature CO oxidation. *Science* **2017**, *358*, 1419-1423.

30. Chen, G.; Zhao, Y.; Fu, G.; Duchesne, P. N.; Gu, L.; Zheng, Y.; Weng, X.; Chen, M.; Zhang, P.; Pao, C.; Lee, J.; Zheng, N. Interfacial effects in iron-nickel hydroxide-platinum nanoparticles enhance catalytic oxidation. *Science* **2014**, *344*, 495-499.
31. Giordano, L.; Pacchioni, G.; Noguera, C.; Goniakowski, J. Identification of active sites in a realistic model of strong metal-support interaction catalysts: the case of platinum (111)-supported iron oxide film. *Chemcatchem* **2014**, *6*, 185-190.
32. Zhu, W.; Gao, X.; Li, Q.; Li, H.; Chao, Y.; Li, M.; Mahurin, S. M.; Li, H.; Zhu, H.; Dai, S. Controlled gas exfoliation of boron nitride into few-layered nanosheets. *Angewandte Chemie-International Edition* **2016**, *55*, 10766-10770.
33. Kresse, G.; Hafner, J. Ab-initio molecular-dynamics for open-shell transition metals. *Physical Review B* **1993**, *48*, 13115-13118.
34. Kresse, G.; Joubert, D. From ultrasoft pseudopotentials to the projector augmented-wave method. *Phys. Rev. B Condens. Matter Mater. Phys.* **1999**, *59*, 1758-1775.
35. Yu, M.; Trinkle, D. R. Accurate and efficient algorithm for Bader charge integration. *J. Chem. Phys.* **2011**, *134*.
36. Sanville, E.; Kenny, S. D.; Smith, R.; Henkelman, G. Improved grid-based algorithm for Bader charge allocation. *J. Comput. Chem.* **2007**, *28*, 899-908.
37. Henkelman, G.; Arnaldsson, A.; Jónsson, H. A fast and robust algorithm for Bader decomposition of charge density. *Comput Mater Sci* **2006**, *36*, 354-360.
38. Tang, W.; Sanville, E.; Henkelman, G. A grid-based Bader analysis algorithm without lattice bias. *J. Phys. Condens. Matter* **2009**, *21*.

39. Liu, X.; Duan, T.; Meng, C.; Han, Y. Pt atoms stabilized on hexagonal boron nitride as efficient single-atom catalysts for CO oxidation: a first-principles investigation. *Rsc Advances* **2015**, *5*, 10452-10459.
40. Lin, S.; Ye, X.; Johnson, R. S.; Guo, H. First-principles investigations of metal (Cu, Ag, Au, Pt, Rh, Pd, Fe, Co, and Ir) doped hexagonal boron nitride nanosheets: stability and catalysis of CO oxidation. *Journal of Physical Chemistry C* **2013**, *117*, 17319-17326.

Chapter 8 - Conclusions

In this thesis, micro-kinetic modelings based on molecular mechanisms derived from first-principles calculations have applied in various scenarios to gain fundamental understandings of how promoters, surface structures, catalyst particle size, and catalyst supports determine catalyst reactivity and selectivity using WGSR as model reaction. The main conclusions are listed as below:

- WGSR pathways become more favored in the presence of K adatoms on Ni(111) with respect to competing methanation pathways.
- Hydrogen production rates decrease with increasing Ni particle sizes (diameters), as a result of decreasing fractions of low-coordinated surface Ni atoms.
- Included with CO self-interactions, the hydrogen production rate increases on the strong CO binding metals (e.g., Ni and Pt), which means Ni and Pt can be active WGSR catalyst if CO poison on these catalysts can be relieved.
- Influence of catalyst supports (e.g., h-BNNS) on active sites structurally and electronically plays significant role in modifying catalyst character and offers opportunity to diversify catalyst functionalities.

So far, first-principles micro-kinetic modeling works quite well for WGSR systems with predicting comparable results to experiment. However, there are still a number of important unsolved issues. The micro-kinetic framework needs to be further developed by including diffusions of reactive intermediates between different sites on nanoparticles and adding more inter-atomic interactions (e.g., OH self-interaction, and CO-OH cross-interaction. The Cu/CeO₂ and Ni/CeO₂ catalysts models need to be revised with a hydroxylated CeO₂ supported to study the critical role of CeO₂ support to WGSR.

This work implies that molecular level information on promoters, surface structures, nanoparticle sizes, and supports effects to catalytic activity and selectivity based on computational methods and provide theoretical insights that improve catalytic properties. The first-hand information provided by computational methods will enable better guidance and more reliable prediction in the scientific process of designing new catalyst materials with high performance.

Appendix A - Vibrational Frequencies of Reaction Intermediates on Ni(111), Ni(100), and Ni(211)

Table A.1. Vibrational frequencies of reaction intermediates in the gas phase and on Ni(111)

	Frequencies [cm^{-1}]
H ₂ O(g)	3820, 3705, 1583
CO(g)	2119
H ₂ (g)	4458
CO ₂ (g)	2366, 1319, 636, 636
CH ₄ (g)	3093, 3091, 3090, 2973, 1511, 1510, 1286, 1285, 1285
H ₂ O	3665, 3556, 1536, 458, 449, 228, 226, 226, 219
CO	1767, 388, 283, 282, 232, 232
CO ₂	2350, 1315, 625, 615, 220, 220, 220, 220, 220
HCOH	3602, 2033, 1595, 1212, 1061, 575, 479, 341, 304, 246, 241, 232
CH ₂ OH	3595, 2508, 2145, 1551, 1262, 1120, 1069, 934, 363, 305, 250, 245, 240, 230, 227
H	1138, 874, 871
OH	3419, 682, 681, 431, 307, 306
COOH	3571, 1469, 1215, 1123, 692, 583, 440, 382, 260, 240, 231, 230
CHO	2903, 1267, 1166, 608, 500, 363, 280, 257, 239
CH ₂	3002, 2340, 1436, 663, 596, 559, 414, 345, 294
COH	3582, 1263, 1084, 474, 455, 433, 240, 237, 236
O	553, 459, 444

CH	3027, 660, 648, 647, 471, 471
C	632, 606, 606

Table A.2. Vibrational frequencies of reaction intermediates on Ni(100)

	Frequencies [cm^{-1}]
H ₂ O	686,3576,1540,476,431,229,217,214,210
CO	1626,312,247,246,237,237
HCOH	3292,2954,1341,1138,1107,815,497,447,351,291,220,218
H	716,517,512
OH	3627,651,650,345,219,217
COOH	3596,1277,1159,1017, 661,555,351,346,295,276,247,233
CHO	2918,1169,1071,631,525,381,377,322,277
COH	3583,1139,1026,454,439,368,250,246,229
O	385,329,329,219,212,211
CH	2886,637,635,497,496,467

Table A.3. Vibrational frequencies of reaction intermediates on Ni(211)

	Frequencies [cm^{-1}]
H ₂ O	3691, 3582, 1550, 488, 444, 269, 253, 250, 249
CO	1851, 421, 353, 327, 250, 245
HCOH	3330, 2968, 1348, 1165, 1105, 810, 516, 444, 371, 288, 251, 247
H	1157, 836, 811

OH 3638, 701, 607, 490, 378, 251

COOH 3489, 1424, 1274, 1096, 681, 650, 412, 400, 271, 251, 248, 245

CHO 2846, 1453, 1192, 699, 545, 351, 260, 249, 248

COH 1820, 1303, 967, 826, 469, 347, 305, 265, 256

O 636, 571, 247

CH 2899, 701, 672, 482, 467, 445

Appendix B - Input Files for Micro-kinetic Modeling on Ni Nanoparticles

B.1. Input Energy File

surface_name	site_name	species_name	formation_energy	frequencies
	reference			
Ni	s1	CH	-1.889 [471, 471, 647, 648, 660, 3027]	Input File Tutorial.
Ni	s1	CH-H	-1.688 []	Input File Tutorial.
Ni	s1	CH-O	-0.152 []	Input File Tutorial.
Ni	s1	CH-OH	-0.58 []	Input File Tutorial.
Ni	s1	CH2	-2.046 []	Input File Tutorial.
Ni	s1	CH2-H	-1.955 []	Input File Tutorial.
Ni	s1	CH3	-2.618 []	Input File Tutorial.
Ni	s1	CH3-H	-2.507 []	Input File Tutorial.
Ni	s1	CHO	-1.188 [239, 257, 280, 363, 500, 608, 1166, 1267, 2903]	Input File Tutorial.
Ni	s1	CO	-1.901 [232, 232, 282, 283, 388, 1767]	Input File Tutorial.
Ni	s1	CO-H	-0.532 []	Input File Tutorial.
Ni	s1	CO-OH	-0.648 []	Input File Tutorial.
Ni	s1	COH	-1.481 [236, 237, 240, 433, 455, 474, 1084, 1263, 3582]	Input File Tutorial.
Ni	s1	COO-H	-0.163 []	Input File Tutorial.
Ni	s1	COOH	-1.089 [230, 231, 240, 260, 382, 440, 583, 692, 1123, 1215, 1469, 3571]	Input File Tutorial.

Ni h1 H -0.539 [871, 874, 1138] Input File Tutorial.
 Ni s1 H-CO -0.998 [] Input File Tutorial.
 Ni s1 H-COH -1.194 [] Input File Tutorial.
 Ni s1 H-OH 0.59 [] Input File Tutorial.
 Ni s1 H2O -0.271 [219, 226, 226, 228, 449, 458, 1536, 3556, 3665] Input
 File Tutorial.
 Ni s1 HCOH -1.295 [232, 241, 246, 304, 341, 479, 575, 1061, 1212, 1595,
 2033, 3602] Input File Tutorial.
 Ni s1 O 0.197 [444, 459, 553] Input File Tutorial.
 Ni s1 O-CO -0.14 [] Input File Tutorial.
 Ni s1 O-H 0.83 [] Input File Tutorial.
 Ni s1 OH -0.145 [306, 307, 431, 681, 682, 3419] Input File Tutorial.
 Ni s2 CH 0.752 [466.581494, 496.374931, 497.187809, 634.589573,
 636.959551, 2886.148424] Input File Tutorial.
 Ni s2 CH-O 2.676 [] Input File Tutorial.
 Ni s2 CH-OH 2.229 [] Input File Tutorial.
 Ni s2 CHO 1.452 [277.656489, 322.268104, 377.606706, 380.894386,
 525.003104, 631.465722, 1070.759304, 1169.496379, 2917.796316] Input File
 Tutorial.
 Ni s2 CO 1.302 [236.803462, 237.180715, 246.470555, 247.146649,
 311.590197, 1626.234975] Input File Tutorial.
 Ni s2 CO-H 2.486 [] Input File Tutorial.
 Ni s2 CO-OH 2.818 [] Input File Tutorial.

Ni s2 COH 1.426 [228.901219, 246.525389, 250.36235, 368.119658,
439.089881, 454.291143, 1026.555991, 1139.732978, 3583.511204] Input File
Tutorial.

Ni s2 COO-H 2.722 [] Input File Tutorial.

Ni s2 COOH 1.662 [233.738328, 246.72071, 275.637245, 295.372999,
345.990209, 350.584425, 554.645026, 660.986204, 1016.559152, 1159.255733,
1276.891396, 3596.903956] Input File Tutorial.

Ni h2 H -0.466 [512.197514, 517.193407, 716.267316] Input File
Tutorial.

Ni s2 H-CO 2.066 [] Input File Tutorial.

Ni s2 H-COH 2.292 [] Input File Tutorial.

Ni s2 H-OH 0.551 [] Input File Tutorial.

Ni s2 H2O -0.357 [210.089556, 214.398593, 217.452095, 229.8459,
431.409321, 476.241737, 1540.093281, 3576.574049, 3686.848316] Input File
Tutorial.

Ni s2 HCOH 1.79 [218.314929, 219.508289, 290.518204, 350.768431,
447.062678, 496.928234, 814.880654, 1106.772078, 1137.992356, 1341.462379,
2953.960663, 3291.643572] Input File Tutorial.

Ni s2 O -0.029 [328.608311, 329.363066, 385.189061] Input File
Tutorial.

Ni s2 O-CO 2.586 [] Input File Tutorial.

Ni s2 O-H 0.648 [] Input File Tutorial.

Ni s2 OH -0.263 [217.031823, 218.87629, 345.310445, 650.061385,
 651.482285, 3626.663306] Input File Tutorial.

None gas CH4 0.0 [3039, 3091, 3090, 2973, 1511, 1510, 1286, 1285, 1285]
 Input File Tutorial.

None gas CO 3.184 [2119] Input File Tutorial.

None gas CO2 2.455 [2366, 1319, 636, 636] Input File Tutorial.

None gas H2 0.0 [4458] Input File Tutorial.

None gas H2O 0.0 [3820, 3705, 1583] Input File Tutorial.

Ni f3 CH 1.038 [] Input File Tutorial.

Ni s3 CH-O 2.446 [] Input File Tutorial.

Ni s3 CH-OH 2.319 [] Input File Tutorial.

Ni s3 CHO 1.738 [] Input File Tutorial.

Ni s3 CO 1.217 [] Input File Tutorial.

Ni s3 CO-H 2.595 [] Input File Tutorial.

Ni s3 CO-OH 2.222 [] Input File Tutorial.

Ni s3 COH 1.668 [] Input File Tutorial.

Ni s3 COO-H 2.603 [] Input File Tutorial.

Ni s3 COO-H-OH 2.541 [] Input File Tutorial.

Ni s3 COOH 2.165 [] Input File Tutorial.

Ni h3 H -0.556 [] Input File Tutorial.

Ni s3 H-CO 1.859 [] Input File Tutorial.

Ni s3 H-COH 1.801 [] Input File Tutorial.

Ni s3 H-OH 0.319 [] Input File Tutorial.

Ni	s3	H2O	-0.551	[]	Input File Tutorial.
Ni	s3	HCOH	1.451	[]	Input File Tutorial.
Ni	s3	O	0.014	[]	Input File Tutorial.
Ni	s3	O-CO	2.765	[]	Input File Tutorial.
Ni	s3	O-H	0.371	[]	Input File Tutorial.
Ni	s3	OH	-0.656	[]	Input File Tutorial.

B.2. Set Up Reaction Parameters

#

#Micro-kinetic model parameters

#

scaler = 'ThermodynamicScaler'

rxn_expressions = [

'*_s1 + CO_g <-> CO_s1',

'*_h1 + H2O_g + *_s1 <-> H-OH_s1 + *_h1 <-> H_h1 + OH_s1',

'CO_s1 + OH_s1 <-> CO-OH_s1 + *_s1 <-> COOH_s1 + *_s1',

'COOH_s1 + *_h1 <-> COO-H_s1 + *_h1 <-> CO2_g + H_h1 + *_s1',

'COOH_s1 + OH_s1 <-> CO2_g + H2O_g + 2*_s1',

'*_h1 + OH_s1 <-> O-H_s1 + *_h1 <-> O_s1 + H_h1',

'CO_s1 + H_h1 <-> H-CO_s1 + *_h1 <-> CHO_s1 + *_h1',

'CHO_s1 + *_s1 <-> CH-O_s1 + *_s1 <-> CH_s1 + O_s1',

'CO_s1 + O_s1 <-> O-CO_s1 + *_s1 <-> CO2_g + 2*_s1',

$\text{'H_h1 + H_h1 <-> H2_g + 2*_h1'}$,
 $\text{'CH_s1 + 3H_h1 <-> CH4_g + 3*_h1 + *_s1'}$,
 $\text{'CO_s1 + H_h1 <-> CO-H_s1 + *_h1 <-> COH_s1 + *_h1'}$,
 $\text{'COH_s1 + H_h1 <-> H-COH_s1 + *_h1 <-> HCOH_s1 + *_h1'}$,
 $\text{'HCOH_s1 + *_s1 <-> CH-OH_s1 + *_s1 <-> CH_s1 + OH_s1'}$,

 $\text{'*_s2 + CO_g <-> CO_s2'}$,
 $\text{'*_h2 + H2O_g + *_s2 <-> H-OH_s2 + *_h2 <-> H_h2 + OH_s2'}$,
 $\text{'CO_s2 + OH_s2 <-> CO-OH_s2 + *_s2 <-> COOH_s2 + *_s2'}$,
 $\text{'COOH_s2 + *_h2 <-> COO-H_s2 + *_h2 <-> CO2_g + H_h2 + *_s2'}$,
 $\text{'COOH_s2 + OH_s2 <-> CO2_g + H2O_g + 2*_s2'}$,
 $\text{\# 'COOH* + O* <-> COO-H-O* + * <-> CO2_g + OH* + *'}$,
 $\text{'*_h2 + OH_s2 <-> O-H_s2 + *_h2 <-> O_s2 + H_h2'}$,
 $\text{\# 'H* + H* <-> H2_g + 2*_s'}$,
 $\text{'CO_s2 + H_h2 <-> H-CO_s2 + *_h2 <-> CHO_s2 + *_h2'}$,
 $\text{'CHO_s2 + *_s2 <-> CH-O_s2 + *_s2 <-> CH_s2 + O_s2'}$,
 $\text{\# 'CHO_s + H_h <-> CHO-H_s + *_h <-> HCOH_s + *_h'}$,
 $\text{'CO_s2 + O_s2 <-> O-CO_s2 + *_s2 <-> CO2_g + 2*_s2'}$,
 $\text{'H_h2 + H_h2 <-> H2_g + 2*_h2'}$,
 $\text{\# 'COH_s + *_s <-> C_s + OH_s'}$,
 $\text{\# 'CH* + H* <-> CH2* + *'}$,
 $\text{\# 'CH2* + H* <-> CH3* + *'}$,
 $\text{\# 'CH3* + H* <-> CH4_g + 2*'}$,

$\text{'CH}_s2 + 3\text{H}_h2 \rightleftharpoons \text{CH}_4_g + 3*_h2 + *_s2'$,
 $\text{'CO*} + * \rightleftharpoons \text{C-O*} + * \rightleftharpoons \text{C*} + \text{O*}'$,
 $\text{'C*} + 2\text{H}_2_g \rightleftharpoons \text{CH}_4_g + *'$,
 $\text{'CO}_s2 + \text{H}_h2 \rightleftharpoons \text{CO-H}_s2 + *_h2 \rightleftharpoons \text{COH}_s2 + *_h2'$,
 $\text{'COH}_s2 + \text{H}_h2 \rightleftharpoons \text{H-COH}_s2 + *_h2 \rightleftharpoons \text{HCOH}_s2 + *_h2'$,
 $\text{'HCOH}_s2 + *_s2 \rightleftharpoons \text{CH-OH}_s2 + *_s2 \rightleftharpoons \text{CH}_s2 + \text{OH}_s2'$,
 $\text{'C}_s + \text{H}_h \rightleftharpoons \text{C-H}_s + *_h \rightleftharpoons \text{CH}_s + *_h'$,
 $\text{'CH*} + * \rightleftharpoons \text{C-H*} + * \rightleftharpoons \text{C*} + \text{H*}'$,
 $\text{'CH}_s + \text{H}_h \rightleftharpoons \text{CH-H}_s + *_h \rightleftharpoons \text{CH}_2_s + *_h'$,
 $\text{'CH}_2_s + \text{H}_h \rightleftharpoons \text{CH}_2\text{-H}_s + *_h \rightleftharpoons \text{CH}_3_s + *_h'$,
 $\text{'CH}_3_s + \text{H}_h \rightleftharpoons \text{CH}_3\text{-H}_s + *_h \rightleftharpoons \text{CH}_4_g + *_s + *_h'$,
 $\text{'CH}_4* \rightleftharpoons \text{CH}_4_g + *'$,
 $\text{'*}_s3 + \text{CO}_g \rightleftharpoons \text{CO}_s3'$,
 $\text{'*}_h3 + \text{H}_2\text{O}_g + *_s3 \rightleftharpoons \text{H-OH}_s3 + *_h3 \rightleftharpoons \text{H}_h3 + \text{OH}_s3'$,
 $\text{'CO}_s3 + \text{OH}_s3 \rightleftharpoons \text{CO-OH}_s3 + *_s3 \rightleftharpoons \text{COOH}_s3 + *_s3'$,
 $\text{'COOH}_s3 + *_h3 \rightleftharpoons \text{COO-H}_s3 + *_h3 \rightleftharpoons \text{CO}_2_g + \text{H}_h3 + *_s3'$,
 $\text{'COOH}_s3 + \text{OH}_s3 \rightleftharpoons \text{CO}_2_g + \text{H}_2\text{O}_g + 2*_s3'$,
 $\text{'*}_h3 + \text{OH}_s3 \rightleftharpoons \text{O-H}_s3 + *_h3 \rightleftharpoons \text{O}_s3 + \text{H}_h3'$,
 $\text{'CO}_s3 + \text{H}_h3 \rightleftharpoons \text{H-CO}_s3 + *_h3 \rightleftharpoons \text{CHO}_s3 + *_h3'$,
 $\text{'CHO}_s3 + *_f3 \rightleftharpoons \text{CH-O}_s3 + *_f3 \rightleftharpoons \text{CH}_f3 + \text{O}_s3'$,
 $\text{'CO}_s3 + \text{O}_s3 \rightleftharpoons \text{O-CO}_s3 + *_s3 \rightleftharpoons \text{CO}_2_g + 2*_s3'$,
 $\text{'H}_h3 + \text{H}_h3 \rightleftharpoons \text{H}_2_g + 2*_h3'$,
 $\text{'CH}_f3 + 3\text{H}_h3 \rightleftharpoons \text{CH}_4_g + 3*_h3 + *_f3'$,

```

'CO_s3 + H_h3 <-> CO-H_s3 + *_h3 <-> COH_s3 + *_h3',
'COH_s3 + H_h3 <-> H-COH_s3 + *_h3 <-> HCOH_s3 + *_h3',
'HCOH_s3 + *_f3 <-> CH-OH_s3 + *_f3 <-> CH_f3 + OH_s3',

]

```

```

surface_names = ['Ni'] #surfaces to include in scaling (need to have descriptors defined for
each)

```

```

descriptor_names= ['temperature','pressure'] #descriptor names

```

```

descriptor_ranges = [[498,600],[1,10]]

```

```

resolution = 15

```

```

species_definitions = {}

```

```

species_definitions['CO_g'] = {'concentration':25./1000.} #define the gas pressures

```

```

species_definitions['H2O_g'] = {'concentration':250./1000.}

```

```

species_definitions['CO2_g'] = {'concentration':125./1000.}

```

```

species_definitions['H2_g'] = {'concentration':375./1000.}

```

```

species_definitions['CH4_g'] = {'concentration':0}

```

```

species_definitions['s1'] = {'site_names': ['s1'], 'total':0.62}

species_definitions['s2'] = {'site_names': ['s2'], 'total':0.07} #define the sites

species_definitions['s3'] = {'site_names': ['s3'], 'total':0.31}

species_definitions['h2'] = {'site_names': ['h2'], 'total':0.07} #define the sites

species_definitions['h3'] = {'site_names': ['h3'], 'total':0.31}

species_definitions['f3'] = {'site_names': ['f3'], 'total':0.31}

species_definitions['h1'] = {'site_names': ['h1'], 'total':0.62}


data_file = 'wgsr.pkl'


#

#Parser parameters

#


input_file = 'energies.txt' #input data


#

#Scaler parameters

#


gas_thermo_mode = "shomate_gas"

#gas_thermo_mode = "ideal_gas" #Ideal gas approximation

#gas_thermo_mode = "zero_point_gas" #uses zero-point corrections only

```

```
#gas_thermo_mode = "fixed_entropy_gas" #assumes entropy of 0.002 eV/K for all gasses  
except H2 (H2 is 0.00135 eV/K)
```

```
#gas_thermo_mode = "frozen_gas" #neglect thermal contributions
```

```
adsorbate_thermo_mode = "frozen_adsorbate"
```

```
#adsorbate_thermo_mode = "harmonic_adsorbate"
```

```
#adsorbate_thermo_mode = "zero_point_adsorbate"
```

```
scaling_constraint_dict = {  
    'CO_s':[None,None,None],  
    'H2O_s':[None,None,None],  
    'O-CO_s':'initial_state',  
    'H-OH_s':'initial_state',  
}
```

```
#
```

```
#Solver parameters
```

```
#
```

```
decimal_precision = 100 #precision of numbers involved
```

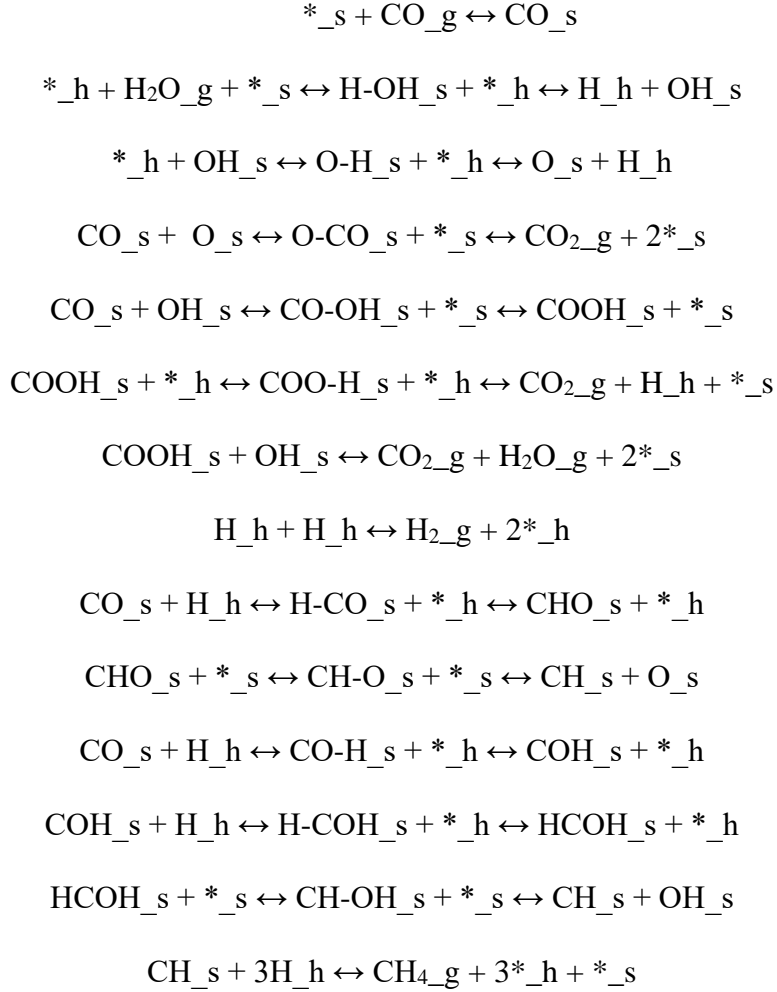
```
tolerance = 1e-50 #all d_theta/d_t's must be less than this at the solution
```

```
max_rootfinding_iterations = 100
```

```
max_bisections = 3
```

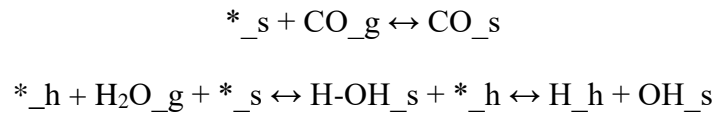
Appendix C - Mechanisms for Micro-kinetic Modeling on Ni(111), Ni(100) and Ni(211) surfaces

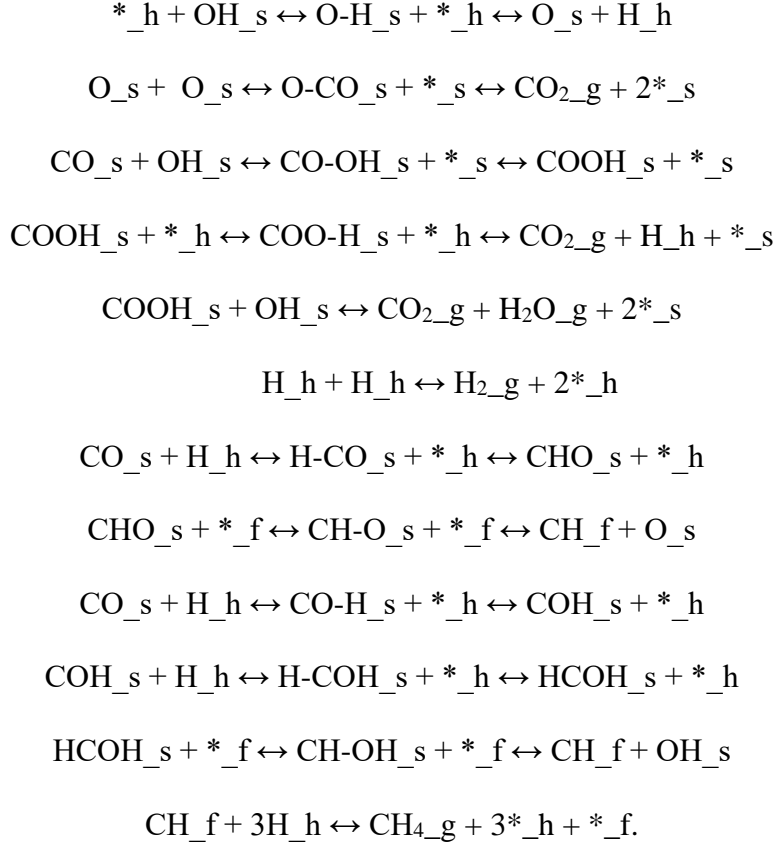
C.1 Elementary Steps on Ni(111) and Ni(100):



where *h represents the “hydrogen reservoir” site, and *s represents the site for all other species.

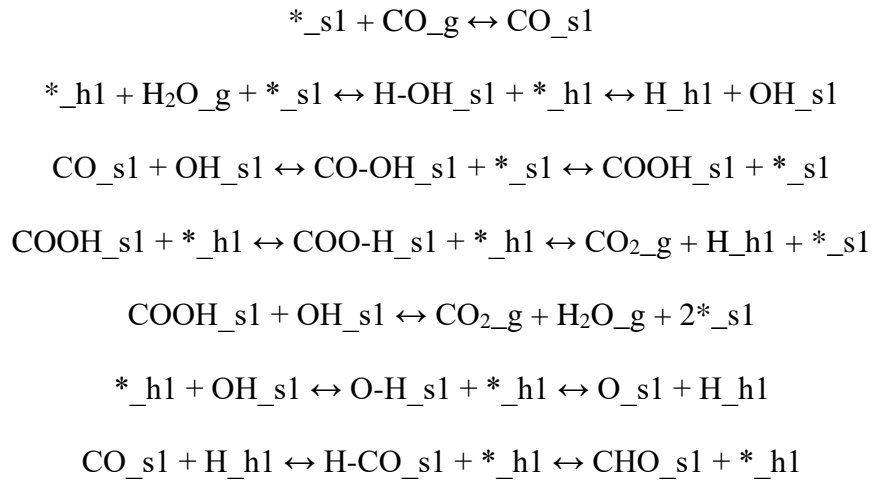
C.2 Elementary Steps on Ni(211):

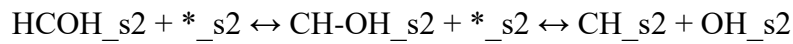
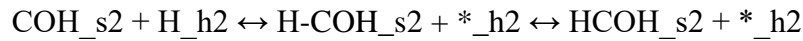
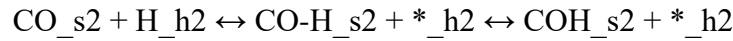
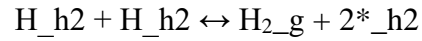
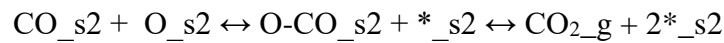
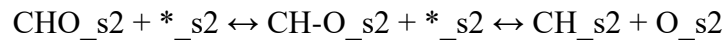
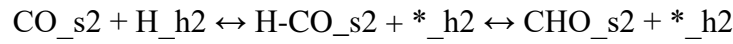
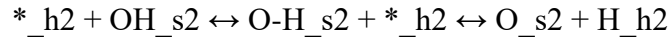
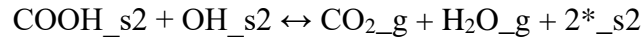
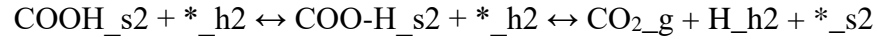
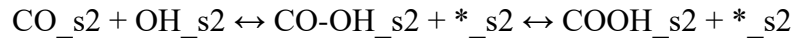
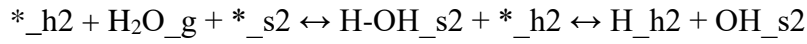
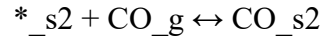
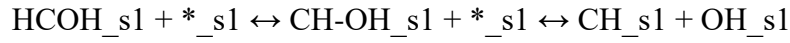
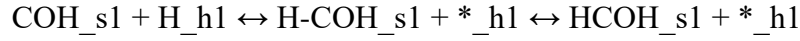
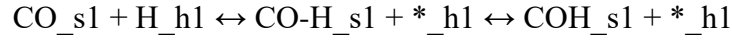
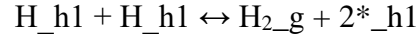
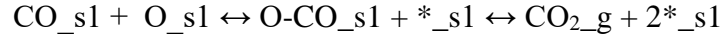
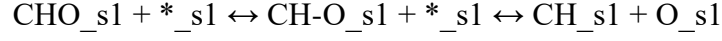


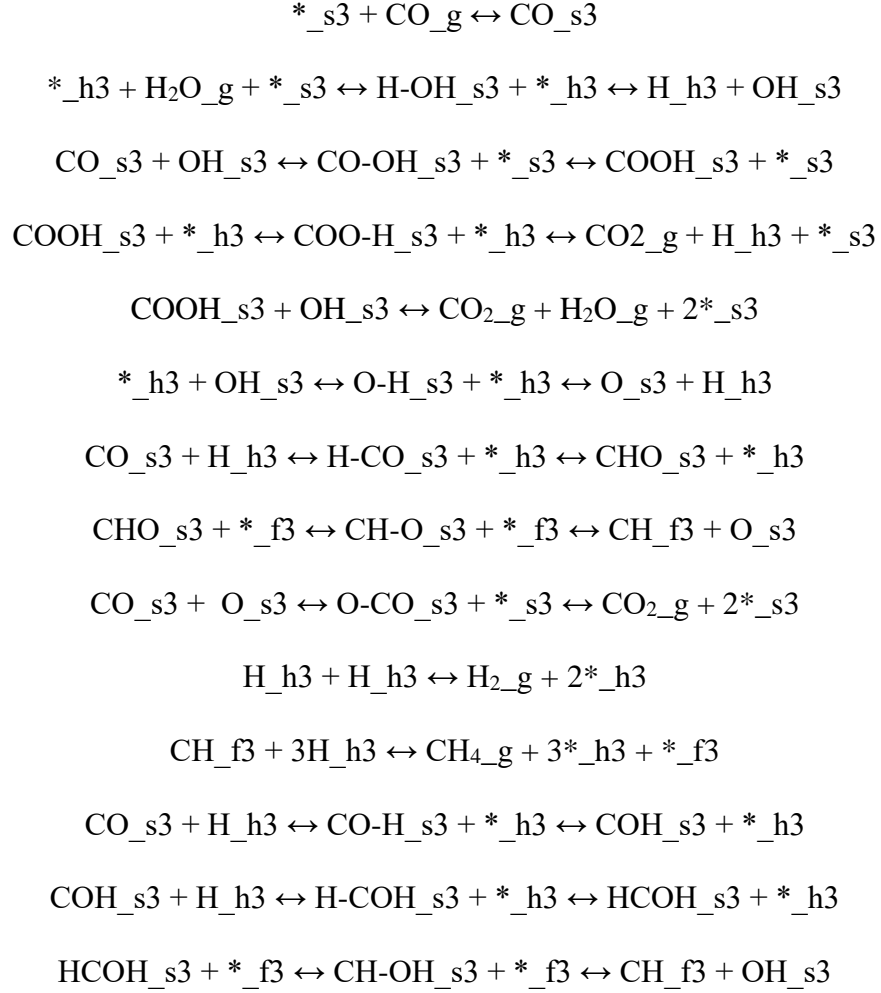


where $*_h$ represents the “hydrogen reservoir” site, $*_f$ represents the “four-fold hollow” site, and $*_s$ represents the site for all other species.

C.3 Elementary Steps for Ni Nanoparticles:







where *h1 represents the “hydrogen reservoir” site on Ni(111), *s1 represents the site for all other species on Ni(111), *h2 represents the “hydrogen reservoir” site on Ni(100), *s2 represents the site for all other species on Ni(100), *h3 represents the “hydrogen reservoir” site on Ni(211), *f3 represents the “four-fold hollow” site on Ni(211), and *s3 represents the site for all other species on Ni(211).

Appendix D - Differential Binding Energies of CO on Pt(111)

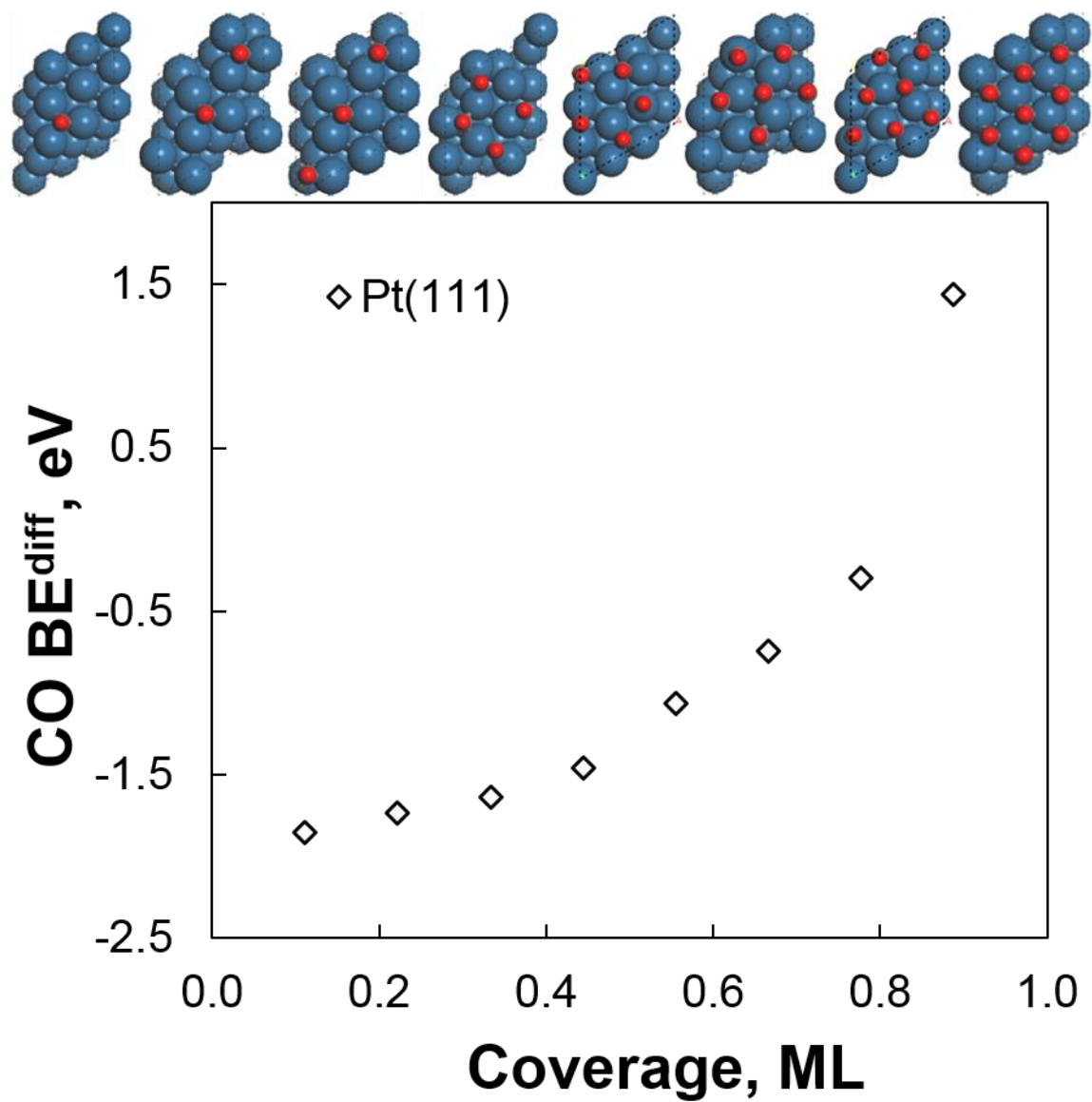


Figure D.1. CO differential binding energies (BE^{diff}) on Pt(111) as a function of surface coverage. Optimized structures at each coverage 1/9, 2/9, 1/3, 4/9, 5/9, 2/3, 7/9, and 8/9ML are shown at the top.